Drift detection in L-PBF process using in-situ monitoring instrumentation and data analytic techniques

Pinku Yadav

To cite this version:

Pinku Yadav. Drift detection in L-PBF process using in-situ monitoring instrumentation and data analytic techniques. Mechanics [physics]. Université de Bordeaux, 2022. English. NNT : 2022BORD0030 . tel-03741173

HAL Id: tel-03741173
https://theses.hal.science/tel-03741173

Submitted on 1 Aug 2022

THÈSE PRÉSENTÉE

POUR OBTENIR LE GRADE DE

DOCTEUR DE

L'UNIVERSITÉ DE BORDEAUX

ÉCOLE DOCTORALE

SPÉCIALITÉ : MÉCANIQUE

Pinku YADAV

Drift Detection in L-PBF Process Using In-situ Monitoring Instrumentation and Data Analytic Techniques

Sous la direction de : Eric LACOSTE
(Co-directrice : Corinne ARVIEU)

February 10, 2022

Membres du jury:

M. KELLER Clément	Professeur, ENIT-Tarbes	Rapporteur
M. SOULIE Fabien	Maître de Conférences HDR, Université de Montpellier	Rapporteur
Mme ARVIEU Corinne	Maître de Conférences HDR, Université de Bordeaux	Co-directrice
Mme BOUVIER Salima	Professeur, Université de Technologie de Compiègne	Président
M. CAHUC Olivier	Professeur, Université de Bordeaux	Examinateur
M. JOFFRE Thomas	Responsable R&D fabrication additive, IPC	Examinateur
M. LACOSTE Eric	Professeur, Université de Bordeaux	Directeur
M. RIGO Olivier	Responsable programme fabrication additive, SIRRIS	Examinateur

DEDICATION

ੴ

To my grandparents,
Meva Devi and *Gahar Singh*
To my parents,
Sushila Devi and *Sajjan Singh*
To my brother and sister-in-law,
Sonu Yadav and *Poonam Devi*
To my beloved Nieces,
Anahat and *Pavika*
To my mentors,
Eric Lacoste, *Corinne Arvieu*, and *Olivier Rigo*

“Luxury and Lies have huge maintenance costs. But Truth and Simplicity are self-maintained without any cost.”
-APJ Abdul Kalam-

ACKNOWLEDGEMENT

By no means was this dissertation possible without the support and kindness of the people involved in ENABLE project, professionally and personally. I would first like to thank my advisors and thesis director Prof. Eric Lacoste, Dr. Corinne Arvieu, and Olivier Rigo, for their advice and continued faith in my abilities. I take this opportunity to acknowledge and show my gratitude to the people who were part of this journey in brief.

SIRRIS, Liege: The journey started in November 2018 with a warm welcome to the additive team at SIRRIS, Liege. During my stay at SIRRIS, Olivier Rigo provided a greater extent in the know-how of the SLM process and the continuous support and guidance daily. Mere words of thanks can never be enough to acknowledge Olivier's Support. However, I will always be indebted to his constant support. The journey in SIRRIS cannot be complete without mentioning the team members and their contributions. I want to thank David, Julien, Bruno from the bottom of my heart, who continuously helped me with the experimental analysis and discussions. Apart from the technical team, I would like to thank Stéphanie Vandermeersch; without her, the administrative paperwork and onboarding could not be imagined. Also, thanks to her, the stay at SIRRIS was more stress-free, especially during the COVID times and Visa problems. Last but not least, thanks to Mario Anneli, my official French tutor (mon meilleur professeur de français), for his continuous support, giving a detailed and informative tour of the Liege and working hard on my French during the coffee breaks.

IPC, Bellignant: I would like to thank my secondment supervisor Thomas Joffre for allowing and helping me during the secondment at IPC. Also, keeping the work going by continuous guidance and suggestions during our exchanges. His support and contribution led us to exploit the very fruitful results, which also got published in a journal.

Bordeaux: Last year at the University of Bordeaux was memorable. I want to thank my supervisors Prof. Eric Lacoste and Dr. Corinne Arvieu, for helping me achieve the results and guiding me with their valuable feedback. No words can do justice to the amount of support and guidance I have received from Prof. Eric Lacoste and Corinne Arvieu in my whole thesis. The interpretation and analysis of the results could not be possible without their know-how and fruitful discussion during the frequent meetings. Starting from the initial phase, active participant and a clear vision led us to complete this project. I would also like to thank Bega Jeremie for helping with EBSD and SEM analysis.

Tecnalia and Lortek: We acknowledge our two partners, Lortek and Tecnalia, contributions for providing the samples for Advanced manufacturing. I would like to thank Pedro from Tecnalia for overseeing my stay at Tecnalia and achieving the results quickly.

No wordly expression can pay gratitude to Prof. Nahum Travitzky from Friedrich Alexander University, Erlangen, who is continuously motivated to work in the AM field. Since my Master's thesis, he has been a continuous path guider for me, and his constant communication during my Ph.D. has always helped me keep going. The amount of affection and compassion shown by him has no words to express.

Enable Team: I would like to thank Prof. Olivier Cahuc and Sara Marin (our Italien Mummy) for providing an excellent opportunity in the ENABLE project. Special Kudos to Sara Marin for making things go well in my case when it was most needed. I would also like to thank all ESRs who have been part of my life in the last three years.

Reviewers: I would pay my sincere gratitude to all my reviewers for their valuable feedback and suggstions that has helped immensely to improve the overall quality of the the present thesis.

At last, I would like to give my highest regards to my family and friends for having been part of this beautiful journey over the years. I wish my grandparents and bhua had been here to see this fulfillment. But they have always showered their kind blessings over me, and I could always hear them in my mind like a clear stream of water in the forest.

मैं आप सभी का तहे दिल से हार्दिक अभिनन्दन करता हूँ। पीएचडी का सफर आप लोगो के सहयोग और मार्ग दर्शन के बिना संभव नहीं था।

Je vous félicite tous chaleureusement. Le voyage du doctorat n'aurait pas été possible sans votre coopération et vos conseils.

ABSTRACT

In recent years, Metal Additive Manufacturing has seen a tremendous paradigm shift from prototyping to batch production and moving forward to serial production due to its ability to produce complex parts easily. Also, metal AM provides a high degree of freedom in design flexibility and functionalities. It is recommended to enhance the commercial machines with quality assurance instruments to achieve the full potential of metal AM. Nowadays, machine suppliers focus on improving quality assurance and providing more insights into the process space with in-situ machine controls. It led to improved part quality, reliability, and repeatability per consumer’s confidence-building measures. However, the full potential of the quality control instrumentation cannot be released if the captured in-situ data is not treated in a meaningful way and correlated with different process steps. It is vital to correlate the in-situ signal to process characteristics such as anomalies to monitor and increase the overall quality of the final part.

This thesis presented a methodology to detect and identify the process anomalies in the Laser-Powder Bed Fusion (L-PBF) process using the commercial in-situ instrumentation. First, it is essential to find the best-suited parameters to study the correlation between the process space, including the process parameters (laser power, scanning speed, feedstock material, etc.) and process outcome (melt pool signals). Initially, an investigation based on the microstructural and mechanical aspects of AlSi7Mg0.6 alloy is carried out, and the best-fit scanning strategy is identified for further study.

Different types of in-situ instrumentation such as infrared cameras and photodiode-based commercial systems are studied to understand the laser-powder interaction better. Camera-based co-axial EOSTATE Optical Tomography supplied by EOS GmbH is exploited, and a case study based on data analytics techniques is proposed to identify the potential drift layers. Similarly, machine learning-based methodology is proposed to extract critical features at a global and local scale for photodiode-based Melt Pool Monitoring in-situ module supplied by SLM Solutions GmbH. As we know, the laser-powder interaction is dependent not only on process parameters but also on the powder bed spread. However, powder bed spread quality can be influenced by feedstock characteristics such as humidity, granularity, .etc. Therefore, it is vital to correlate the metal pool signal to powder spread health to understand better. To do so, the critical characteristics of the powder bed spread are identified using Layer Control System and computer vision algorithms. The proposed methodology successfully identifies powder bed spread anomalies and their influence on the melt pool signal. Also, a case study is presented to investigate the efficiency and robustness of the proposed methodology.

Additionally, to provide the experimental data for the constitutive-based modeling approach (Work Package 1), the thermomechanical response of the L-PBF processed Inconel 718 alloy is investigated. The influence of deformation conditions, i.e., temperatures and strain rates, are studied using hot torsion tests. It is noticed that the deformation conditions strongly influence the microstructural refinement influenced by dynamic recrystallisation and recovery. Also, the material's initial state, such as production state (in our case, the L-PBF process), plays a critical role. The L-PBF processed Inconel 718 samples showed a deformation activation energy of 353 KJ/mol. The samples deformed at 1000℃ showed the highest elongation %, which can be attributed to the dynamic behavior of the material.

Lastly, the feasibility study of the advanced manufacturing combining L-PBF and Laser melt deposition (LMD) processes is presented for Inconel 718. The microstructural and fracture evolution of the samples is studied using the in-situ tensile tests. Alongside, the performance of the interface between two technologies is investigated.

GRAPHICAL ABSTRACT

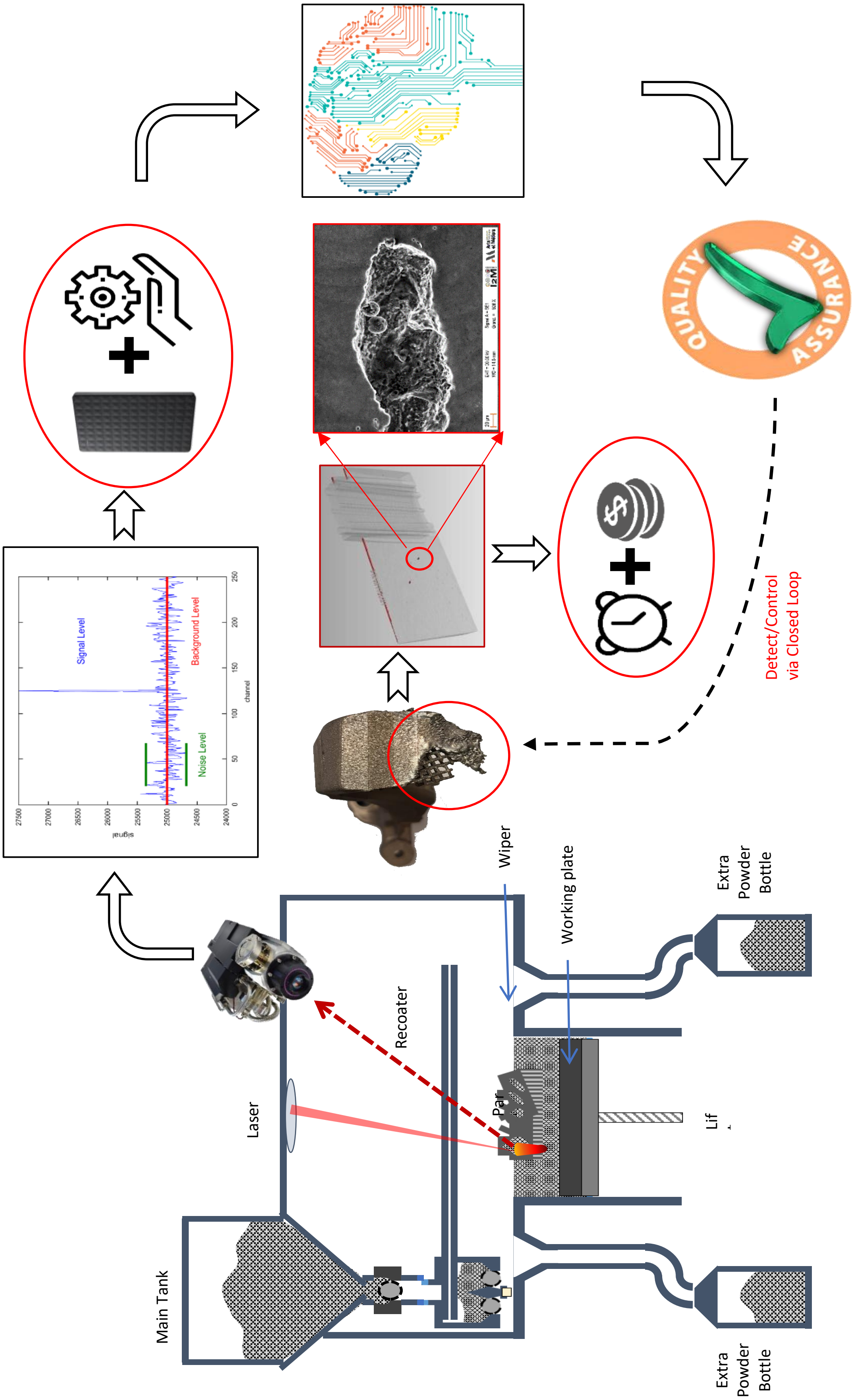

ABBREVIATIONS

ADC	Analog to Digital Converter
AE	Auto Encoder
AI	Artificial Intelligence
AM	Additive Manufacturing
ANN	Artificial Neural Networks
ASTM	American Society for Testing and Materials
ATR	Average True Range
BD	Building Direction
CCD	Charge-Coupled Device
CDRX	Continuous Dynamic Recrystallization
CET	Columnar to Equiaxed Transition
CMOS	Complementary Metal–Oxide–Semiconductor
CNN	Convolutional Neural Network
CSL	Coincidence Site Lattice
CT	Computed Tomography
DBN	Deep Belief Networks
DDRX	Discontinuous Dynamic Recrystallization
DMLS	Direct Melt Laser Sintering
DRV	Dynamic Recovery
DRX	Dynamic Recrystallization
DT	Decision Tree
EMF	Electromotive Force
FGPA	Field Programmable Gate Array
G	Temperature Gradient
GMM-EM	Gaussian Mixture Model- Expectation-Maximization
GOS	Grain Orientation Spread
HAGBs	High Angle Grain Boundaries
HAZ	Heat Affected Zone
IOU	Intersection Over Union
KNN	k-Nearest Neighbors
LAGBs	Low Angle Grain Boundaries
LCS	Layer Control System

LOF	Lack of Fusion
L-PBF	Laser-Powder Bed Fusion
LSTM	Long Short Term Memory
ML	Machine Learning
MPM	Melt Pool Monitoring
NN	Neural Network
OT	Optical Tomography
PC	Principal Component
PCA	Principal Component Analysis
RL	Reinforcement Learning
SD	Scanning Direction
SIFT	Scale Invariant Feature Transforms
SLM	Selective Laser Melting
SVM	Support Vector Machine
TD	Transverse Direction
TGM	Temperature Gradient Mechanism
TI	Texture Index
VED	Volumetric Energy Density
WH	Work Hardening

TABLE OF CONTENTS

Dedication ii
- Acknowledgement iii
- Abstract vi
- Graphical Abstract viii
- Abbreviations ix
- Table of Contents xi
- List of Tables xv
- List of Figures xvi
- CONTEXT OF THE STUDY AND OBJECTIVE ..... - 1 -
- GENERAL INTRODUCTION ..... - 1 -
- Chapter 1 ..... - 7 -

Literature Review ..... - 7 -
- 1.1. General Introduction: Additive Manufacturing ..... - 7 -
  - 1.1.1. Processes ..... - 7 -
  - 1.1.2. Applications ..... - 10 -
  - 1.1.3. Challenges ..... - 11 -
- 1.2. L-PBF Process ..... - 12 -
  - 1.2.1. Defects ..... - 13 -
  - 1.2.2. Process Space ..... - 18 -
  - 1.2.3. Melt Pool Signatures ..... - 21 -
- 1.3. In-Situ Monitoring in L-PBF ..... - 22 -
  - 1.3.1. In Situ Sensing Devices ..... - 23 -
  - 1.3.2. Temperature Correlation ..... - 26 -
  - 1.3.3. In-situ monitoring Systems Configuration Layout ..... - 29 -
- 1.4. Machine Learning in L-PBF ..... - 30 -
  - 1.4.1. Problem Description ..... - 30 -
  - 1.4.2. Introduction to ML ..... - 31 -
- 1.5. In Situ Data Processing Using ML ..... - 33 -
  - 1.5.1. Supervised Learning Approach ..... - 33 -
  - 1.5.2. Unsupervised Learning Approach ..... - 35 -
  - 1.5.3. Semi-Supervised Learning ..... - 35 -
  - 1.5.4. Challenges ..... - 37 -
- 1.6. Materials ..... - 38 -
  - 1.6.1. Al Alloys ..... - 38 -
  - 1.6.2. Inconel 718 Alloy ..... - 42 -
- Chapter 2 ..... - 51 -

Process Optimization for AlSi7Mg0.6 ..... - 51 -
- 2.1. Theory and History ..... - 51 -
- 2.2. Experimental Setup ..... - 53 -
  - 2.2.1. Material ..... - 53 -
  - 2.2.2. Machine and Process Parameters ..... - 53 -
  - 2.2.3. Test Samples ..... - 54 -
- 2.3. Experimental Investigations ..... - 55 -
  - 2.3.1. Porosity ..... - 55 -
  - 2.3.2. Hardness ..... - 55 -
  - 2.3.3. Tensile Tests ..... - 55 -

2.3.4. Micrographic Examination and SEM - 55 -
2.3.5. Cooling Rate - 56 -
2.3.6. Cell Size Measurements - 57 -
2.3.7. Residual Stress Measurements by X-ray Diffraction Technique - 57 -
2.4. Results and Discussion - 58 -
2.4.1. Porosities and Mechanical properties - 58 -
2.4.2. Microstructural Investigations - 60 -
2.4.3. Fractography - 73 -
2.4.4. Residual Stresses - 74 -
2.5. Conclusions - 77 -
Chapter 3 - 79 -
Optical Tomography In-Situ Monitoring Module - 79 -
3.1. Definitions - 79 -
3.2. Theory - 80 -
3.2.1. K-Means Clustering - 80 -
3.2.2. K-Nearest Neighbour Classifier - 81 -
3.2.3. Distance Metrics - 81 -
3.3. Materials and Methods - 82 -
3.3.1. In-Situ Monitoring Module: EOSTATE OT - 82 -
3.3.2. Materials and Methods - 83 -
3.3.3. Image Analysis - 84 -
3.4. Semi-Supervised Learning Approach - 87 -
3.4.1. Initial Data Labeling and Suitable Distance Metric Selection Through K-means Clustering Algorithm - 87 -
3.4.2. Number of Nearest Neighbor Parameter Selection for k-NN Classifier - 89 -
3.5. Results and Discussions - 90 -
3.5.1. Testing on Certified Data - 90 -
3.5.2. Case Study 1: Benchmark Part - 91 -
3.5.3. Case Study 2: Industrial Case Automotive Steering “Knuckle.” - 92 -
3.6. Conclusions - 93 -
Chapter 4 - 95 -
Melt Pool Monitoring - 95 -
4.1. In-Situ Monitoring MPM Set-Up - 95 -
4.2. Sensitivity Analysis of MPM - 96 -
4.2.1. Volumetric Energy Density Sensitivity Analysis - 96 -
4.2.2. Down-Skin Sensitivity Analysis - 97 -
4.2.3. Varying Hatch distance - 98 -
4.3. Data analytics for MPM Data: Global Scale - 99 -
4.3.1. Theory - 99 -
4.3.2. Process Parameters and Part Geometry - 101 -
4.3.3. Definitions - 102 -
4.3.4. Training Data Preparation - 102 -
4.3.5. Bayesian Optimization and Training of SVM Classifier - 102 -
4.3.6. Results and Discussions - 104 -
4.4. Data Analytics: Local Scale - 107 -
4.4.1. Materials and Parts - 107 -
4.4.2. Pre-Processing of the Data - 108 -
4.4.3. Removal of Outliers. - 110 -

4.4.4. Data Selection for Model Training ..... - 110 -
4.4.5. Architecture of LSTM ..... - 111 -
4.4.6. Training and Validation ..... - 114 -
4.4.7. Case Study ..... - 115 -
4.5. Conclusions ..... - 118 -
4.6. Statistical Approach: Global Scale ..... - 118 -
Chapter 5 ..... - 122 -
Layer Control System (LCS) ..... - 122 -
5.1. LCS Setup ..... - 122 -
5.2. Terminology ..... - 123 -
5.3. Types of Machine Learning Models ..... - 123 -
5.4. Approach 1: Image processing using CNN models ..... - 124 -
5.4.1. Theory ..... - 124 -
5.4.2. Image Processing ..... - 129 -
5.4.3. Anomalies Description ..... - 131 -
5.4.4. Scale Variant of Anomalies in Pre and Post-Exposure Cases ..... - 132 -
5.4.5. Training and Testing of Models ..... - 133 -
5.4.6. Case study ..... - 136 -
5.4.7. Limitations of CNN models ..... - 140 -
5.5. Approach 2: Image processing using Semantic Segmentation ..... - 141 -
5.5.1. Semantic Segmentation Using UNet ..... - 141 -
5.5.2. Residual Networks ..... - 141 -
5.5.3. Combination of ResNet and UNET ..... - 142 -
5.5.4. Training Dataset ..... - 142 -
5.5.5. Model Training ..... - 143 -
5.5.6. Case Study ..... - 145 -
5.6. Relation between MPM and LCS ..... - 147 -
Example 1: Benchmark Part ..... - 148 -
Example 2: Ti6Al4V Cubes ..... - 150 -
5.7. Conclusions ..... - 151 -
Chapter 6 ..... - 152 -
Thermomechanical deformation of SLMed Inconel 718 ..... - 152 -
6.1. Theory and Background ..... - 152 -
6.2. Experimental ..... - 154 -
6.2.1. Material and Methods ..... - 154 -
6.2.2. Torsion Tests ..... - 155 -
6.2.3. Microstructural Observations ..... - 156 -
6.3. Results ..... - 156 -
6.3.1. Analysis of Stress-Strain Curves ..... - 156 -
6.3.2. Critical Stress and Strain ..... - 158 -
6.3.3. Zener-Holloman Parameter and Activation Energy ..... - 160 -
6.3.4. Microstructural Investigations ..... - 162 -
6.3.5. Recrystallization Mechanism ..... - 172 -
6.4. Conclusions ..... - 176 -
Conclusions ..... - 178 -
Future Outlook ..... - 182 -
..... - 182 -
References ..... - 184 -

Appendix .... - 198 -
A.1. Experimental Set-Up .... - 198 -
A.1.1. Material .... - 198 -
A.1.2. Machine .... - 198 -
Selective Laser Melting (SLM) .... - 198 -
Laser Melt Deposition (LMD) .... - 198 -
A.1.3. Specimen Geometry .... - 199 -
A.1.4. Process Parameters .... - 200 -
A.1.5. Analysis .... - 200 -
A.2. Results .... - 201 -
A.2.1. Process parameter optimization .... - 201 -
A.2.2. Layer height optimization .... - 203 -
A.3. Bibliography .... - 203 -
Résumé .... - 204 -

LIST OF TABLES

Table 1: Categories of the AM processes and their capabilities. - 8 -
Table 2: List of literature on the processing of L-PBF in-situ data using machine learning approaches. - 36 -
Table 3: Equations for analytical models. - 40 -
Table 4: Inconel 718 alloy composition and the effect of the alloying elements [96]. - 43 -
Table 5: Phases in Inconel 718 and its composition [98]. - 44 -
Table 6: ASTM F3055 recommended heat treatment for AM Inconel 718. - 50 -
Table 7: Elemental composition of as received AlSi7Mg0.6 powder (All the values are given in wt. %).
Table 8: Process parameters used in this study. - 53 -
Table 9: Nomenclature of the samples used in this study. - 54 -
Table 10: Process parameters for the printing. - 84 -
Table 11: Performance of the different distance metrics on certified data. - 88 -
Table 12: Process parameters. - 101 -
Table 13: The performance and accuracy % of the different hyperparameters. - 103 -
Table 14: Process parameters used for Ti6Al4V samples (Optimized parameters are marked in bold). - 107 -
Table 15: LSTM-AE architecture used in this study. - 113 -
Table 16: The decision matrix for scale 2 and scale 3 labels. - 135 -
Table 17: Chemical composition of Inconel 718 powder. - 154 -
Table 18: Process parameters used for this study. - 154 -
Table 19: Hot torsion test conditions. - 155 -

LIST OF FIGURES

Figure 1: Objective summary of ENABLE project. .... - 1 -

Figure 2: Main objective of the thesis. .... - 3 -

Figure 3: Outline of the thesis. .... - 6 -

Figure 4:(a) Schematic diagram of L-PBF process [5], (b) Laser-melt interaction region [7]. .... - 13 -

Figure 5: Micrographs of defects observed in L-PBF such as (a) gas porosities [10], (b) key hole porosity [12], (c) lack of fusion defect [10], (d) balling [22], and (e) thermal crack [30]. Reused under Creative Commons Attribution License. .... - 14 -

Figure 6: (a) Temperature gradient mechanism during laser heating, (b) representation of the evolution of thermal stress and strains in the irradiated zone (c) Evolution of stresses during solidification phase, (d) representation of the evolution of residual stresses and strain in the irradiated zone [26]. Reused under Creative Commons Attribution License. .... - 17 -

Figure 7: Relative density as a function of energy density [39]. Reused under Creative Commons Attribution License. .... - 19 -

Figure 8: Effect of scanning strategies and scan speed on the porosity % of AlSi10Mg parts [40]. Reused under Creative Commons Attribution License. .... - 20 -

Figure 9: Illustration of types of emitting radiation from melt pool. .... - 21 -

Figure 10: Wavelength response of detectors. .... - 23 -

Figure 11: Schematic of working principle of PIN photodiode [47]. .... - 24 -

Figure 12: Wavelength sensitivity of common detectors. .... - 25 -

Figure 13: Spectral radiance of an ideal black body at different temperatures [47]. .... - 27 -

Figure 14: Schematic layout for on-axis monitoring. .... - 29 -

Figure 15: Off-axis layout of the sensors. .... - 30 -

Figure 16: List of Machine Learning algorithms. .... - 32 -

Figure 17: The phase diagram of Al-Si [76]. .... - 39 -

Figure 18: (a) Solidification map, showing the effect of temperature gradient and growth rate [82], (b) Suppression of dendrites during high solidification rates [83], and (c) schematic of primary dendrite arm spacing (PDAS), and secondary dendrite arm spacing (SDAS) [84]. .... - 40 -

Figure 19: (a) Microstructure of melt pool, and (b) its corresponding eutectic cells. .... - 41 -

Figure 20: Dark field TEM image of γ'' precipitates [99]. .... - 45 -

Figure 21: Delta phase formation in Inconel 718 by (a) cellular precipitation at <700 °C, (b) cellular precipitation and transformation from γ ″ at 750-800 C, (c) direct precipitation from the γ′ matrix at 960 °C, and (d) laves phase. .... - 46 -

Figure 22: (a) Solidification path [123], and (b) its constituents [124]. .... - 48 -

Figure 23: Solidification map for Inconel 718 [125]. .... - 49 -

Figure 24: Schematic of the scanning strategies (a) stripes with rotation of 67°, (b) chessboards with (0°) no rotation, (c) chessboards with 90° rotation, and (d) chessboards with 45° rotation. .... - 54 -

Figure 25: Schematic for rosenthal equation. .... - 56 -

Figure 26: Effect of scanning strategies on (a) porosity (b) vicker's hardness. .... - 58 -

Figure 27: Optical micrograph of C_10*10_90 sample in (a) building direction, (b) transverse direction, (c) SEM image of LOF defect observed at the junction of the island, and (d) sample orientation. .... - 59 -

Figure 28. Effect of the scanning strategies on yield strength, ductility, tensile strength. .... - 60 -

Figure 29: An example of the phase morphology in AlSi7Mg0.6 .... - 61 -

Figure 30: Optical micrograph of as-built C_5*5_45 (a) transverse, (b) building direction. (SD: Scanning direction, TD: Transverse direction, BD: Building direction). .... - 61 -

Figure 31: SEM micrographs of S_10_67 sample in (a, b) building direction and (c, d) transverse direction. .... - 62 -
Figure 32: SEM images of the melt pool for sample showing the three distinct regions i.e. fine (1), coarse (2) and HAZ (3) regions. .... - 63 -
Figure 33: Example of cooling rates variation inside the melt pool. Also, the numbers mark the location of the measurements of the cells. .... - 64 -
Figure 34: (a) Cell spacing and (b) calculated cooling rates. In X-axis, the numbers denote the location within the melt pool i.e. 1: Top edge, 2: Centre, 3: Bottom edge, 4: Coarse region of the melt pool. Also marked in Figure 33. .... - 65 -
Figure 35: IPF images showing the grain morphology for samples (a)S_5_67, (b)S_10_90, (c)S_10_45, (d)S_10_67, (e)C_3*3_no, (f) C_2*2_no, (g) C_10*10_no, (h) C_5*5_no, (i) C_10*10_90, and (j) C_5*5_45. .... - 66 -
Figure 36: Average grain size. .... **Error! Bookmark not defined.**
Figure 37: Area fraction of LAGBs and HAGBs. .... - 67 -
Figure 38: Texture index of the samples. .... - 68 -
Figure 39: Mackenzie plot comparison. .... - 69 -
Figure 40: Intensity pole figures for samples (a) C_2*2_no, (b) C_3*3_no, C_5*5_no, and C_10*10_no. .... - 70 -
Figure 41: Intensity pole figures for samples (a) S_5_67 and (b) S_10_67. .... - 71 -
Figure 42: Intensity pole figures for samples (a) S_10_45, and (b) S_10_90. .... - 72 -
Figure 43: Intensity pole figures for samples (a) C_5*5_45, and (b) C_10*10_90. .... - 72 -
Figure 44: SEM micrographs of fracture surface for (a) S_10_90, (b) S_10_67, (c) C_10*10_no, and (d) C_10*10_90. .... - 73 -
Figure 45: Fracture surface for samples (a) S_10_67, and (b) C_10*10_no at different magnifications. - 74 -
Figure 46: (a) Location of the measurement points i.e. Start, Centre, and End (marked in red circles), (b) schematic of the measurement directions based on laser scan track. .... - 75 -
Figure 47: Change in residual stresses based on the location of the measurement points at the surface of the parts. .... - 75 -
Figure 48: Comparison of start and end edges in (a) transverse, (b) longitudinal directions. (1: S_5_67, 2: S_10_67, 3: S_10_90, 4: S_10_45, 5: C_2*2_no, 6: C_3*3_no, 7: C_5*5_no, 8: C_10*10_no, 9: C_5*5_45, 10: C_10*10_90) .... - 76 -
Figure 49: Change in residual stresses based on the location of the measurement points at the 2 mm depth of the parts. .... - 76 -
Figure 50: Schematic diagram of the EOSTATE exposure module. .... - 83 -
Figure 51: The CAD design of (a) An automotive steering knuckle (3d printed within the framework of the European project Maestro [36]), the length of this part is approximately 500 mm, only a section was 3D printed, (b) benchmark used to determine the critical overhanging angle in additive manufacturing processes. .... - 84 -
Figure 52: (a) Mean, and (b) variance per layer for the case study part “Knuckle”. .... - 85 -
Figure 53: Example picture of (a) OT image without hotspots, (b) CT image of corresponding layer (a) without hotspots, (c) OT image with hotspots, (d) CT image of corresponding layer (c) with hotspots, and (e) histogram comparison between (a) and (c). .... - 86 -
Figure 54: Flowchart for extraction of features from the OT pictures. .... - 86 -
Figure 55: Clustering using (a) correlation, (b) cosine, (c) city block, and (d) squared Euclidean distance metrices. .... - 89 -
Figure 56: Accuracy versus k plot for the k-NN classifier. .... - 90 -

Figure 57: (a) CAD geometry, (b) Labels predicted by the k-NN model, and (c) printed part geometry with drift layers (in bright color) . ... - 91 -
Figure 58: (a) Labels predicted by the k-NN model, (b) part geometry with drift layers (in bright color), and (c) location of the hot spot (marked in white color) in the drift layer. .... - 92 -
Figure 59: (a) Labels predicted by the k-NN model, and (b) printed part geometry with overheated region........ - 92 -
Figure 60: Schematic of Melt pool monitoring system, and Layer control system installed on SLM 280HL........ - 96 -
Figure 61: The mean thermal emissions recorded by MPM systems for the induced drift detection in the specimens shown in right corner of graphs (dark red color: drift area, red area: optimized processed parameters)........ - 97 -
Figure 62: Scan vector wise MPM signal for down-skin layer for (a) cylindrical sample, (b) cuboid sample. .... - 97 -
Figure 63: MPM signal for different hatch distances (a) 0.13 mm, (b) 0.26 mm, (c) 0.52 mm, (d) Overall comparison of hatch distances. .... - 98 -
Figure 64: Schematic of the hyperplane that maximally separates the support vectors corresponding to each of the two classes. .... - 99 -
Figure 65: (a) hard margin on linearly separable dataset where no training errors are allowed. (b) the soft margin where two training errors are permitted to make data non-linearly separable. .... - 100 -
Figure 66: Sketch of the specimens (a) cubic overhang (size 10*10 *10 mm3), (b) cylindrical overhang (diameter: 10 mm and height 10 mm), (c) specimen with inner groove, and (d) Benchmark part (125*125*775 mm3). .... - 101 -
Figure 67: (a) The un-clustered training dataset, and (b) labels predicted by the trained fine gaussian SVM classifier model. .... - 103 -
Figure 68: ROC-AUC curve for the trained SVM classifier on 600 training data. .... - 104 -
Figure 69: SVM model predicted labels for (a) cubic overhang specimen, and (b) cylindrical specimen.
Figure 70: (a) Predicted labels for the lack of fusion defect, (b) optical micrograph of the defect.- 105 -
Figure 71: SVM classifier predicted labels for benchmark part for (a) photodiode 1, (b) photodiode 2, and (c) printed benchmark part. .... - 106 -
Figure 72: Process window for SLM Ti-6Al-4V powder. .... - 108 -
Figure 73: Example of (a) raw, and (b) pre-processed ADC2 signal for layer 31........ - 109 -
Figure 74: CT scan corresponding to layer 31 (approximately) and its raw data for ADC2 is shown in Figure 73........ - 111 -
Figure 75: Schematic of LSTM-AE........ - 112 -
Figure 76: Loss distribution obtained during training. .... - 115 -
Figure 77: CT scan projections in (a) X-Y plane, (b) Y-Z plane, (c) X-Z plane, (d) Isometric, and (e) as-printed sample. .... - 116 -
Figure 78: Anomalies predicted by proposed model Vs layer number........ - 116 -
Figure 79: (a) CT scan, (b) hotspots shown by MPM viewer and (c) hotspot predicted by the proposed model for layer 575. .... - 117 -
Figure 80: (a) X-Z projection (Hot spots are depicted by black points) and (b) isometric 3D projection (hotspots are marked by dark yellow) of the hotspots predicted from the proposed methodology (Figures are not subject to scale). .... - 117 -
Figure 81: Schematic diagram of the proposed methodology........ - 118 -
Figure 82: Volatility plot (ATR) for the benchmark part shown in Figure 71c........ - 119 -
Figure 83: Volatility plot (ATR) for the overhang part........ - 120 -
Figure 84: (a) Volatility variance, and corresponding (b) as-built Ti6Al4V part. .... - 120 -
Figure 85: Types of computer vision models for image classification. .... - 124 -

Figure 86: Schematic of the proposed convolutional neural network used in this study..............- 125 -
Figure 87: Example of calculation of a convolution layer. ....- 126 -
Figure 88: Example of a Max pooling operation. ....- 127 -
Figure 89: Block diagram proposed CNN architecture used in this study....................................- 129 -
Figure 90: An Example of (a) captured raw image, and (b) pre-processed image.........................- 131 -
Figure 91: An example of anomalies extracted from pre-exposure images (a)Part-Hopping, (b) Recoater streaking, (c) Uneven powder spreading, (d) OK powder layer, and (e) OK part layer. ..- 131 -
Figure 92: An example of anomalies extracted from post-exposure images (a)Part-overheating, (b) Recoater streaking, (c) Uneven powder spreading, (d) OK powder layer, and (e) OK part layer. ..- 132 -
Figure 93: An example of scale variance of different types of anomalies is shown. Red box represents the scale 1 of size 20*20 px2 whereas the scale 3 represented by green box which has size of 150*150 px2. ....- 133 -
Figure 94: Flow chart for labeling the pre-exposure test images. ....- 134 -
Figure 95: Flow chart for labeling the post-exposure test images..- 135 -
Figure 96: Confidence matrices for trained CNN models for (a) pre-exposure images, and (b) post-exposure images..- 136 -
Figure 97: (a) The percentage of pre-exposure anomalies predicted by the CNN model along the build height, (b) An pre-exposure image example showing the exact location of predicted anomalies (Red: “Uneven Powder Spreading”, Green: “Part-Hopping”, and Blue: “Recoater streaking.” ....- 138 -
Figure 98: (a) The percentage of anomalies predicted by the CNN model along the build height, (b) A post-exposure image example showing the exact location of predicted anomalies (Red: “Uneven Powder Spreading”, Green: “Part-Overheating”, and Blue: “Recoater-Streaking”) for layer 2580..- 139 -
Figure 99:The schematic representation of (a) standard CNN block, and (b) residual block. ....- 141 -
Figure 100: Graphical representation of Res34-UNet used in this study [207]. ....- 142 -
Figure 101: (a) Raw pre-exposure image with types of anomalies (marked by arrows), and (b) corresponding labeled image...- 143 -
Figure 102: Graphs showing predicted anomaly % for (a) Overheating, (b) Recoater streaking, and (c)Uneven powder spread...- 146 -
Figure 103: Example of Res-UNet anomalies prediction for layer number 577 (a) raw pre-exposure image, and (b) corresponding predicted labels...- 147 -
Figure 104: Screenshot from MPM viewer showing presence of hotspots in layer 2561 for (a) Photodiode 1 with higher thermal emission values, and (b) Photodiode 2, (c) the pre-exposure powder spread image, and (d) post-exposure image. ....- 148 -
Figure 105: Screenshot from MPM viewer showing presence of hotspots in layer 559 for (a) Photodiode 1 with higher thermal emission values, and (b) Photodiode 2, (c) the pre-exposure powder spread image, and (d) corresponding predicted labels. ....- 150 -
Figure 106: (a) Heat treatment profile, (b) As built sample and heat-treated machined test sample. ...- 155 -
Figure 107: (a) Deformed samples, (b) Stress-strain curves for the deformed samples. ....- 157 -
Figure 108: (a) Smoothened stress-strain curve for sample deformed at temperature of 1000 °C and strain rate of 0.1 s-1, (b) indication of critical stress and critical strain on the flow curve, (c) plot of θ vs σ, and (d) plot of $\partial\theta\partial\sigma$ vs σ. ....- 159 -
Figure 109: Relationship between peak strain and critical strain. ....- 160 -
Figure 110: Plots of (a) ln $\dot{\epsilon}$ vs σp, (b) ln $\dot{\varepsilon}$ vs lnσp,(c) ln $\dot{\epsilon}$ vs lnsinh (ασp), and (d) ln($\dot{\epsilon}$)-ln(sinh(α*σp)..- 161 -
Figure 111: Heat treated samples perpendicular to build direction (a,b), and along build direction (c,d)...- 162 -

Figure 112: IPF maps for samples (a) Heat treated undeformed, (b) 1000 °C-0.01s^{-1}, (c) 1000 °C-0.1s^{-1}, (d) 1000 °C-1s^{-1}, (e) 1100 °C-0.01s^{-1}, (f) 1100 °C-0.1s^{-1}, and (g) 1100 °C-1s^{-1}. .... - 164 -
Figure 113: Average grain size of the samples along with the elongation (%). .... - 165 -
Figure 114: Misorientation angle distribution of the samples. .... - 166 -
Figure 115: Average area fraction for annealing twins in the deformed samples. .... - 167 -
Figure 116: (a) Twin boundary per grain, (b) twin density for the deformed samples. .... - 168 -
Figure 117: (a) Grain boundary character distribution, (b) Interaction between annealing twins in a grain for sample deformed at 1100 C and stain rate 0.1 s-1 (Black lines: Σ3 boundaries, Blue lines: Σ9, Brown line: Σ27). .... - 169 -
Figure 118: Twin boundaries marked in blue presented for samples. The arrows indicated the evolution of twins behind the moving grain boundary. .... - 170 -
Figure 119: Area fraction of the DRX/undeformed grains and deformed grains based on GOS. ... - 171 -
Figure 120: Optical micrographs of etched samples deformed at 1100 °C and strain rate, (a) 0.01 s-1, (b) 0.1 s-1. .... - 172 -
Figure 121: Grains indicating the lines in the grains for cumulative misorientation presented in Figure 122. .... - 173 -
Figure 122: Cumulative misorientation for the lines indicated in Figure 121 (a, b) Line A1 &A2, (c, d) Line B1 & B2, (e, f) Line C1 & C2, (g, h) Line D1 & D2. (i, j) Line E1 &E2, and (k, l) Line F1 & F2, respectively. .... - 175 -
Figure 123: Evolution of inner grains for samples deformed at 1100 C and strain rates of (a) 0.01 s-1, (b) 0.1 s-1, and 1s-1. .... - 176 -
Figure 124: Feedback control loop for L-PBF process. .... - 183 -

CONTEXT OF THE STUDY AND OBJECTIVE

GENERAL INTRODUCTION

European **N**etwork for **A**lloys **B**ehaviour **L**aw **E**nhancement (ENABLE) is an H2020 MARIE SKŁODOWSKA-CURIE ACTIONS ITN project, divided into 3 WP, each WP comprising 3 Thesis (ESR). The ENABLE project's main objective is to understand better complex Multiscale Multiphysics phenomena in materials involving manufacturing processes (Machining, Friction Stir Welding, Additive Manufacturing) using sophisticated experimental equipment and modeling tools (Figure 1). The findings of ENABLE can be used to create specifically tailored material microstructures to understand material properties and residual stress states to improve the components' performance. These advances will lead to the development of new tools, service life, improved tools, etc., and will reduce production time and thereby production costs.

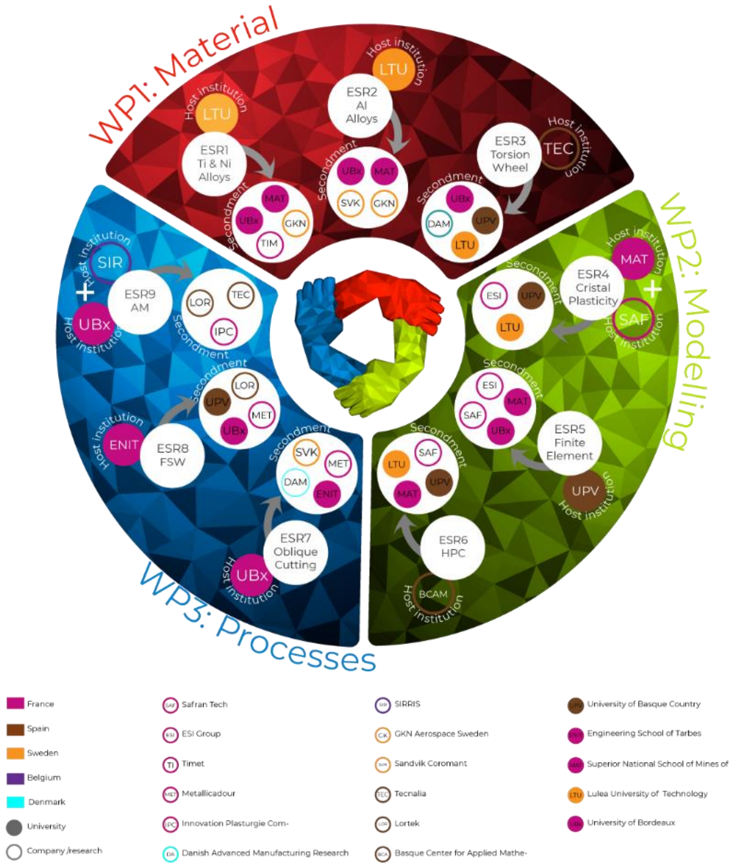

Figure 1: Objective summary of ENABLE project.

Work Package 1: WP1 (Material properties) includes all metallurgical aspects (hardening, grain size, precipitation, phase transformation, etc.). This section aims to study the microstructural evolution of selected alloys during extreme solicitations. The aim is to provide local material behavior laws for selected alloys coupled with models for microstructure evolution. WP1 includes ESR1, ESR2, and ESR3.

Work Package 2: WP2 (Numerical modeling) aims to develop a new finite element (based on the theory of strain gradients) enabling thermo-mechanical and microstructural coupling. This multiscale modeling will then be optimized for high power computing and implemented in digital simulation software for new generation processes. WP2 includes ESR4, ESR5, and ESR6.

Work Package 3: WP3 (Industrial processes: FSW, AM, Machining) aims to provide solutions to the complex behavior of the materials undergoing manufacturing processes such as machining, friction stir welding, and additive manufacturing. WP 3 is dedicated to identifying and measuring physical quantities such as temperature and kinetic fields for standard test cases and understanding and improving the processes. WP3 includes ESR7, ESR8, and ESR9, which is the topic of this manuscript.

AM has enormous applications, and the market is growing day by day. The need for robust supply chain and enhanced quality assurance is required. Rapid growth in the development of new alloys specifically for AM process has also pressed the question of quality assurance like never before. Understanding the laser-material interaction is also essential as new material is being developed for the AM process.

L-PBF involves complex interactions between the laser and metal powders, and additive manufacturing processes involve coupled physical phenomena of thermal (with phase changes related to the melting phenomena of metal powders and the solidification of the liquid metal), metallurgical (diffusion phenomena), mechanical (presence of residual stresses due to temperature gradients during the process) and hydrodynamic (convection in the melting bath). From a metallurgical point of view, the L-PBF process involves rapid melting-solidification kinetics of small-sized (<1 mm) melt zones, leading to very specific microstructures. Finally, the improved quality assurance and process reliability with the current commercial systems can only be possible with a better understanding of these systems and the development of models to control the quality inline.

The main objective of the thesis is to study the phenomena induced by laser/powder interactions, on the one hand from in situ instrumentations allowing a real-time observation and on the other hand from more classical post-mortem characterization tests. All the experimental results are used to develop models for detecting defects and to feed the models of behavior laws developed by the other ESR of the project (Figure 2). Experimental studies have been carried out on the equipment available with the various partners of this work. Instrumented SLM machines and experimental test benches have been used to reproduce fusion kinetics observed in additive manufacturing on powder beds. The reference alloy of the study is AlSi7Mg0.6, but we have also developed some works based on Inconel 718 and steel.

The tasks performed at the partner's corner are summarized as follows:

- **SIRRIS, Belgium:** To set-up test cases and validate the methodology for photodiode-based monitoring systems installed on SLM 280^{HL}. Also, to investigate the mechanical testing and residual stress measurements to select optimized processing parameters.
- **University of Bordeaux, France:** Study the evolution of the metallurgical phenomena concerning the varying process parameters, experimental analysis of thermomechanical behavior, and validation of the results based on the literature study.
- **IPC, France:** Study and development of models for optical-based monitoring equipment installed on EOS M290 machine.
- **Lortek, Spain:** Manufacturing of SLM samples for the studies concerning Inconel 718.

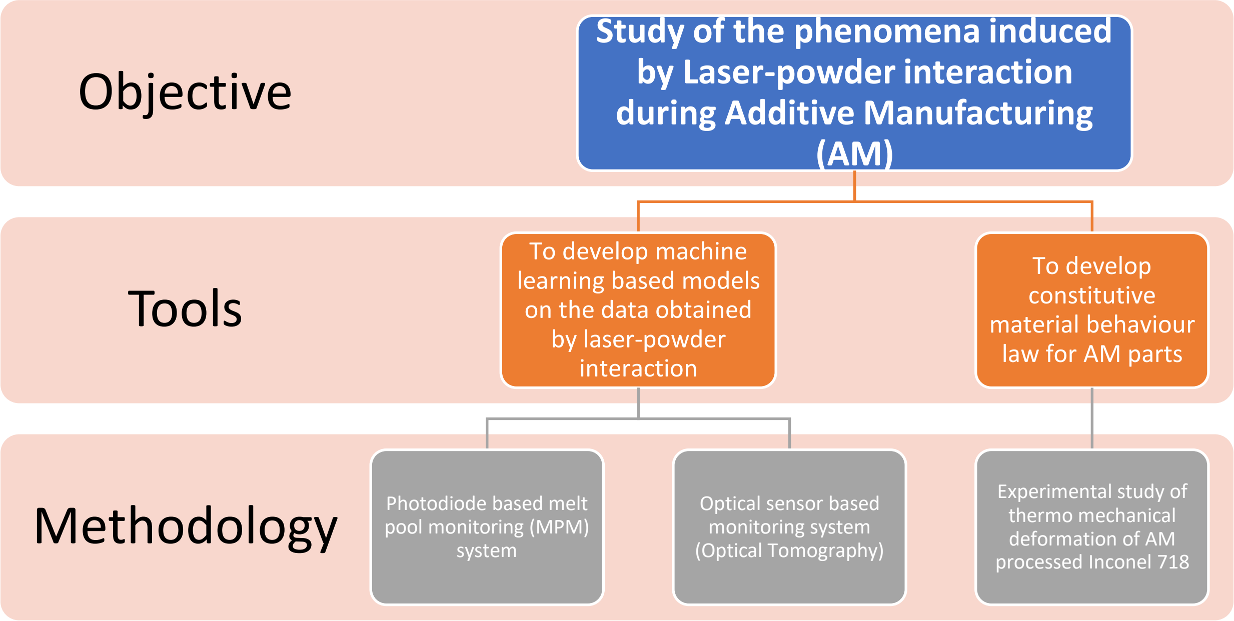

Figure 2: Main objective of the thesis.

- **Tecnalia, Spain:** Feasibility study of the future perspective involving advanced manufacturing of the Inconel 718.

For our study, we exploited the commercially available in-situ monitoring modules (MPM, LCS, OT) from EOS GmbH and SLM Solutions, respectively. The working principle of the in-situ sensing modules is discussed in the respective chapters.

The outline of the thesis can be divided into below parts and also summarized in Figure 3:

The **first chapter** presents a detailed literature review study showing the conclusive evidence of this study's need. Also, in the literature review, we try to give a basic understanding of the L-PBF process and its process space, including the solidification behavior for Al alloys and Inconel 718 Alloys used in our study. Moreover, the terminology related to machine learning and in-situ monitoring devices is also presented.

The **second chapter** provides the base for the investigations on the next steps related to the laser-material interaction. Choosing a set of process parameters used in further experiments is crucial for data acquisition systems. Therefore, this chapter chooses the best-fit process parameters for AlSi7Mg0.6 (primary alloy for our study) and investigates the microstructural and mechanical behavior with different scanning strategies and parameters.

The **third chapter** focuses on the camera-based in-situ monitoring module called “EOSTATE Optical Tomography” supplied by EOS GmbH. We utilized a semi-supervised learning method to explore how to identify the drift layers in the printed parts.

The **fourth chapter** explores the sensitivity analysis and advances of the photodiode-based in-situ monitoring module supplied by SLM solutions. Firstly, we have used a supervised learning method to identify the layers with probable drifts called the global approach. Then, the exact location of the highest potential areas of the drift within the layers is identified using LSTM models. This approach is termed the local approach.

The **fifth chapter** is focused on another monitoring system called “Layer Control System (LCS)” provided by SLM solutions. The LCS system focuses on monitoring the key characteristics of the powder bed spreadability. Locally spatial variation in powder bed can significantly influence the laser-material interaction. In the end, we presented a case study to interlink the MPM data and LCS data to enhance quality assurance.

The **sixth chapter** is vital for developing the constitutive material behavior law for AM parts. As mentioned earlier, the thesis is an integral part of the project ENABLE, so it is imperative to share and communicate the results among different partners. Therefore, we have investigated the thermomechanical deformation of the L-PBF processed Inconel 718 parts using hot torsion tests to fulfil the requirement. The experimental results will provide a basis for developing relevant material behavior models. The choice of the Inconel 718 is made based on the Project ENABLE requirements and to collaborate with other WPs.

In the **appendix**, we have presented a short overview of the future perspective of AM technology. A feasibility study on the development of parts combining two AM processes, i.e., L-PBF and LMD, is carried out.

Finally, the thesis conclusion highlights the key finds and presents the future possibilities. Also, the research findings in context of the L-PBF process and their contribution to industrial and academic work are discussed.

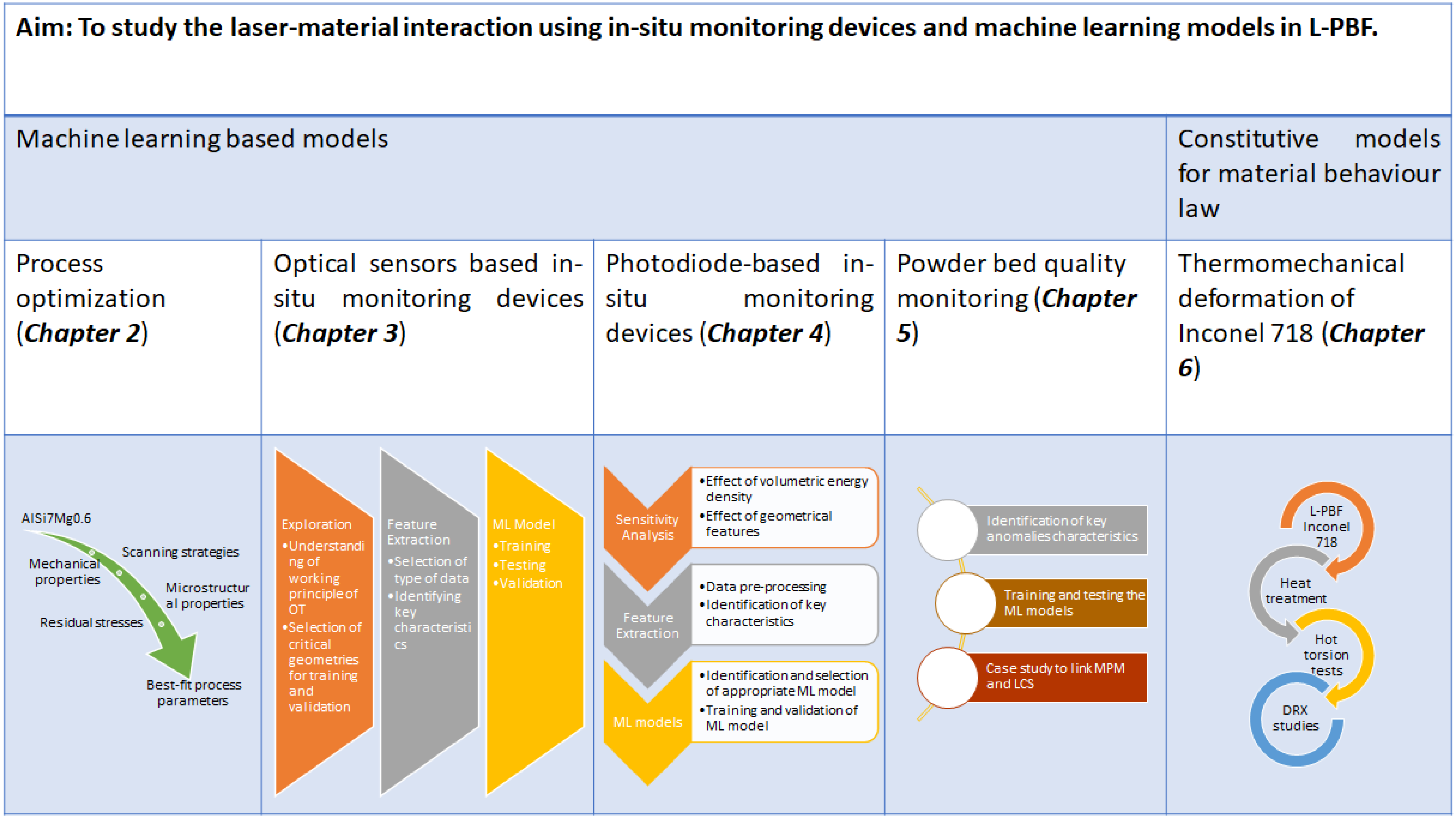

Figure 3: Outline of the thesis.

CHAPTER 1

Literature Review

> *“Additive Manufacturing (AM), or colloquially known as “3-Dimensional Printing,” is the general term for the manufacturing process that enables complex 3D parts to be created by adding material where needed rather than subtracting material where it is not. Usually, this is achieved in a layer-by-layer manner in which each layer further consists of line tracks deposited or solidified adjacent to each other. This complex 1D to 2D to 3D approach opens up the field for much more complicated designs. It introduces physical and metallurgical phenomena specific to this manufacturing process, as will be made clear further on. Laser-Powder Bed Fusion (L-PBF) or Selective Laser Melting (SLM) is one such AM process studied throughout the research. The comparison of the L-PBF process with other AM processes and its particularities for completing this project are highlighted and discussed in this Introduction section. Also, the advantages and disadvantages and the current applicability and future outlook of the process are discussed, which will clarify the need for the research conducted in this project. To conclude, the aim of this research is explained, and the methodology followed to achieve the stipulated goals.*

1.1. General Introduction: Additive Manufacturing

1.1.1. Processes

According to the ASTM F42 committee, AM process is defined as *“the process of joining materials to make objects from 3D model data, usually layer upon layer, as opposed to* *subtractive manufacturing methods"* [1]. It is widely accepted definitions of the processes formerly described as 'Rapid Prototyping' or 'Rapid Tooling' [2]. It gained attraction with the invention of stereolithography by Chuck Hull in 1986 [3]. Stereolithography was initially intended to fabricate polymer-based prototypes at pace, which led to the early name of "Rapid Prototyping or Rapid Tooling." Over the years, the technological progress in the technique led to the development of new processes which allowed the fabrication of metal and ceramics parts. Nowadays, state-of-the-art parts fabricated using AM processes are being used in various niche industries such as aerospace, biomedical and automotive. The acceptance of AM parts in these critical industries provide evidence of the economic viability of the AM processes. All AM processes work on the primary working principle of fabricating 3D structure by adding layers of raw material on top of each other, in contrast to traditional manufacturing techniques such as subtractive and molding. However, all AM processes differ based on feedstock, deposition technique, and consolidation mechanism. The International Organization Standardization (ISO) has categorized the AM processes into 7 classes as listed in Table 1 based on all these mentioned factors [4]. The table summarizes the feedstock type, deposition mechanism, and qualitative comparison of cost, printing speed, resolution, and performance.

Table 1: Categories of the AM processes and their capabilities.

Category Name	Material	Material Form	Working Mechanism	Cost	Speed	Resolution	Performace
Material Extrusion	Polymer	Wire	Warm extrusion of polymer wire fed through a heated nozzle.	+++	0	-	-
Material Jetting	Polymer	Liquid	Material is deposited in droplet form through heated nozzle	0	-	+	-
Binding Jetting	Sand Metal Ceramic	Powder	Binder in droplet form deposited on the powder bed, followed by debinding, sintering and infiltration	-	+	-	-
Powder Bed Fusion	Polymer Metal	Powder	Energy source fully melts powder particles in the top layer of powder bed	---	--	+++	-
Directed Energy Deposition	Metal	Powder Wire	Powder or wire is fed into the energy source mounted on a robotic arm	-	++	0	++

Vat Polymerisation	Polymer	Liquid	UV light polymerizes a liquid prepolymer layer by layer	+	0	++	+
Sheet Lamination	Paper Metal	Sheet	Sheet cutouts are stacked and bonded	++	-	---	--

Material Extrusion: Polymer wire is used as feedstock material fed through a preheated nozzle that moves in the X, Y, and Z direction. In other configurations, the nozzle is kept stationary in the Z direction, whereas the base plate on which the part is being fabricated moves in the Z direction. The heating of the polymer lowers its viscosity which enables smooth deposition of continuous tracks. Most desktop 3D printers work based on the material extrusion principle.

Material Jetting: In material jetting, the feedstock material is also fed through a preheated nozzle, but the output from the nozzle exists as liquid droplets rather than as a semi-viscous material. The process is similar to 2D inkjet printing, and the liquid droplets are deposited on a base plate and then on top of each other. The solidification of the droplets is fast enough to fabricate 3D parts. With this technique, fabrication of multiple material single components is relatively easy. Material jetting is one of the less used categories with commercial machines and applications still to be announced. Stable liquid droplets need to be obtained at workable temperatures. Therefore, wax is the go-to material for this technique.

Binder Jetting: uses the nozzle to deposit droplets of binder material onto the powder bed. The sole purpose of the binder material is to bind the powder particles together effectively. The fragile "Green Part" is obtained by repeatedly depositing the powder layer and binding it together. The "Green Part" is left into the powder bed for some time, allowing it to gain strength. Before post-processing steps such as sintering, melt infiltration, the green part is dusted very carefully so that there is no loose powder left attached to the green part.

Further, the binder is first burned away, and the powder is sintered together. Often, the sintered part is melt infiltrated to achieve full densification. Compared to other techniques, binder jetting produced parts have average mechanical properties. The most significant advantage of this technique is that the fabrication of large parts is possible as it does not use high temperatures for processing.

Powder-Bed Fusion: In the powder-bed fusion process, a heat source is focussed onto a metal or polymer powder bed resulting in the fully melting of material powder particles. The Laser or

Electron beam can be used as the heat source or energy source. The powder is spread onto a powder bed using a recoater, either a roller, rake, or scraper. Rapid heating and cooling of the powder particles result in the incorporation of residual stresses in the built part, limiting the size of the produced parts. A powder bed can act as a support for the layers to be deposited on top. Still, support structures are often needed for better heat conduction, part anchoring, and avoiding failure due to overheating. The Selective Laser Melting (SLM) or Laser Powder Bed Fusion (L-PBF) and Electron Beam Melting (EBM) are the two categories of the powder-bed fusion process. The ability to produce fully dense parts makes this process most suitable for comprehensive applications in structural or functional applications.

Directed Energy Deposition: DED process is similar to the powder-bed fusion process, but powder material is either coaxially sprayed into the energy beam, or material wire is fed into the melt pool created by the beam, which is placed on a robotic arm allowing free movement in different directions. The melt pool created by the DED process is larger compared to the melt pool obtained from the powder bed fusion process. Therefore, the geometrical deviation is higher in the DED process. Laser Net Shaping (LENS), also referred to as Laser Cladding (LC) or Laser Melt Deposition (LMD), are prominent processes in this category.

Vat Polymerization: also referred to as Stereolithography, uses a liquid bath of prepolymer to fabricate parts. The prepolymer bath is selectively illuminated utilizing the UV light allowing the polymerization, which results in solidification. The parts are attached to the base plate, which gradually lowers into the prepolymer bath as the process proceeds. A thin liquid prepolymer layer is illuminated from below in the bottom-up configuration, and the base plate is gradually pulled upwards out of the liquid.

Sheet Lamination: As the name suggests, sheet lamination uses a sheet of material that is first cut to the right shape and stacked or laminated on top of other cut-outs. The sheets are bonded together using ultrasonic vibrations or glue. This technique is not often used and only marginally considered AM process.

1.1.2. Applications

Although AM is considered an advanced manufacturing technology, it cannot replace other manufacturing technologies. The additional cost incurred by the AM parts is compensated by exploiting the advantages offered by AM compared to other technologies. The four main advantages of the AM are listed below.

- In AM, the costs of producing the same part 100 times are the same as producing 100 different parts. It is called "Mass customization," which is particularly important in the medical sector. As every patient's body is different and unique, AM can produce complex customized implants with enhanced durability and better comfort level for the patient.
- Secondly, the topological optimization of the traditional components is another major advantage offered by AM. As in AM, the material is added rather than removed, the part designs can be optimized to have the same functionality with less material. Based on certain boundary conditions and load cases, existing parts can be redesigned with the help of sophisticated software to minimize the weight. Topological optimization is vital for aerospace applications. For example, 1kg of weight reduction translates to $80,000 in savings in one year of the normal operation of an airplane.
- Topological optimization can often be combined with improved performance as well. Currently, the parts are designed while considering the limitations of conventional production techniques in mind. Other optimal designs for a particular application may be possible but may not be possible to produce with traditional techniques. For example, in the case of conformal cooling, cooling channels can be placed in the vicinity of the cooling zone, while the heat exchanger surface can be maximized.
- Also, AM is regarded as a fast manufacturing technique. Ironically, the actual manufacturing process is relatively slow, but the process chain leading up to the production is fully digital. Therefore, for the fabrication of new design, it is a matter of days before a 3D file is printed, as opposed to weeks if molds need to be prepared. Moreover, preparing molds for individual parts is expensive, while in AM, the digital design can quickly be adjusted.

AM has other additional advantages, such as a +90 % material usage rate, compared to buy-to-fly ratios as low as 5 % for some aerospace parts. Moreover, it allows the manufacturing of complex parts of high melting point materials such as tungsten or tantalum or other hard materials that are difficult to the tool.

1.1.3. Challenges

Despite all the advantages mentioned earlier, several challenges are associated with AM that need to be overcome. One of the major drawbacks is that the actual production of parts is very slow, with printing jobs lasting as much as one week or longer. Its reputation as a "fast production process" comes from the time gained in pre-processing. Improving the build rates will further lower down the cost of AM.

Other active topics of research in metal AM are:

1. **Quality Assurance:** AM is the main candidate for producing parts in critical applications. Therefore, the safety and quality assurance of AM parts is vital. However, poor process control and lack of repeatability is still major concern to enhance the overall confidence in AM parts. Therefore, every part needs to be checked further, which adds additional time and cost to the whole process. If the part quality could be guaranteed during the process itself could save both time and money.
2. **Higher cooling rates** during printing can create metastable phases (undesirable phases which can be detrimental to other properties) or unique microstructures for which the mechanical behavior is not yet wholly documented. The response of the AM parts is different when subjected to well-established heat treatment profiles.
3. Another major drawback of a higher cooling rate is the evolution of residual stresses in the AM parts. If the stresses exceed the yield strength of the material, it can permanently deform the part during printing. Also, it can induce cracks in the final part which are detrimental to mechanical properties.
4. **Process parameter optimization** for new material is still a very challenging task. Non-optimized process parameters can lead to porosity in the final part, which can influence the overall performance of the part. The influence of the porosities on the dynamic properties is not well understood yet.
5. **Material Range:** The processability of limited metallic alloys by metal AM limits its applicability in many fields.

1.2. L-PBF Process

Laser powder bed fusion (L-PBF), also known as selective laser melting (SLM) and Direct melt laser sintering (DMLS), is an additive manufacturing process in which laser source (thermal energy) selectively fuses regions of powder-bed in a layer by layer fashion [5]. The schematic of L-PBF is shown in Figure 4a [5]. The complex thermo-mechanical process in a melt pool occurs locally due to laser-material interaction [6]. The schematic of the laser-material interaction region is shown in Figure 4b [7]. The non-uniformity of temperature distribution in the melt pool (center of melt pool is at a higher temperature) develops surface tension gradient, which leads to the thermo-capillary motion of the liquid, i.e., the liquid from the center of the melt pool is transported to the edges (colder region). When the laser source moves away from the molten pool, a negative surface tension gradient develops in the melt pool, which generates a shallow and well-distributed liquid mass. Similarly, the segregated melt at melt pool edges will acquire sufficient surface energy, which flows back to the hotter region and completes the convection loop [8]. Rapid solidification with cooling rates of 10^6 K/s of melt pool allows inter-layer bonding [9].

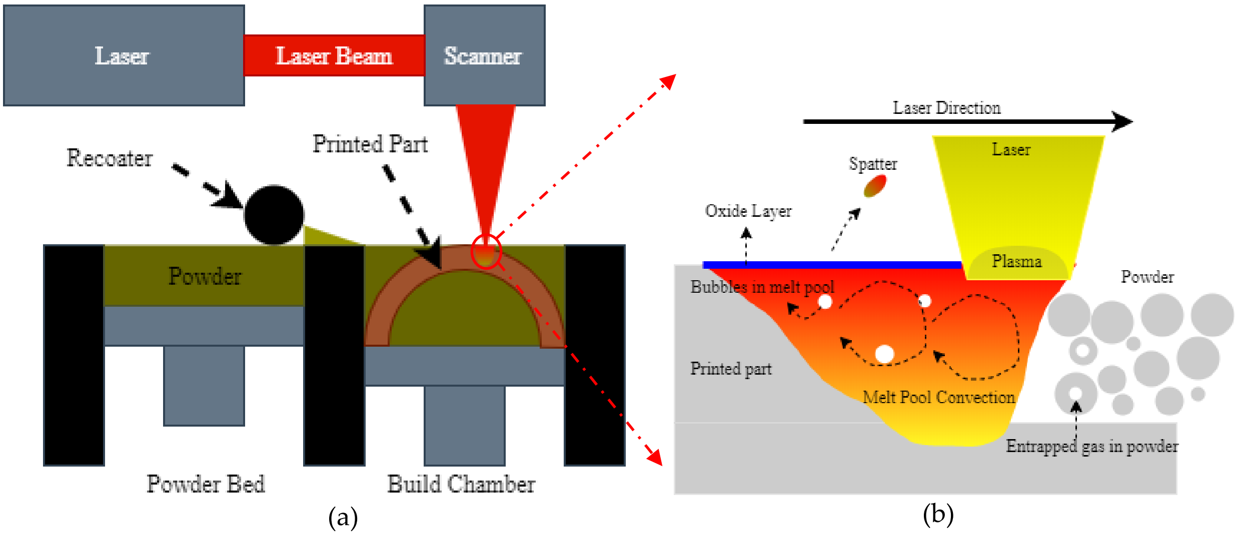

Figure 4:(a) Schematic diagram of L-PBF process [5], (b) Laser-melt interaction region [7].

The support structures must anchor parts and their features to the build plate for metallic alloys. It is necessary because the thermal gradients in the building part are high, which can lead to thermal stresses and warping if the anchors are not used. The thick build plate serves as the heat sink and prevents the parts from warping while printing. The preheating of the build plate, which depends on the material manufactured, is done to minimize thermal stresses in part. The dimensional accuracy and ability to print good surface finish products and fine feature details are advantages of the L-PBF process.

1.2.1. Defects

As discussed, the L-PBF process is a complex thermomechanical process affected by many controllable process parameters such as laser power, scan speed, hatch distance, powder material, and powder morphology. These parameters can strongly influence the laser-material interaction, influencing the thermophysical mechanism, resulting in various physical phenomena such as material evaporation, microstructural evolution, melt pool instabilities, and thermal stresses. Thus, the formation of various defects during the process is inevitable. Here, we review the formation mechanism of the most prevalent defects, such as porosities, lack of fusion, balling, and cracking defects that can be detrimental to the mechanical properties of the final part.

Porosities

Spherical and non-spherical porosities, which are usually smaller in size (100 µm), are the most common defects in the L-PBF process, which significantly influence the fatigue properties of the part [10]. The leading cause for the formation of gas porosities (generally spherical, as shown in Figure 5a) [10] is the entrapping of gas in the melt pool due to rapid solidification. The rapid solidification of the melt pool does not allow dissolved gas to come out on the surface. As we know, at high temperatures, the gas dissolves in the melt pool very easily. Moreover, enrichment of gas in the liquid melt can be due to various factors such as low packing density of powder bed, gas inclusion during gas atomization of powders, and evaporation due to high laser power. Dissociation of oxide films, adsorbed gas, and moisture on the powder material also results in gas formation [11]. For example, Gong et al. [12] showed the presence of gas porosities due to the entrapping of gas bubbles, which originated due to the vaporization of the low melting material in the alloys. The gas bubbles could not escape to the surface due to rapid solidification.

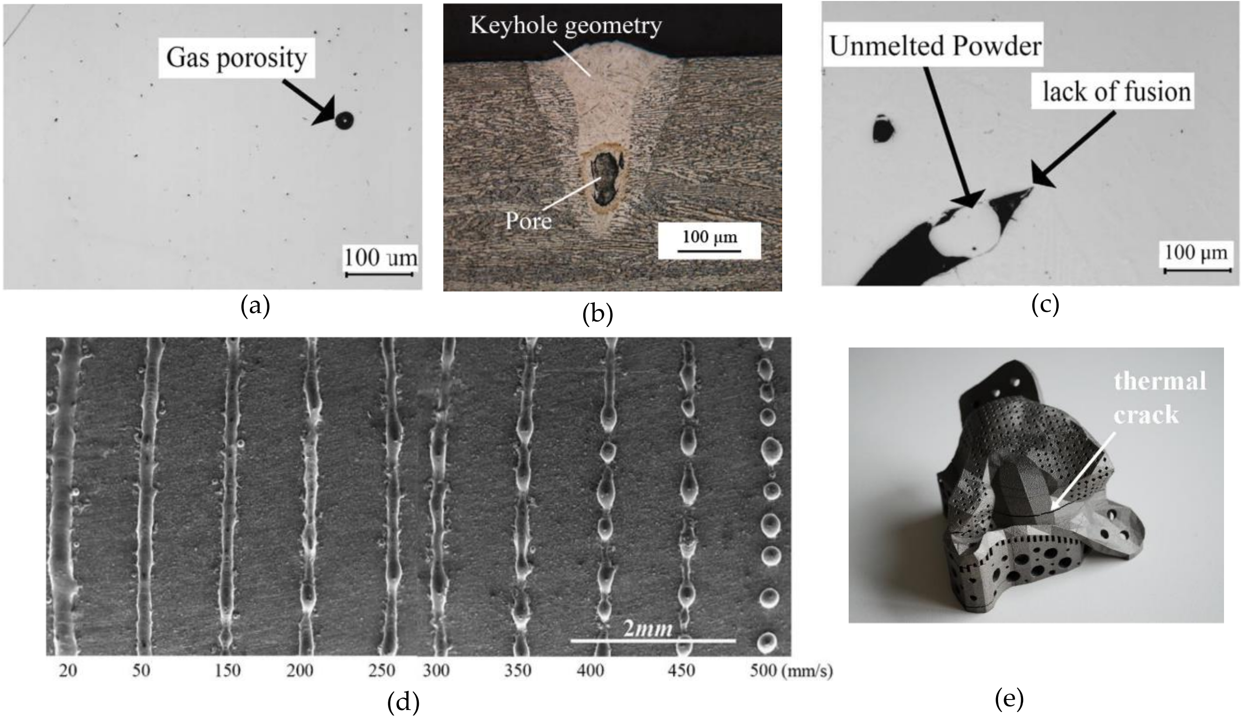

(a) (b) (c)

(d) (e)

Figure 5: Micrographs of defects observed in L-PBF such as (a) gas porosities [10], (b) key hole porosity [12], (c) lack of fusion defect [10], (d) balling [22], and (e) thermal crack [30]. Reused under Creative Commons Attribution License.

Another type of porosity called "keyhole porosity" is due to excessive energy input, which leads to temperatures beyond the boiling point of the material, which causes evaporation of the material and forms a plasma. The laser beam penetrates the powder bed deep through the vapor voids, which creates a large melt pool. High energy density can occur at lower scan speeds, where the longer exposure time initiates boiling, which unstabilizes the melt pool and induces small metallics balls. The intense recoil pressure creates denudation along the scan track and, together with Marangoni convection (thermocapillary convection), forms a melt pool depression into the powder layers. The breakdown of the melt pool sidewalls during solidification leads to entrapped irregular porosities in the printed layer (as shown in Figure 5b [12]).

Still, there is a lack of universal consensus among researchers on the evolution mechanism of keyhole porosities [12]. For example, according to reference [13], the keyhole porosities occur when the Marangoni effect outweighs the buoyancy. Similarly, Svenungsson et al. [14] stated that vortices, high fluid speed, and recirculation in the melt pool lead to keyhole phenomena. It is challenging to observe this defect experimentally and requires a sophisticated setup to observe it inline. For instance, Cunningham et al. [15] used ultrahigh-speed X-ray imaging to capture keyhole evolution in titanium alloy while printing. They have explained the evolution of the keyhole porosity, which is as follows: As the laser turned on, the powder began to melt, and a solid–liquid interface is formed. Once the melt pool temperature reached near the boiling point of the material, localized vaporization led to recoil pressure and formed a depression. Due to recoil pressure, the melt pushed up and out of depression, which developed instability in the melt pool. Soon after, the shallow vapor depression transitioned to deep, conical depression. Then, deep vapor depression rapidly penetrated the melt pool, and displacement of the melted liquid from the center of the melt pool occurred. The displacement in the liquid introduced the liquid-vapor interface fluctuations and changed the melt pool shape from quasi-semicircular to a bimodal shape to form keyhole porosity.

Lack of Fusion

Another common defect observed in L-PBF is the lack of fusion defect (LOF), which occurs due to incomplete fusion of two adjacent layers (as shown in Figure 5c [10]). It can happen due to (i) insufficient energy input leading to incomplete melting of the powder layer, (ii) insufficient material due to shrinkage during solidification, and (iii) poor bonding between layers due to oxidation, which influences the wetting angle between layers [16], [17]. The L-PBF process selectively melts the powder line by line and layer by layer, and the LOF defects are usually present between the layers or between the scan vectors. Sometimes, the uneven powder layer spreading in consecutive layers also leads to incomplete powder melting, resulting in a LOF defect in the final part. Clijsters et al. and Read et al. [18], [19] showed that the rapid formation of an oxide layer on the solidified layer of AlSi10Mg leads to poor wettability between layers, which results in poor wettability in a LOF defect.

Balling

Another common defect in the L-PBF process is called “balling,” which disrupts interlayer bonding, poor surface quality, and porosity in the final part [19]. It occurs mainly at high scan speeds, which leads to an elongated melt pool that breaks into small beads (10 µm) to reduce the surface tension due to Rayleigh instability. Due to low input energy, partially melted powder leads to limited melt formation and produces coarser-sized beads (500 µm). The oxide layer or moisture on the powder surface can also disrupt the melt pool surface tension, resulting in balling. These impurities reverse the capillary motion at the melt pool surface, and a positive surface tension gradient forces the melt pool to flow inwards to the center, which develops unfavorable wetting conditions and leads to spheroidization. Remelting/double exposure or deoxidizing agents can significantly reduce the balling phenomena [20], [21]. Li et al. [22] presented the SEM images of the balling phenomena for stainless steel w.r.t different scanning speeds in the L-PBF process (as shown in Figure 5d). Other authors, for example [21], [23], reported the balling phenomenon in L-PBF for different materials.

Residual Stresses and Cracks

The residual stresses are the stresses that remain in part after fabrication; these stresses are significantly detrimental to the mechanical strength of the final part. Due to rapid heating and cooling cycles, a higher thermal gradient develops residual stresses in part and results in delamination, part distortion, and warping [24], [25]. The temperature gradient mechanism (TGM) and the rapid solidification mechanism are responsible for the evolution of residual stresses. During TGM, the pre-solidified layer underneath the melted layers is heated up very rapidly upon laser exposure, which tries to expand but is restricted by the cold solidified material. This restriction in thermal expansion develops compressive residual stresses at the regional heat-affected zone (see Figure 6a) [26]. The melted zone cools rapidly during the solidification mechanism, and shrinkage is again restricted by the underlying layer, developing tensile residual stresses in the upper layer (Figure 6c). Therefore, during printing, the cyclic heating, and cooling phases result in larger tensile residual stresses in the top surface layers and residual compression stress at the bottom of the printed part (Figure 6b and Figure 6d) [26].

When the tensile residual stresses cross the material's ultimate tensile strength at a given time and temperature, it leads to cracking in part [27]. As reported [28], the crack initiation and propagation start on the as-built surface as it is adhered to the partially melted material and leads to interlayer delamination, also called interlayer cracking. Materials like nickel-based alloys, copper, and stainless steel are highly susceptible to cracking due to their low thermal conductivity [29]. The pre-heating of the build plate is often applied to reduce the effect of the residual stresses in the final part.

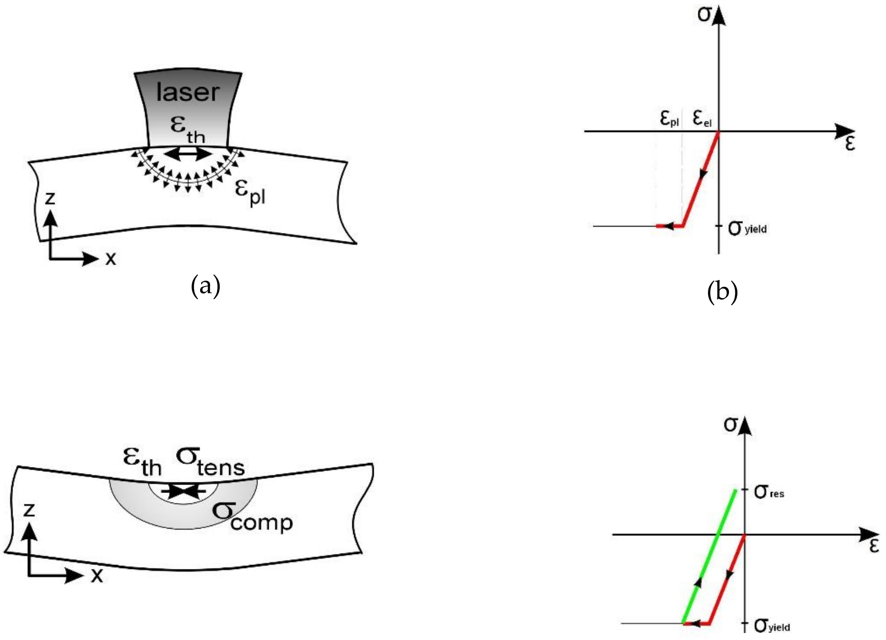

(a)

(b)

(c)

(d)

Figure 6: (a) Temperature gradient mechanism during laser heating, (b) representation of the evolution of thermal stress and strains in the irradiated zone (c) Evolution of stresses during solidification phase, (d) representation of the evolution of residual stresses and strain in the irradiated zone [26]. Reused under Creative Commons Attribution License.

Part Distortions

Another critical aspect of residual stresses on the overall quality of the part health is "part distortion." If the thermally induced local residual stresses exceed the material's yield stress, it can lead to part distortion in the middle of the process. Part distortion can also damage the recoater permanently. Kruth et al. [30] reported the warping in the SLMed parts due to high thermal fluctuations experienced by the material in a short time interval. After removing the finished part from the base plate and support structures, the relaxation in the residual stresses leads to macroscopic distortion in the final part (as shown in Figure 5e). Mugwagwa et al. [31] studied the influence of process parameters such as laser power, scanning speed, scanning strategies on the evolution of residual stresses, and part distortion experimentally and with finite element modeling. Sometimes, the warping of the parts can lead to the failure of the bolts of the build plate as well. Mishurova et al. [32] studied the influence of support structures on part distortion using the X-ray diffraction method. The stress redistribution occurs for the samples with support structures after removal from the base plate, whereas only simple stress relaxation is observed for parts without support structures. They have concluded that the support structures decrease the amount of residual stresses in part.

This section does not discuss other defects or anomalies such as surface defects, material contamination, and geometrical inaccuracy. However, interested readers can refer to references [33]–[35].

1.2.2. Process Space

L-PBF process involves many critical parameters that can influence the quality of the final part and lead to the defects as mentioned above if not optimized. Sharratt et al. [36] categorized the influencing parameters into three categories, which are (i) process defects, (ii) equipment-induced defects, (iii) design defects. Equipment defects are basically due to aberration in the machine's equipment, such as f-theta lens aberration, improper calibration, wear of recoating blade, etc. Due to significant technological advancements, most commercial machines are well-calibrated and standardized to minimize such defects. Design defects are due to improper design optimization as per AM standards, such as lack of support structures, overhang angle, and bad orientation. These defects can be minimized by using commercial software such as AdditiveLab, Simufact, Virfac, etc., which helps find the best support structure placement based on the thermomechanical simulations.

A lot of time and money is consumed to find best-fit process parameters such as laser power, scan speed, hatch distance, layer thickness, etc., to reduce the third type of defect called "process defects." All the above parameters can be combined in the empirical formula of 'Energy density (E (J/mm^3))' given by Equation 1, where $P\ (W)$, $v\ (mm/s)$, $h\ (mm)$, and $t\ (mm)$ represent laser power, scan speed, hatch distance, and layer thickness, respectively.

$$E = \frac{P}{v * h * t}$$

Equation 1

Each parameter in Equation 1 affects the final quality of the part. For example, at lower scan speed and high laser power, the energy density is higher, and its attributes to porosity defects are due to gas entrapment. Thijs et al. [37] stated that high energy input in Ti6Al4V powders leads to a large melt pool size, which causes denudation. Thus, insufficient material is available to fuse the adjacent scan vector, leading to bigger pores in part. The higher residual stresses are also reported for low scan speed and higher laser power [29].

Similarly, at low laser power and higher scan speed, a lack of fusion defects is more pronounced due to a lack of energy input to fully melt the powder layer [12], [17], [38]. Sun et al. [39] showed the relationship between the part density and input energy density for Al0.5CoCrFeNi High Entropy Alloys (Figure 7). It can be observed that the highest porosity is reported for lower energy density. Therefore, it is crucial to optimize the process parameters to attain the maximum dense parts.

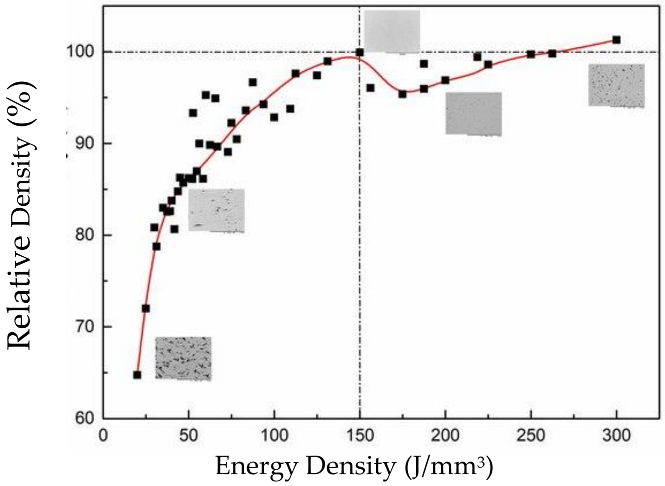

Figure 7: Relative density as a function of energy density [39]. Reused under Creative Commons Attribution License.

It is important to note that the scanning strategy also impacts the overall quality of the part. Although it has not been considered in the energy density equation, the scanning strategy directly influences the heat balance of the part. For example, Aboulkhair et al. [40] showed the relation between the scan speed and different scan strategies, as shown in Figure 8. The different strategies used are: “2X” is similar to “X” but each layer is scanned twice, “X&Y 2HS” means that each layer is scanned twice, having each scan pass perpendicular to the one before and with different hatch spacings for each scan, “pre-sinter” means to first scan the layer with half the power followed by a second scan with full power, “overlap” strategy indicates where each layer is scanned twice with the second scan melting the overlap between each two adjacent melt pools, and “alternating” strategy indicates scanning each layer in a direction rotated by 90° to its precursor. As can be concluded from Figure 8, the pre-sinter scanning strategy and scanning speed of 500 mm/s report a high density of AlSi10Mg parts.

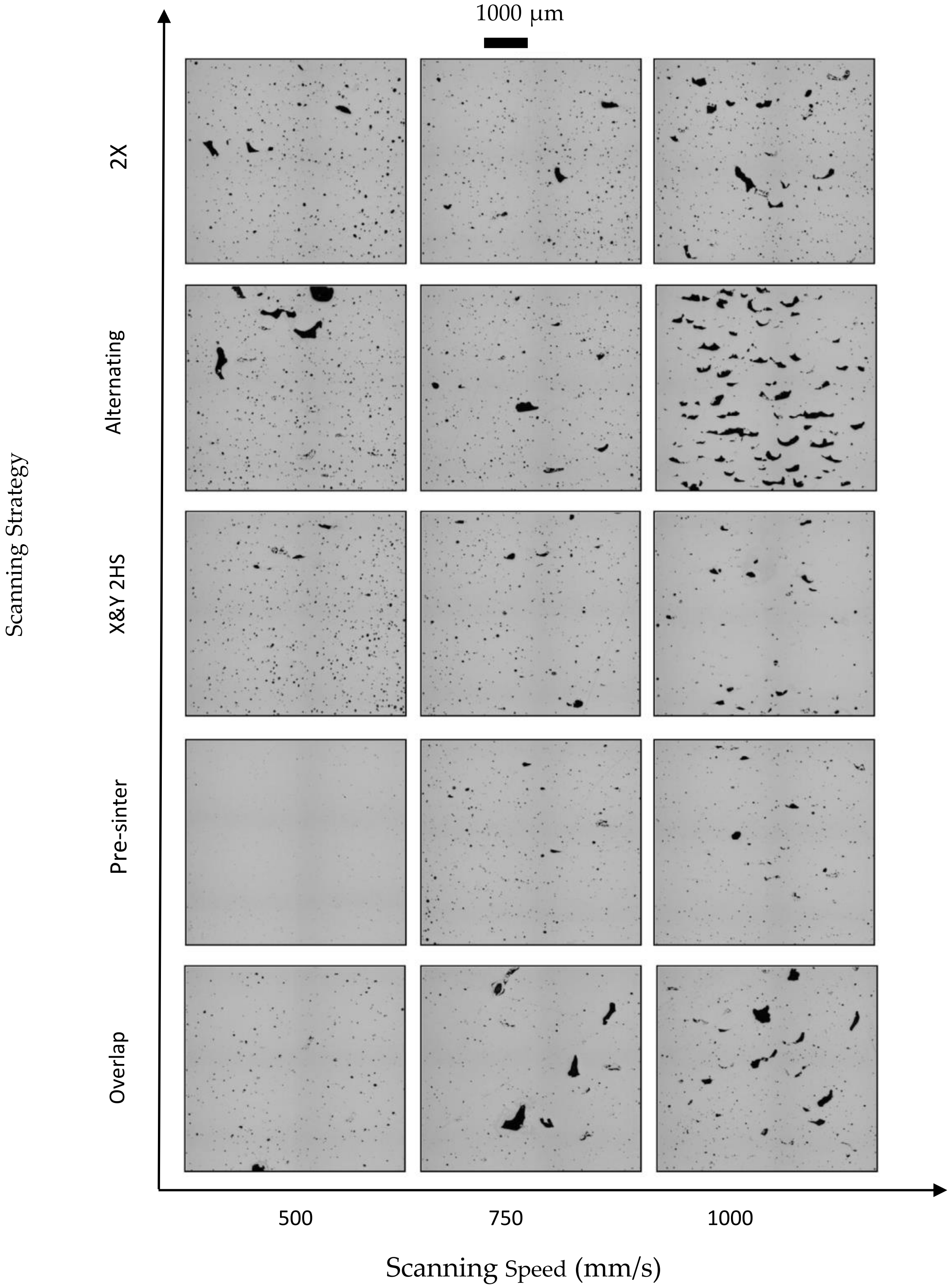

Figure 8: Effect of scanning strategies and scan speed on the porosity % of AlSi10Mg parts [40]. Reused under Creative Commons Attribution License.

1.2.3. Melt Pool Signatures

Laser–material interaction in L-PBF is a complex thermophysical phenomenon occurring in a short time interval. The process parameters and geometrical factors significantly influence the shape and size of the melt pool. Therefore, melt pool signatures provide essential information about the quality of the part. A different range of electromagnetic spectrum emanates from the melt pool, which serves as the input variable for in situ sensing devices. The types of electromagnetic radiations observed from the melt pool are shown in Figure 9. As we know, scattering, absorption, and diffraction of laser light are common phenomena that occur. Hence, the backscattering of the laser light is a common phenomenon that occurs in L-PBF. Therefore, it is vital to eliminate the backscattering of the laser light in the in-situ sensing module by installing correct mirrors. Thermal emissions from the melt pool occur at the wavelengths that correspond to the melt temperature. High laser energy can lead to melt evaporation and ionization of the gas, resulting in a plasma plume above the melt pool. The electromagnetic radiation from the plasma can also add noise to the captured signatures [41], [42]. Sometimes, the plasma also hinders the laser beam, which results in low input energy to the powder bed. Thermal radiation ranges from 900 to 2300 nm, is captured to monitor the process and link it to the melt pool's temperature field. Plasma radiations, which are in the range of visible wavelengths (400–600 nm), are eliminated [43]. These melt pool signatures are captured using in situ sensing sensors, discussed in the next section.

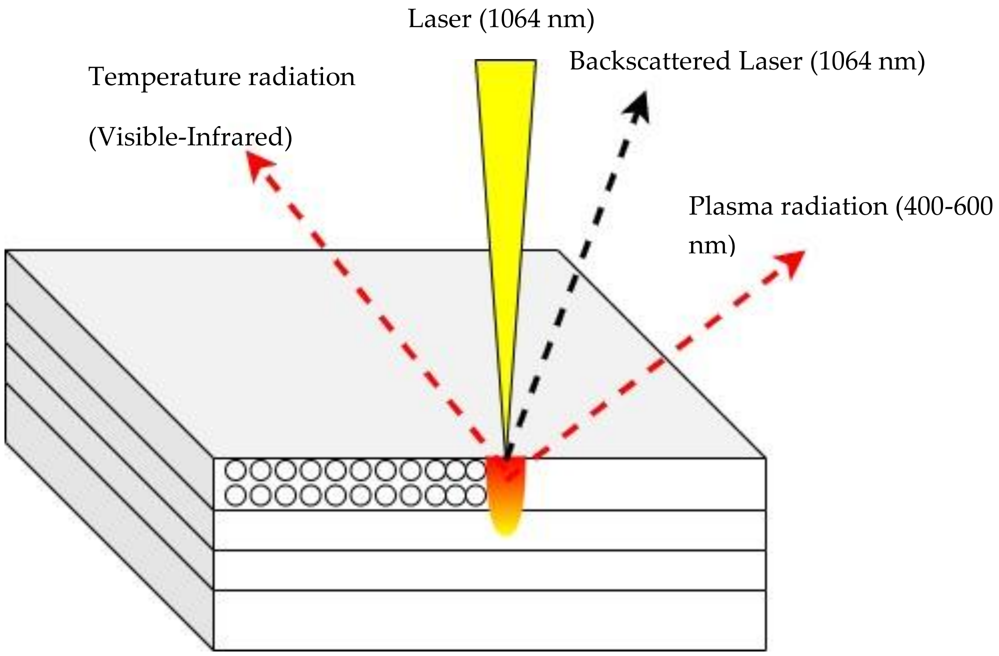

Figure 9: Illustration of types of emitting radiation from melt pool.

1.3. In-Situ Monitoring in L-PBF

Quality assurance is essential in full-scale manufacturing, where reproducible part qualities are significant. Therefore, the technological advancements of the commercial machines allowed the possibility of in-situ monitoring of the L-PBF process. In-situ monitoring setups, including various sensors, offer more comprehensive process monitoring and quality assurance. Real-time monitoring is a key to creating an economically viable process chain. For example, In-situ sensing enables the customers to significantly reduce the downstream costs (non-destructive testing using computed tomography) by rejecting the potentially defective parts early.

Therefore, commercial suppliers of L-PBF systems are now equipped with inbuilt in-situ sensing modules. The layout of the monitoring system, detection range, and sensor types differentiate commercial supplier monitoring systems. There is no common consensus on the detection range of the melt pool emissions among different suppliers. The reason to choose a specific detection range is protected under the confidentiality clause by the supplier. Therefore, each module has its disadvantages and advantages. For example, the EOSTATE Optical Tomography (OT) module detects every layer's light emitted from the melt pool. The EOSTATE Exposure analysis tool provided by EOS GmbH uses a statistical algorithm to detect so-called “hotspots” and “cold spots,” which are the regions of high and low intensity compared to the rest of the layer.

Similarly, Melt Pool Monitoring (MPM) provided by SLM solutions captures the melt pool emissions in the near-infrared region using two photodiodes with different spectral ranges. Then, captured thermal emissions can be studied in the software module supplied by SLM solutions in a layer-by-layer fashion. The Layer Control System (LCS), also supplied by SLM solutions, uses the visible range camera to monitor the quality of the powder bed spread. After the powder bed spreading, an automatic algorithm processes the captured image in real-time and automatically activates the recoating operation in case of inhomogeneous powder spread. Renishaw supplied the InfiAM module composed of MeltView, which captures the in-situ data in a wide spectral range, and LaserView to monitor the part build and laser power. It provides the captured data in 2D and 3D view as the build progresses. It shall be noted that the author’s aim is not to comment on the capabilities of the available commercial systems as the authors have not personally used all these systems.

1.3.1. In Situ Sensing Devices

As discussed in the last section, capturing the melt pool signatures is essential to monitor the process. Therefore, this section reviews the working principle of the most used devices or sensors for in situ sensing of melt pool signatures in the L-PBF process. Generally, two entities related to the melting pool are measured, i.e., melt pool morphology (shape and size) and temperature. There are two types of sensors available for temperature measurements, i.e., photon detectors, also called non-contact sensors, and thermal detectors, referred to as contact detectors. As shown in Figure 10, the thermal detector response is constant with the wavelength (radiations emanating from the melt pool), whereas the wavelength of the light greatly influenced the photon detector response. The link of the photon detector's output to the melt pool temperature will be discussed next. Besides monitoring the melt pool signatures, other process signatures such as powder bed spreading and part geometry are also studied using different sensor techniques, such as ultrasonic, line profiling, optical coherence tomography, etc., as reported in references [44].

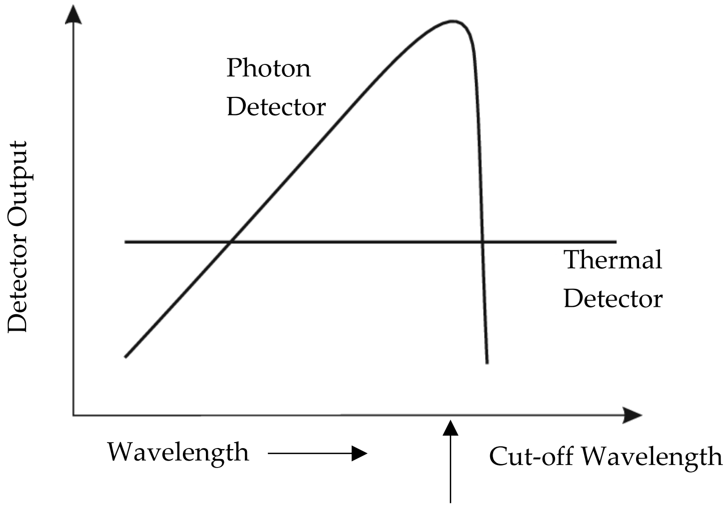

Figure 10: Wavelength response of detectors.

1.3.1.1. Non-Contact Temperature Measurement Devices

Most studies involve monitoring the temperature field or electromagnetic radiations from the melt pool in a co-axial/on-axis and off-axis manner. The melt pool signatures capture the most invaluable information, such as the temperature profile of the melt pool and the morphology of the melt pool that directly influences the quality of the part [45], [46]. Electromagnetic emissions are associated with the melt pool and plasma plume [37]. Therefore, to capture electromagnetic signatures, mostly non-contact measurement sensors are used. Broadly, these sensors can be classified as spatially integrated, i.e., photodiodes and pyrometers; spatially resolved, i.e., cameras; spectrally resolved, i.e., spectrometers [43]. Regardless of the sensors, the essential requirement for AM applications is the ability of the sensor to capture the rapid melt pool dynamics. Below, we discuss the working mechanism of the two most common photodevices used in the L-PBF process.

Photodiodes

Spatially integrated, single-channel detectors such as photodiodes are semiconductor devices that convert light (radiation) into electric current. The basic principle of the photodiode or photodetector is that when photons of sufficient energy (radiation) hit the device's active area, it generates an electron-hole pair, which changes the effective resistance or conductance of the detector. A bias voltage is applied to collect the charge carriers, and the signal (photocurrent) is measured across a load resistor RL, as shown in Figure 11. The photocurrent is directly proportional to the intensity of the photons hitting the device's active area. The intensity of photons is directly linked to the melt pool temperature. Photodiodes have the advantages and disadvantages of reducing the signal to a single data point, i.e., photovoltage corresponding to the amount of light hitting the photodiode. Reducing the signal to a single point relates to data shrinkage, making it easier to post-process. Low cost, high sensitivity, and high sampling rates (typically ~50 kHz) make them suitable for in situ sensing of the L-PBF process. The detection range of these devices is limited to over a range of the spectrum; for example, germanium (Ge) and InGaAs-based photodiodes are used for visible to infrared light detection. In contrast, silicon-based photodiodes are used for the UV and visible spectrum [47], [48].

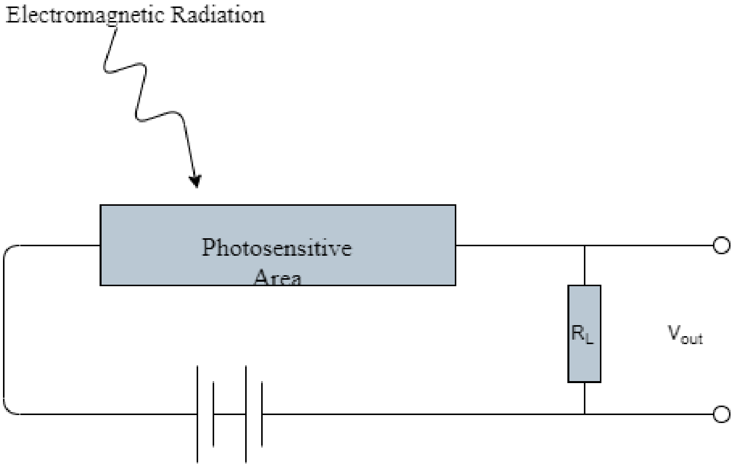

Figure 11: Schematic of working principle of PIN photodiode [47].

Digital Cameras

The digital cameras, also called spatially resolved sensors, are an array of photodiodes where each photodiode is labeled as a pixel. The different types of photodiodes with their detection wavelength range are given in Figure 12. Each pixel detects the photon coming from the melt pool and converts it into photocurrent. Afterward, signal processing is done to extract a picture corresponding to the melt pool's temperature fields. Based on the detection range of the devices, it can be classified either as a regular digital camera with a detection range in the visible spectrum or a thermal camera, which has a detection range in the infrared spectrum. Thermal cameras are preferred for monitoring melt pool signatures with a detection range of over 700 nm. The digital cameras can be classified into two categories based on the signal processing method, i.e., charge-coupled device (CCD) and complementary metal-oxide-semiconductor (CMOS). In a CCD camera, all the pixel information is processed by a single circuit, whereas, in a CMOS camera, each pixel has its processing circuit. Therefore, the CMOS cameras have better signal processing speed, but the capture area is limited than a CCD camera. The main disadvantage of using cameras for in situ sensing of the L-PBF process is the speed of the process, which requires a high frame rate camera that results in an enormous size of data that are difficult to post-process [49], [50].

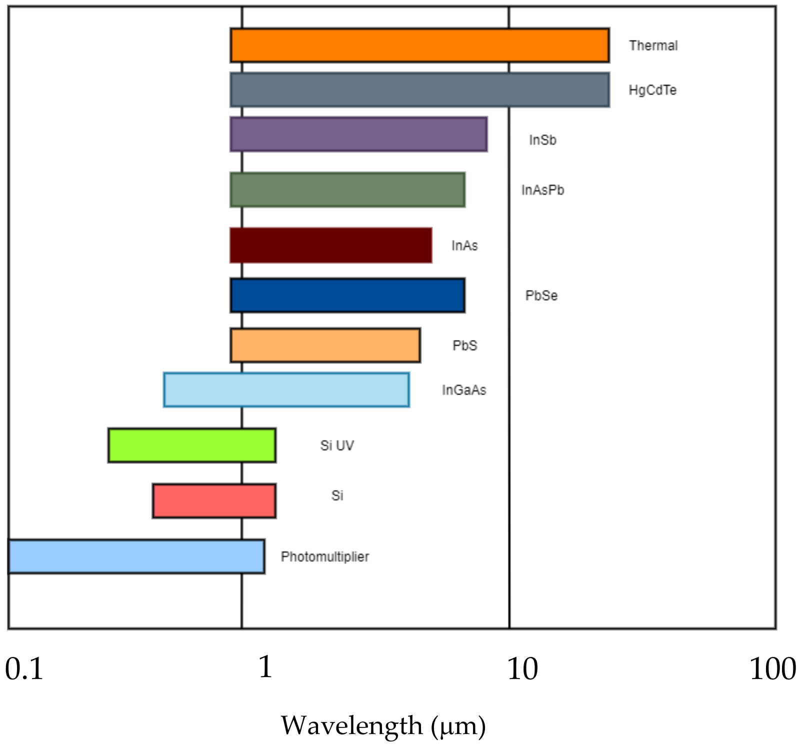

Figure 12: Wavelength sensitivity of common detectors [49].

1.3.1.2. Contact Temperature Measurement Devices

Another category of the devices or sensors used for monitoring the temperature fields in the L-PBF process is direct contact-based measurement devices such as thermocouples. The thermocouple is an electric device that produces a temperature-dependent voltage due to the thermoelectric effect. The working principle of the thermocouple is based on the Peltier effect. The thermocouple consists of two electric conductors joined together to form two junctions. If junctions are attached to the surface at different temperatures, an electromotive force (EMF) is generated due to the temperature gradient between the two junctions of the circuit; then, total EMF can be calculated based on the temperature of the junctions and the properties of the electric conductors used. A measurement point is connected to one of the junctions in the circuit, also called a hot junction. Another body of known temperature is connected to the other junction, also called a cold junction or a reference junction. A voltmeter measures voltage or current generated due to the temperature gradient between the two junctions. This voltage or current is then converted into the temperature. Thermocouples can be used to monitor the overall heat flow of the part while printing. However, one limitation of the thermocouple is that it requires physical contact to measure the temperature, which is difficult in the L-PBF process and often requires extra preparation such as drilling holes or slots. Some researchers have monitored the L-PBF process using thermocouples, found in the reference article [48].

1.3.2. Temperature Correlation

One of the key advantages of photodiodes and digital cameras is monitoring the melt pool temperature fields or process signatures without physical contact with the target surface. It provides the freedom to monitor the processes like AM, in which it is challenging to access the target surface. Another advantage of these sensors is detecting high temperatures such as 2000 °C. Although these sensors provide great flexibility and easy detectability, calibration of these sensors properly is a vital issue. The main principle of the sensors is to generate a photocurrent or photovoltage based on the emitted radiation from the melt pool. Therefore, it requires much understanding of the process and complex thermophysical phenomena occurring in that short time interval. Usually, the melt pool is compared with the black body phenomenon to compute the actual temperature. However, the melt pool does not behave as an ideal black body rather than a real body in reality. In addition, the emissivity of the material concerning different temperatures is not known. Therefore, a better understanding of black body phenomena is inevitable. Here, we present an insight into black body radiation and its correlation with the melt pool physics in L-PBF.

All bodies above absolute zero (0 K) emit thermal radiation due to the thermal vibrations of atomic particles. The quantity of the power emitted is expressed by the radiative intensity. The total energy is distributed across the electromagnetic spectrum. The emission intensity and shape of the distribution are dependent on the temperature. Conversely, the body's temperature can be calculated by its emitted energy's quantity and spectral distribution across the spectrum.

Firstly, a black body is a physical body that absorbs all the incident electromagnetic radiation and emits electromagnetic radiation called black body radiation. The radiation emitted by the black body is dependent on the temperature alone, not on body shape and composition. For an ideal black body at a specific temperature (T), spectral radiance (B) is given by Planck's law (Equation 2), where h is Planck's constant; c is the speed of light; k_B is the Boltzmann constant.

$$B = \frac{2hc^2}{\lambda^5}\left(\exp\left(\frac{hc}{k_B \lambda T}\right) - 1\right)^{-1}$$

Equation 2

Figure 13 shows the spectral radiance of ideal black body radiation at different temperatures. It can be seen that the radiant intensity increases with increasing temperature at all wavelengths and for all temperatures. For any given temperature, the radiant intensity reaches a maximum at a specific wavelength, and there are two wavelengths where the radiant intensity is equal for intensities less than the maximum or peak intensity. The wavelength at maximum radiant intensity decreases with increased temperature (Wien's displacement law) [47].

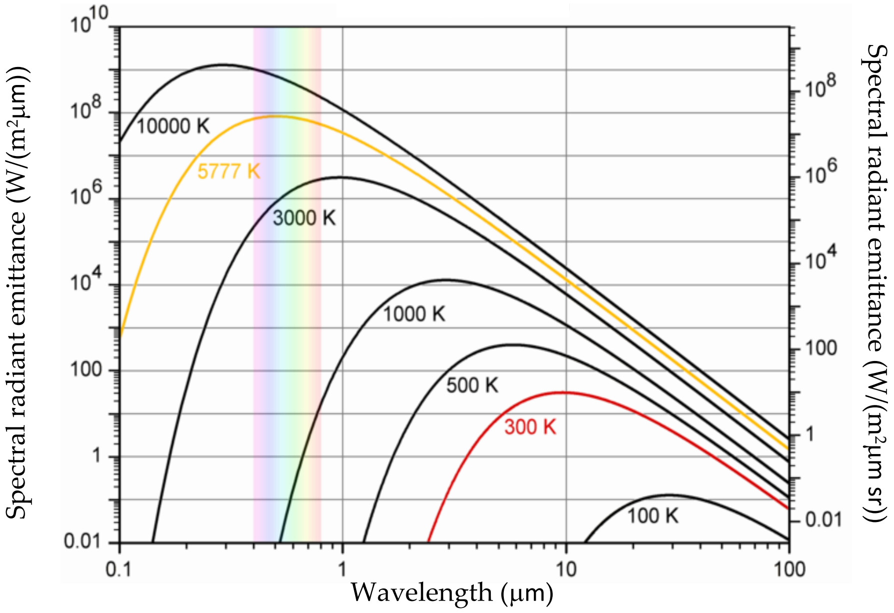

Figure 13: Spectral radiance of an ideal black body at different temperatures [47].

Nevertheless, real surfaces do not emit radiations like an idealized black body. The fraction of the emitted radiation from the real body is relative to a black body, known as spectral emissivity. However, spectral emissivity is temperature and wavelength-dependent. Therefore, it is challenging to obtain the spectral emissivity of every material for each temperature and wavelength. Therefore, the direct application of Planck's law for temperature correlation cannot be used. Instead, to overcome this challenge, there are three possibilities which are as follows:

- For a single measurement, assume the emissivity and calculate the temperature (spectral method).
- Make two measurements at different wavelengths, assume a relationship between the emissivities at each wavelength, and calculate a single temperature (ratio method).

Make multiple measurements at different wavelengths, assume some functional form of the emissivity, and find the best fit for the temperature and emissivity (multispectral method).

Primarily, the ratio method is used to calculate the actual temperature. In the ratio method, the two intensity measurements (I_1 and I_2) at two different wavelengths λ_1 and λ_2, are calculated. The ratio of intensities I_1 and I_2 are taken to calculate the temperature as given by Equation 3.

$$\frac{I_1}{I_2} = \frac{A_1 \epsilon_1 \lambda_2^5}{A_2 \epsilon_2 \lambda_1^5} \exp\left(\frac{hc}{k_B T}\left(\frac{1}{\lambda_2} - \frac{1}{\lambda_1}\right)\right)$$

Equation 3

The difference between the two wavelengths (λ_1 and λ_2) chosen is very small so that it is assumed that the emissivities (ϵ_1 and ϵ_2) are equal. The calibration curve can be calculated once the constants A_1 and A_2 are known, which relates the intensity ratio to the object's temperature irrespective of the emissivity. Therefore, the choice of the two wavelengths is very critical. Because too close wavelengths can lead to low signal and noise ratio from the sensors, i.e., the noise will dominate the measurement. If too distinct wavelengths are chosen, the assumption of equal emissivities will no longer be valid. Most engineering materials have a melting point above 1000 K and vaporization temperature around 3000 K. Therefore, most monitoring devices have detection ranges in the visible-near infrared region. Typically, for calibration of the sensors and to find the values of the constants A_1 and A_2, the tungsten halogen light source with known spectral radiance is used. The halogen lamp is placed inside the build chamber, and the spectral radiance measured by the sensors is then compared with the radiance obtained by the calibrated spectrometer. Then, the A_1 and A_2 values are computed [47].

Moylan et al. [51] also used a multispectral method to calculate the imaged temperature from captured infrared images using a hyperspectral camera in the L-PBF process. The imaged temperature can be calculated by using this method. It shall be noted that the imaged temperature is different from the true temperature, as the true temperature is highly dependent on the emissivity of the material, which is subjected to the temperature.

1.3.3. In-situ monitoring Systems Configuration Layout

In this section, we exploit the configuration layouts for mounting the sensing devices in the SLM machine. The two layouts, i.e., co-axial/on-axis and Off-axis layout, are commonly used based on the configuration.

1.3.3.1. On-axis or Co-axial Layout

In a co-axial or on-axis configuration layout, the sensing devices such as photodiodes, thermal cameras are placed in the same optical path of laser and follow the laser movement locally. Kruth et al. at KU Leuven developed a co-axial monitoring system consisting of a photodiode and a high-speed NIR CMOS camera licensed by Concept Laser [52]. The schematic diagram of the monitoring system is shown in Figure 14. As it can be observed that the radiations from the build chamber follow the same optical path of the laser and are reflected in the sensing unit using a partially reflective mirror. The partially reflective mirror passes the wavelengths in the range of 780-950 nm. The backscattered laser is not reflected in the sensing unit. Then the radiation is split and captured by the two sensors, which are sensitive to the wavelength range of 400- 1000 nm placed in the sensing unit. The radiation is integrated into one value stored as the melt pol intensity. The CMOS camera has a resolution of 1280 x 1024 pixels and a sampling rate of 10 kHz, which can capture the shape and size of the melt pool spatially and temporally [52].

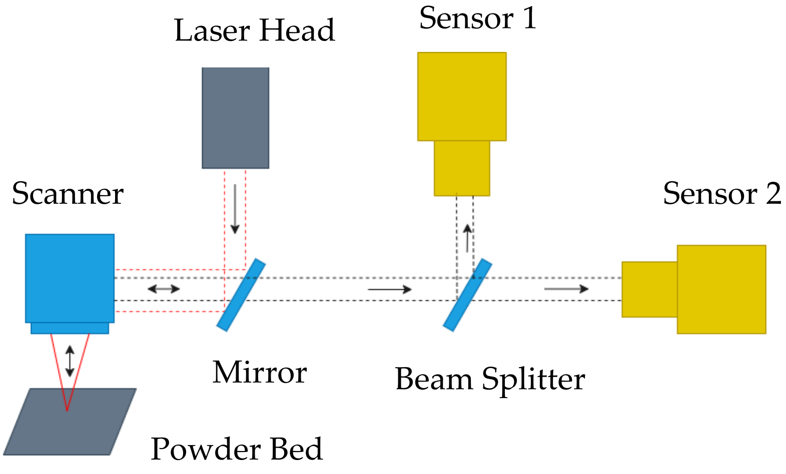

Figure 14: Schematic layout for on-axis monitoring.

1.3.3.2. Off-axis layout

In the Off-axis layout, the sensing devices such as cameras, photodiodes have a stationary field of view of the whole build plate (see Figure 15). Unlike Co-axial or on-axis layouts, the sensing devices do not follow the laser optical path but capture the radiations from the whole build plate. The off-axis layout is common in an electron beam melting (EBM) system where a co-axial setup is impossible. Apart from the melt pool signature monitoring devices, off-axis cameras can also capture the powder bed image after each recoating step. It should be noted that in the off-axis layout, the sensing devices are mounted either on the front door or top of the build chamber; therefore, angle correction is a necessary and unavoidable step.

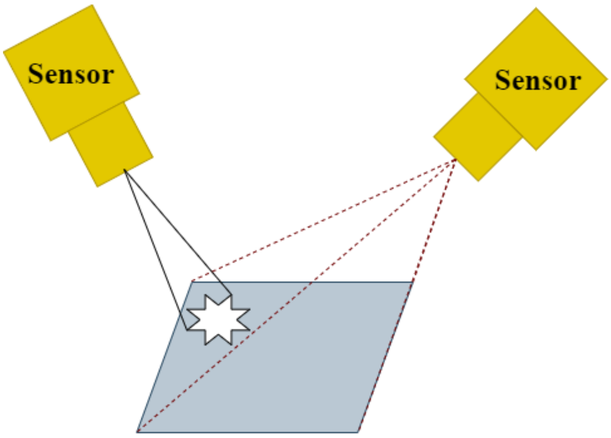

Figure 15: Off-axis layout of the sensors.

1.4. Machine Learning in L-PBF

1.4.1. Problem Description

In the L-PBF process, the quality of the final part and the reliability of the whole process are highly dependent on various process parameters, as discussed earlier. The above-discussed process parameters incorporate inconsistency in the part quality, which is difficult to monitor. The inconsistency during the process can be effectively controlled and monitored using in situ-monitoring systems. However, there are numerous problems associated with monitoring systems, which hinder the full exploitation of these systems. Firstly, the data size, real-time processing, and data storage are significant challenges. For example, consider a laser printing a part with geometrical tolerances of ±100 µm with a scanning speed of 100 mm/s. The sensors will have a data collection rate of ~10 kHz, i.e., one data point for every 10 µm to achieve a spatial resolution of 10 µm. Most researchers have reported a sampling rate of 50 kHz and used more than two sensing devices, such as a digital camera, photodiode, or combination of both. Therefore, if a single data value is stored in a binary fashion, it occupies 32 bits. With a 50 kHz data sampling rate and five sensing devices, the data will be stored at 1 Mb/s. Therefore, if the machine runs for three days, it will generate at least 233 GB of data. The post-processability of this dataset and storage is difficult [53]. Secondly, linking the obtained in situ sensing data to the quality of the product is a significant challenge. The research community has been integrating ML methods into AM in recent years.

1.4.2. Introduction to ML

Machine learning (ML) is a subset of Artificial Intelligence (AI) that can learn and improve in an automated fashion from experience without being explicitly programmed. The process of learning starts with data observation and data pattern recognition to allow algorithms to learn automatically and adjust actions accordingly. The main aim of ML is to learn and improve from data without human intervention. The ML algorithms are used in AM for design and process optimization, in situ monitoring, inspection and validation, and cost estimation. The data used for training the ML algorithms decide the effectiveness of the ML approach. In other words, the ML algorithms are as good as the training dataset [54].

ML algorithms can be broadly classified into supervised, unsupervised, and reinforcement learning.

Supervised Learning

In supervised machine learning, the algorithm is trained with a labeled dataset. The labeled dataset is the dataset in which the output is known for the input variables. Therefore, the model is trained to infer the functional relationship between input and output variables. Supervised learning can be used for regression and classification problems. For instance, classifying the part quality as “good” and “bad” is a classification problem, whereas predicting the porosity level or mechanical properties is regression.

Unsupervised Learning

The output labels are not known for the input training dataset in unsupervised learning. The algorithm separates the training dataset into different clusters based on the relationship among input data. Unsupervised learning is helpful in clustering problems such as detecting anomalous conditions.

Reinforcement Learning

The third ML category, called reinforcement learning (RL), is learning by interacting with an environment. The RL algorithm learns from the consequences of its actions, and it selects its actions based on its experience and new choices, which is trial and error learning. The RL algorithm receives a numerical reward that encodes the success of an action's outcome. The RL algorithm selects actions that maximize the accumulated reward over time. Applications of the RL algorithm are game theory and self-driving cars. The list of various ML algorithms is shown in Figure 16 [55].

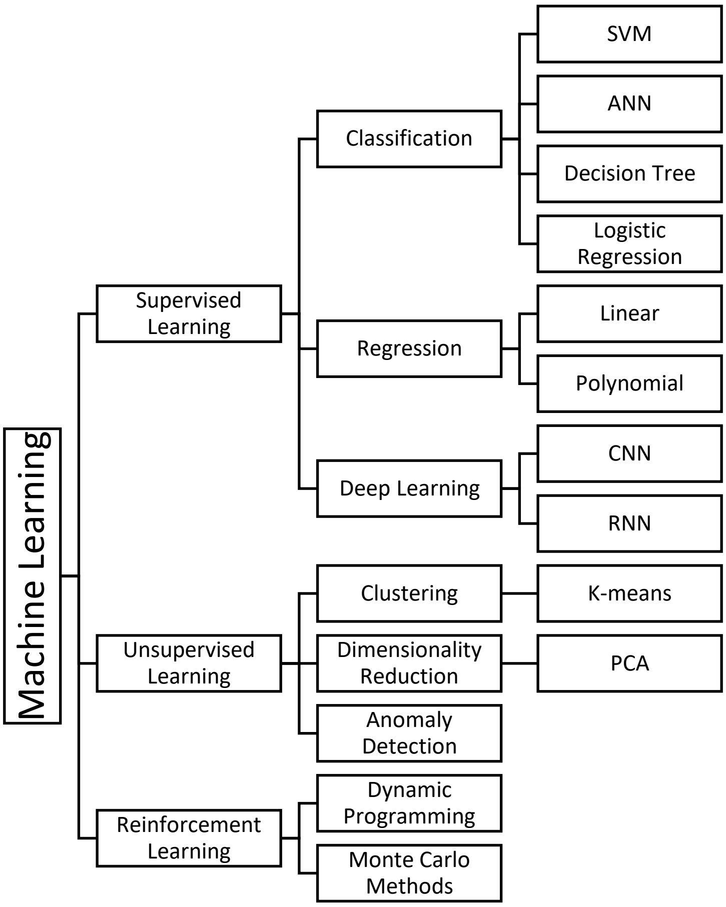

Figure 16: List of Machine Learning algorithms.

Semi-Supervised Learning

Another type of ML algorithm called "semi-supervised learning" combines unsupervised and supervised learning. Semi-supervised learning combines the small or limited amount of the labeled dataset with a large amount of the unlabeled dataset during training the algorithm [56]. This type of learning is beneficial in AM applications, where obtaining the labeled dataset is challenging. The decision to use a type of ML approach is based on the available dataset, and specific output is preferred. The use of the abovementioned ML approaches for monitoring the L-PBF process is discussed in the following sections.

1.5. In Situ Data Processing Using ML

This section presents the post-processing of the in-situ monitoring data using the ML approach classes. This section focuses on in situ defects related to melt pool signatures and the powder layer spread. The use of the ML approach in other domains such as geometric control, cost estimation, process optimization, etc., is not covered in this literature review.

1.5.1. Supervised Learning Approach

Supervised learning is one of the most commonly used ML approaches for detecting defects in the L-PBF process. The first step in supervised learning is to prepare a labeled training dataset. Labeling the in-situ data is the most challenging and error-prone task, affecting the overall accuracy of the supervised ML model. Therefore, labeling the in-situ data, such as IR images, photodiode signals, pyrometer signals, can be done via making a statistical comparison between in situ data and CT images, which captures the ground truth labels. The same can be used for labeling the different clusters obtained by unsupervised learning. Gobert et al. and Petrich et al. [57], [58] used a 36.3-megapixel digital single-lens reflex (DSLR) CCD camera (Nikon D800E) mounted inside the build chamber of EOS M280 (L-PBF system) to detect discontinuity defects such as overheating, pores and unmolten powder. The ground truth bales are extracted by comparing the post-CT scan data with captured in situ images. The labeled dataset is then used to train supervised ML approaches such as support vector machine (SVM) and neural network (NN). Imani et al. [59] used ML techniques like SVM, K-NN, and NN to find the process parameters such as hatch distance, laser power, and scanning speed likely to produce more porous parts. The link between process parameters and the pores' location, size, and frequency is studied. Aminzadeh et al. [60] used an 8.8-megapixel USB Digital Camera with high focus lenses to capture the post-printed images of every layer in L-PBF. They used Bayesian inference to detect the porosity and quality of the final part. Based on visual inspection, the training dataset is labeled “defective” and “non-defective” based on visual inspection. The frequency-domain features are extracted, and a trained Bayesian classifier is used to predict the quality of the part. Zhang et al. [61] used a high-speed camera to capture process images such as melt pool, plume, and spatters. These images are used to train SVM classifiers and CNN to detect the process anomalies. The CNN model showed a higher accuracy of 92.7 % compared to the SVM classifier, which showed an accuracy of 90.1 %.

Baumgartl et al. [62] used a convolutional neural network (CNN) to detect defects from thermographic images. CNN showed an average accuracy of 96.80 %. The thermographic images are captured using an infrared camera, placed above the build chamber with an angle of 60° to the build plate. Delamination and spatter defects are successfully identified and cross-validated with the CT scan. However, the model does not identify other defects, such as balling, lack of fusion, and keyhole.

Scime et al. [63] used a one-megapixel Photron FASTCAM Mini AX200 high-speed camera in the visible range to capture melt pool images. The machine learning technique, called Scale Invariant Feature Transforms (SIFT), extracted features from the captured melt pool signatures. The bag-of-words (or Keypoints) are used to obtain a scale-agnostic description of melt pool morphology. The melt pool morphology represents the shape of the melt pool, spatter, and vapor plume. With the ML approach, the author classified the individual melt pool morphologies into four categories: desirable, balling, under-melting, and keyhole porosities. A supervised classification ML technique called support vector machine (SVM) is used to train and test the model. The percentage of the melt pool morphologies linked to process parameters such as laser power and scan speed is obtained.

In another study, Scime et al. [64] used a computer vision algorithm to predict the percentage of defects present in part based on the powder bed images. Scime et al. extracted the images' regions and classified such as anomaly-free, recoater hopping, recoater streaking, debris, superelevation, part failure, and incomplete spreading. These categories are used as the fingerprints for the computer vision algorithm. A percentage of the particular defect in the respective layer is classified. The approach did not use melt pool signatures and instead used powder bed spreading as their prominent signature. Repossini et al. [65] used a high-speed camera to capture spatter images and used them as an indicator for process stability. They have developed a supervised learning logistic regression model to classify different energy density conditions to various quality states using spatters as a descriptor.

Some researchers also studied the acoustic signals to detect the defects in the L-PBF process using a supervised learning ML approach. For example, Ye et al. [66] used deep belief networks (DBN) to analyze the acoustic signals to detect defects such as balling, keyhole, and cracking. Shevchik et al. [67] used Bragg grating acoustic sensors to capture the acoustic signals during melting, solidification, and spattering processes. The time-domain captured signal is transformed into the frequency domain using the wavelet transformation technique. Spectral

CNN is used to identify the particular defect signals. The presented sCNN model showed an accuracy of 83–89 %.

1.5.2. Unsupervised Learning Approach

The use of unsupervised machine learning is limited in the field of the L-PBF process. However, unsupervised can be useful when obtaining the labeled training dataset is not possible. Another advantage of using unsupervised learning compared to supervised learning is that it does not require human interaction to the label training dataset. Grasso et al. [68] demonstrated the use of the T-mode Principal Component Analysis (PCA) for image data obtained by an OlympusTM I-speed 3 camera mounted outside the build chamber at an angle of 40° w.r.t build plate to define a spatial statistical descriptor and to detect local over-heating phenomena along the scan path by analyzing the intensity profile of each pixel. These local hotspots correspond to the regions where slow cooling occurred due to variation in heat flux; it can be observed at sharp corners and overhang structures. K-means clustering learning is applied to the spatially distributed PCA descriptors to detect a defect in an automated fashion. Although an iterative updating of the k-means clustering based on the new dataset allowed to detect defects in complex shapes, the approach depends on the comparisons between data collected at different layers or on the signal from successful builds of the same geometry, which limits the design its applicability to other situations. Grasso et al. [69] used an off-axis IR camera to monitor the plume of zinc material to design a data-driven and automated approach for process monitoring. The region of interest (ROI), the plume, is extracted from the IR images. A multivariate control-charting method is proposed to monitor the ROI features, i.e., mean intensity and area of the plume, to detect the deviation from the stable plume patterns. However, in this work, the author did not consider the morphology of the melt pool.

1.5.3. Semi-Supervised Learning

Okaro et al. [70] proposed another perspective of the ML approach for data treatment and predicted the quality of the parts based on their mechanical property as a descriptor. Key features are extracted from the photodiode signals, and a semi-supervised classification algorithm called "Gaussian Mixture Model-Expectation Maximization (GMM-EM)" is applied to classify the samples as "faulty" and "acceptable" based on the ultimate tensile strength of the tensile bars. This approach showed the possibility for automatic certification of the L-PBF parts based on their mechanical properties. However, the method of Okaro et al. does not illustrate any possibility of detecting defects in the parts, which is the cause of inferior mechanical properties.

Yuan et al. [71] used a high-speed 1 kHz video camera, with its focal point moving along with the laser spot, to acquire in situ video data to monitor scan track width and continuity. Image processing algorithms label a small amount of data using structured light measurements. The labeled in situ videos are used to train a semi-supervised CNN model based on the temporal ensemble method, with a small amount of labeled data and a large amount of unlabeled data. Yuan et al. showed that the semi-supervised CNN approach performs better than the supervised CNN approach. They also studied the average measuring time for 100 videos, 1.4 ms, and concluded that the trained CNN approach is adequately fast to monitor in real-time. The summary of the discussed literature is presented in Table 2.

Table 2: List of literature on the processing of L-PBF in-situ data using machine learning approaches.

Reference	Data type	Monitoring Quantity	ML technique
	Supervised Learning Approach		
Gobert et al. [58] and Petrich et al. [57]	Images of post-printing	Defects such as overheating, pores, and unmolten powder	SVM, NN
Imani et al. [59]	process parameters such as hatch distance, laser power, and scanning speed	Porosity level	K-NN, SVM, NN
Aminzadeh et al. [60]	Images of post-printing	Porosity	Bayesian inference
Zhang et al. [61]	Melt pool, spatters, and Plume images	Process anomalies	SVM and CNN
Baumgartl et al. [62]	Thermographic images	Delamination and spatter defects	CNN
Scime et al. [63]	Melt pool images	Types of melt pool shapes	SIFT, SVM
Scime et al. [64]	Powder bed images	Powder bed defects	Computer vision
Ye et al. [66]	Acoustic signals	Defects such as balling, keyhole, and cracking	DBN
Shevchik et al. [67]	Acoustic signals	Defect signals	sCNN
	Unsupervised Learning Approach		
Grasso et al. [68]	Images	Overheating defect	T-Mode PCA, K-means
	Semi-supervised Learning Approach		
Okaro et al. [70]	Photodiode signal	Defective parts based on tensile strength	GMM-EM
Yuan et al. [71]	Video	Scan track width and continuity	Semi-supervised CNN

The final aim of in situ monitoring is to improve the overall reliability of the process via a feedback control loop. This will significantly reduce the material waste and time needed to qualify for quality assurance. Yao et al. [72] developed a closed-loop feedback control system for real-time monitoring of the L-PBF process. Firstly, the defect level of each printed layer is calculated based on irregular and non-homogeneous patterns using multifractal analysis. Secondly, the composite index is decided for each porosity level based on Hotelling T2statistics from the multifractal spectrum. Finally, the stochastic dynamics of the layer to layer defect conditions are modeled as a Markov process to determine an optimal control policy.

1.5.4. Challenges

Although there are tremendous possibilities of the ML approach in the AM industry, a few limitations or problems are associated with the AM methods that can have a deterministic effect on ML outcomes.

- **Size of data:** ML approaches are data-driven methods that require a sufficient amount of data to make accurate predictions. The amount of training data needed increases exponentially with a number of input variables. However, in some applications such as AM, data acquisition and labeling the training data is extremely difficult and expensive. For example, obtaining a large amount of data for particular defects such as keyhole and lack of fusion in the L-PBF process is challenging. Thus, using neural networks that require a copious amount of data for defect detection can be challenging.
- **Lack of knowledge for feature extraction:** Selecting good features that can capture the distinction in the dataset is most vital. Sometimes, it is very tricky to identify and extract these features. For example, it is challenging to identify the features that distinguish an unstable melt pool signal from a stable melt pool signal in photodiode data.
- **Lack of labeled data:** As discussed earlier, the supervised learning ML approach requires a labeled dataset for training. Therefore, a better understanding of the acquired data is needed to label it. However, sometimes it is challenging to label the data accurately and effectively. For example, in the case of melt pool in situ monitoring data, it is very tricky to identify the "acceptable" melt pool profile from the "unacceptable" melt pool profile. There are high chances of human error and misclassification. It can affect the accuracy of the whole model.
- **Machine learning training problems:** Overfitting and underfitting are the most common problems in machine learning models. Overfitting occurs when the model tries to fit every data point precisely in the training dataset. It makes the model vulnerable to noise and outliers. Usually, overfitting is most likely with non-parametric and non-linear models that are more flexible while learning a target function. For example, the Decision

tree (DT) is a nonparametric algorithm that is very flexible and subjected to overfitting training data. The overfitting problem can be eliminated by running a tree after it has learned to remove some of the detail it has picked up. Underfitting occurs when the model cannot extract a reasonable relationship among training data points. An underfit model will perform poorly on training data and will not be able to generalize to new data. Drop-out and regularization techniques can be used to overcome underfitting and overfitting problems [73], [74].

1.6. Materials

This section has discussed the metallurgical aspects of the Al and Inconel 718 alloys. These two alloys are primarily used in our study.

1.6.1. Al Alloys

1.6.1.1. Background

The word Aluminum was first used in 1807, later changed to Almunium by the international union of pure and applied chemistry (IUPAC) [75]. However, the American chemical society changed it back to Aluminum in 1925. Aluminum or Al is the most commonly used material compared to other non-ferrous metals. Annually, 24 million tons of Al is used worldwide, out of which 18 million is extracted directly from the ore, whereas the rest is recycled from the scarp. Al has a high oxygen affinity, which means it is easily oxidized to form Alumina or another oxide form [75]. Al makes 8 % of total metallic materials in the earth's crust, making it the second most abundant material, followed by Iron, Mg, Zn [75], [76]. From a chemistry point of view, Al is the third group element with an atomic number of 13 and an atomic weight of 26.98. Al has a face-centered cubic crystal structure with coordination of 12 and a packing factor of 0.74 [75], [77]. Al has a melting temperature of 660 °C, boiling temperature of 2520 °C, and specific heat for temperatures from 0 °C to 100 °C is 917 $J.kg^{-1}. K^{-1}$ [77]. Al is available in various sizes and shapes such as powder, flakes, sheets, plates [78].

1.6.1.2. Physical Metallurgy of Aluminium and its Alloys

Al is mostly used in its alloy form as pure Al shows the lowest strength of its alloys [79]. The applications of pure Al are mostly in electrical appliances as a conductor cable. The alloying elements such as Mg, Si, and Cu are substituted to strengthen the pure Al. Ti and Cr are used as grain refinements, Mn and Sb enhance corrosion resistance properties, Ni is used to enhance thermal strength, and Co, Bi, and Fe are used to improve machineability [77], [79]. Si improves the castability of the Al alloys by increasing the fluidity and reducing the solidification shrinkage [80]. The Al-Si phase diagram shows that the eutectic reaction occurs at 12.6 wt. %

Si and at temperature of 577 °C (Figure 17) [76], [77]. The Al-Si alloys are difficult to machine due to hard phase Si [77]. The addition of Mg to the Al-Si alloy leads to the formation of Mg_2Si precipitates, enhancing the strength and making the alloy heat-treatable [77], [80]. Also, Mg is the most desirable strengthening element due to its high solubility [77]. Si and Mg are two main alloying elements for Al as their atomic structures are similar to that of Al. Although their crystal is different, Al has FCC crystal structure, Si has diamond-type cubic, and Mg has a hexagonal close-packed crystal structure. T6 precipitate hardening or tempering is recommended heat treatment profile for the Al-Si alloys. The steps involved in the heat treatment are as follows: Solution heat treatment (SHT) followed by quenching and ageing. The nucleation of precipitates occurs at the Guinier-Preston zones [75].

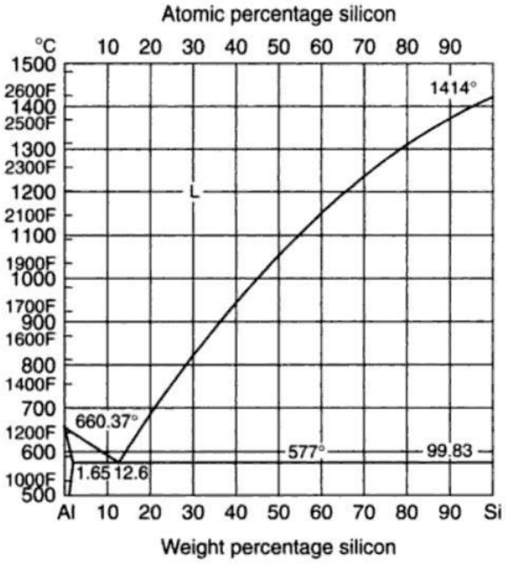

Figure 17: The phase diagram of Al-Si [76].

1.6.1.3. Solidification of Al-Si

The material's final microstructure strongly relies on the type of solidification. As in the L-PBF process, the melt pool moves at a speed of around 1m/s, undergoing a rapid solidification which develops a fine structure.

Scheil solidifications and equilibrium conditions are applied to predict the solidification temperature range of the Al-Si eutectic alloy. The main difference between the two models is that infinite diffusivity of solid state diffusion is considered, whereas, in scheil solidification, solid-state diffusion is neglected (Table 3). Thermodynamic simulation software such as thermocalc can calculate the mass fractions and solidification temperature range for different phases.

Table 3: Equations for analytical models.

Model	**Lever or Equilibrium rule**	**Scheil rule[81]**
Solid diffusion	complete	no
Liquid diffusion	complete	complete
Equation	$C_s = \frac{kC_0}{(1-f_s)+kf_s}$	$C_S = kC_0(1-f_s)^{k-1}$

The typical solidification map for alloy systems is shown in Figure 18a [82]. During solidification, the interface morphology (i.e., planar, dendritic, or cellular) is decided by the thermal gradient (G, unit: °C/m) and growth rate (R, unit: m/s). Figure 18b shows the possibility of dendritic morphology suppression at a high solidification rate could be the reason behind the absence of dendritic structure in AM parts [83]. Figure 18c shows directional solidification's primary and secondary arm spacing [84].

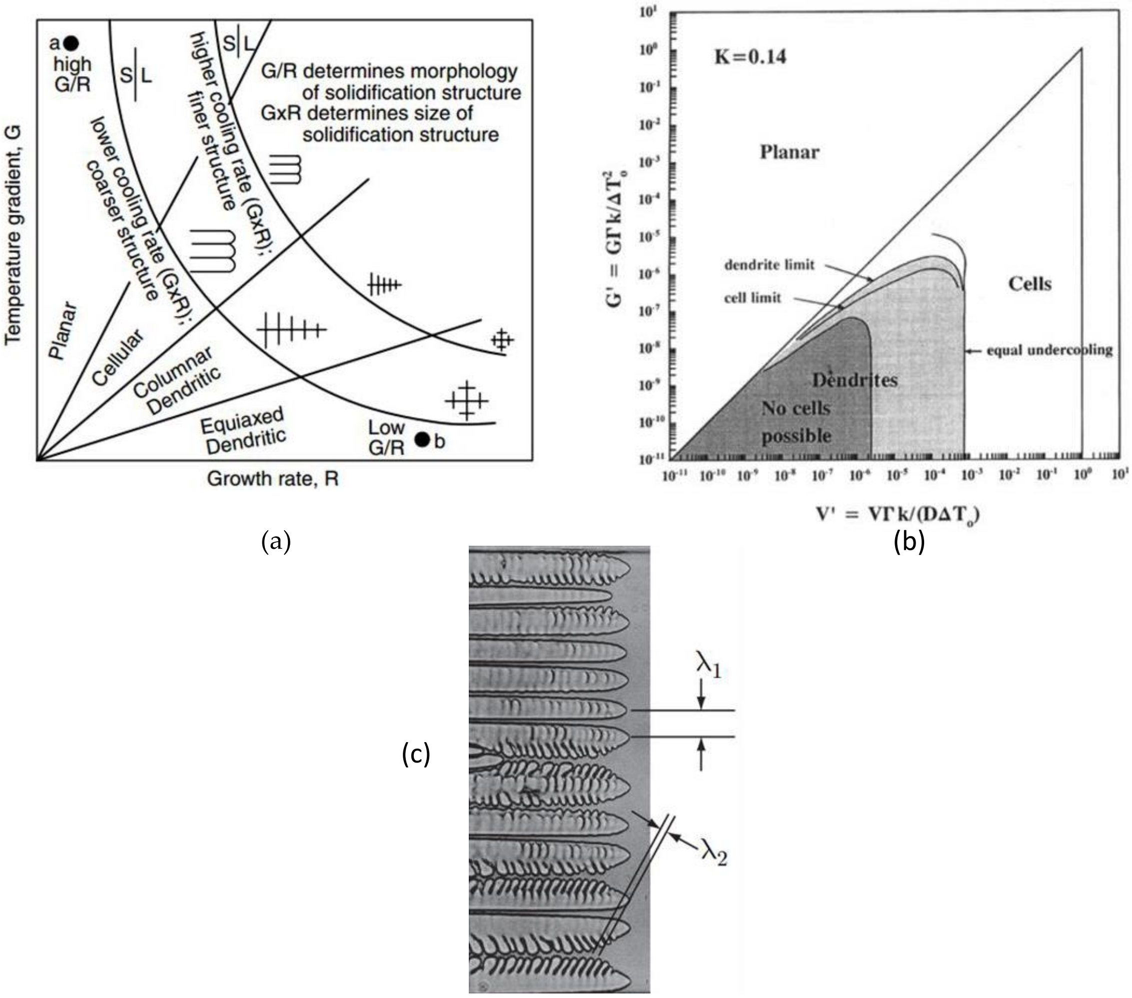

(a)

(b)

(c)

Figure 18: (a) Solidification map, showing the effect of temperature gradient and growth rate [82], (b) Suppression of dendrites during high solidification rates [83], and (c) schematic of primary dendrite arm spacing (PDAS), and secondary dendrite arm spacing (SDAS) [84].

The relationship between the dendritic arm spacing and cooling rate is expressed as (Equation 4)

$$\lambda_1 = a\dot{T}^{-n}$$

Equation 4

where λ_1 is primary dendrite arm spacing or cell size, $\dot{T}$ is the local cooling rate, and a and n are proportional constants.

The value of n is 0.32 to 0.38 for cellular morphology and 0.21 for dendritic microstructure [85]. Similarly, the value of n is 0.33 for secondary arm spacing. In the L-PBF process, the solidification rate is associated with the laser scan speed. A high solidification rate leads to higher cooling rates, leading to cellular microstructures for near eutectic Al-Si alloys in the L-PBF process where solidification rates are more significant than 0.2 m/s [86].

1.6.1.4. Al Alloys Processed by L-PBF Process

Al alloys are difficult to be processed by the L-PBF process due to their high reflectivity, high thermal conductivity, and low laser absorptivity in the wavelength range of 1.06 µm [87]. Therefore, the AM of Al alloys is primarily restricted to cast alloys, i.e., AlSi10Mg and AlSi12, a hypoeutectic and eutectic alloy, respectively. Other wrought alloys such as Al6061 and Al7075 gained attraction due to their use in aerospace applications, but unfortunately, they are very difficult to process by L-PBF due to their non-weldability. High affinity to oxygen at room temperature and elevated temperatures also makes Al alloys difficult to be processed by L-PBF. The room temperature oxidation creates a thin Al_2O_3 oxide layer on the Al alloy powder. This oxide layer could develop cracks and binding issues while printing using the L-PBF process. Moreover, complications can arise due to the vaporization of low-melting

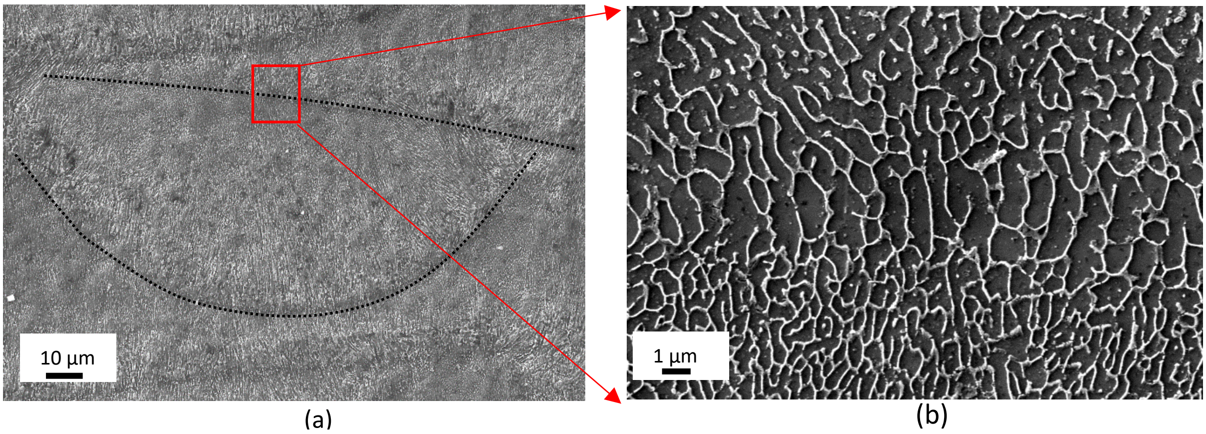

Figure 19: (a) Microstructure of melt pool, and (b) its corresponding eutectic cells.

materials such as Mg and Zn in significant quantities in Al7075 alloys while processing using EBM [88].

However, most commonly AM processed Al alloys, i.e., AlSi10Mg and AlSi12Mg, show a similar microstructure consisting of Al cells towards the center of the melt pool, along with fine Al+Si eutectic in between as depicted in Figure 19. The most common porosity in AM processed AL alloys is hydrogen or gas porosity. Hydrogen is highly soluble in the melt, but the solubility decreases rapidly during solidification leading to small spherical porosities in the melt pool. Low power pre-scan can be applied to remove the moisture from the powder layer to minimize the number of gas porosities [13]. But the fine homogeneously dispersed Si in Al matrix in L-PBF parts shows excellent mechanical properties compared to casted alloys. The as-built alloys showed a hardness values of 125 to 135 HV, comparable to those of die-casted and aged material 130-135 HV [89], [90]. However, the hardness value significantly rose to 150 HV when aged between 120 °C and 170 °C, causing the formation of small Si precipitates into Al cells from the supersaturate Al matrix. Also, the L-PBF processed AlSi10Mg alloys showed good ductility in the range of 3.5-5.5 % compared to cast and aged AlSI10Mg reported in the range of 3.5-5 % [90]. Moreover, fatigue can also be improved by tailoring the scanning orientation, preheating temperatures, and porosities [91].

1.6.2. Inconel 718 Alloy

Due to its superior mechanical properties and low cost, Inconel 718 (IN 718) has always been the material of interest for many applications, like aerospace, gas turbine, liquid-fuelled rockets, cryogenic tankage, and the space shuttle.

Inconel 718 belongs to the family of a nickel-base superalloy, which was developed by the International Nickel Company of Delaware and New York in 1959 [92]. Superalloys refer to high-temperature materials that can withstand extremely high temperatures and loads and retain excellent mechanical and corrosion-resistant properties [93]. The development of the Inconel 718 alloy in 1962 was a massive success as it shows good weldability, manufacturability, and high strength. Especially its ability to be resistant to strain-age cracking. Aerospace giants such as Pratt & Whitney are the first to use Inconel 718 components for gas turbines and rocket engines [92]. Nowadays, over 50 % of superalloys components of commercial engines are made of Inconel 718 alloy. Besides the aerospace industry, Inconel 718 alloy is heavily used in the power industry, including internal parts in nuclear reactor plants [94], [95].

1.6.2.1. Compositional Element in Inconel 718

Inconel 718, also known as UNS identifier N07718, corresponds to the chemical composition mentioned in the table. The main principle element is Ni that forms austenitic matrix phase γ. A combination of various alloying elements mentioned in the table is added to the γ matrix to achieve desirable properties [96]. Each element has its purpose; for example, Fe, Co, Cr, Ru, Mo, W, and Rh act as matrix stabilizers due to their similar atomic radii to Ni. Whereas elements Al, Ti, and Nb, which has larger atomic radii (Al has smaller radii than some stabilizers), promotes the formation of strengthening precipitates γ′ and γ″.

Similarly, the Ir, Re, Ru, Pt, W, Rh, and Mo elements improve the creep resistance due to their low interdiffusion coefficients, and Cr makes the alloys corrosion resistant. Co promotes the increase in the solubility temperature of γ', increasing the maximum service temperature of the Inconel 718 alloy. The specific effects of the alloying elements are summarized in Table 4 [96]. Interestingly, all the listed alloying elements do not behave positively, and instead, many might form topologically closed-packed phases. Due to their brittle nature, these phases can hold the strengthening elements to act as crack initiation sites [97]. Therefore, the microstructure and properties of nickel-based superalloys are correlated to the chemical composition and the interdependence of alloying elements and processing [96]. So, it is vital to tailor the processing route from melting to casting and heat treatments to obtain the alloying elements in desirable form.

Table 4: Inconel 718 alloy composition and the effect of the alloying elements [96].

Element	**Value**	**Effect**
Ni	50-55	FCC matrix stabilisation
Fe	Bal.	
Cr	17-21	Solid-solution strengthening, enhanced hot corrosion resistance
Mo	2.80-3.30	Solid-solution strengthening
Nb+Ta	4.75-5.50	γ″, NbC carbide, TaC carbide, and delta-Ni3Nb precipitation
Ti	0.65-1.15	γ′ precipitation
Al	0.20-0.8	γ′ precipitation, retarded formation of Ni3Ti
Co	0-1.0	Higher solvus temperature of γ′
P	0-0.015	Improved carbide precipitation
B	0-0.006	Improved ductility and creep strength
C	0.08	MC formation

Moreover, Inconel 718 shows a nominal density of 8.19 g/cc, the specific heat of 435 J/(kg*°C, the thermal conductivity of 11 W/(m*K)), and elastic modulus of 200 GPa.

1.6.2.2. Phases in Inconel 718

Inconel 718 primarily consists of γ-phase (matrix of Ni) and alloying elements in solid solution, making secondary phases. As Inconel 718 is a precipitate-strengthened superalloy, the phases listed in Table 5 are essential in determining the Inconel 718 properties. Out of these, γ'' is the primary strengthening phase whose formation is strongly dependent on the Nb concentration [98]. Nb segregates in the inter-dendritic regions during solidification, forming Nb-rich regions. In the absence of proper homogenization, these regions can lead to the formation of Laves phases which can be detrimental to the mechanical properties of Inconel 718.

Table 5: Phases in Inconel 718 and its composition [98].

Phase	**Crystal Structure**	**Formula**
γ	FCC	N/A
γ'	FCC, Ordered $L1_2$	$Ni_3(Al,Ti)$
γ''	BCT, Ordered $D0_{22}$	Ni_3Nb
δ	Orthorhombic, Ordered $D0_a$, Ordered Cu_3Ti	Ni_3Nb
MC	Cubic, B_1	NbC
Laves	Hexagonal, C_{14}	Fe_2Nb Fe_2Ti Fe_2Mo
σ	Tetragonal	FeCr FeCrMo CrFeMoNi CrCo CrNiMo

γ′ and γ′′

Both γ′ and γ′′ are coherently present in the γ matrix of Inconel 718. The typical picture of γ′′ can be observed in the TEM picture, as shown in Figure 20 [99]. Alloys with Al + Ni/Nb ratio > 0.8 nucleate γ′ first, whereas alloys with Al + Ni/Nb ratio > 0.7 nucleate γ′′ first. The results of the atom probe indicate the formation of Nb clusters before Al/Ti, which leads to the conclusion that γ'' nucleates first in some alloys. The formation of γ'' and NbC at the grain boundaries is greatly influenced by the segregation behavior of Nb [100], [101]. It is also observed that high-density small cubes are precipitated during the first stage of formation of γ'', whereas in the second stage, more ellipsoidal discs are precipitated [102]. Volumetric fraction measurements using the electrochemical extraction method showed that the ratio of γ''/γ is 3.0 [103]. As listed in the Table 5, γ′′ has a D022 crystal structure whereas γ′ phase has an L12 crystal structure. The lattice parameter a of D022 is equal to that of L12, but the lattice parameter c is roughly twice that of L12; that's why phase is termed as γ′′. The lattice mismatch between coherent γ'/γ and γ''/γ interfaces, intrinsic strengths of γ'' & γ', and anti-phase boundary energy in ordered γ'' & γ' phases are the main reason behind the strengthening of γ matrix [96].

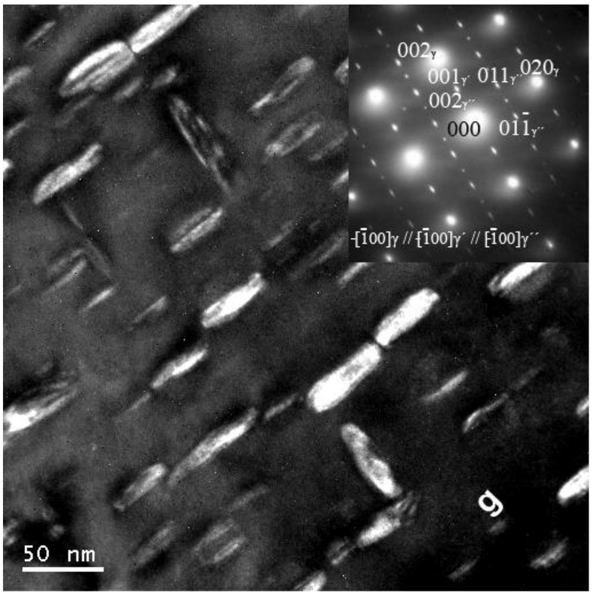

Figure 20: Dark field TEM image of γ'' precipitates [99].

Delta

The γ'' phase is metastable. Therefore, It can convert to a thermodynamically more stable δ phase with a plate or needle-like morphology depending on temperature and time, as shown in Figure 21. The formation of δ-phase may follow several pathways, dependent on temperature and time (Figure 21). At low temperatures, i.e., <700 °C the cellular shaped δ- phase is precipitated at the grain boundaries [104], at 750-800 °C, transformation $\gamma'' \rightarrow \delta + \gamma'$ occurs, which gives γ' in addition to cellular δ-phase precipitation [102], And at high temperatures (~960 °C), there is direct precipitation of δ-phase from the supersaturated matrix [105]. The δ phase is incoherent with the γ matrix, which can be detrimental to the strength of Inconel 718 if present in large quantities. As the δ phase precipitation occurs at the expense of the Nb, which is associated with loss of γ'' phase could decrease the overall strength of the Inconel 718 alloy [96], [106]. The material condition and temperature are essential factors deciding the morphology and quantity of precipitated δ phase. Precipitation of δ phase is believed to be a result of the excessive coherent mismatch between γ'' and γ matrix that can be retarded by increasing the Al/Ti ratio or Al+Ti content in Inconel 718 alloy [107]. Higher Al+Ti content or Al/Ti ratio can reduce the size of γ'' phase, which results in reducing the lattice mismatch between γ'' and γ matrix, thus directly reducing the formation of δ phase. However, sometimes, the δ phase has favorable effects on the mechanical and microstructural properties. For example, over 4 % of the δ phase is present at the grain boundaries, which can inhibit the grain growth during the heat treatment and working conditions that can favorably influence the strength of Inconel 718 [96], [108]. Also, the globular grain boundary δ phase is helpful in retarding the intergranular crack propagation, which is beneficial for creep and stress rupture properties [109], [110], [111].

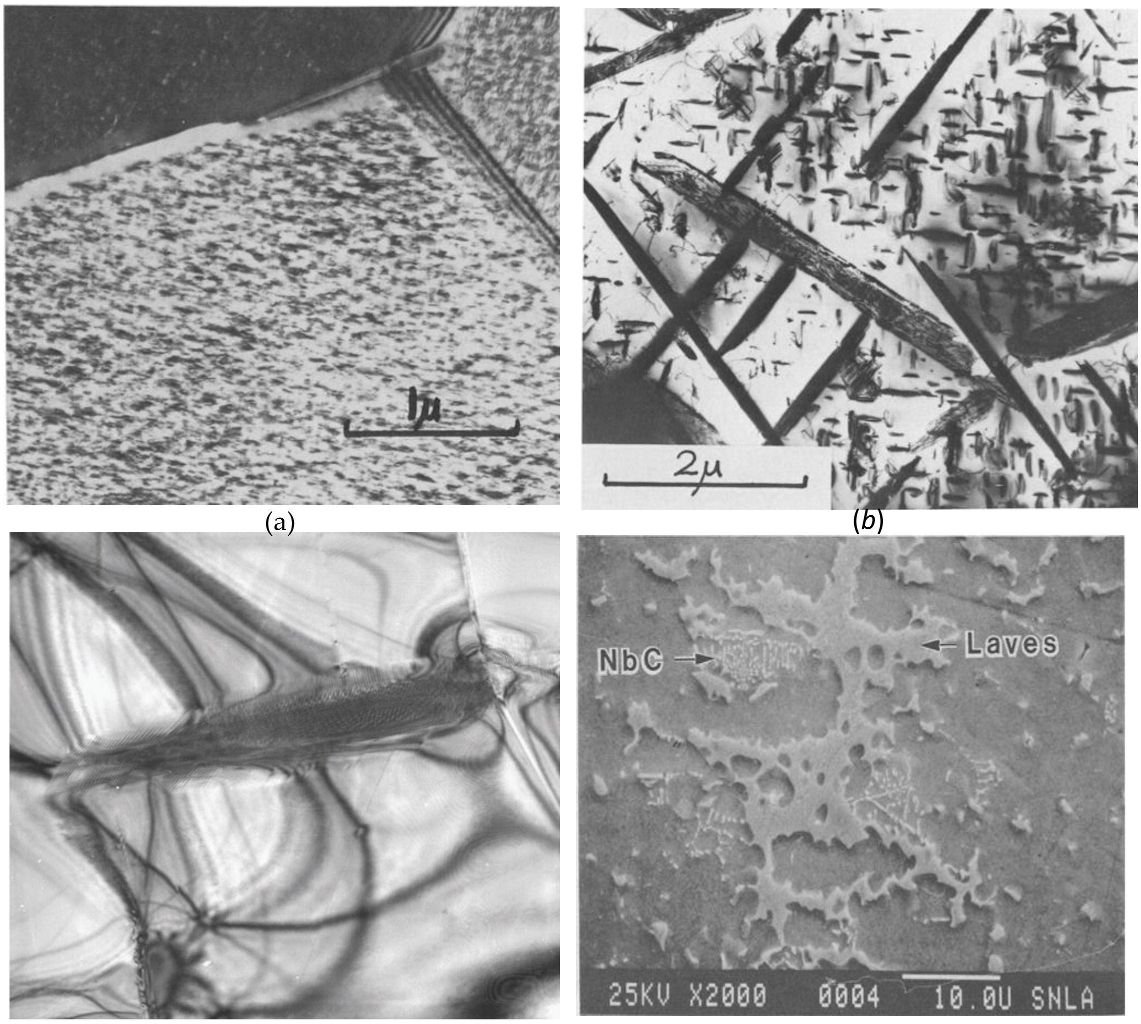

(a) (b)

(c) (d)

Figure 21: Delta phase formation in Inconel 718 by (a) cellular precipitation at <700 °C, (b) cellular precipitation and transformation from γ'' at 750-800 C, (c) direct precipitation from the γ′ matrix at 960 °C, and (d) laves phase.

Laves Phase

Another phase called Laves phase is a topologically close packaged phase resulting from the segregation of Nb, Si, and Mo during solidification due to the rejection from the dendrites into inter-dendrites regions (Figure 21d). The laves phase is undesirable as it is brittle intermetallic, which can be detrimental to the mechanical properties [98], [112]. Chang et al. [113] reported that apart from segregation of Nb, high content of Fe and Cr is highly desirable for the formation of laves phase. Generally, the chemical composition of the laves phase is (Ni, Fe, Cr)2(Nb, Mo, Ti), but it can differ during solidification. Also, laves phase is responsible for the depletion of the Nb matrix and γ″ phase (principle strengthening phase). Schirra et al. [114] reported the effect of laves phase on the mechanical properties of cast-Hot isostatic pressing (HIP) Inconel 718 and wrought Inconel 718 alloy. In wrought Inconel 718, the laves phase is presented at the grain boundaries as a continuous network that can act as a preferred crack propagation site during fatigue. Also, it leads to poor tensile properties and toughness at room temperature. In cast-HIP, precipitation of laves phase occurs as irregular aggregates, leading to poor tensile properties at room temperature and poor stress rupture at higher temperatures. Also, the laves phase sites act as crack initiation sites reducing the crack growth resistance property in Low cycle fatigue. Apart from that, the laves phase precipitation can also affect the good weldability of the Inconel 718. During the heating cycles of welding, the low melting point laves phases presented at the grain boundaries can be liquified, resulting in hot cracking under thermal stresses [115], [116].

Carbides

The high content of Nb promotes the formation of the Nb-rich MC-type carbide phase in Inconel 718. Ti is also present in this type of carbide, resulting in the lattice parameters between NbC and TiC phase [117]. But the NbC is more predominant, and primary MC carbide is denoted as (Nb, Ti)C in Inconel 718. The discrete blocky-shaped primary MC carbide is distributed non-uniformly through the grains and at the grain boundaries [117], [118]. Intergranular MC carbide contributes little to the strength of the matrix compared to γ″ precipitation but can contribute to impeding the movement of dislocations. Grain boundary MC carbide promotes the fracture transition from trans granular to intergranular at room temperature [117]. Under plastic deformation, the stress will be concentrated at the carbide and matrix interface resulting in a microcrack to relax the localized stresses. The microcracks can easily add up and lead to intergranular fracture if the MC carbides are closely distributed along the grain boundary. It is expected that discretely distributed GB MC carbide enhances the rupture life by impeding the grain growth at elevated temperatures. The size, distribution, precrack, oxidation and test conditions decide the effect of MC carbide on the mechanical properties. For example, Mitchell et al. [119] reported that TiN acts as a heterogeneous nucleation site that can substantially manipulate the distribution of precipitation of MC carbide.

1.6.2.3. Solidification

The resulting microstructure of the final alloy is strongly dependent on the conditions of the solidification from liquid to solid. There are three types of solidifications possible, i.e., dendritic, cellular, or planar, out of which dendritic solidification is most common [84]. The type of solidification route is dependent on the solid-liquid interface velocity (R), thermal gradient (G), and other boundary conditions of the melt pool. Inconel 718 shows a dendritic solidification route during casting and welding [120]. However, the spacing among dendrites will vary depending on solidification kinetics. Typically there are two types of dendrite arm spacing, i.e., primary dendrite arm spacing (PDAS) and secondary dendrite arm spacing (SDAS). PDAS represents the spacing between the primary cores of the dendrites, whereas the SDAS represents the spacing between the branches of cores. As the solidification starts, the alloying elements such as Nb, Ti, and Mo segregate into the inter-dendritic regions. These segregated regions lead to localized phase formation into the inter-dendritic regions. A cooling rate equal to G*R and the quantity G/R are essential factors in predicting the stability of the planar solidification front [121]. The cooling rate strongly influences diffusion, solidification type, and partition coefficient [122]. For example, as the cooling rate increases, the solidification route changes from the dendritic to cellular and further into diffusionless. Cooling rates from 0.25 to 20,000 °C/s have been studied, and it is noticed that during rapid solidification, the inter-dendritic regions contain less Nb element; hence no laves phase. Whereas slower solidification promotes more segregation, increasing in laves phase. The diffusion rate and partition coefficient increase with the cooling rate increase, as confirmed with increased lattice defects during higher cooling rates [122]. During rapid solidification, the nucleation sites are of diffusion less in nature which results in cell like solidification. At cooling rates < 500 °C/s, enhanced Nb and C segregation into inter-dendritic regions leads to the precipitation of laves phase and NbC as shown in Figure 22a [123].

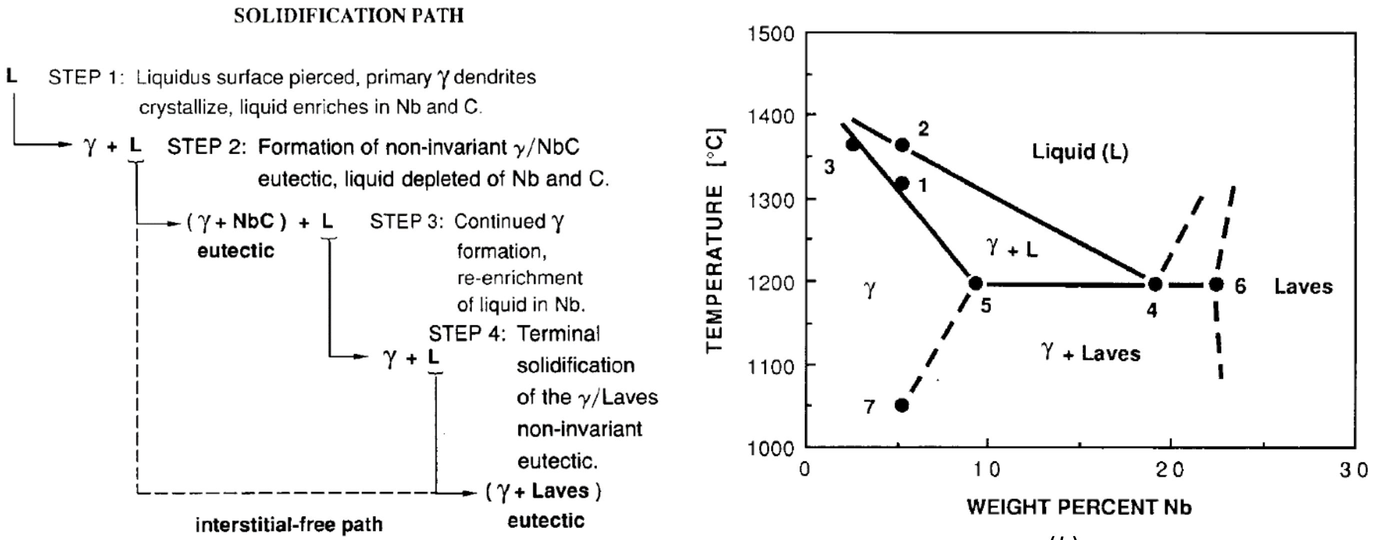

(a)

(b)

Figure 22: (a) Solidification path [123], and (b) its constituents [124].

Figure 22b shows that Nb segregation during solidification can form a pseudo phase diagram to predict the laves phase precipitation. Phases that evolve during solidification are termed primary phases whereas those that evolve during solid state heating and cooling are called secondary phases. The carbide size increases with decreased cooling rates as the relationship is developed for the remelt ingots at limited cooling rates. While during rapid solidification of Inconel 718, carbides are reported to be precipitated between the dendritic arms [124]. Process modification can affect the dimensions of microsegregtion and grain size, improving the mechanical properties. For example, nitrogen contamination can form TiN which acts as a nucleation site for NbC that affects the precipitation kinetics [119].

Additionally, the G and R can also determine the nature of grain structure based on columnar to equiaxed transition (CET). The diagram shown in Figure 23 [125] depicts the CET for Inconel 718. It can be noticed that the equiaxed grains are favored as G increases and R decreases, whereas columnar grains are favored when G increases and R decreases. However, the CET is not studied for the solidification rates above 104 °C/s in Inconel 718.

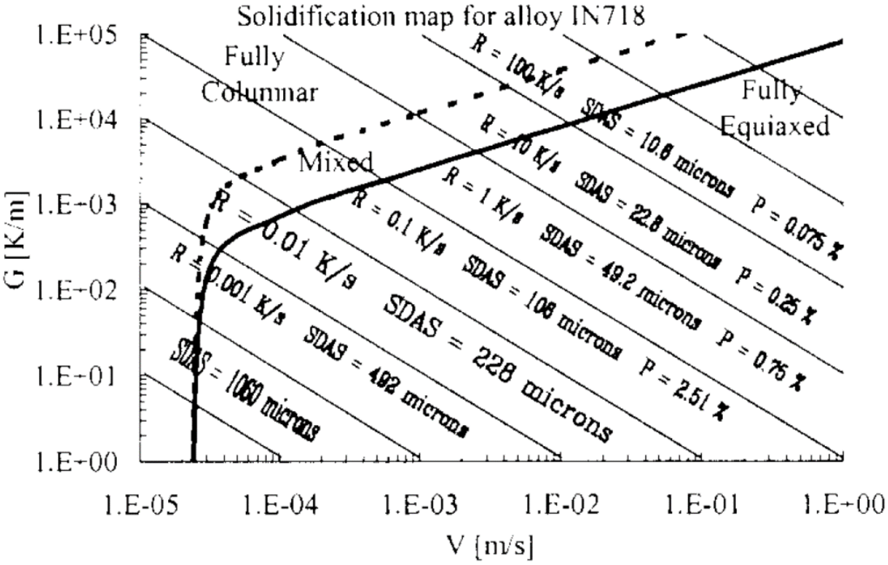

Figure 23: Solidification map for Inconel 718 [125].

1.5.2.4. Inconel 718 AM

The microstructural and mechanical properties of additively manufactured Inconel 718 can differ depending on the processing history. For example, different processing parameters such as scanning strategy and part geometry can lead to different microstructures in the same AM process. The high cooling rates during AM processing limit the precipitation by limiting the diffusion time and distance. For example, single-phase microstructure is observed for L-PBF processed Inconel 625, whereas vertical rows of γ'' precipitates are observed for EBM processed

IN625 [126]. Similarly, many authors have reported the presence of γ'' phase in as-built Inconel 718 [127]–[129] along with additional phases such as (Ni, Cr, Fe)2(Nb, Mo, Ti), Laves phase at the grain boundaries [128]–[130], and carbides [128], [130]. In LMD processed Inconel 718, the presence of carbides, δ precipitates and laves phases are higher incase of high speed and high power compared to samples processed at lower speed and lower power [130]. Therefore, the post-heat treatment of Inconel 718 shall be customized based on its processing history. Table 6 summarizes the ASTM F305 recommended heat treatment profiles for L-PBF processed Inconel 718. It is found that γ' precipitates are formed during conventional two-step heat treatment, further strengthening the material [127]–[129], [131].

Table 6: ASTM F3055 recommended heat treatment for AM Inconel 718.

Stress relief	**Hot isostatic pressing**	**Solution+Ageing**
1065±15 C for 85~105 min with parts attached to the build plate.	1120~1185 C at > 100 MPa in an inert atmosphere for 240±60 min, followed by furnace cool to ≤425 C.	AMS 2774

CHAPTER 2

Process Optimization for AlSi7Mg0.6

> “
>
> It is important to find the best-fit parameter prior the investigations of the laser-material interaction. In this Chapter, we have presented the effect of different scanning strategies parameters on the evolution of the microstructural (grain morphology, crystallographic texture, and phases) and mechanical properties (tensile tests, hardness and porosity). Also, we have investigations the cooling rate evolution in the individual melt pool along with the effect of residual stresses.

2.1. Theory and History

As presented in the literature review (Chapter 1), the L-PBF process is of great interest to manufacturing due to its capability and adaptability to fabricate a new complex part. But one of the most significant disadvantages of the L-PBF process is that it takes a lot of time and experiments to find best-fit process parameters for new material. In the L-PBF process, many parameters such as laser power, scanning speed, hatch distance, layer thickness, and scanning strategy can strongly influence the final part properties. Therefore, optimizing and exploring the influence of each parameter is of vital importance in achieving desired microstructural and mechanical properties [132], [133]. Scanning strategy representing the spatial motion of the input energy (laser or electron beam) can influence the thermal gradient in a layer, affecting the overall part quality [134]. Several critical defects such as residual stresses, lack of fusion, and balling can be tailored by adapting suitable scanning strategies [135]. Various parameters such as scan vector length, scanning pattern, and scan vector rotation need to be optimized to achieve desired part properties. The different scanning patterns are as follows:

1. *Uni-directional scanning:* It is a scanning pattern in which the energy source scans the surface as single adjacent scan vectors moving in the same direction.
2. *Bi-directional scanning:* It is also referred to as “zig-zag scan,” It is principally similar to uni-directional. The only difference is that adjacent scan vectors are in opposite directions.

3. *Chessboard scanning:* The scan area is divided into small square cells similar to the chessboard, and the energy source scans individual cells. The length, rotation, and scanning direction of the individual cells can be varied. The size of the scan vectors is comparatively smaller than the above-discussed strategies. This helps to optimize the residual stresses in the final part.

4. *Stripes scanning:* It is similar to uni-directional or bi-directional strategies. The only difference is that the scan area is divided into small stripes with smaller individual scan vectors. The rotation between consecutive layers can be applied too. Also, it is the most common scanning strategy in the L-PBF process.

The above-presented scanning strategies significantly affect the thermal gradient, cooling rate, and heat flow of the individual layers, resulting in a change in crystallographic texture, grain size, solidification cell size, and grain aspect ratio for the building part [27], [136], [137]. Generally, higher cooling rates and a lower ratio of a thermal gradient to solidification rate lead to lower texture strength due to columnar to equiaxed transition (CET) [136], [138].

Apart from microstructural changes, the scanning strategies also partly influence the residual stresses' evolution, which can be detrimental if not optimized. Dunbar et al. [139] reported that the residual stresses are reduced by applying rotation between consecutive layers. Cheng et al. showed that the residual stresses are higher in the longitudinal direction (along the scan vector direction) compared to the transverse direction [140], [141]. Also, the longitudinal stresses increase with an increase in the scan vector length, so it can be concluded that the long scan vectors can lead to distortion in part [142]. Kruth et al. [30] and Mercelis et al. [24] reported that the island's size in chessboard strategy does not affect the residual stresses. Contrary to that, Lu et al. [133] observed that island size of 2*2 mm^2 has the lowest residual stresses followed by 5*5 mm^2, 7*7 mm^2, and 3*3 mm^2 for SLMed Inconel 718 alloy. So, it can be concluded that the evolution of residual stresses in chessboard strategy is not well understood.

Al-Si alloys are excellent materials for casting and are historically used for sand casting. It shows good corrosion resistance, good weldability, and mechanical properties. In the L-PBF process, AlSi10Mg and AlSi12Mg are the most commonly used material and extensively studied by researchers. But recently, AlSi7Mg0.6 also being used as a potential candidate for the L-PBF process [143]. Recently, a study has been reported on investigations of the best-fit parameters to obtain fully dense parts [144]. Other authors have identified the links between the distribution of Si particles in SLM samples and the mechanical properties [145]. But not many studies are available on investigating the effect of scanning strategies on the microstructure, residual stresses, and mechanical properties of AlSi7Mg0.6, which is the aim of this chapter.

2.2. Experimental Setup

2.2.1. Material

The AlSi7Mg0.6 powder with composition summarized in Table 7 is used for this study; supplied from SLM Solutions had a spherical morphology with a particle size distribution of 20 – 63 µm and an average diameter of 41.88 µm. The powder is kept in air-tight containers, and humidity is checked before printing. The powder's apparent density is 1.53 g/cm^3.

Table 7: Elemental composition of as received AlSi7Mg0.6 powder (All the values are given in wt. %).

Element	**Al**	**Cu**	**Fe**	**Mg**	**Mn**	**Si**	**Ti**	**Zn**	**Others**
Minimum [wt %]	Balance	-	-	0.45	-	6.50	-	-	-
Actual [wt %]	Balance	<0.01	0.08	0.55	<0.01	6.90	0.07	0.01	<0.03
Maximum [wt %]	Balance	0.05	0.19	0.70	0.10	7.50	0.25	0.07	0.03

2.2.2. Machine and Process Parameters

The commercial SLM 280^{HL} (SLM Solutions Group AG, Lübeck, Germany) is equipped with 700 W twin continuous wave (CW) ytterbium fiber lasers with an emitting wavelength of 1070 nm spot diameter of 115 µm is used for printing. The build envelope volume is 280*280*365 mm^3, and the build chamber is maintained in the Ar gas environment with an oxygen level below 0.1 %. The Aluminium base plate is preheated to 150 °C before printing to reduce thermal stresses in part [89]. The chessboard and stripes scanning strategies are used with varying stripes and chessboard island sizes. The rotation between two consecutive layers also changes between 0° to 90°. The process parameters and the sample's nomenclature are tabulated in Table 8 and Table 9, respectively.

Table 8: Process parameters used in this study.

Varied Parameter	**Values**
Power (W)	350
Scanning speed (mm/s)	1650
Hatch distance (mm)	0.13
Layer thickness (mm)	0.03
Scanning strategy	Stripes, Chessboard
Rotation in layers for Stripes(°)	45, 67, 90
Rotation in layers for Chessboard(°)	0, 45, and 90

Stripes Size/Island Size (mm)	5, 10/ 2*2, 3*3, 5*5, 10*10

Table 9: Nomenclature of the samples used in this study.

S.No.	***Scanning Strategy***	***Size (mm)***	***Rotation (°)***	***Sample ID***
1	Stripes	5	67	S_5_67
2	Stripes	10	67	S_10_67
3	Stripes	10	90	S_10_90
4	Stripes	10	45	S_10_45
5	Chessboard	2*2	No	C_2*2_no
6	Chessboard	3*3	No	C_3*3_no
7	Chessboard	5*5	No	C_5*5_no
8	Chessboard	10*10	No	C_10*10_no
9	Chessboard	5*5	45	C_5*5_45
10	Chessboard	10*10	90	C_10*10_90

The 0°, 45°, 67°, and 90° alternating strategy procedure involves turning the orientation of each over-building layer by 0° (Figure 24b), 45° (Figure 24d), 67° (Figure 24a), and 90° (Figure 24c) respectively.

2.2.3. Test Samples

Three different geometrical types of AlSi7Mg0.6 test samples are printed for this study:

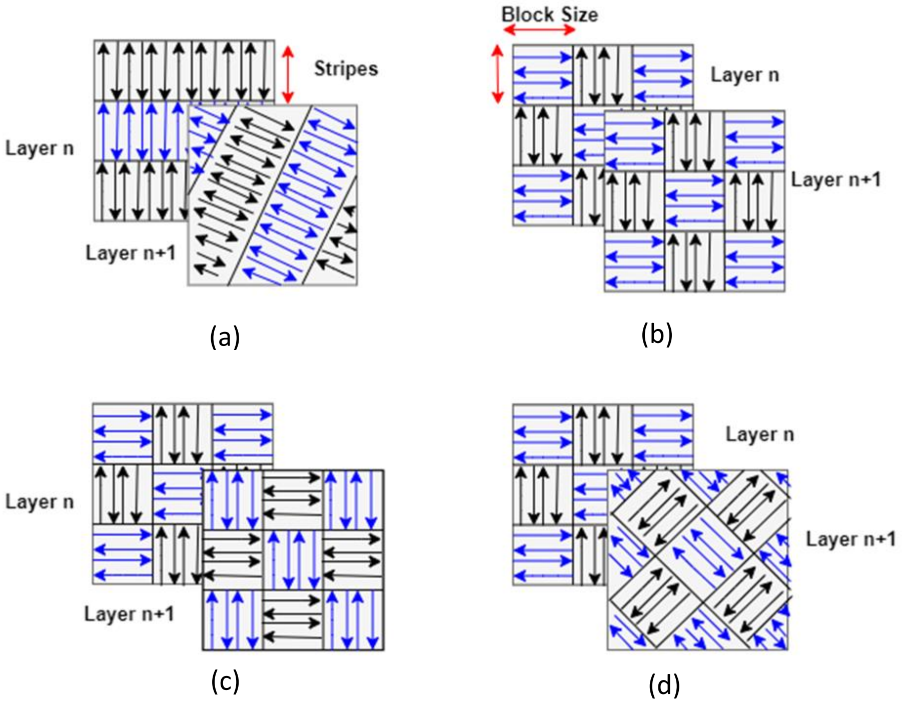

(a) (b)

(c) (d)

Figure 24: Schematic of the scanning strategies (a) stripes with rotation of 67°, (b) chessboards with (0°) no rotation, (c) chessboards with 90° rotation, and (d) chessboards with 45° rotation.

- For microstructural and density measurements: cubes with dimensions 10*10*10 mm^3;

- For hardness measurements: cubes with dimensions 15*10*10 mm^3;
- For tensile and residual stress measurements: cylinder with a diameter of 16 mm and length of 55 mm printed in X-Y plane;

2.3. Experimental Investigations

2.3.1. Porosity

Porosity measurements are conducted based on the archimedes principle [146]. It is the most often used method for quickly analyzing the porosity of printed parts. An average of 3 samples is used to conclude the average porosity level.

2.3.2. Hardness

Vickers hardness tests are conducted according to B EN ISO 6507-1:2005 standard [147] using a load of 5 kg. An average of 5 indentations is taken along the X-Z plane (building direction) of each sample's 15*10*10 mm3 block cross-section.

2.3.3. Tensile Tests

The tensile samples are machined from the cylinders of diameter 16 mm and length 55 mm printed horizontally (X-Y plane). Tensile tests are performed per the ASTM- E8/E8M-13a standard [148]. Tensile tests are performed at a 0.5 mm/min crosshead displacement rate using an Instron 5567B723 with clip-on extensometers based on BS EN ISO6892-1 standard. The yield stress is calculated at the 0.2 strain of the stress-strain curve.

2.3.4. Micrographic Examination and SEM

The microstructure of the SLMed samples is observed by using Scanning Electron Microscope (Carl Zeiss NTS GmbH, Germany). Also, crystallographic orientations investigations are carried out by the electron backscatter diffraction (EBSD) technique. All the samples are mirror polished before microstructural investigations. For SEM observations, samples are chemically etched with Keller's solution (95 mL H2O, 2.5 mL HNO3, 1.5 mL HCl, and 1.0 mL HF) for 10 s. Whereas, for EBSD observations (secondary electron imaging mode), the polished samples are electrochemically polished at 20 V for 10s with a Bruker solution. EBSD analysis is carried out on a cross-section of 200*200 µm^2 and at a step size of 1.5 µm in the X-Z plane, i.e., building direction. The samples directions are marked as building direction (BD), transverse direction (TD), and scanning direction (SD).

2.3.5. Cooling Rate

During solidification, the cooling rate is essential for developing the final microstructure. Therefore, finding the cooling rate variation in each scanning direction is interesting. It is a challenging and complex task to measure the cooling rates experimentally. Usually, analytical solutions are implemented to predict the cooling rates, such as the Rosenthal equation.

Rosenthal equation [149] is used to estimate the thermal history for the melt pool (Equation 5):

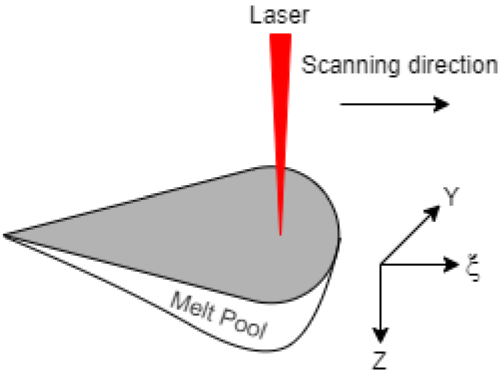

Figure 25: Schematic for rosenthal equation.

$$T = T_0 + \frac{Q}{2\Pi k} \exp\left[\frac{-V(\xi + R)}{2\alpha}\right]$$

Equation 5

Where, T: local temperature, T_0: plate temperature, Q: heat input, R: radial distance from the laser source (given by r = $(\xi^2 + Y^2 + Z^2)^{½}$, i.e., ξ, Y and Z directions are illustrated in Figure 25), V: beam scanning speed, α: thermal diffusivity (given by $k/\rho C$, where ρ and C are the density and specific heat of the workpiece, respectively)

Although the Rosenthal equation gives the 3-dimensional thermal distribution in the semi-infinite plate for the melt pool case, it has limitations. For example, it only considers conduction and neglects the heat of fusion. Also, it considers only temperature-independent properties and does not consider the remelting phenomenon occurring in L-PBF [149]**.** The Rosenthal equation cannot estimate the temperature inside the melt pool as the convection currents decrease the temperature gradient, which is not considered in the analytical equations. Rosenthal equations are suitable for calculating melt pool profiles in the conduction zone, i.e., outside the melt pool. But the analytical equations cannot be used to describe thermal histories fully. Still, they can be used to estimate the average surface cooling rate between the solidus and liquidus at the end of the melt pool long the scanning direction (Y=Z=0) [150].

$$\dot{T} = 2\Pi k(T_{solidus} - T_0)(T_{liquidus} - T_0)\frac{V}{Q}$$

Equation 6

where $\dot{T}$ is the cooling rate, $T_{solidus}$ and $T_{liquidus}$ are the liquidus and solidus temperatures, and T_0 is the plate temperature.

But for our study, we have calculated the cooling rates within the melt pool using Equation 7 (cell) as the analytical solution only works outside the melt pool.

2.3.6. Cell Size Measurements

SEM images of the X-Z cross-section are used to calculate the cell size, also known as the dendritic arm spacing, directly related to the cooling rate. The relationship between the cell size and cooling rate is expressed by Equation 7. Cell size is measured into the met pool for each scanning condition. Apart from the narrow heat-affected zone, the cells appeared uniform through the melt pool (therefore, reheating effect from multiple passes is neglected) and can easily be measured using ImageJ. For each sample, an average of 100 cell measurements from 10 melt pools is used to evaluate the cell size variation in the melt pool.

The relationship between the dendritic arm spacing and cooling rate is expressed as (Equation 7) [151]

$$\lambda_1 = a\dot{T}^{-n}$$

Equation 7

where λ_1 is primary dendrite arm spacing or cell size, $\dot{T}$ is the local cooling rate, and a = 43.2 [150] and n are proportional constants.

The value of n is 0.32 to 0.38 for cellular morphology and 0.21 for dendritic microstructure [85]. Similarly, the value of n is 0.33 for secondary arm spacing. In the L-PBF process, the solidification rate is associated with the laser scan speed. A high solidification rate leads to higher cooling rates, leading to cellular microstructures for near eutectic Al-Si alloys in the L-PBF process where solidification rates are more significant than 0.2 m/s [86].

2.3.7. Residual Stress Measurements by X-ray Diffraction Technique

The residual stress measurements are conducted using the non-destructive X-ray diffraction technique, which involves measuring the diffraction angle of rays returning to the detector. The diffraction angle is directly related to the distance between atoms of material as the interatomic distance between two atoms reduces compressive residual stresses develops and vice versa for tensile stresses. The residual stresses are calculated using the "$\sin^2\psi$" technique described in the DIN EN 15305:2009 standard, which involves monitoring the change in diffraction angles due to variation in the incident beam angles. The measurements are performed on the as-built surface and at 2 mm depth of the samples using the Xstress 3000 G2R instrument. A collimator of size 3 mm and a Cr tube as an x-ray generation source are used.

2.4. Results and Discussion

2.4.1. Porosities and Mechanical properties

It can be seen from Figure 26a that the samples with stripes (S_5_67, S_10_67, S_10_45, S_10_90) have the lowest porosity levels ranging from 0.83 to 0.99 %, whereas the chessboard strategy contributes higher porosity ranging from 0.91 to 2.35 %. But there is no significant effect of stripes size and rotation angles on porosity level observed in the case of stripes. Whereas the rotation angle has an effect on porosity level in chessboard strategy. For example, chessboard samples without rotation i.e. C_5*5_no, C_10*10_no has porosity levels 1.48 % and 1.42 % where chessboard samples with rotation i.e. C_5*5_45, C_10*10_90 has porosity levels of 0.91 % and 0.94 %. Similarly, the chessboard island with smaller island sizes is more porous than large ones. For instance, C_2*2_no, C_3*3_no has porosity levels of 2.35 %, 2.03 % in comparison with samples C_5*5_no, C_10*10_no has porosity levels of 1.48 %, 1.42 %. The higher porosity level in chessboard samples is linked to the lack of fusion porosity at the junction of the islands, as shown in Figure 27. This phenomenon can be explained as: When the laser hits the powder bed, it creates a denudation zone along the scan vector. At some places

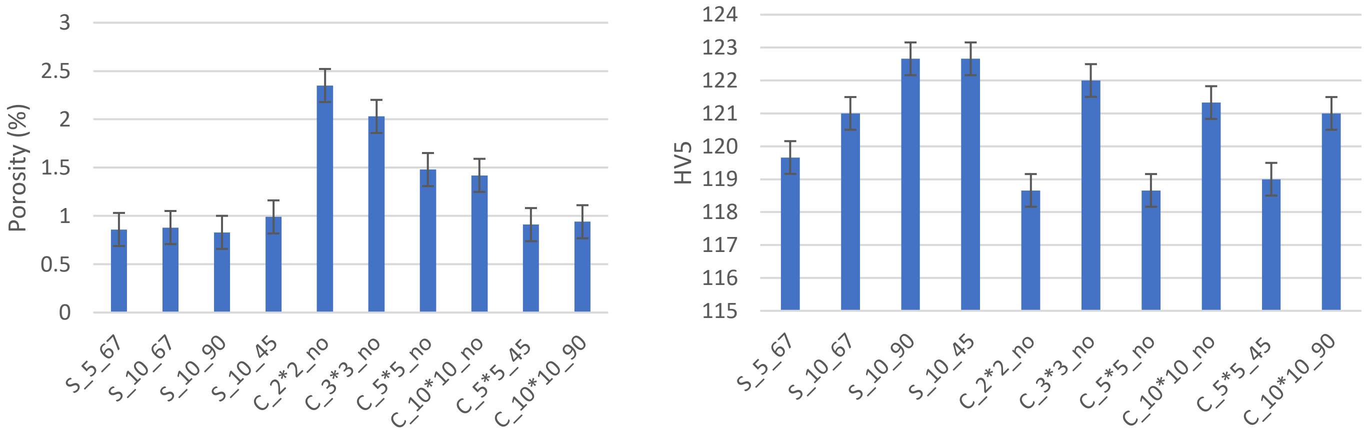

(a)

(b)

Figure 26: Effect of scanning strategies on (a) porosity (b) vicker's hardness.

near the edges of the islands, there may be the case that there is not enough powder for island bonding leading to porosity at the junction.

As smaller island sizes, samples have a higher number of islands than large island sizes, leading to higher porosity. Figure 26b shows that scanning strategies have no considerable effect on the Vickers hardness of the samples. The slight variation between stripes and chessboard strategies could be due to measurement errors or the variation of indentation location on the samples for Vickers hardness. But there is no significant change observed for rotation angle in Stripes and similarly, no pattern observed for chessboard strategies. Chessboard samples generally reported lower hardness values than stripes due to higher porosity levels in these samples, but no conclusive trend could be observed. Ali et al. [152] reported similar findings for SLMed Ti6AL4V samples.

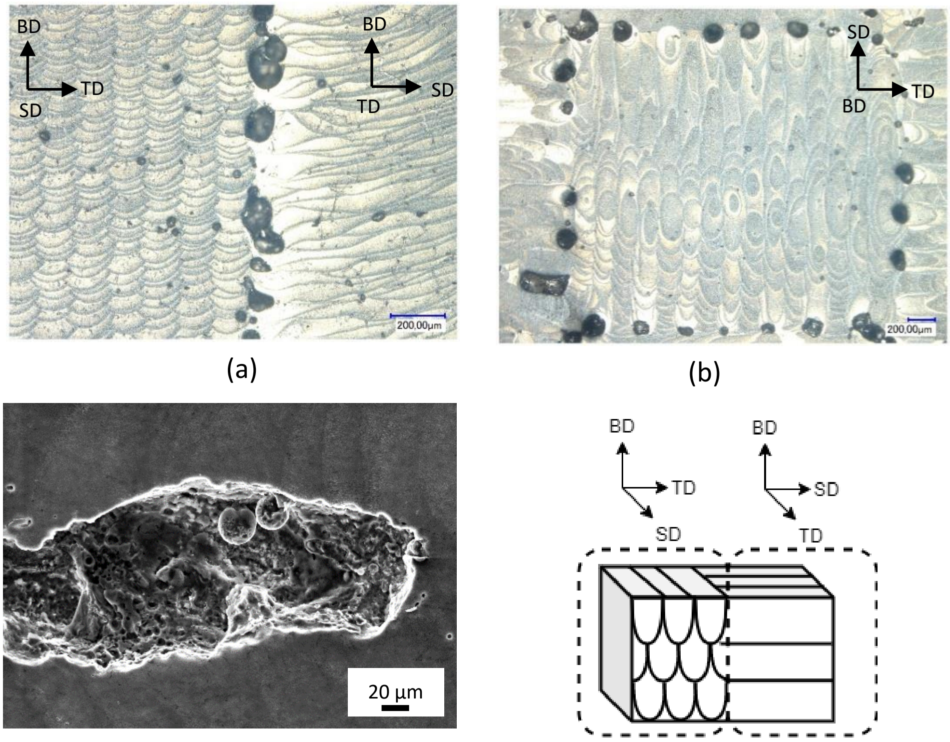

(a) (b)

(c) (d)

*Figure 27: Optical micrograph of C_10*10_90 sample in (a) building direction, (b) transverse direction, (c) SEM image of LOF defect observed at the junction of the island, and (d) sample orientation.*

It can be seen from Figure 28 that the scanning strategy does not affect the yield strength of SLM AlSi7Mg0.6 samples considerably, and the slight variation can be attributed to the stochastic nature of the process. The elongation % shows a clear transition from stripes and chessboard strategies. The stripes have an elongation of 13 % for stripe size 10 regardless of rotation, with a maximum of 17 % for stripe size 5. In contrast, the chessboard strategy without rotation shows the lowest elongation of 0.45 %, similar to the porosity trend. The elongation increases with the chessboard strategy with rotation until 10%, which is lower than the stripe strategy obtained. It also suggests that the rotation between layers improves the elongation %, but there is no visible trend for stripes and island size variation. Similarly, the chessboard strategy without rotation has the lowest tensile strength, but no visual effect of the scanning strategy with rotation could be observed.

Interestingly, most of the samples (except for samples with chessboard strategies without rotation) have a better yield strength and elongation % than as-cast Al-Si, which has a yield strength of 120-140 MPa and elongation of 1-2 % [153], [154].

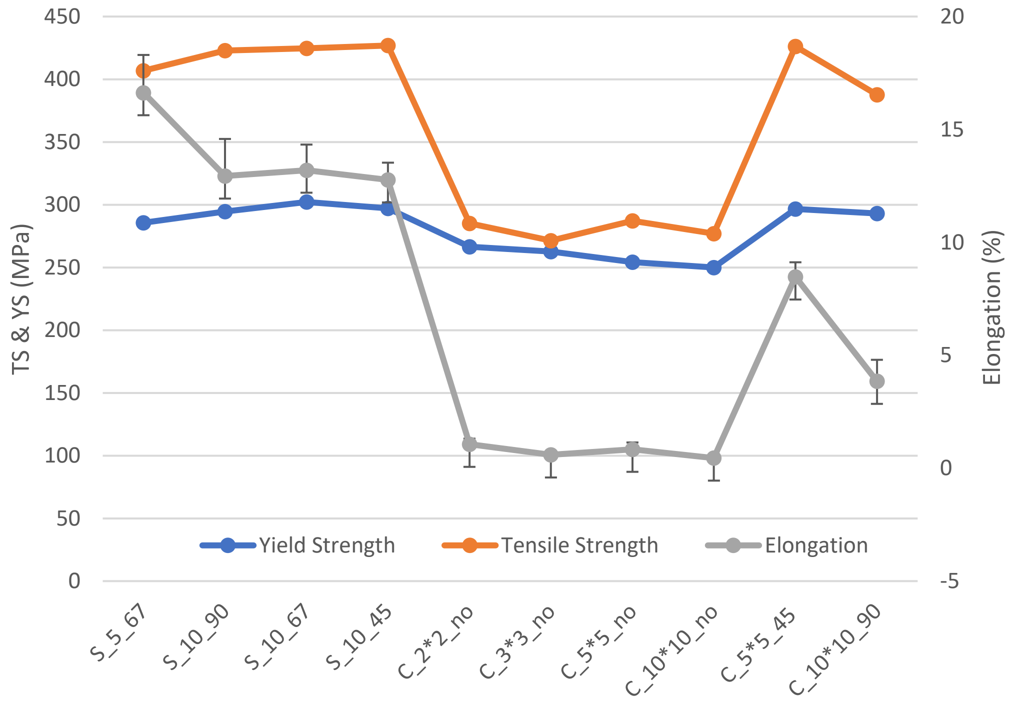

Figure 28. Effect of the scanning strategies on yield strength, ductility, tensile strength.

2.4.2. Microstructural Investigations

2.4.2.1. Phase Morphology

AlSi7Mg0.6 is a hypoeutectic alloy that primarily shows α-Al matrix surrounded by fibrous Si-rich phase as shown in Figure 29 when processed by the L-PBF process. A similar microstructure has been reported for AlSi7Mg processed by the L-PBF process [155]. Apart from the fibrous network, Si particles are also dispersed inside the matrix, which may be precipitated from the supersaturated α-Al matrix afterward due to heat dissipation during part fabrication. The Si content in the α-Al matrix is higher than the eutectic composition under equilibrium conditions. Due to rapid cooling, the non-equilibrium solidification conditions lead to a supersaturated α-Al matrix or pseudo eutectic composition. Indeed, the high cooling rate in the L-PBF process develops a large undercooling at the solidification front, which doesn't provide enough time for Si precipitation [156]. Therefore, high content of Si is retained in the cellular or columnar α-Al matrix and leaving residual Si at the grain boundaries. Also, Dinda et al. [157] reported that Si content in the Al matrix increases with solidification velocity.

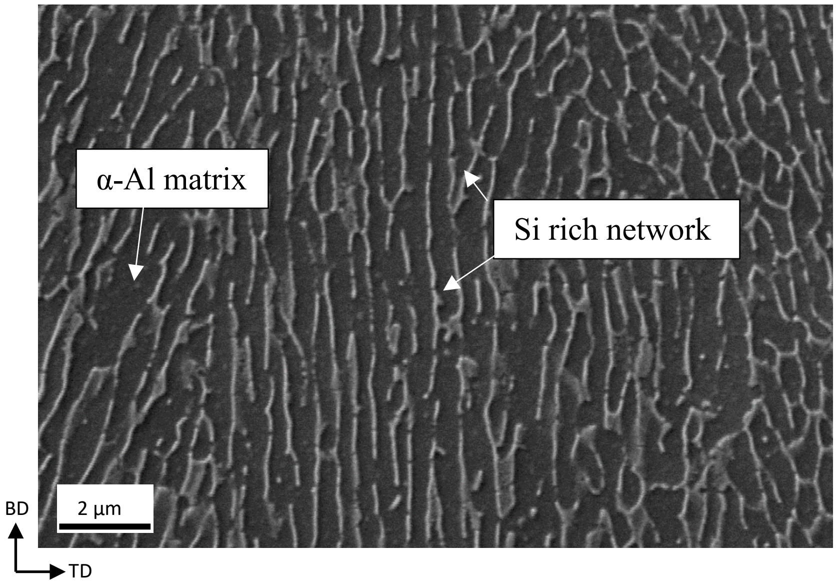

Figure 29: An example of the phase morphology in AlSi7Mg0.6

2.4.2.2. Optical Micrographs

The complex pattern of the scan tracks can arise due to different scanning parameters. For example, the woven-like melt pools result from applied scanning rotation between the consecutive layers, as shown in Figure 30a. The scan tracks are also not continuous in the cross-section due to variation in the melt pool dimensions especially melt pool depth. The optical micrograph of etched as-built samples shows contrast at the edges of the scan tracks.

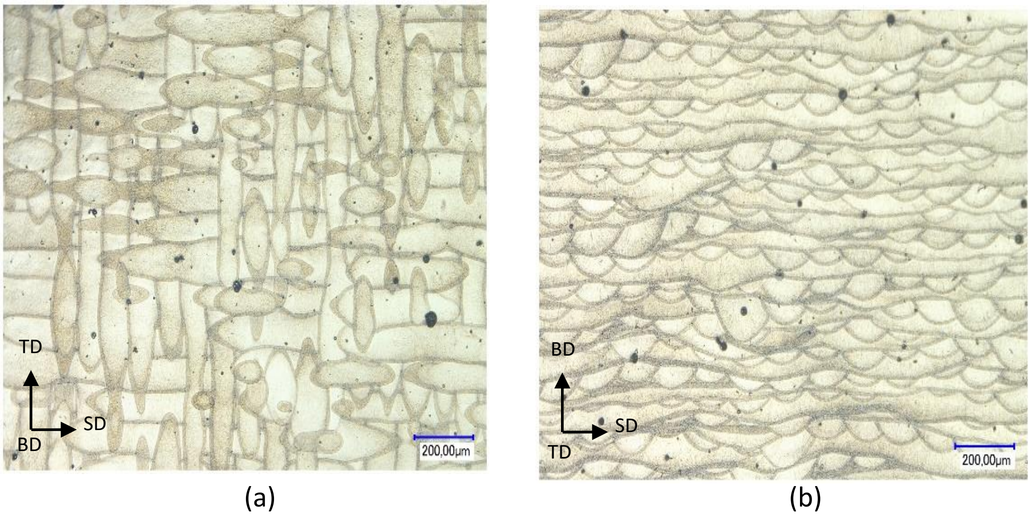

(a)

(b)

Figure 30: Optical micrograph of as-built C_5*5_45 (a) transverse, (b) building direction. (SD: Scanning direction, TD: Transverse direction, BD: Building direction)

This contrast arises because the cell size is of the order of the wavelength of the visible light. Also, the melt pool boundary is visible (See Figure 30b).

2.4.2.3. Melt Pool Evolution

The unique microstructure in the melt pool is due to the variation of cooling rate and thermal gradient across the melt pool. Epitaxial growth of the α-Al phase along the thermal gradient is evident in Figure 31: the melt pool shows elongated dendritic morphology in the longitudinal or building direction and cellular morphology in the transverse cross-section. Grain formation during solidification depends on the G/R parameter, where G is temperature gradient and R cooling rate. Thus, depending on the evolution of G/R, different morphologies, planar, cellular, columnar, can be obtained. When the laser melts the powder and the previous layers, many small grains nucleate at the melt pool's border due to the high value of G [158], [159]. These newly nucleated grains competitively grow into columnar or cellular grains due to higher G/R value. Crystallographic texture results indicate that these grains have a specific orientation, i.e., < 100 > along with the scanning direction. Some of the grains remain equiaxed at the border of the melt pool. There is also a possibility of forming equiaxed grains at the top of the melt pool due to columnar to equiaxed transition (CET). CET can be observed during the laser treatment

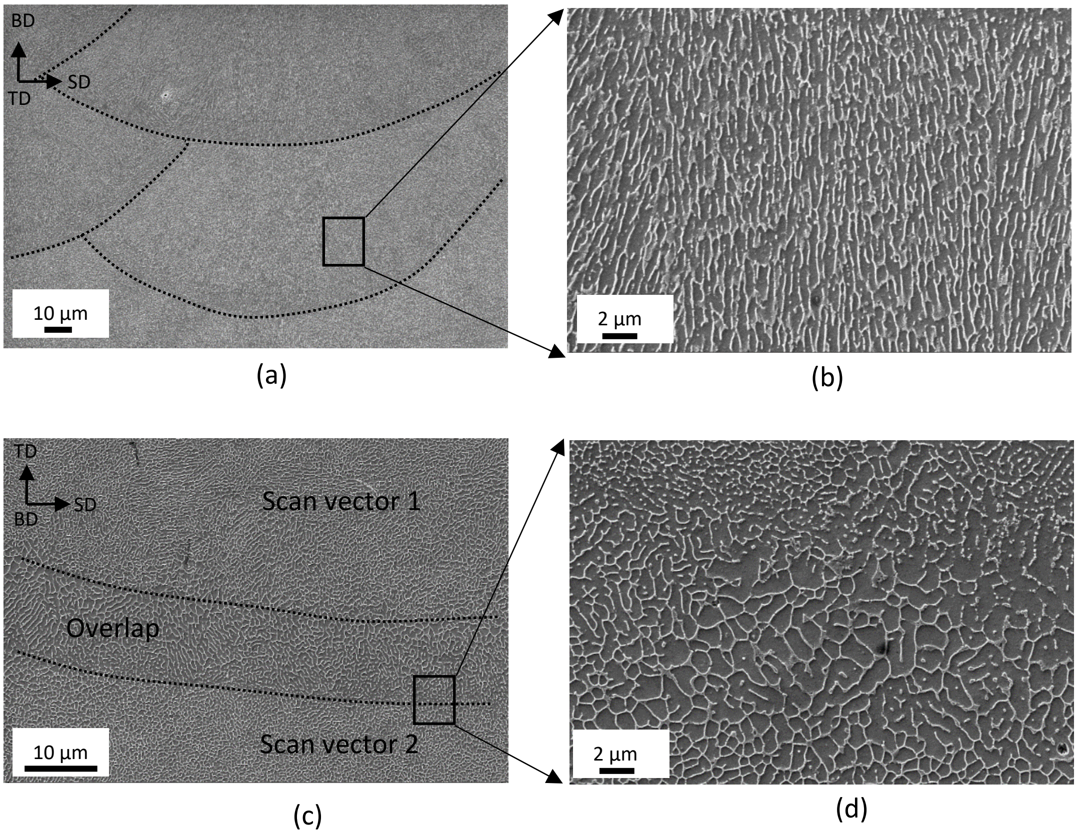

Figure 31: SEM micrographs of S_10_67 sample in (a, b) building direction and (c, d) transverse direction.

when the nucleation of large equiaxed grains occurs in the constitutionally undercooled liquid in front of the dendritic columnar front, as reported by [160]. However, the CET equiaxed grains at the top of the melt pool are not visible as the subsequent remelting passes destroy them.

Three distinct regions are highlighted in the melt pool micrographs, (a) a fine grains region, (b) a coarser grains region, and (c) a heat-affected zone (HAZ). The different regions of the grains are related to undercooling variation due to the Gaussian distribution of laser energy: the laser energy is higher at the center of the melt pool and lowers at the edges, and then G is higher at the center of the melt pool and lower at the edges of the melt pool. The factor G*R determines the fineness of the grains. Therefore G*R is higher at the center of the melt pool leading to fine cellular or columnar microstructure. On the contrary, a lower value of G*R leads to coarser microstructure at the edges of the melt pool [158], [161]. The transition from fine to coarse microstructure is visible in Figure 32. Another possible reason for coarser microstructure could be the formation of a semi-solid-state during the melting of successive passes. A semi-solid state or mushy zone can be generated when the temperatures are between the liquidus and solidus [162]. As reported by previous studies, the obtained semi-solid state can lead to coarser microstructure [163], [164].

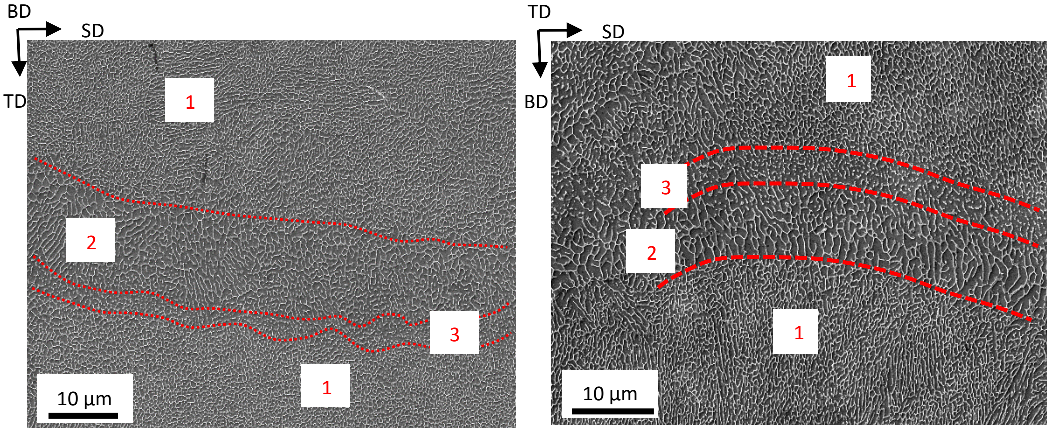

Figure 32: SEM images of the melt pool for sample showing the three distinct regions i.e. fine (1), coarse (2) and HAZ (3) regions.

Heat affected zone is another distinct region along the melt pool boundary. It can be characterized by a discontinuous silicon phase, which may be due to the increasing rate of silicon [158], [161]. When the laser melts the next layer, the temperature is lower than the solidus in the previous layer and acts as the heat treatment for the beneath layer creating a HAZ. Due to high scanning speeds and high cooling rates, the time for the HAZ to maintain that temperature is too less. Therefore, we only observed a small strip of HAZ with randomly dispersed Si cells. The temperature in the HAZ allows the precipitation of Si particles from the supersaturated α-Al matrix, which is formed due to higher cooling rates. As Si particles form and grow, the Si network finally disappears [161], [165].

2.4.2.4. Cell Size and Cooling Rates

The cell size variation inside the melt pool regions is measured using the ImageJ software from SEM images. Figure 33 presents the variation inside a melt pool obtained with the presented strategy: it is observed that the cell size varies concerning the location within the melt pool. The cooling rate based on the cell size is calculated using Equation 7. For example, it is found that there is a higher cooling rate of $1.8*10^6$ K/s at the top of the melt pool where the cell size is smaller and a lower cooling rate of $1.3*10^5$ K/s in the coarser region (Figure 33b). Also, the cell size and cooling are calculated for different scanning parameters (Figure 34): it is noticed that there is no significant influence of scan strategy and its parameters, such as scan vector length and rotation, on the cooling rates and cell sizes.

The cooling rate and cell size predominate the power and scan, as Farshidianfar et al. [166] reported for the direct deposition process.

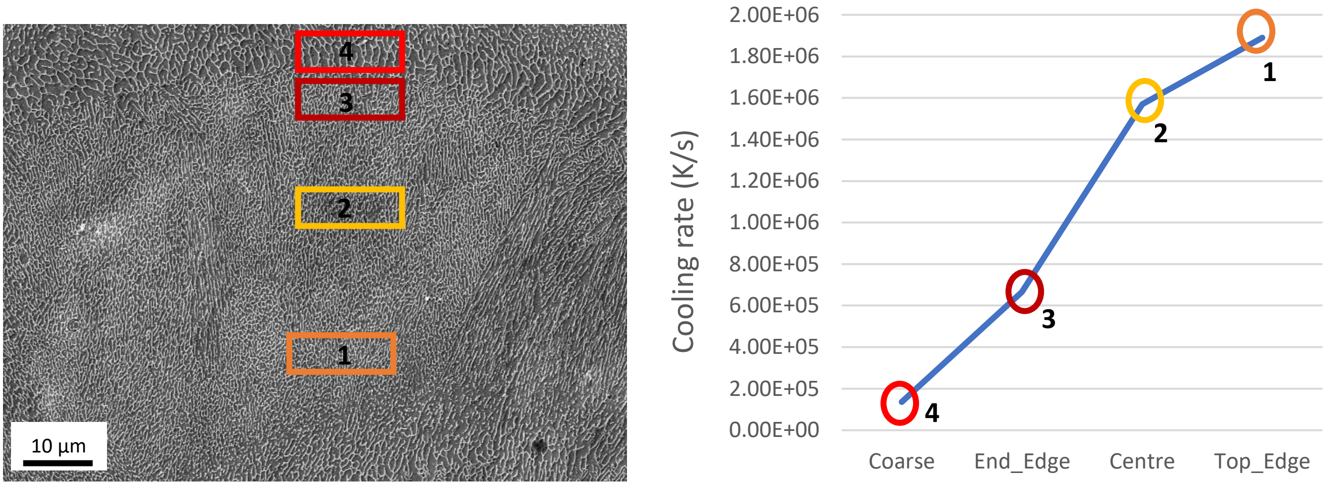

Figure 33: Example of cooling rates variation inside the melt pool. Also, the numbers mark the location of the measurements of the cells.

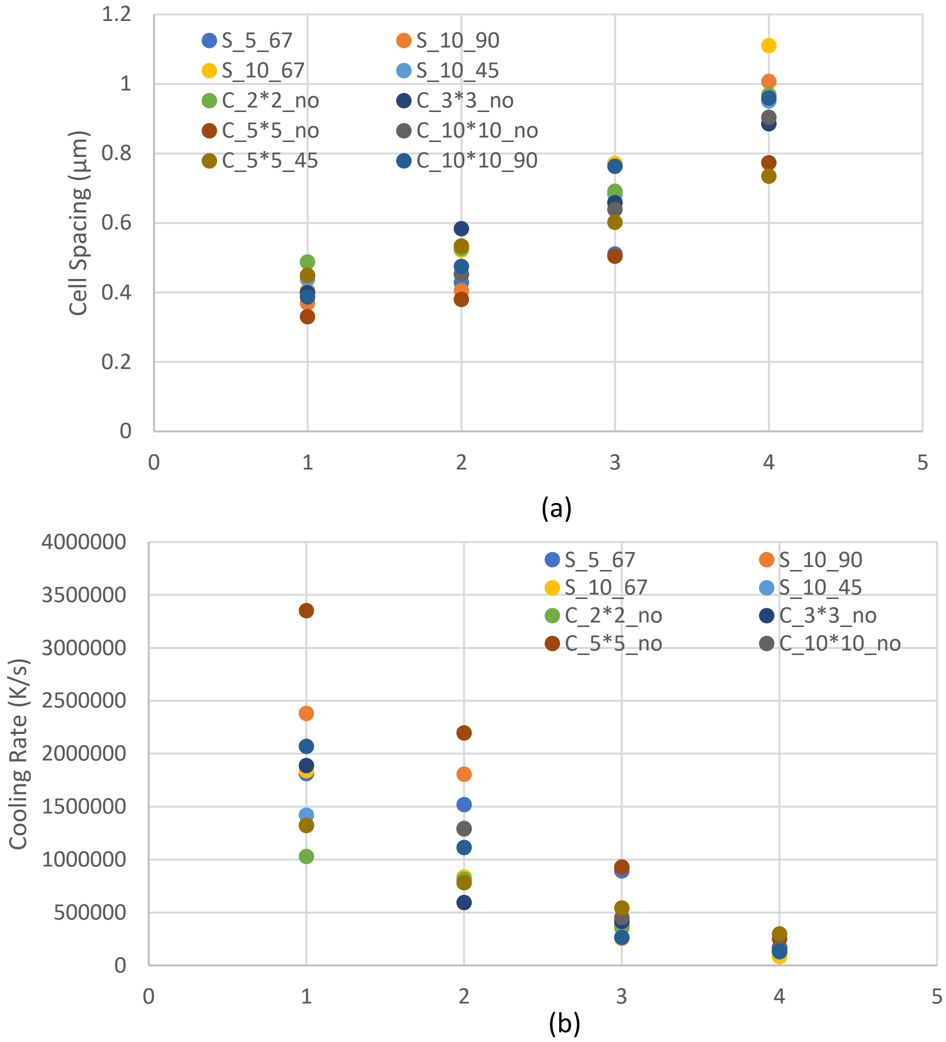

Figure 34: (a) Cell spacing and (b) calculated cooling rates. In X-axis, the numbers denote the location within the melt pool i.e. 1: Top edge, 2: Centre, 3: Bottom edge, 4: Coarse region of the melt pool. Also marked in Figure 33.

2.4.2.5. Grain Morphology

Figure 35 shows the grain morphology of the SLMed AlSi7Mg0.6 alloy samples obtained by EBSD analysis. It can be observed that the microstructure is mainly composed of elongated grains, which are parallel to the building direction. Because of the growth of elongated grains towards the center of the melt pool and the existence of small equiaxed grains, some of the melt pool boundaries could be distinguished. In the vicinity of the melt pool boundary, small equiaxed grains appear. Grains are measured using a boundary misorientation angle definition of 2°. The crystallites of size less or equal to two map pixels are ignored to reduce noise in the data.

There is no significant observable difference in mean grain size for different scanning strategies as shown in **Error! Reference source not found.**. The average grain size for the samples S_5_67, S_10_90, S_10_45, S_10_67, C_3*3_no, C_2*2_no, C_10*10_no, C_5*5_no,

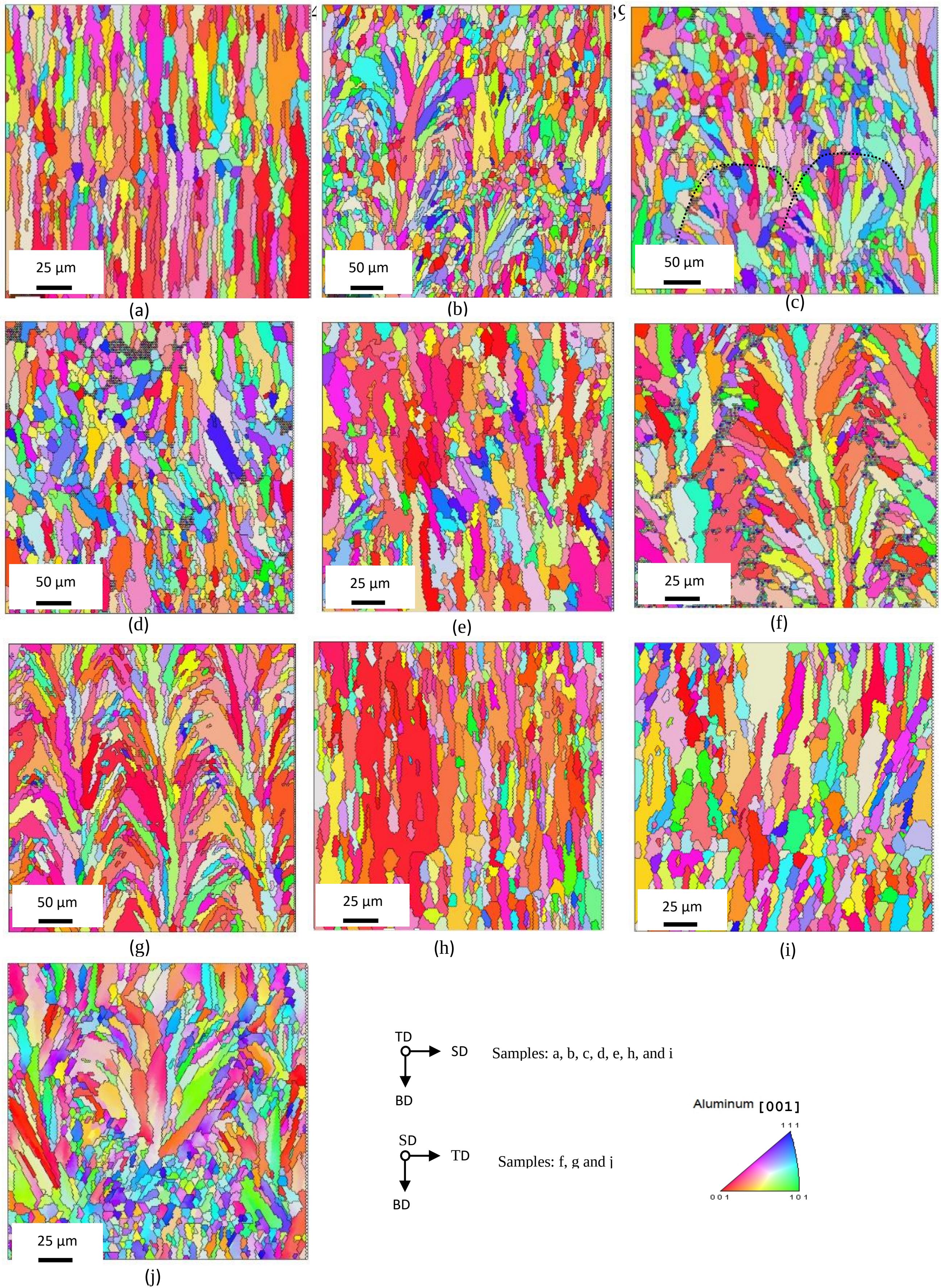

*Figure 35: IPF images showing the grain morphology for samples (a) S_5_67, (b) S_10_90, (c) S_10_45, (d)S_10_67, (e) C_3*3_no, (f) C_2*2_no, (g) C_10*10_no, (h) C_5*5_no, (i) C_10*10_90, and (j) C_5*5_45.*

µm, 12.38 µm, 12.41 µm, 13.71 µm, and 10.21 µm, respectively.

2.4.2.6. Grain Misorientation Angle

The grain boundary misorientation angles are also considered for different scanning strategies. The misorientation values higher than 15° are regarded as the high angle grain boundaries (HAGBs), and those lower than 15° are termed as lower angle grain boundaries (LAGBs). The fraction of LAGBs is higher than the HAGBs in the samples (Figure 37). The boundary misorientation distribution has no significant difference between the samples. A high density of LAGBs is present in the columnar α-Al grains, as also observed by Takata et al. [165]. A fine substructure within the α-Al grains is responsible for the high-density LAGBs.

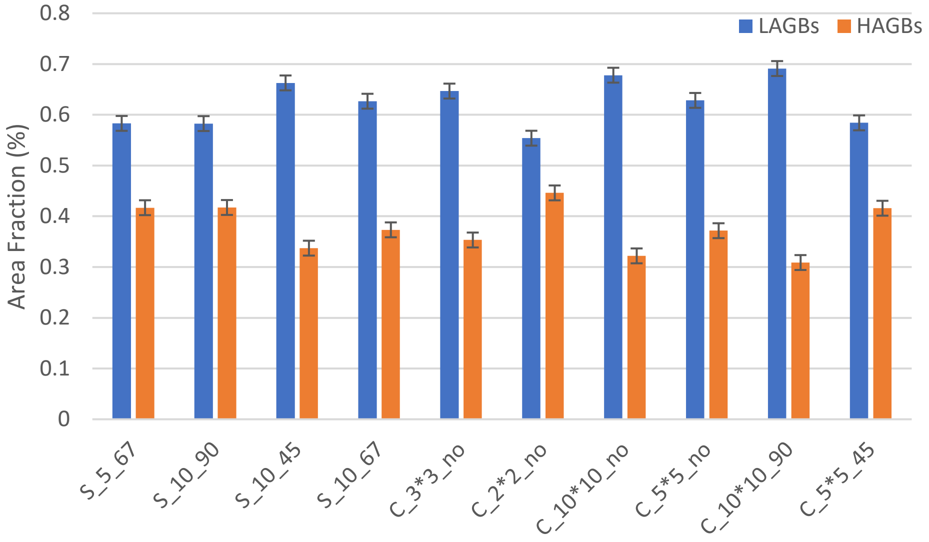

Figure 36: Area fraction of LAGBs and HAGBs.

2.4.2.7. Crystallographic Texture

a. Texture Index

Each grain has preferred orientations that grow much faster than other orientations during the solidification. This preferred growth during the solidification of the melt pool leads to crystallographic texture in the printed part. For example, <100> fiber texture parallel to the scanning direction is expected because the melt pool is elongated in the scanning direction, and solidification starts along that direction. But the crystallographic orientation can be controlled and modified according to the processing parameters such as scanning direction, laser power, scanning speed, and layer rotation angle [166]. For instance, Liu et al. [138] reported the effect of laser power on the crystallographic texture evolution in AlSi10Mg alloys. Similarly, Thijs et al. [158] reported that the strong fiber texture in AlSi10Mg alloy changes to weak cubic texture by rotating each layer 90° from the previous. This research studied the effect of scanning strategy, rotation angle, and scan vector length on crystallographic texture evolution.

Only a few studies investigated the crystallographic texture in Al Alloys. Usually, the crystallographic textures do not contribute much to overall anisotropy in the material, which is an attribute related to the orientation of parts.

Since the Al has FCC crystal structure, columnar grains usually prefer <100> texture [166], [167]. Texture can be categorized into two, i.e., Micro-texture and Macro-texture. The macro-texture can be measured by X-rays, neutrons, electron diffraction techniques. Whereas the micro-texture can be studied using the scanning electron microscopy-based electron backscatter diffraction technique (SEM-EBSD).

The overall texture index (TI) is given by the texture index, which is expressed as

$$TI = \int_{Eulerspace} (\mathrm{f}(g))^2 \, dg$$

Equation 8

Where f denotes the orientation distribution function of the Euler space coordinates g [168], the texture index (TI) defines the volume fraction of the crystals having a particular orientation compared to others. If TI = 0, there is no crystal having this specific orientation. If TI = 1, then it denotes one crystal for each possible orientation, also termed as "random distribution." If TI>1, for example, TI =3, then it defines the number of crystals with a particular orientation 3 times the utterly random distribution. TI values are read in terms of "multiples of random orientation (MRD)," higher the TI value, the more textured the material is. From Figure 38 (calculated on the obtained EBSD data), it can be observed that for chessboard strategy, TI

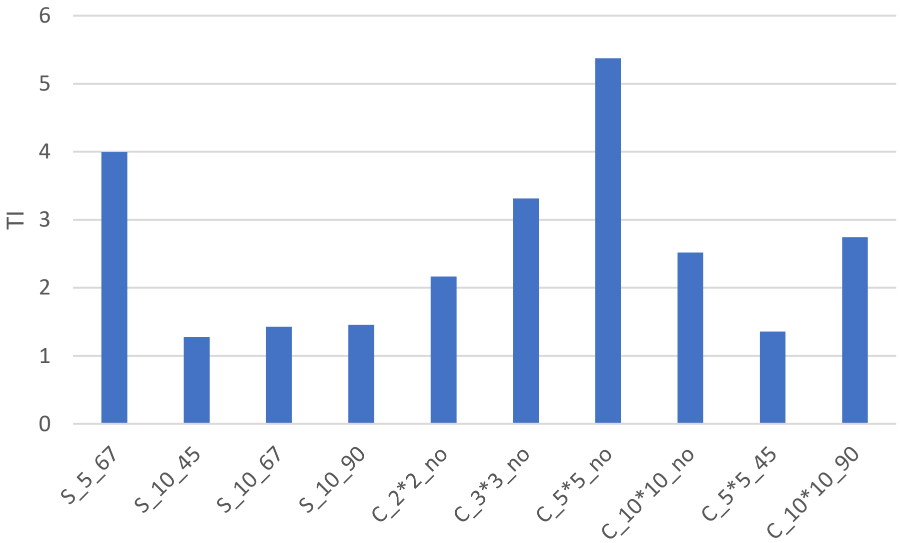

Figure 37: Texture index of the samples.

increases with an increase in the island sizes until 5 mm and then drops for an island of size 10 mm. However, comparing samples C_5*5_no and C_5*5_45, it can be noted that the TI decreases significantly from 5.3 (no rotation) to 1.3 (application of 45° rotation between consecutive layers). In the case of stripes, we observed that TI is close to 1 for a stripe length of 10 mm for all rotation angles, while TI is close to 4 when the stripe length is reduced to half.

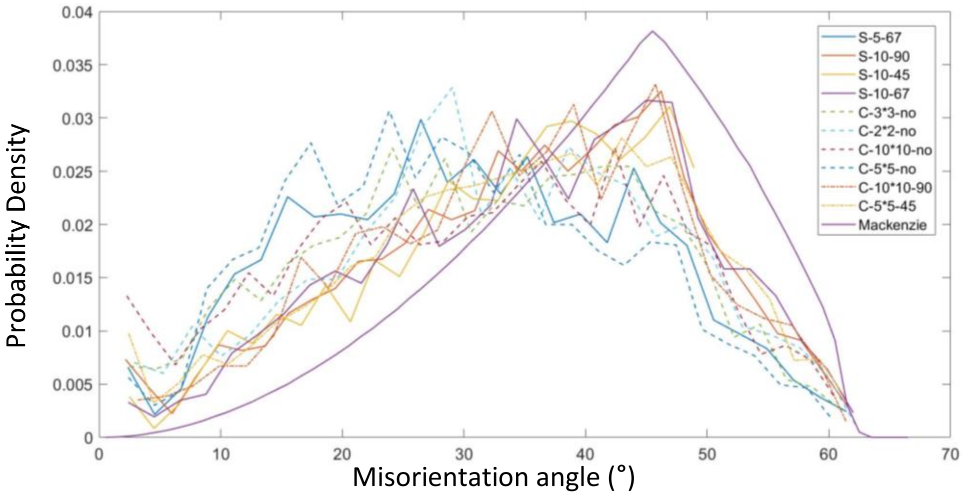

Figure 38: Mackenzie plot comparison.

Mackenzie plot represents the misorientation distribution for a cubic sample with a random texture. Suppose at any misorientation angle the frequency of the actual distribution is higher than the corresponding frequency in the Mackenzie distribution. In that case, it means that the material has texture in one of the preferred orientations. It can be seen in Figure 39 that all the samples show the actual frequency distribution higher than the Mackenzie distribution, especially for misorientation angles < 35°. So, it can be concluded that all the samples have a preferred orientation.

b. Inverse Pole Figure Intensity

Pole figure intensity is a measure of how dissimilar the crystals are when compared to random orientation distribution. Although the calculation is different from TI, the pole intensity measures crystallographic anisotropy or texture in the material by using SEM-EBSD.

Effect of Scan Vector Length

C_2*2_no, C_3*3_no, C_5*5_no, and C_10*10_no samples scanned with varying scan vector lengths, and the scanning angle is kept constant for each layer. It is noticed that a strong <100> along the scanning direction is observed, and weaker <110> texture along building texture arise,

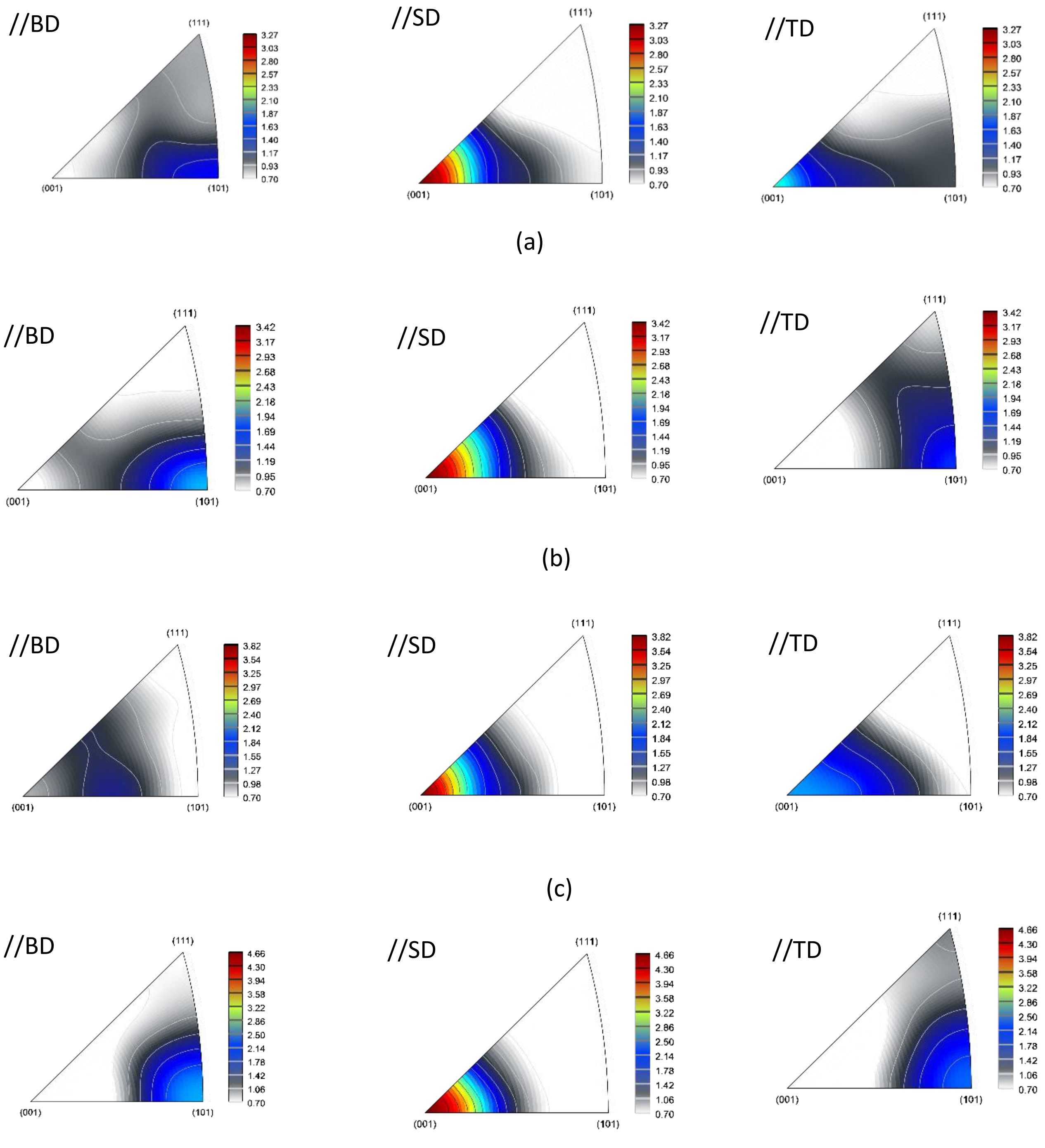

(a)

(b)

(c)

(d)

*Figure 39: Intensity pole figures for samples (a) C_2*2_no, (b) C_3*3_no, (c) C_5*5_no, and (d) C_10*10_no.*

as shown in Figure 40 (except for Figure 40c). The pole figure intensity increases as the scan vector length increases for <100> direction parallel to the scanning direction.

In samples S_5_67 and S_10_67, the scan vector length changes from 5 mm to 10 mm while the rotation angle in consecutive layers is kept constant at 67°. Like chessboard strategy, there is strong <100> along the scanning direction. Still, the overall texture intensity is lesser for bigger scan vectors than chessboard cases, as shown in Figure 41.

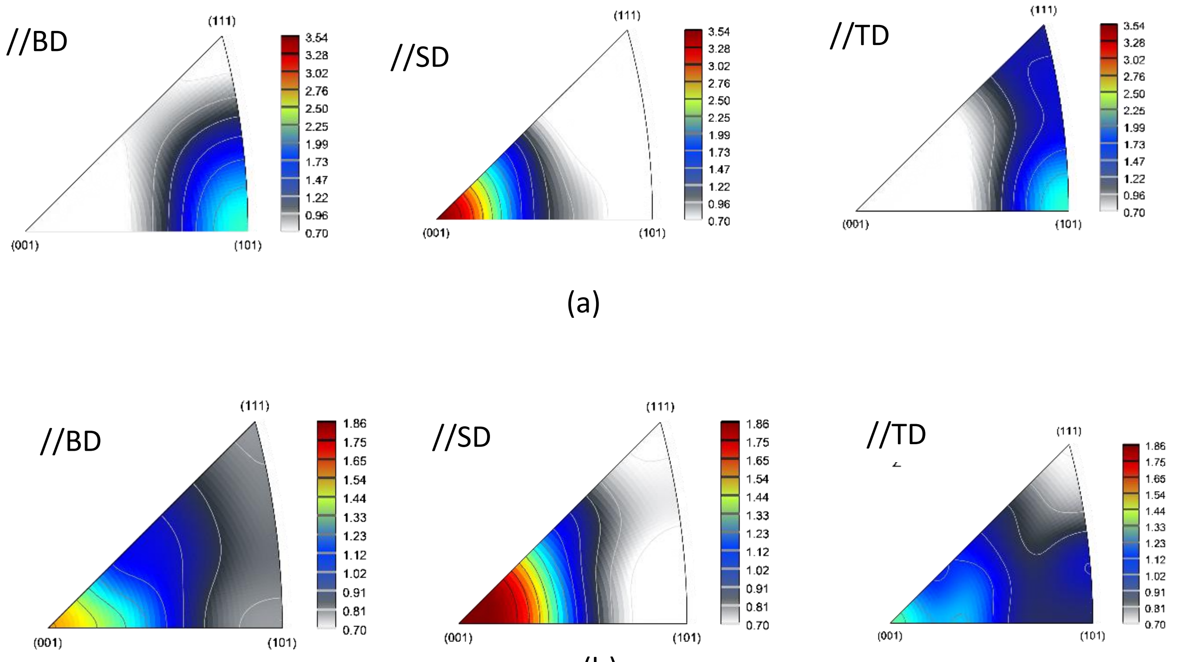

(a)

(b)

Figure 40: Intensity pole figures for samples (a) S_5_67 and (b) S_10_67.

Effect of Rotation Angle

Samples S_10_45, S_10_67, and S_10_90 are printed with the same scanning vector length, but the rotation angle between the layers is changed to 45°, 67°, and 90°, respectively. All the samples show <100> texture along the scanning direction, but a significant texture pattern is also observed for building direction, as shown in Figure 42.

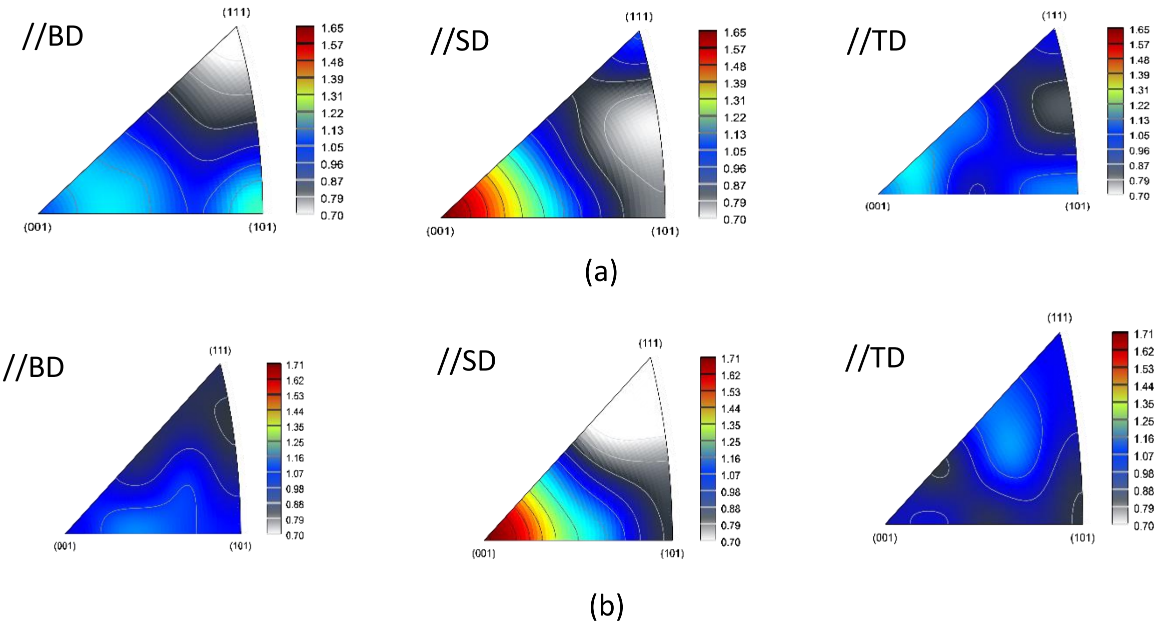

(a)

(b)

Figure 41: Intensity pole figures for samples (a) S_10_45, and (b) S_10_90.

Samples C_5*5_no and C_10*10_no are compared with samples C_5*5_45 and C_10*10_90 (Figure 43) to investigate the rotation effect in chessboard strategy. As observed earlier, there is <100> texture parallel to the scanning direction for all the samples. But the pole intensity decreases from 4.66 to 1.59 when the C_5*5_no rotated by 45° (C_5*5_45). Also, the texture

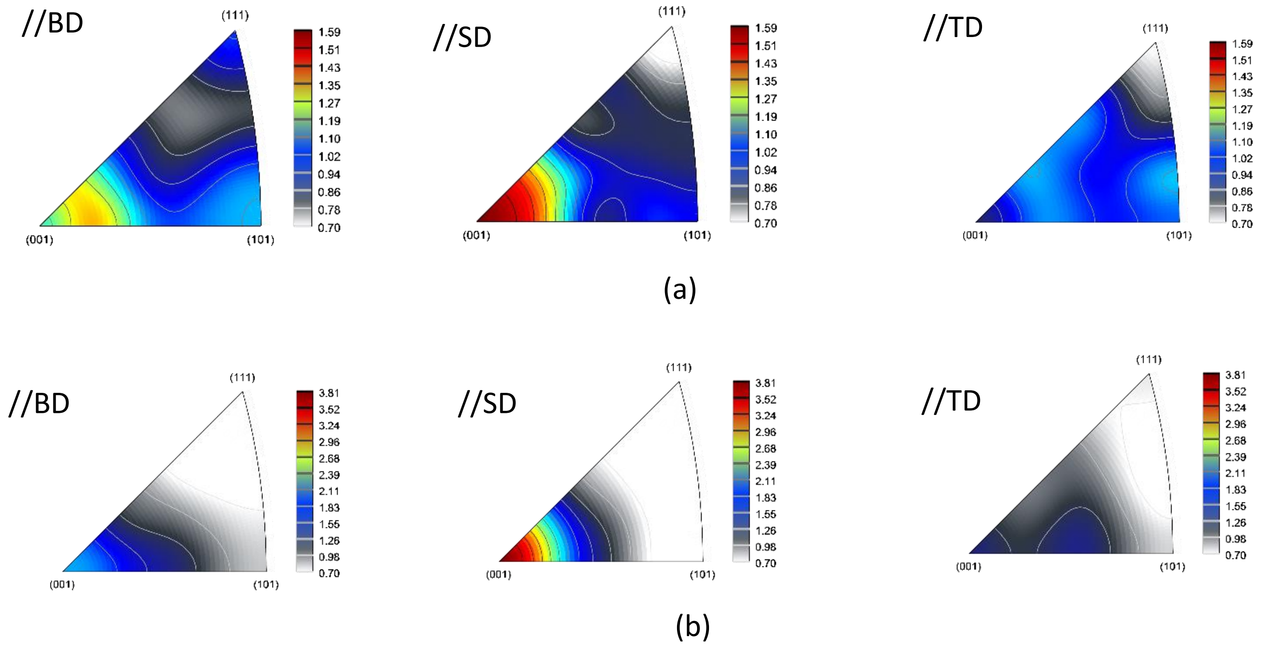

(a)

(b)

*Figure 42: Intensity pole figures for samples (a) C_5*5_45, and (b) C_10*10_90.*

<101> parallel to building direction for non-rotated samples decreases, and texture <100> starts to arise for building direction. The same can be seen for the sample C_10*10_no, where the pole intensity decreases by applying a rotation of 90° between layers. Also, the <100> texture orientation parallel to building direction starts to arise. So, it can be concluded that applying rotation between layers can decrease the texture intensity in the material. In other words, it lowers the intensity of crystallographic anisotropy in the material.

Overall, Stripes (except S_5_67 and C_5*5_45) show the lower texture intensity in <100> direction parallel to scanning direction compared to chessboard strategy, which is also confirmed by the texture index discussed in the previous section.

2.4.3. Fractography

In the fracture micrographs, it is noticed that the effect of scan vector length and rotation is not significantly visible (Figure 44). However, there is a clear difference in the fracture behavior in stripes and chessboard scanning strategy. Figure 45 shows the micrographs of the fracture surfaces of the tensile samples for stripes and chessboard strategies. In chessboard strategy, the samples fail like a brittle fracture linked to the presence of elongated porosity at the island junction, as shown in Figure 45b.

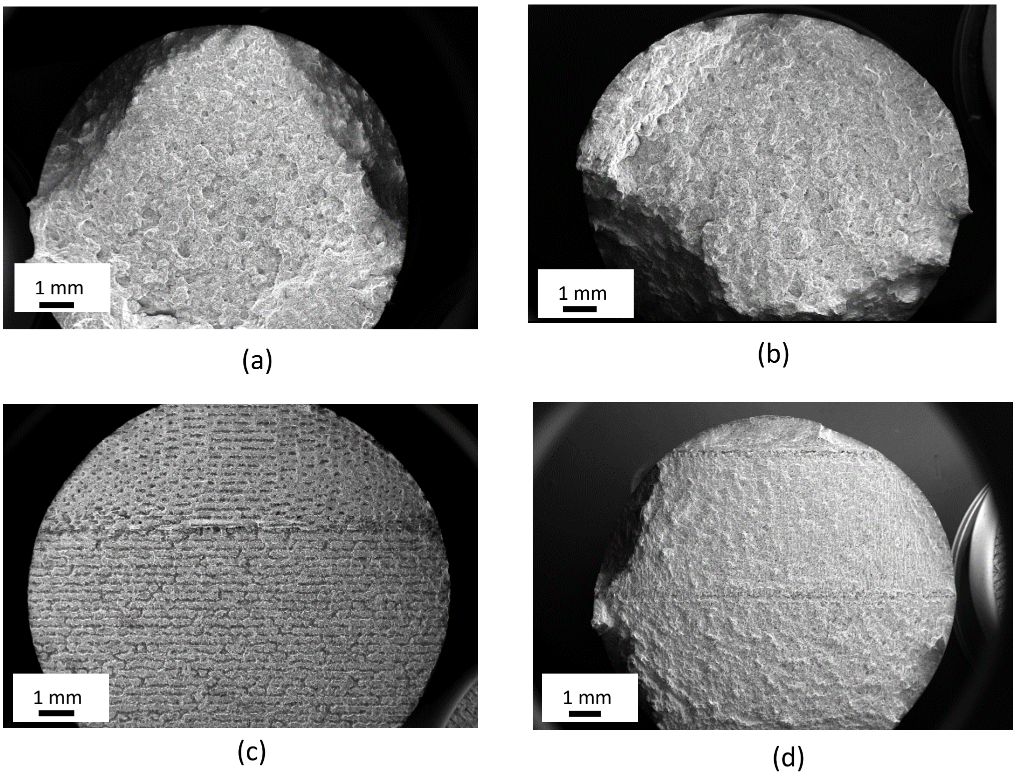

(a) (b)

(c) (d)

*Figure 43: SEM micrographs of fracture surface for (a) S_10_90, (b) S_10_67, (c) C_10*10_no, and (d) C_10*10_90.*

In stripes, the fracture looks like a ductile fracture. In Figure 45a, the micro-voids or microporosity on the edge of the samples could be the crack initiation site. It is noticed that the tearing occurs along the melt pool boundaries. The evidence of fracture due to Si particles at the center of the grains is not found.

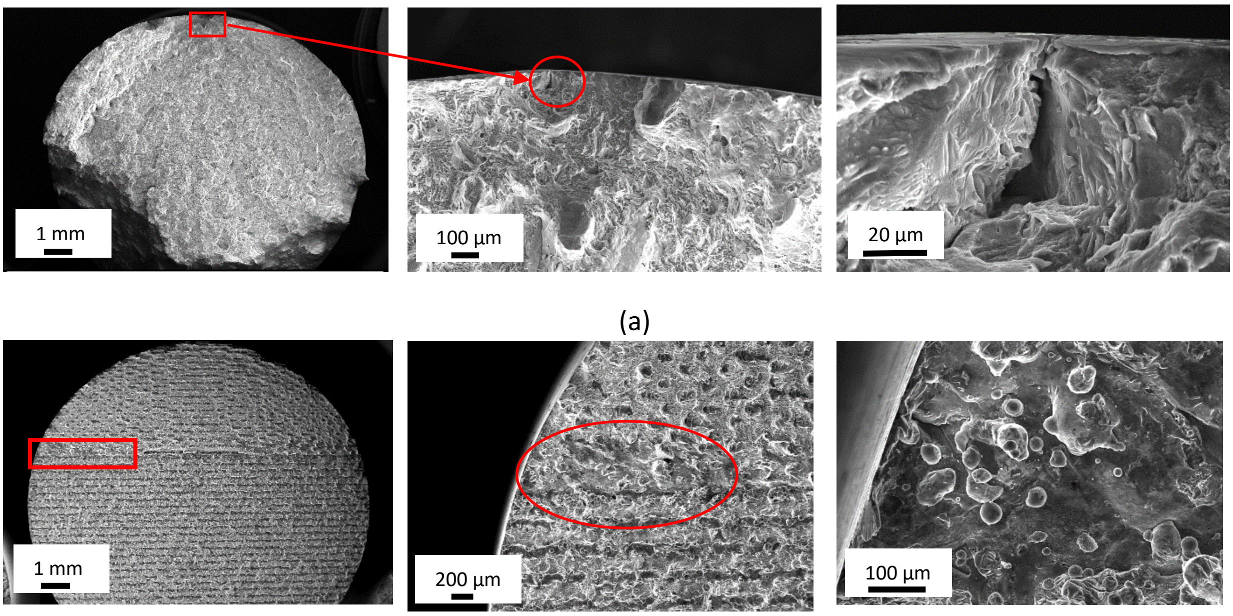

(a)

(b)

*Figure 44: Fracture surface for samples (a) S_10_67, and (b) C_10*10_no at different magnifications.*

2.4.4. Residual Stresses

Residual stresses are internal stresses that remain in part after completing the manufacturing process. The type and nature of the residual stresses are subjected to the entire manufacturing route used to produce that part. The uncontrolled relaxation of the residual stresses can negatively affect the manufactured part. The residual stresses can act as additional stress when subjected to service conditions. This can have a severe impact on the lifetime of the part. Sometimes, the residual stresses are beneficial and desired. For example, the compressive residual stresses at the part's surface can increase resistance to fatigue or corrosion under stress. Tensile residual stresses are penalizing and correspond to areas at risk of premature failure. The samples used for the study of residual stresses are cylinders with a diameter of 16 mm and length of 55 mm (attached from the manufacturing plate).

the residual stresses are measured at the surface and 2 mm depth for three locations: at two edges (start: represents where the printing started and end: represents where the scanning vector ends) and in the center of the bar (Figure 46a)

The measurement directions are circumferential direction (0°) and axial direction (90°) (Figure 46b)

It is important to note that the measurement uncertainty is estimated at ±7 % in case of a 95 % confidence interval.

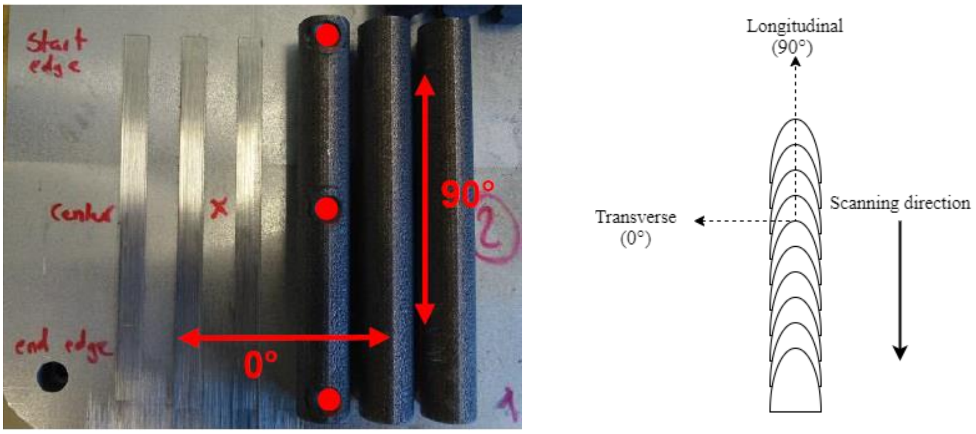

(a)

(b)

Figure 45: (a) Location of the measurement points i.e. Start, Centre, and End (marked in red circles), (b) schematic of the measurement directions based on laser scan track.

2.4.4.1. At Surface

The residual stress at the surface in the circumferential direction of all the samples are very low tensile or low compressive stresses, as shown in Figure 47. In contrast, we could observe very high tensile stresses in the axial direction (Figure 47). Similarly, the stresses are very high in the center of the part for both directions for all the samples. Typically, the start edge has higher stresses than the end edge except for C_3*3_no and C_10*10_90 for transverse direction (Figure 48a); in contrast, the same could not be observed for longitudinal direction (Figure 48b). However, the difference in the start and end edges is not very significant compared to the center

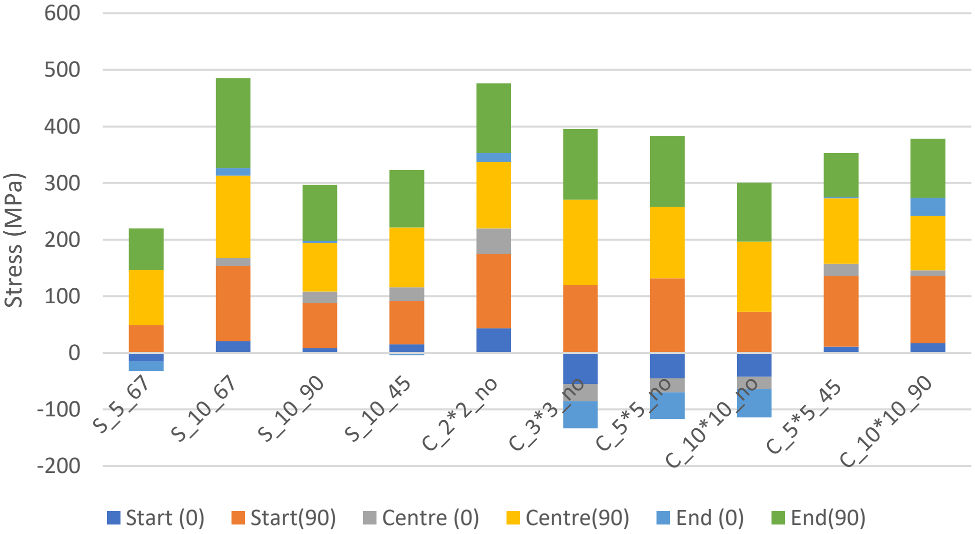

Figure 46: Change in residual stresses based on the location of the measurement points at the surface of the parts.

region. Based on the above results, we can confirm that the residual stresses are higher in the longitudinal direction at the part's surface, which is also the direction of laser printing (Figure 46b). Therefore, there are higher stresses along the melt pool length axis than the width axis. No significant effect of scanning strategies could be observed in residual stresses.

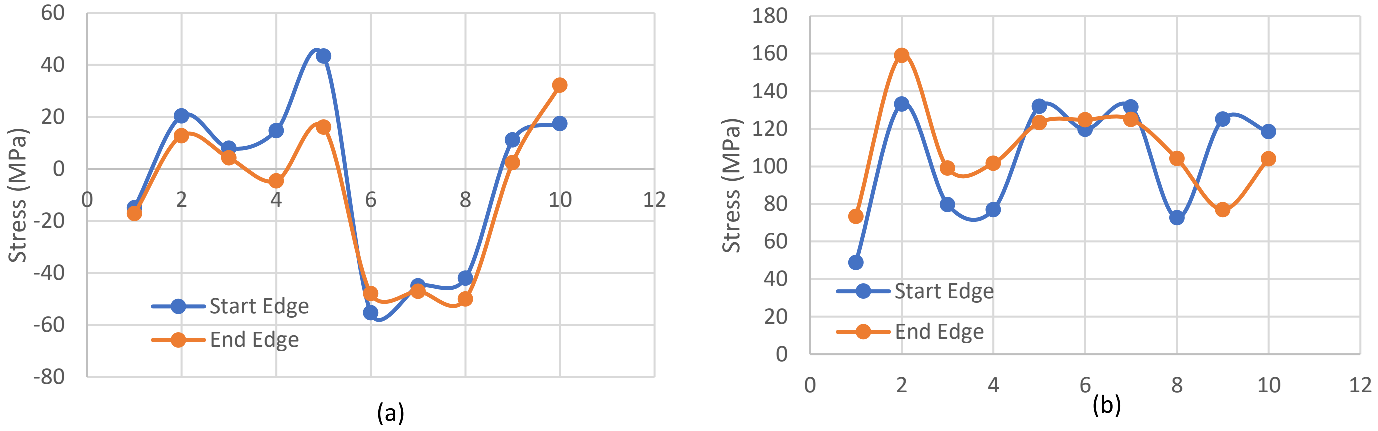

*Figure 47: Comparison of start and end edges in (a) transverse, (b) longitudinal directions. (1: S_5_67, 2: S_10_67, 3: S_10_90, 4: S_10_45, 5: C_2*2_no, 6: C_3*3_no, 7: C_5*5_no, 8: C_10*10_no, 9: C_5*5_45, 10: C_10*10_90)*

2.4.4.2. At 2 mm Depth

Similar to results at the surface, the residual stresses are higher in the longitudinal direction than in the transverse direction (Figure 49). However, the stresses are higher at 2 mm depth than the stresses at the surface. It is essential to notice no significant variation in the stresses at the edges and center of the part for both directions (except S_10_45).

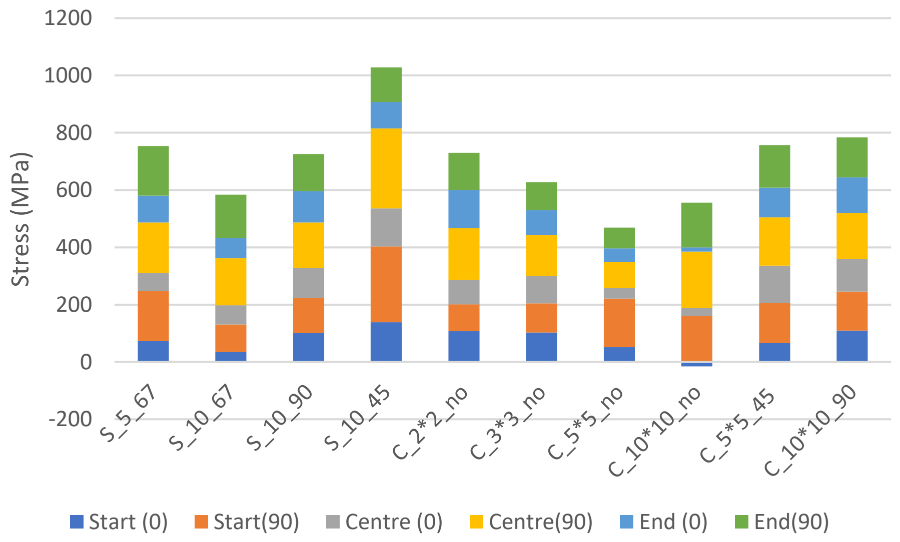

Figure 48: Change in residual stresses based on the location of the measurement points at the 2 mm depth of the parts.

2.5. Conclusions

The scanning strategy plays a pivotal role in influencing the final part's overall mechanical and microstructural properties. The findings of this study can be summarized as follows:

1. The stripes have higher densification than chessboard strategy due to the present lack of fusion porosity at the junction of the islands. Also, the stripes with rotation exhibit good mechanical properties such as tensile strength and hardness.
2. Microstructurally, both equiaxed and columnar grains are observed, which is linked to a higher value of G at the melt boundary. The same microstructure has been reported for AlSi10Mg alloys as well. Three distinct regions within the melt pool are investigated, i.e., fine, coarse, and HAZ zone. A Si-rich phase existed as a fibrous structure in a pseudo eutectic structure.
3. Cooling rates are estimated using the cell size within the melt pool, and it can be concluded that the cooling rates vary within the melt pool due to rapid cooling. The center or top of the melt pool has the highest cooling rates, and it decreases gradually at the end edge of the melt pool. However, no significant distinction is observed w.r.t. different scanning parameters.
4. The EBSD analysis shows that the grains are preferentially ordered in <100> crystal direction parallel to scanning direction as reported in the literature. But the Texture Index varies with varying the scan vector length. In the chessboard case, TI increases with an increase in island size until 5 mm. Also, rotation angle has a significant effect on lowering the overall TI of the material. Overall, the stripes have lower TI compared to the chessboard strategy.
5. The fracture surface of the samples is investigated using SEM analysis. It is observed that the chessboard samples show a brittle-like fracture which can also be confirmed with the elongation % obtained during mechanical properties. The brittle fracture is linked to the porosities that act as fracture initiation sites. In comparison, stripes showed typical ductile fracture behavior. The micro-voids or microporosity on the edge of the samples could be the crack initiation site. It is noticed that the tearing occurs along the melt pool boundaries. The evidence of fracture due to Si particles at the center of the grains is not found.
6. Finally, the residual stresses at the surface and 2 mm depth are studied along the scanning direction, i.e., longitudinal and transverse direction. For all the samples, the residual stresses are higher in the longitudinal direction compared to the transverse

direction. The highest stresses are observed at the center of the samples compared to the two edges. The higher residual stresses are observed for 2 mm depth. But no significant pattern is observed w.r.t. to scan vector length and rotation.

Remarks: AlSi7Mg0.6 will be used as a basis for the studies in chapters 4 and 5. On the other hand, for technical and administrative reasons, we will use AlSi10Mg in chapter 3, an alloy which has a very similar metallurgical behaviour.

CHAPTER 3

Optical Tomography In-Situ Monitoring Module

“

In this chapter, we have focussed on the treatment of the data obtained using the EOSTATE Optical Tomography monitoring system. A balanced dataset is obtained with the help of computed tomography of the certified part (Stainless Steel CX cylindrical samples), through which a feature matrix is prepared, and the layers of the part are classified either having “Drift” or “No-drift”. The model is trained with the feature matrix and tested on benchmark parts (Maraging Steel) and on an industrial part (knuckle, automotive part) manufactured in AlSi10Mg. The proposed semi-supervised approach shows promising results for presented case studies. Thus, the semi-supervised machine learning approach, if adopted, could prove to be a cost-effective and fast approach to post-process the in-situ monitoring data with much ease.

3.1. Definitions

- **Hot spot:** The local areas with high light intensity than the rest of the layer. These hotspots areas indicate the highest probability of defect occurring in the final part.
- **Drift:** The drift layer indicates the presence of the hotspots in a particular layer. If the local hotspots are present in the layer, the whole layer is termed the “Drift layer.”
- **No-Drift:** In contrast to the “Drift layer,” the non-existing hot spots in a particular layer, termed the “No-drift layer.”
- **Feature:** In machine learning, a feature is a measurable property that can be quantified and recorded. Features are extracted from the input data to simplify the classification task. In our application, the mean and median are the feature extracted from each layer’s image.
- **Feature matrix:** A n×m dimensional matrix, where n is the number of data, and m is the number of features. In other words, a feature matrix contains n number of 1×m dimensional feature row vectors.

- **Balanced dataset:** A dataset having an equal number of layers for each label ("drift" and "no-drift").

3.2. Theory

The field of machine learning is concerned with how to construct computer programs that automatically improve with experience. This section will define the machine learning algorithms utilized in this work through mathematical modeling.

3.2.1. K-Means Clustering

K-means clustering or Lloyd's algorithm [169] is one of the literature's most widely studied unsupervised machine learning algorithms. It is an iterative partitional clustering algorithm that divides n data/feature samples into K disjoint clusters that minimize the squared error criterion, and each cluster is characterized through a centroid. It is important to note that the initial centroid seeds play an important role in K - means clustering algorithm, as different initial centroids can provide different results [170]. We have utilized the K-means++ algorithm [171] to choose initial centroid seeds that achieve faster convergence to a lower sum-of-squares point-to-cluster-centroid distance than Lloyd's algorithm but offer no optimality guarantees. The parameter K (i.e., number of clusters) is apriori selected, which in our case is 2.

Let us define a $n \times m$ dimensional dataset/feature matrix $D = [x_1, x_2, \ldots, x_n]^T$ with n samples, and the set of K centroids be $C = [c_1, c_2, \ldots, c_K]^T$, where x and c are necessarily represented points on an m-dimensional plane. The steps used to implement the K-means++ algorithm are as follows:

1. Select an observation x_a uniformly at random from the dataset/feature matrix, D. The chosen observation is the first centroid denoted as c_1.
2. Denoting the distance from an i^{th} data point x_i to j^{th} centroid c_j as $d(x_i, c_j)$. Now we compute distances from each observation to c_1, i.e., $d(x_i, c_i)$.
3. Now we choose the next centroid c_2 with a probability of $\frac{d(x_t,c_1)^2}{\sum_{j=1}^{n} d(x_j,c_1)^2}$. This step implies that if the data point x_t is near to centroid $c_1$the likelihood of x_t to become centroid $c_2$would be negligible.
4. We now repeat step 3 until all initial K centroids get assigned, i.e., $c_3, \ldots, c_K$.
5. Now for each $l \in \{1,2, \ldots, K\}$, set the cluster C_l to be the set of data/feature points in D that are closer to C_l then they are to C_p, $\forall l \neq p$.
6. Now for each $l \in \{1,2, \ldots, K\}$, update the centroid c_l to be the center of mass of all data

points in C_l, i.e., $c_l = \frac{1}{|C_l|} \sum_{\{x_i \in C_l\}} x_i$. This process is equivalent to calculating a mean, hence *K-means clustering*.

7. Now iteratively repeat steps 5 and 6 until cluster assignments do not change.

In K-means clustering, the distance metric d plays an important role, and in the literature, various distance metric has been suggested, e.g., Euclidean, correlation, cosine, and city block distance. We have experimented with various distance metrics to find the most suitable one for our application in our work.

3.2.2. K-Nearest Neighbour Classifier

The k-nearest neighbor (k-NN) is a supervised learning classification algorithm, one of the most studied classifiers in the literature, and even with a simplistic formulation, it has a performance at par the most complex classifier available [172]. The k-NN learning algorithm requires labeled training data and a predefined value of the number of nearest neighbors parameter k, which the classifier uses to find *k*-nearest neighbors to a query data (unclassified data), based on a distance metric. The *k*-nearest neighbors can have different classes, and the algorithm predicts the class of the query data as the majority class of nearest neighbors. Let $T = (x_{i'}, L_{i'})\ \forall\ i' = 1, 2, \cdots, N$ denote the training set, with N samples and $x_{i'} \in R^m$ is a m-dimensional training feature vector have a known class label $L_{i'}$.

A query data, $x'_{i'}$ be an m-dimensional vector of data or features, to which a label $L'_{i'}$ will be assigned. Now let $T' = \left(x^k_{i'}, L^k_{i'}\right)$ for $i' = 1,2, \dots, k$, denotes the set of *k*-nearest neighbors based on a distance metric and based on the majority class of T', $d'_{i'}$ will be assigned a label, i.e.,

$$L'_{i'} = \arg max_L \sum_{\left(x^k_{i'}, L^k_{i'}\right) \in T'} \delta_{L,\, L^k_{i'}},$$

Equation 9

where $\delta_{L, L^k_{i'}}$ is a Kronecker delta function.

3.2.3. Distance Metrics

As both supervised (k-NN) and unsupervised (K-means) learning algorithms rely on a distance metric, we mathematically define them in this section. For any two points $x'_{i'}$ & $x^k_{i'}$ in an *m*-dimensional space, the *Euclidean distance* can be defined as,

$$d\left(x'_{i'}, x^k_{i'}\right) = \sqrt{\left(\left(x'_{i'} - x^k_{i'}\right)\left(x'_{i'} - x^k_{i'}\right)^T\right)}$$

Equation 10

City Block distance as

$$d\left(x'_{i'}, x^k_{i'}\right) = \sum_{n=1}^{\mathrm{m}} \left| x'_{i'}[n] - x^k_{i'}[n] \right|,$$

Equation 11

Cosine distance as

$$d\left(x'_{i'}, x^k_{i'}\right) = \left(1 - \frac{x'_{i'}\, {x^k_{i'}}^T}{\sqrt{\left(x'_{i'} {x'_{i'}}^T\right)\left(\, x^k_{i'}\, {x^k_{i'}}^T\right)}} \right),$$

Equation 12

,and *Correlation distance as*

$$d(x'_{i'}, x^k_{i'}) = \left(1 - \frac{(x'_{i'} - \underline{x}'_{i'})\,(x^k_{i'} - \underline{x}^k_{i'})^T}{\sqrt{(x'_{i'} - \underline{x}'_{i'})\,(x'_{i'} - \underline{x}'_{i'})^T}\sqrt{\,(x^k_{i'} - \underline{x}^k_{i'})(x^k_{i'} - \underline{x}^k_{i'})^T}} \right),$$

Equation 13

where $\underline{x}'_{i'} = \frac{1}{m}\sum_{n=1}^{m} x'_{i'}[n]$ and $\underline{x}^k_{i'} = \frac{1}{m}\sum_{n=1}^{m} x^k_{i'}[n]$.

3.3. Materials and Methods

3.3.1. In-Situ Monitoring Module: EOSTATE OT

For our study, we used the EOSTATE melt pool monitoring module installed on EOS M290, for which the schematic diagram is shown in Figure 50. The optical tomography (OT) comprises an off-axis scientific Complementary metal-oxide-semiconductor (sCMOS) camera with a spectral detection range in the near-infrared region (NIR). Usually, the radiation from the build chamber consists of three components, i.e., backscattered laser (1064 nm), plasma radiations due to evaporation and ionization of gases (400-600 nm), and thermal emissions, which range from visible (380-780 nm) to near-infrared (~1400 nm) spectrum [41]. Since the part quality mainly depends on the thermal emissions from the melt pool, other wavelength radiations are eliminated by installing a bandpass filter (the type of bandpass filter cannot be relieved due to the machine provider confidentiality clause) in front of the camera. The OT

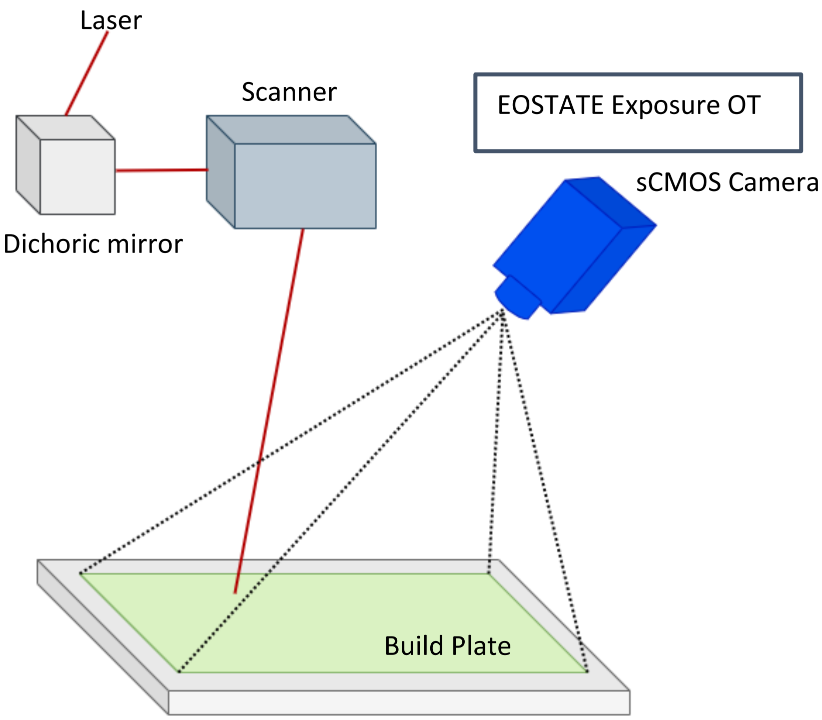

Figure 49: Schematic diagram of the EOSTATE exposure module.

system has a camera resolution of 2560 x 2160 pixels, allowing a spatial resolution of 125 µm/pixel across the entire build platform. The OT system has a frame rate of 10 frames per second. At the end of every scanned layer, all the images are superimposed, and a holistic picture for the whole layer is saved in a 16 bit TIFF single image. The final image of the particular layer represents the process map that can be correlated with the emitted light intensity by the process. Due to the non-centralizing position of the camera, the geometric correction is applied to the images via software.

3.3.2. Materials and Methods

In our study, a total of 18 Stainless Steel CX cylindrical samples with a diameter of 10 mm and a height of 15 mm are printed on EOS M290. The input volumetric energy density is varied over a range to prepare a dataset of certified samples that would be used further for training and verification of the model. The deliberately varied process parameters induce drift during the process, resulting in varied porosity levels. The optimized printing process parameters are summarized in Table 10. The laser power and scan speed varied ± 30 % from the optimized processed parameters tabulated in Table 10. Also, the layer thickness is varied to 30, 60, and 90 µm. It is worth noting that the possibility of having drift due to bad powder layer spreading is not considered for this study. Computed tomography is performed on printed samples for analysis using an X-ray inspection system to determine pores with a 180 kV microfocus tube and an area detector with a voxel size of 19 or 22.5 microns to prepare a labeled dataset training. The smallest evaluated pore has a volume of 5 voxels.

For testing the supervised learning classifier, two case studies are chosen, which are: an automotive part called “Knuckle” and a benchmark part called “Overhang structure” (Figure 51). The automotive part called “knuckle” is printed with AlSi10Mg, and the benchmark part is printed with Maraging steel. The “knuckle” and “overhang part” are chosen as a case study because the location of the overheating failure in these parts is detectable via visual inspection. The EOS analysis tool can detect cold and hotspots, treated as areas with the highest probability of finding a defect in the final part. EOSTATE Exposure OT analysis tool is used to cross-validate results obtained from the supervised learning approach for the presented case studies.

Table 10: Process parameters for the printing.

Material	**Power (W)**	**Scanning speed (mm/s)**	**Hatch distance (µm)**	**Layer thickness (µm)**	**Energy density (J/mm^3)**
Stainless Steel CX	260	1000	100	30	80

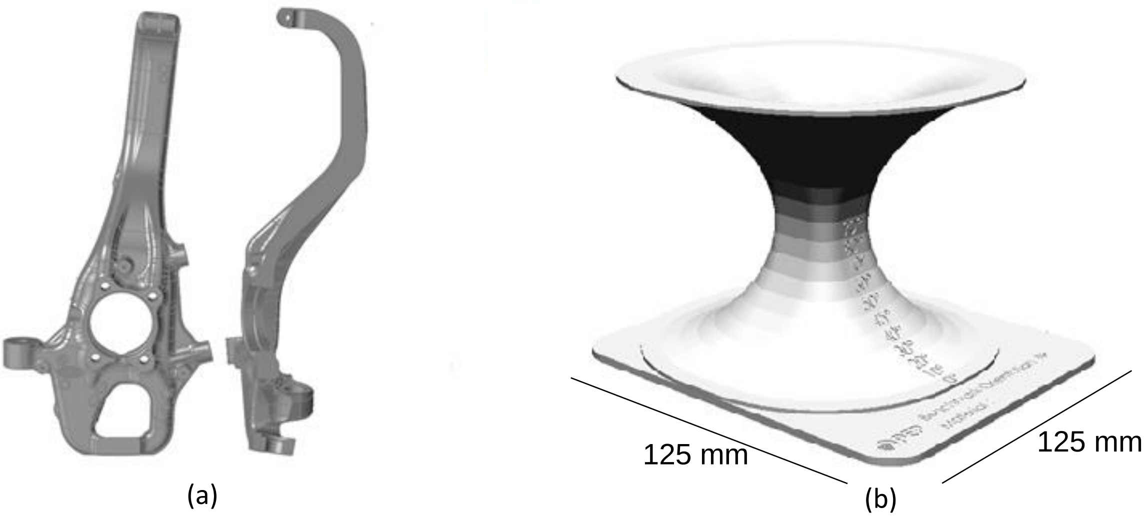

Figure 50: The CAD design of (a) An automotive steering knuckle (3d printed within the framework of the European project Maestro [36]), the length of this part is approximately 500 mm, only a section was 3D printed, (b) benchmark used to determine the critical overhanging angle in additive manufacturing processes.

3.3.3. Image Analysis

Clijsters et al. [18] used a co-axial setup (CMOS camera and photodiode in NIR range) to capture the melt pool signatures such as melt pool area and intensity to monitor the quality of the SLMed parts. Clijsters et al. prepared a dataset based on the melt pool area and intensity for different scan vectors such as fill and contour scans. It is presented that the heat transfer depends mainly on the environment of the melt pool: the heat flux is higher when the metal pool is surrounded by printed material than when it is surrounded by powder. A confidence interval is defined for each of these classes (fill scan and contour scan), and errors are detected based on the defined confidence interval. The proposed method is studied for small cube structures. However, our study also noticed that such a confidence window based on mean and standard deviation could not be defined for complex and real case parts. To prove this, the mean and variance of each layer for the complex part called “Knuckle” (refer to Figure 51a for part geometry) are plotted in Figure 52. It can be observed that the mean and standard deviation are dependent on the printed area of each layer and change with the shape of the complex part. Therefore, the global threshold limit based on the mean and standard deviation cannot be applied for the complex geometries, and thus the ML is a suitable approach for post-processing of in-situ data. For training our ML classifier, selecting suitable features from the given dataset is required.

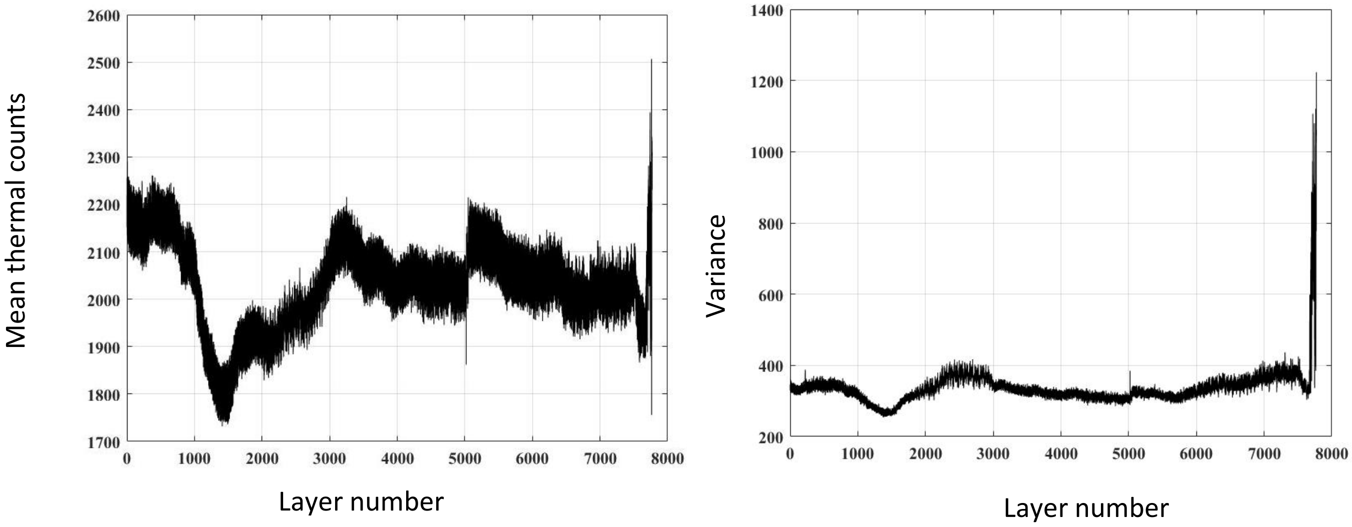

(a) (b)

Figure 51: (a) Mean, and (b) variance per layer for the case study part “Knuckle”.

Preprocessing the OT images is necessary before feature extraction and further ML processing. As the OT image captures the whole build plate, the specific part region is cropped. The removal of the background from the cropped part images is performed based on a suitably selected intensity threshold. A preliminary statistical analysis performed on individual image layers shows that the mean and the median of the corresponding images increase significantly due to hotspots in the thermal images compared to the cases of absence (Figure 53). Localized hotspots in the layer are due to local variation in the melt pool shape and size. The localized variation in melt pool signatures can be influenced by the localized variation in powder bed spreading or process parameters. The more hotspots there are in the images, the highest probability of drift. For example, Zenzinger et al. [41] demonstrated the link between the hotspots in OT images to the defect in the µCT scan of the layer. Recently, Mohr et al. [38] also studied the OT images to detect a defect in the final part and compared the OT images with the µCT images. It is also verified that the hotspots in the OT images link to defect in the final part.

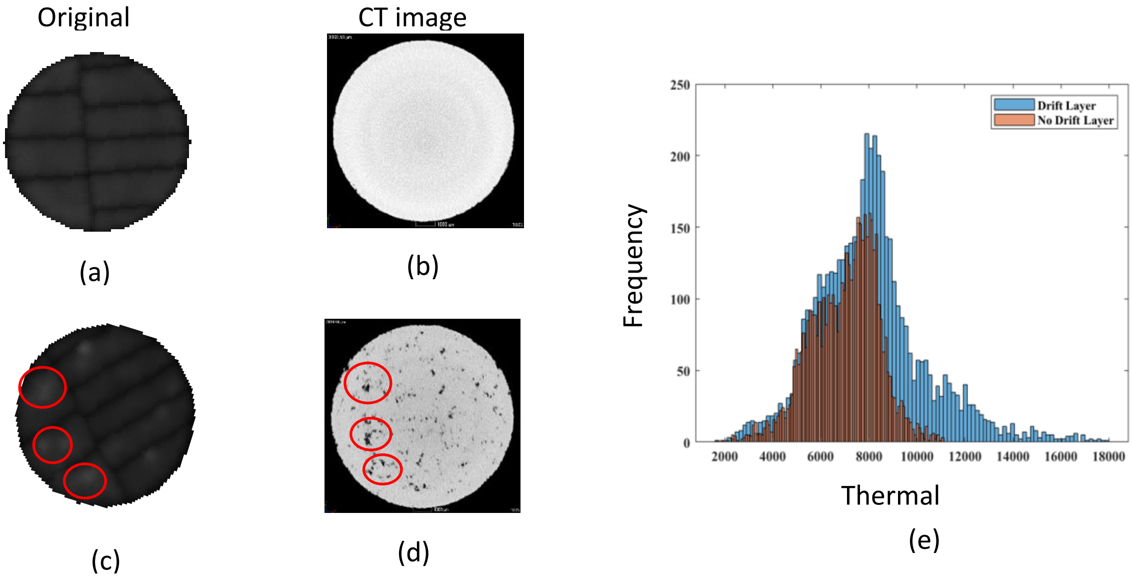

Figure 52: Example picture of (a) OT image without hotspots, (b) CT image of corresponding layer (a) without hotspots, (c) OT image with hotspots, (d) CT image of corresponding layer (c) with hotspots, and (e) histogram comparison between (a) and (c).

For example, Figure 53a represents the layer image without any hotspots, verified with CT image (Figure 53b) and, another image with hotspots (marked by red circles) is shown in Figure 53c. The corresponding CT image with the porosity (marked by red circles) is also shown in Figure 53d. On comparing the histogram of images in both scenarios, the image's histogram, which represents a probable drift layer (layer with hotspots is termed as drift layer), shows a right shift compared to the image of the layer with no possible drift (layer without hotspots). The right shift in the histograms is due to hotspots, which leads to a higher mean in the layer than no drift layer (see Figure 53e).

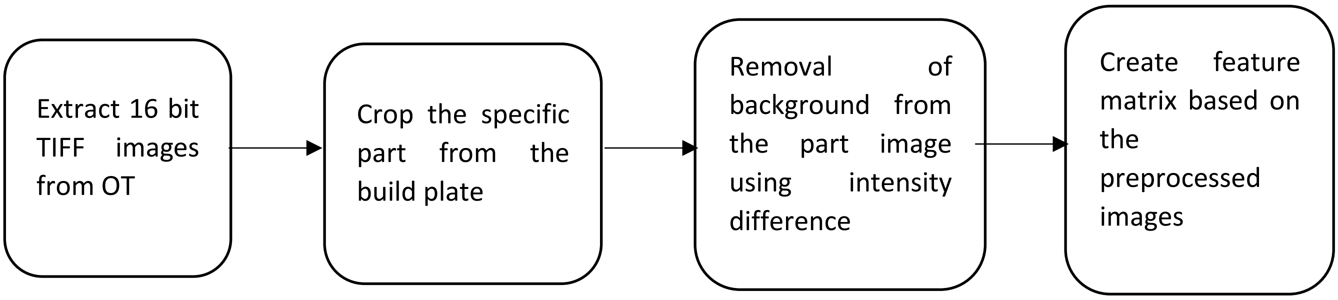

Figure 53: Flowchart for extraction of features from the OT pictures.

As the relative value of the mean and median of the image pixels can describe the degree of right/left shiftiness of the histogram, based on these observations, we decided on the mean and median being the features of choice for training and testing the classifier. The flowchart of the feature extraction procedure is shown in Figure 54.

3.4. Semi-Supervised Learning Approach

3.4.1. Initial Data Labeling and Suitable Distance Metric Selection Through K-means Clustering Algorithm

Another essential aspect of ML algorithms like K-means and k-NN is the distance metric. As discussed previously in Section 3.2.3, there are many distance metrics already proposed in the literature, but for a particular application, only a few will suit. This section discusses the initial labelling of sample layers as “drift” or “no-drift” and chooses the suitable distance metric for our application based on the experimentation done on the *certified dataset*.

Due to the complex nature of the DMLS process, obtaining the labeled dataset in an automated fashion is a challenging task. Therefore initially, a labeled dataset of 40 layers (20 layers of each label, i.e., “drift” and “no-drift”) from a set of 14 Stainless Steel CX cylindrical samples are prepared manually. The categorization of specific layers as “drift” and “no-drift” is based on the visual comparison between of particular OT image with the corresponding CT image (see Figure 53). However, the resolution difference between OT and CT images hinders a visual comparison of all the images. Thus, it is impossible to label and prepare a large dataset manually. Therefore, in this case, the unsupervised algorithm K-means clustering come to the rescue and is used to automate the task of labeling. As seen in comparison with CT data, it can be concluded that a higher number of OT hotspots results in a higher probability of having a real defect in that layer. Based on this hypothesis, a dataset of another 200 unlabelled layers is prepared such that it comprises an approximately equal number of “drift” and “no-drift” labels. Nevertheless, it shall be noted that it does not mean that every image with an OT indication will lead to a real defect in the printed layer due to the repetitive nature of printing of the DMLS process, as the existing defect in the previously printed layer may be resolved in the following printing scan.

Next, the 40 labeled and 200 unlabelled layers are mixed up to perform a cluster analysis. We extract $m = 2$ features (mean and median) of each layer image, and a total of $n = 240$ feature vectors are formed, resulting in a feature matrix D of dimension 240×2. The clustering parameter $K = 2$ (as the data has to be divided into two clusters) and maximum iterations to 1000 are set. The clustering process is repeated 5 times using new initial cluster centroid positions/seeds. The final clustering solution will have the lowest sum of points to centroid distance (ref. Section 3.2.1). The accuracy of K-means algorithm cluster assignments is cross-validated with the initially labeled 40 labeled samples utilizing multiple distance metrics, and the *Correlation* distance metric shows the maximum validation accuracy. The high validation accuracy also indicates that selecting mean and median as features is sufficient to differentiate between "drift" and "no-drift" conditions. The cluster assignment using different distance metrics on the expanded dataset is shown in Figure 55. The validation accuracies of the different distance metrics are listed in Table 11. Based on the highest percentage accuracy achieved through the K-means method, we choose the correlation distance as the suitable distance metric for our application and finalize the resultant labels for training further a supervised learning-based classifier, i.e., k-NN classifier.

Table 11: Performance of the different distance metrics on certified data.

S. No.	Distance Algorithm	Accuracy (%)
1.	Cosine	85.00
2.	Squared Euclidean	82.50
3.	City Block	85.00
4.	Correlation	100.00

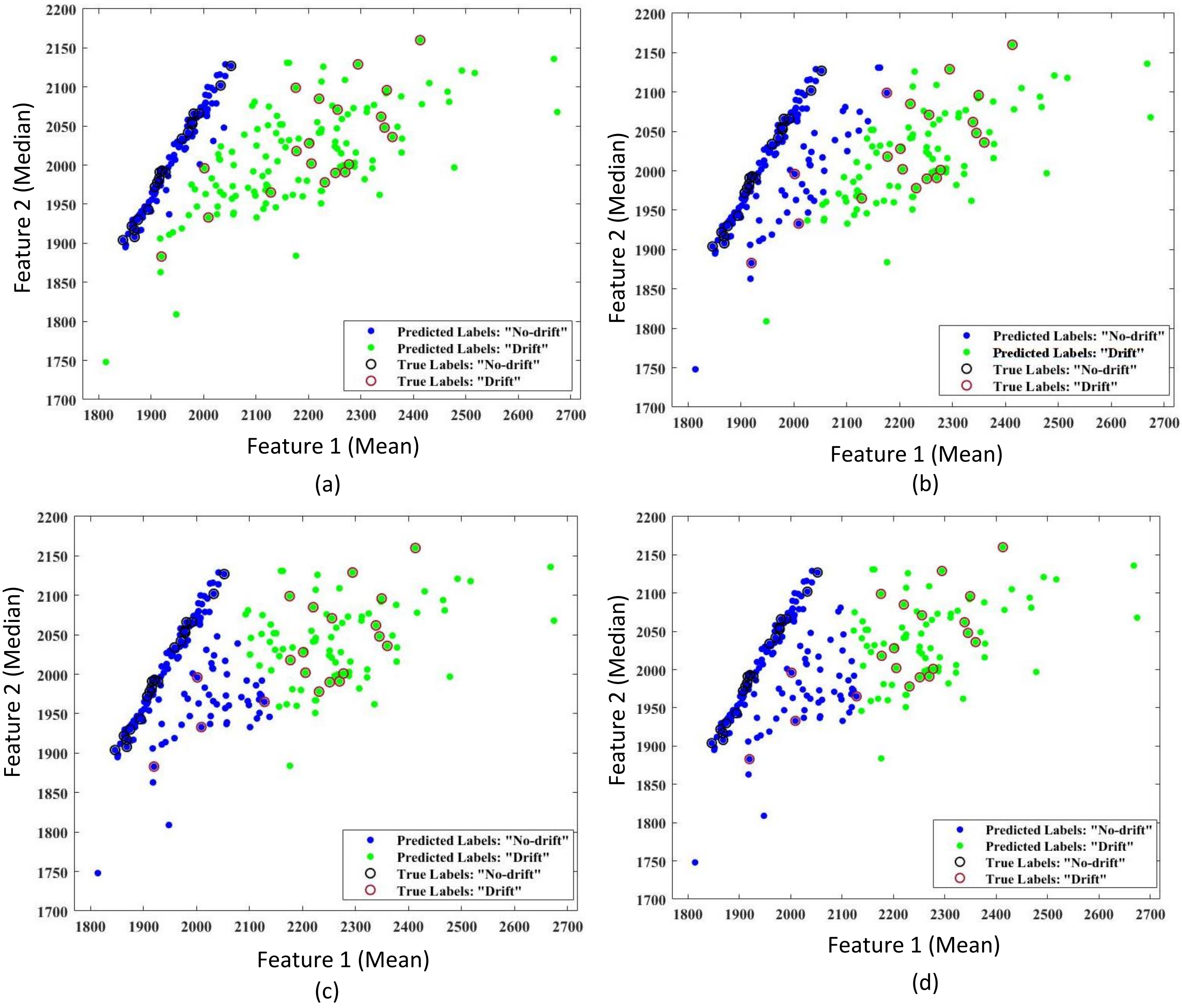

Figure 54: Clustering using (a) correlation, (b) cosine, (c) city block, and (d) squared Euclidean distance metrices.

3.4.2. Number of Nearest Neighbor Parameter Selection for k-NN Classifier

After identifying the suitable distance metric, the next important step is to prepare a balanced training dataset (dataset with an equal number of each label) to train a k-NN classifier (a supervised machine learning algorithm). It is imperative to prepare a balanced dataset to avoid the biasing problem. Therefore, 100 data points for each label (total 200) are chosen randomly from the dataset of 240, which resulted from the K-means clustering. Although we prepared a balanced dataset for training, one can apply methods like "*Class confidence weighting*" in case only an imbalanced dataset is available [173], [174]. The training dataset is divided into a 70:30 ratio for preparing the training and validation dataset. To find the best value for the number of nearest neighbors, i.e., k, the accuracy of the trained k-NN classifier with varying k is tested on the validation set, which is also shown in Figure 56. The accuracy vs. k graph plot suggests that a value of $k \in (9, 23)$, can be chosen for the maximum classification accuracy. As choosing a large value of k results in the increase of computational complexity of k-NN classifier, we choose the minimum indicative value $k = 9$.

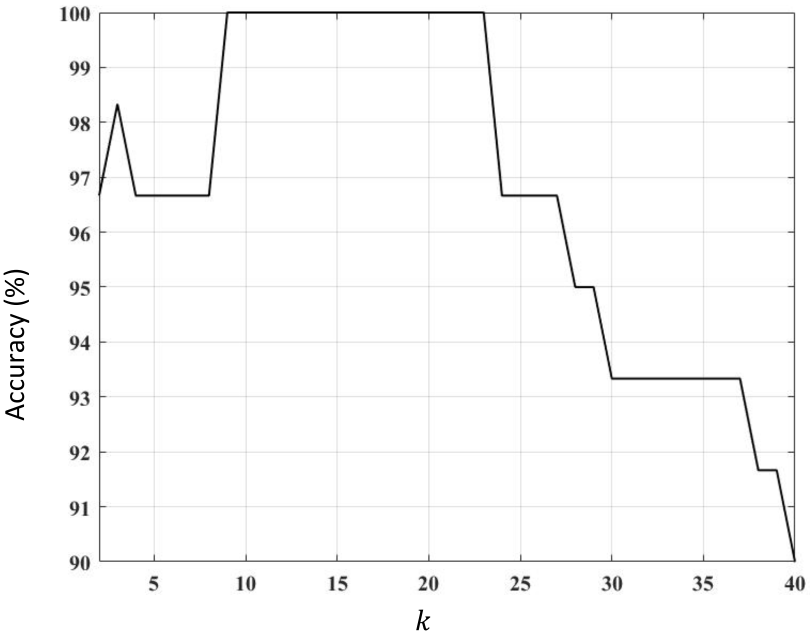

Figure 55: Accuracy versus k plot for the k-NN classifier.

3.5. Results and Discussions

3.5.1. Testing on Certified Data

In the experimental section, the stainless steel CX cylindrical samples are printed with different process parameters such as layer thickness, power, scanning speed, and hatch distance to generate a certified dataset for training the algorithm. The certification of the samples is done through a CT scan. A total of four certified cylindrical samples with CT porosities of 0.0033 %, 0.0054 %, 4.3967 %, and 0.1436 % are chosen for testing the trained k-NN classifier. It should be noted that the data of the four chosen cylinders are not used to train the classifier. The semi-supervised model predicted 20.82 %, 1.9543 %, 1.1363 %, and 0.4862 % layers as "drift" for the sample with CT scan porosities of 4.3967 %, 0.1436 %, 0.0054 %, and 0.0033 %, respectively. The k-NN classifier-based test results indicate that the sample with CT scan porosity of 4.3967 % has the highest number of layers with hotspots due to non-optimized processing parameters. As the dataset size is limited, further comments on an analogy between porosity and drift detected (particularly at lower porosity levels) are out of the scope of this work.

3.5.2. Case Study 1: Benchmark Part

We now apply our trained k-NN classifier on the data obtained through real complex parts, and for that, we choose benchmark parts that are often used for material development in the industry. Out of different benchmark parts, “Overhang” is one of the critical parts shown in Figure 57a, which aims to find the critical overhang angle for a particular material that can be printed without the support structures. As we know, above a critical overhang angle, the support structures are used as an anchor to prevent the failure of the part. Therefore, it is vital to know the overhang angle to optimize process parameters for new material development in the DMLS process. The surety of the failure of the part at a particular overhang angle makes this part a suitable candidate for our case study. The location of the failure of this part is known and can be used as a ground truth label. The OT images of the part are exported and pre-processed as described in the previous sections and the feature matrix is prepared. As mentioned in the previous section, the k-NN classifier is already trained with labeled data of the certified part, and the predicted labels are shown in Figure 57b. The location of the layers labeled as “drift” is shown in Figure 57c; the poor thermal conductivity due to a large overhang angle has led to the overheating drift in the layers numbered from 1535 to 1564. This hypothesis is validated by the EOSTATE Exposure analysis tool, which shows the presence of hotspots in the “drift” labeled layers. Thus, the labels predicted by the ML model correlate with the results from the analysis tool as well.

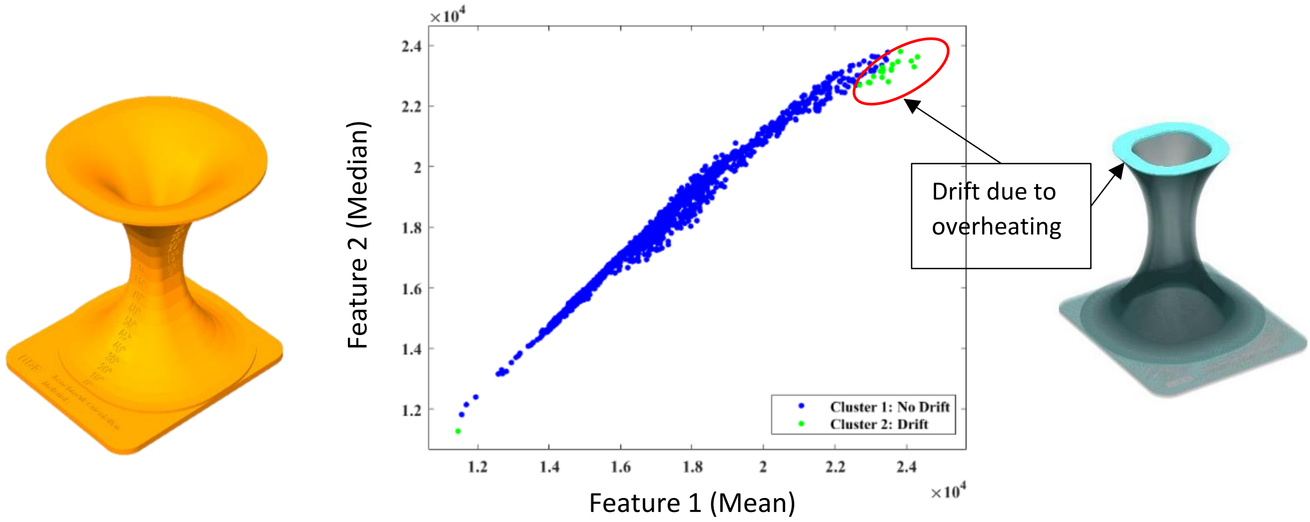

(a) (b) (c)

Figure 56: (a) CAD geometry, (b) Labels predicted by the k-NN model, and (c) printed part geometry with drift layers (in bright color) .

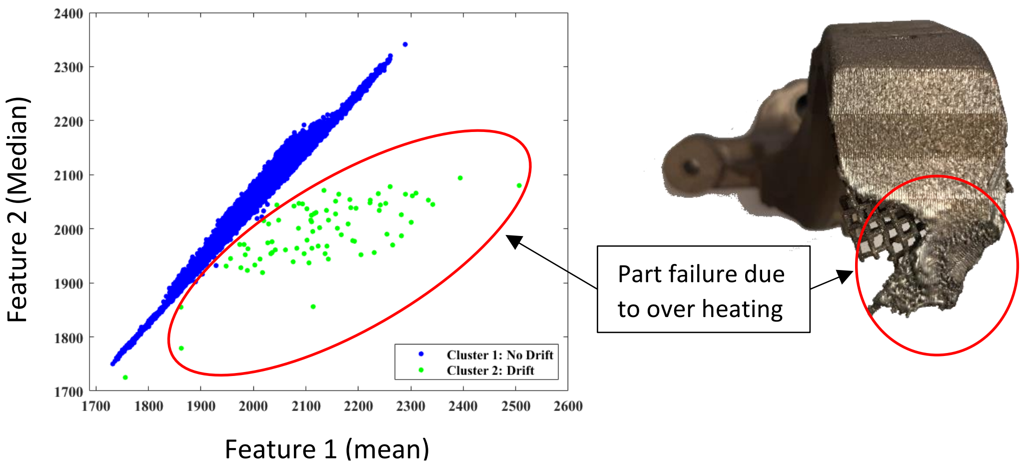

(a) (b)

Figure 57: (a) Labels predicted by the k-NN model, and (b) printed part geometry with overheated region.

3.5.3. Case Study 2: Industrial Case Automotive Steering "Knuckle."

We chose an automotive part called "Knuckle for another case study." Figure 58a contains the scatter plot of resultant predicted labels, and the last few layers of the part are classified as "drift" layers. This classification correlates with the visual inspection of the part quality as well. As shown in Figure 58b, the topmost layers from layer number 7682 until 7764 of the part failed due to overheating. The failure of these layers is due to the lack of heat dissipation. This part is a good example of the need for design optimization in AM, as poor support structures lead to part failure. It is also be verified by the EOSTATE Exposure analysis tool that the overheating leads to hotspots in the captured images.

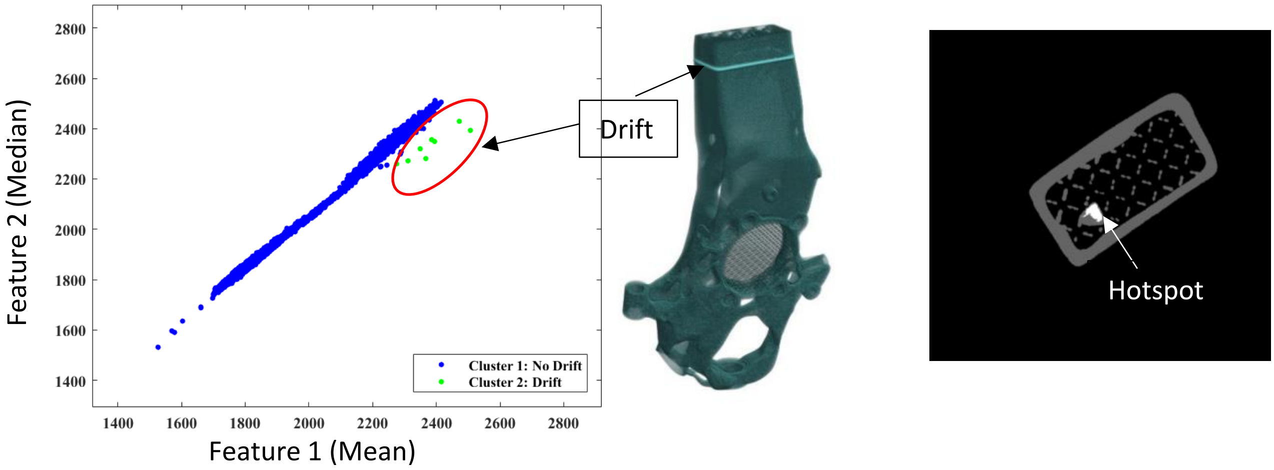

(a) (b) (c)

Figure 58: (a) Labels predicted by the k-NN model, (b) part geometry with drift layers (in bright color), and (c) location of the hot spot (marked in white color) in the drift layer.

Another optimized design knuckle is printed with optimized support structures for better heat dissipation. Figure 59a represents the predicted labels, and it shows that only 8 layers are classified as “drift” layers due to the presence of hotspots in the layers numbered from 6150 to 6158. This hypothesis is cross-validated with the EOSTATE Exposure analysis tool, as shown in Figure 59c, which shows the hotspot's location in layer number 6150. It shall be noted that the hotspot continues to be present at the exact location for the subsequent 8 layers (from layer number 6150 to 6158), which is also predicted by the proposed K-NN approach. The automotive part called “Knuckle” shown in Figure 59b is printed within the framework of the European Union project titled “MAESTRO.”

The initial tests utilizing the proposed semi-supervised ML model are performed for three parts printed with different process parameters and different materials (Benchmark part- Maraging Steel, Knuckle- AlSi10Mg). Therefore, it can be concluded that the proposed algorithm and feature extraction are independent of the process parameters and material of the printed part.

It is also to be noted that the OT is not sensitive to all kinds of defects during the printing process. As the DMLS process is very complex in terms of printing, hundreds of factors could affect the quality of the final part. For example, Galy et al. listed all the different parameters that can influence the quality of the Al alloy parts during printing [175]. Therefore, it is challenging to monitor all the possible factors with optical tomography, and certification for quality assurance requires expensive techniques like a CT scan. However, the CT scan is a costly technique, and part size limitation makes it more challenging to use it for every part certification. Therefore, the proposed model based on ML can be used to select suitable parts for the other expensive post-processing techniques.

3.6. Conclusions

In-situ monitoring of the DMLS process can significantly improve the reliability of the whole process for quality assurance of the product. But there are a few issues with the monitoring systems which need to be solved for fast and easy anomaly detection. Firstly, processing the enormous amount of unlabelled data obtained from these monitoring systems is a huge challenge. Secondly, it is very laborious to detect the drift in the final part of the in-situ monitored data. Therefore, using ML algorithms to treat in-situ monitoring data has merit. This study continues the research going into data treatment in additive manufacturing.

The key contributions of this work are summarized as follows:

- An unsupervised K-means clustering algorithm is used to label the unlabelled data with the help of a small set of labeled data and helps in choosing the most suitable distance matric. The accuracy of the algorithm is verified using the computed tomography-based certified data.

- The labeled dataset is utilized for training the k-NN classifier. The optimum value of a number of nearest neighbors k is judged based on accuracy vs. k plot.
- The semi-supervised approach successfully classifies the layers into either “drift” or “no-drift” for presented case studies and the cross-validated through the EOSTATE Exposure OT analysis tool.

Semi-supervised machine learning shows that machine learning in additive manufacturing can be a robust method to improve the post-processability of the in-situ data. Therefore, it is essential to study the robustness of the proposed methodology for other in-situ monitoring devices such as photodiode-based. The coupling with data from other sensors, such as photodiodes, is studied in Chapter 4.

CHAPTER 4

Melt Pool Monitoring

> "
>
> This chapter discusses another commercial photodiode-based in-situ monitoring module, i.e., Melt Pool Monitoring (MPM), provided by SLM Solutions. MPM captures the melt pool emissions generated from laser-material interaction, which helps monitor the melt pool's quality.
>
> This study is the initial step to discuss the possibilities of post-processing the photodiode data and improving product confidence interval regarding product health.

4.1. In-Situ Monitoring MPM Set-Up

The co-axial melt pool monitoring (MPM) system installed on the commercial machine SLM 280HL is used to collect thermal emissions from the melt pool formed due to laser-powder interaction. The melt pool systems are co-axial systems, which means it is in the laser path's alignment and collects the real-time emissions from the laser path at an acquisition frequency of 100 kHz. The MPM module consists of two photodiodes with different sensitive areas. The spectral range of the photodiodes cannot be revealed due to confidentiality issues. However, both photodiodes capture the thermal emission in the near-infrared region. The schematic diagram of the MPM system is shown in Figure 60. Only the emissions traveling perpendicular to the build platform are considered. The thermal radiations follow the same path as the laser and are directed into the MPM module with a semi-transparent mirror, which does not allow laser wavelength to pass. The signal is split into two different spectral ranges and captured by the two photodiodes. The received signal is forwarded to associated ADCs (Analog to digital convertor) and provided in an FPGA (field-programmable gate array) by the individual photodiodes. The captured thermal emissions from photodiodes 1 and 2 are stored along with the x/y-coordinates (16-bit). The values are stored parallel with the laser on/off signal from FPGA to PC every 10 µs. All the data is stored for every layer in a data file, accessed as 2D representation in MPM software provided by SLM Solutions [176]. The new file is created automatically for each layer after the complete exposure. For this work, no additional modifications are made to the installed hardware.

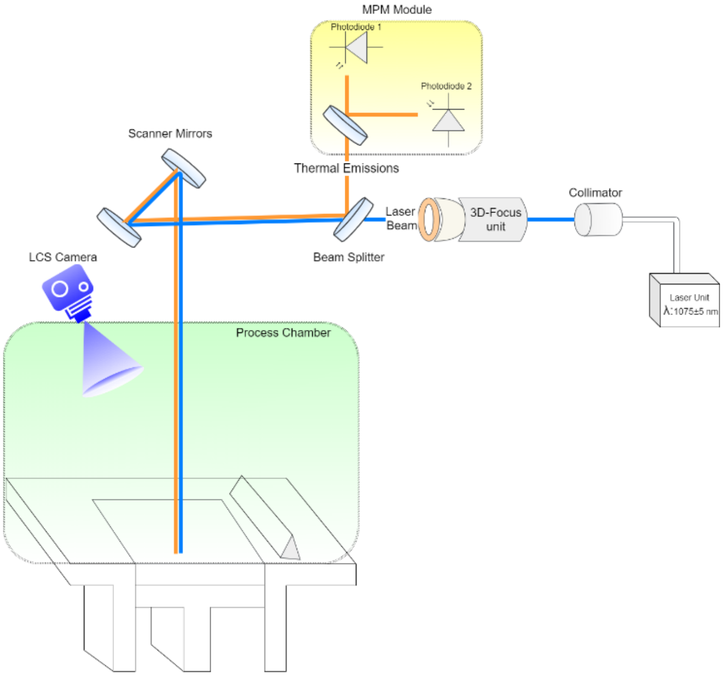

Figure 59: Schematic of Melt pool monitoring system, and Layer control system installed on SLM 280HL.

4.2. Sensitivity Analysis of MPM

4.2.1. Volumetric Energy Density Sensitivity Analysis

The sensitivity of the MPM system for the volume energy density is studied. The AlSi7Mg0.6 cylindrical specimens with the sandwich structure are printed, where the bottom and upper part of the cylinder is printed with the optimized process parameters presented in Table 12 (marked in bold italics). The chemical composition and powder morphological data are discussed in section 2.2.1. In contrast, the middle part's varied volumetric energy density is expressed by Equation 1. The geometry of the samples and corresponding VED values for the middle region is shown in Figure 61. Also, it shows the mean thermal counts for every layer, and it can be observed that photodiode 2 is sensitive to change in volume energy density in the samples, which ranges from 40-73 J/mm^3.

It should be noted that the same behavior is also observed for photodiode 1. The first 50 layers that account for a higher signal represent the support structure of the part. Therefore, removing support structure data from the data preparation before processing. The layers from 300 to 580 indicate the input volumetric energy region variation. Sample 3 has the lowest energy density of 40.48 J/mm^3, contributing lower mean thermal emissions, whereas sample 7 has the highest volume energy density of 73.26 J/mm^3, which shows higher mean thermal emissions. So, it can be concluded that the MPM system signal is proportional to input volumetric energy density.

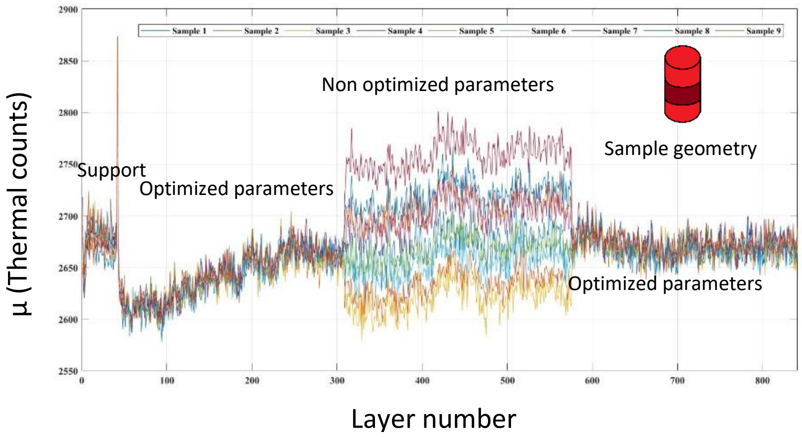

Sample	Energy Density (J/mm3)
1	54.94
2	46.62
3	40.48
4	64.10
5	54.39
6	47.23
7	73.26
8	62.16
9	53.98

Figure 60: The mean thermal emissions recorded by MPM systems for the induced drift detection in the specimens shown in right corner of graphs (dark red color: drift area, red area: optimized processed parameters).

4.2.2. Down-Skin Sensitivity Analysis

Overhang samples are printed to study the sensitivity of the MPM system for down-skin, as shown at the bottom of Figure 62a and Figure 62b. It is observed that the photodiode signal shows a gradual increase in the thermal emissions as the laser exposure moves from the printed part to the overhang part (Figure 62). This is in conjunction with the theory that the powder has lower thermal conductivity than the consolidated part. Voids in loose powder make it an inferior heat conductor to the printed part. Thus, the consolidated part acts as a major heat sink in the SLM process. Therefore, when the region above the powder is exposed, the melt pool thermal emissions are higher compared to the melt pool region on the printed part. The same phenomenon could also occur during a lack of fusion defects. As sometimes, due to bad powder spreading, there is non-uniformity in the powder bed, and some regions are not covered with the powder uniformly for a few layers.

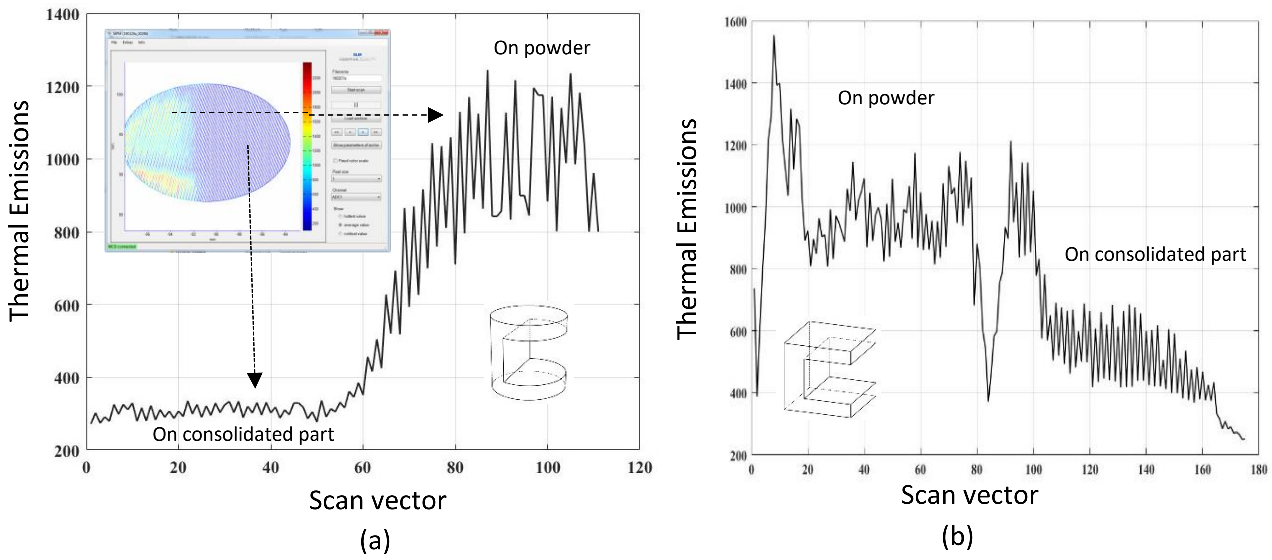

(a)

(b)

Figure 61: Scan vector wise MPM signal for down-skin layer for (a) cylindrical sample, (b) cuboid sample.

Nevertheless, in the successive passes of recoating, the regions with a lack of powder are uniformly covered. Then the laser prints a thicker layer than other areas with uniform powder spreading. This phenomenon can lead to a lack of fusion defects as laser energy is not enough to melt the powder layer fully. So, it can be concluded that the MPM systems are also sensitive to the lack of fusion defects.

4.2.3. Varying Hatch distance

The effect of standardized volume energy by varying hatch distance on the MPM system is detected and evaluated. The three hatch distances chosen are 0.13, 0.26, and 0.52 mm. The evolution of the MPM signal for the first five layers is shown in Figure 63. For the first layer, the mean of thermal counts is relatively higher for both ADC1 and ADC2, whereas after the 3rd layer, the thermal counts seem more constant. Higher values for the first layer are due to local conditions for heat conductivity. Based on volume energy, the highest values of the first

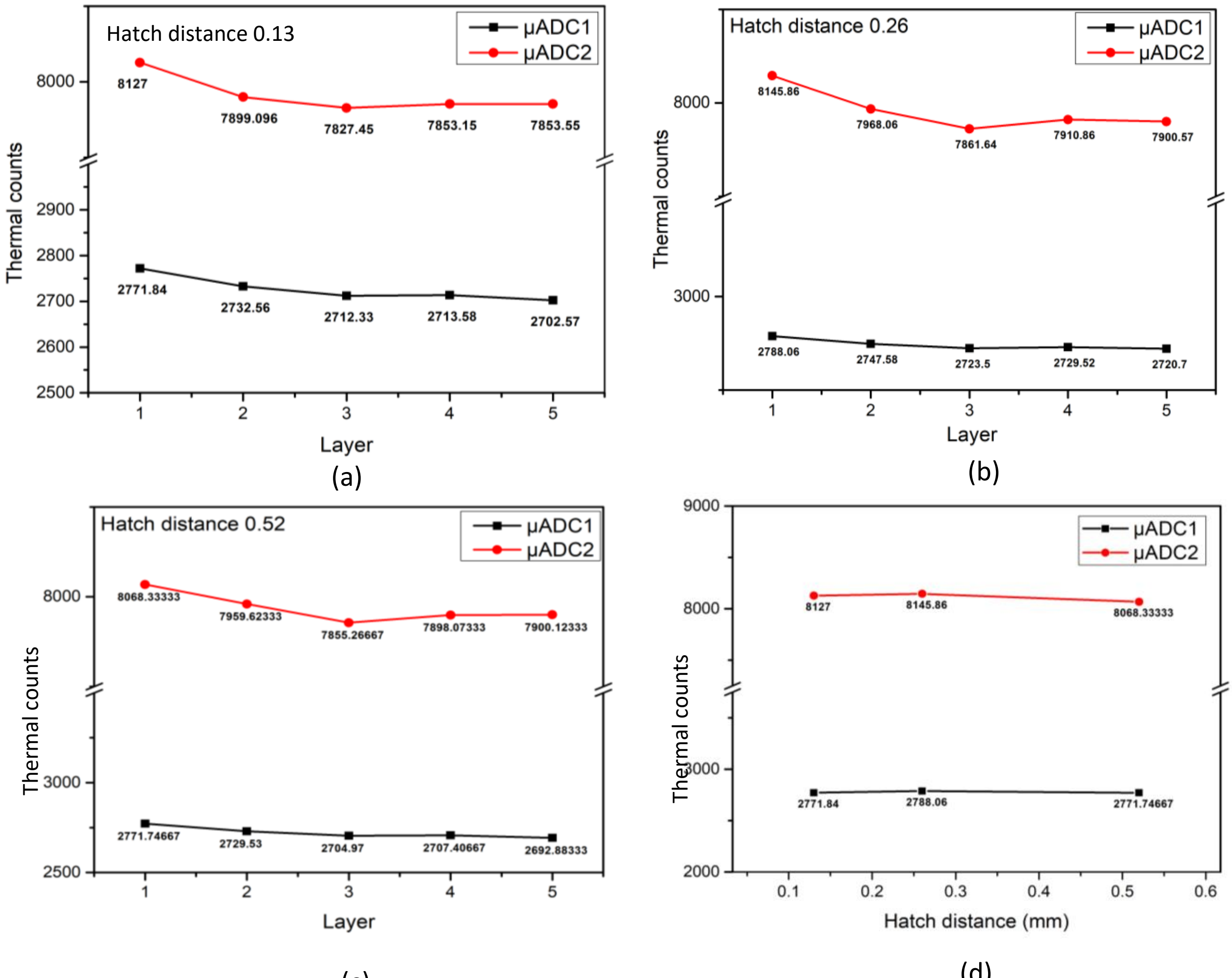

Figure 62: MPM signal for different hatch distances (a) 0.13 mm, (b) 0.26 mm, (c) 0.52 mm, (d) Overall comparison of hatch distances.

3rd layer, the thermal counts seem more constant. Higher values for the first layer are due to local conditions for heat conductivity. Based on volume energy, the highest values of the first layer vary with hatch distance, as shown in Figure 63. The highest value for ADC1 and ADC2 is observed for hatch distance 0.26 mm.

4.3. Data analytics for MPM Data: Global Scale

It is noticed that the semi-supervised method combining K-means clustering and K-NN classifier (Chapter 3) used for EOSTATE OT does not work effectively for the MPM data. The main reason is that the nature of Photodiode based data is different compared to OT images data. Secondly, K-NN classifier is best for easily identifiable clustering problems whereas in MPM dataset the clusters are comparatively complex in nature. Therefore, the need for more sophisticated classifier is necessary. For MPM dataset we, preferred to use SVM as it assigns clusters based on hyperplane than distance metrics.

4.3.1. Theory

The supervised learning approaches work for classification and regression problems, whereas unsupervised approaches work for clustering problems. The main difference between both approaches depends on the type of data required as input for training. In supervised, one has to provide a labeled dataset in which each data point belongs to a specific class as categorized by the label associated with it. In contrast, unsupervised learning is used when we do not have the labels for the dataset or, in other words, when we do not have ground-truth knowledge about the dataset. It is challenging and expensive for the AM process to obtain a ground truth dataset for training. Therefore, a small dataset is prepared for training the algorithm. This study uses a supervised learning model called “Support vector machine” (SVM), which works sufficiently well for small datasets.

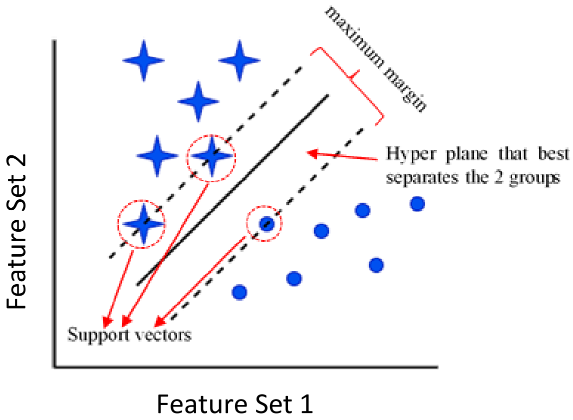

Figure 63: Schematic of the hyperplane that maximally separates the support vectors corresponding to each of the two classes.

SVM is a classification algorithm that divides the dataset into multiple classes. In this study, the in-situ data is treated as a binary classification problem, i.e., only two types (“drift” and "no-drift") are identified, so the SVM classifier perfectly fits this case. During training the SVM classifier, the decision function amounts to identifying a suitable reproducible hyperplane that maximizes the distance (also called "margin") between the support vectors of both class labels (Figure 64). SVM classifier can work for both linear and non-linear classification problems. Further, the linear SVM problems vary depending on the number of selected features. For example, in two feature dimensions, the hyperplane corresponds to a line, whereas in the case of three features, the hyperplane is a two-dimensional plane. Regardless of the SVM's complexity (i.e., dimensionality), classification problems are often linear, which means that hyperplane used is a straight line, not a curved line. If the features selected for the SVM classifier are linearly separable, we can draw a straight hyperplane to separate the two labels of the class of interest. Usually, there are two types of margins: hard margins and soft margins. We restrict the classifier from making errors while training with a hard margin. Although the hard margin is computationally less expensive, the linear separability of the features is not always easy. Therefore, allowing the classifier to misclassify allows a more significant margin to obtain greater generalizability to new data. This misclassification can be obtained by the so-called "Soft margin," which relies on the variable ξ. The values of ξ lie in the range $0 \leq \xi \leq 1$. In turn, the non-zero values of ξ can allow classification error when outliers in the training data lead to the hyperplane making mistakes, i.e., misclassification (Figure 65 [177]). This hard margin is a particular case of soft margin when the slack variable (ξ) is zero. A soft-margin constant denoted by C is introduced to incur a penalty on ξ. The parameter C helps to choose the trade-off between the tanning errors and complexity and reduces the chances of overfitting, which means fine-tuning the classifier for maximum accuracy in the training dataset. The decision boundary of a non-linear classifier depends on the data in a non-linear way. The kernel

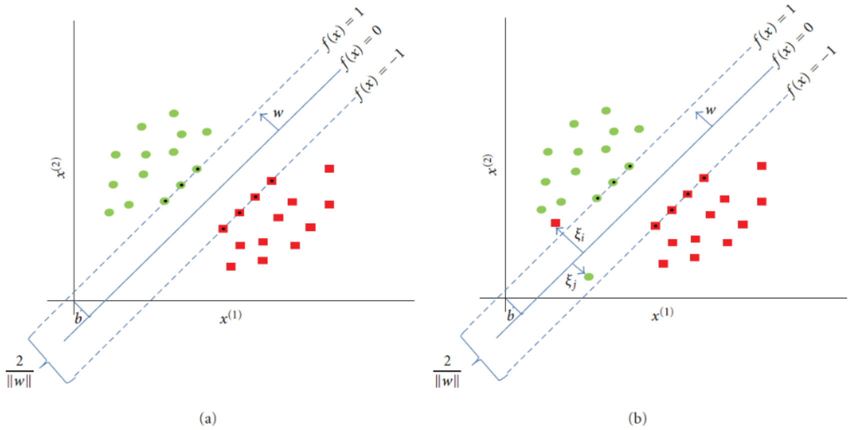

Figure 64: (a) hard margin on linearly separable dataset where no training errors are allowed. (b) the soft margin where two training errors are permitted to make data non-linearly separable.

method transforms the support vectors into a high-dimensional space in these cases. A detailed explanation for SVM can be studied in the literature [178].

Typically, there are three stages in the SVM classifier: (a) feature selection and preparing feature dataset, (b) training the classifier and testing, and (c) checking the accuracy of the classifier. All three stages for our case are discussed in the following sections.

4.3.2. Process Parameters and Part Geometry

A balanced dataset comprising an equal number of drift and no-drift layers is necessary to prepare a training dataset for the SVM classifier model. An artificially drift is introduced in the samples to obtain the balanced dataset. Therefore, the unique geometrical specimens are printed shown in Figure 66. The process parameters tabulated in Table 12 are varied to obtain varied volumetric energy density in the range of 40-73 J/mm^3 for each shown geometry. The overhang samples (Figure 66a and 66b) with an overhang of 8 mm are printed without any support structure and stripes rotation of 67° for the overhang layer. No down-skin parameters are used for the overhang layer. For lack of fusion samples (Figure 66d), an internal cuboid type groove with dimensions 10*8*0.09 mm^3 is printed. The thickness of the groove is set to 0.09 mm, i.e., three times the layer thickness of 30 microns. The printed parts are cut along the build direction (z-direction), and 3 microns are polished for microscopic analysis. The optical microscope supplied by Leica systems is used for analyzing the porosity.

Table 12: Process parameters.

Varied Parameter	**Values**
Power (W)	300, ***350***, and 400
Scanning speed (mm/s)	1200, 1400, ***1650***, and 1900
Hatch distance (mm)	***0.13***, 0.26, and 0.52
Layer thickness (mm)	***0.03***
Scanning strategy	Stripes
Rotation in layers (°)	67

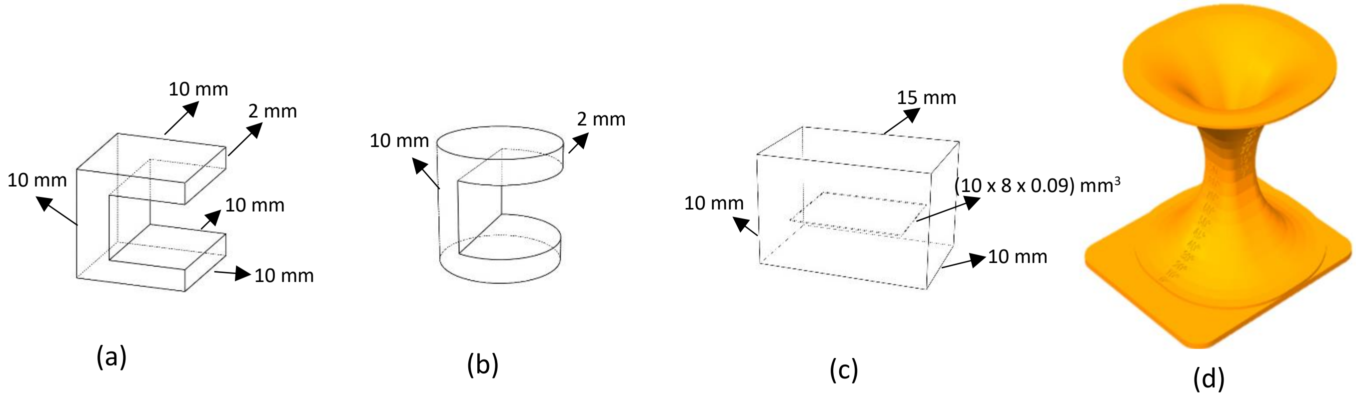

*Figure 65: Sketch of the specimens (a) cubic overhang (size 10*10 *10 mm3), (b) cylindrical overhang (diameter: 10 mm and height 10 mm), (c) specimen with inner groove, and (d) Benchmark part (125*125*775 mm3).*

4.3.3. Definitions

- **Drift:** Non-uniformity in the melt pool signatures results in the “hotspots,” which are the areas where the signal's intensity is higher than the rest of the layer. These hotspots indicate drift and the areas of highest probability to generate real defects. Recently, Mohr et al. linked hotspots in the MPM layer to the final porosity in part using computed tomography [179]. Therefore, in our study, the whole layer is termed “Drift” if a hotspot is confirmed via the MPM visualization tool.
- **No-Drift:** The layer with no significant hotspots is termed a no-drift layer.
- **Labeled Data:** The layer for which the labels such as “drift” and “no-drift” are known.
- **Unlabeled Data:** The layer for which the labels, i.e., “drift” and “no-drift,” are unknown.
- **Balanced Dataset:** The dataset contains an equal number of data points for each label.

4.3.4. Training Data Preparation

Recently, the Machine learning approach has gained much attention in AM due to its capabilities to resolve the issue of big data and easy post-processability of the in-situ monitoring data. To perform supervised machine learning, the need for labeled data is vital. However, it is challenging to obtain ground truth-certified data for the AM parts as the drift in the process can be linked to many parameters [180]. Usually, expensive techniques such as computed tomography of the part are used to get a labeled dataset, commonly referred to as a certified dataset. This study created an artificially drift (overheating and lack of fusion) in the parts with special geometrical features and varying process parameters. The careful selection of the layers from the build parts (81 parts) and labeling it as ‘Drift’ and ‘No-drift’ is performed by analyzing the layers in the MPM software provided by the SLM solutions and statistical analysis. It is noticed that the hotspots layers show a right shift in the histogram compared to the layers without any hotspots. This relation led us to decide the mean and median for every layer's features. A balanced labeled dataset of 600 data points, which comprises an equal number of drift and no drift layers so that the biasing of the SVM model can be avoided, is prepared. Before preparation, the SVM classifier has to be optimized for best-fit parameters, as discussed in the next section.

4.3.5. Bayesian Optimization and Training of SVM Classifier

The best-fitting parameters are to be selected for the SVM classifier to increase the success rate of the classifier. A Bayesian optimization algorithm is used to find the best-suited hyperparameters for the model. A hyperparameter is an internal parameter of an algorithm that needs to be optimized. For example, in our case (SVM model), the box constraint, kernel function, and kernel-scale are the hyperparameters. These parameters can significantly influence the performance of the algorithm. Thus, optimization of the hyperparameters is advisable. However, optimization is difficult and time-consuming. Therefore, Bayesian optimization is well suited for classification and regression algorithms in machine learning. The Bayesian optimization algorithm minimizes the objective function $f(x)$ for x in a bounded domain. The $f(x)$ can be stochastic or deterministic, which means it can return different results for the same point x. The overall working principle of Bayesian optimization can be found elsewhere [181], [182].

Table 13: The performance and accuracy % of the different hyperparameters.

Linear SVM	94.2 %
Quadratic SVM	93.8 %
Cubic SVM	78.7 %
Fine Gaussian SVM	95.5 %
Medium Gaussian SVM	93.5 %
Coarse Gaussian SVM	91.0 %

The cross-validation of the optimized SVM classifier is performed on the training dataset. The whole dataset is partitioned into 70 % and 30 % sub-datasets to cross-validate and check the performance of different hyperparameters of the SVM model. The performance and accuracy % of the different hyperparameters are tabulated in Table 13. It can be seen that the fine gaussian SVM has the highest accuracy with a cross-validation success rate of 95.5 %. So, a fine gaussian hyperparameter to train our SVM classifier is used for our dataset.

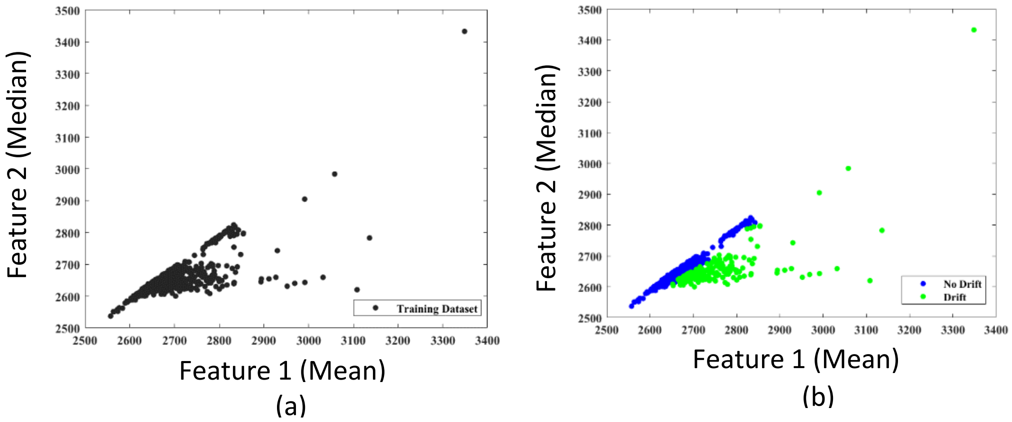

(a) (b)

Figure 66: (a) The un-clustered training dataset, and (b) labels predicted by the trained fine gaussian SVM classifier model.

Finally, the SVM classifier is trained on the whole dataset, as shown in Figure 67a, and predicted labels are shown in Figure 67b. Further, testing of the SVM classifier is performed using the different datasets (which are not used during training), as discussed in the results section.

4.3.6. Results and Discussions

The Receiver Operating Characteristic- Area under the curve (ROC -AUC) is analyzed to check the classification performance at different thresholds. ROC represents the threshold probability of the classifier, and AUC indicates the separability of the classifier, i.e., how well the classifier can distinguish between different classes. The higher the AUC, the better is the model separability. ROC curve is plotted between TPR (True positive rate) vs. FPR (False positive rate). The ROC curve is plotted for the model, as shown in Figure 68. The threshold probability is 95.5 % (marked by an asterisk (*)), and the AUC for the model is 98.53 %. In other words, the proposed model is 98.53 % capable of allocating each data point with the correct label.

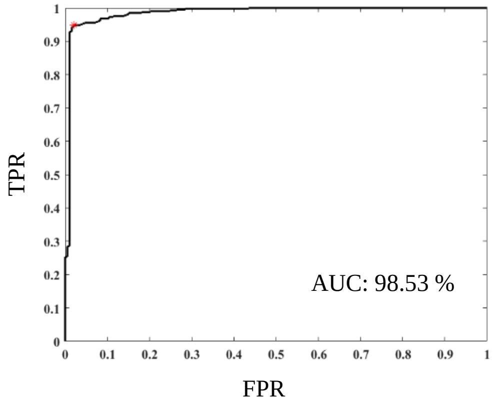

Figure 67: ROC-AUC curve for the trained SVM classifier on 600 training data.

Overheating Drift

The trained SVM classifier is tested for the overheating samples. The feature dataset (mean and median) is prepared for two different overhang samples (Figure 69a and 69b), which failed due

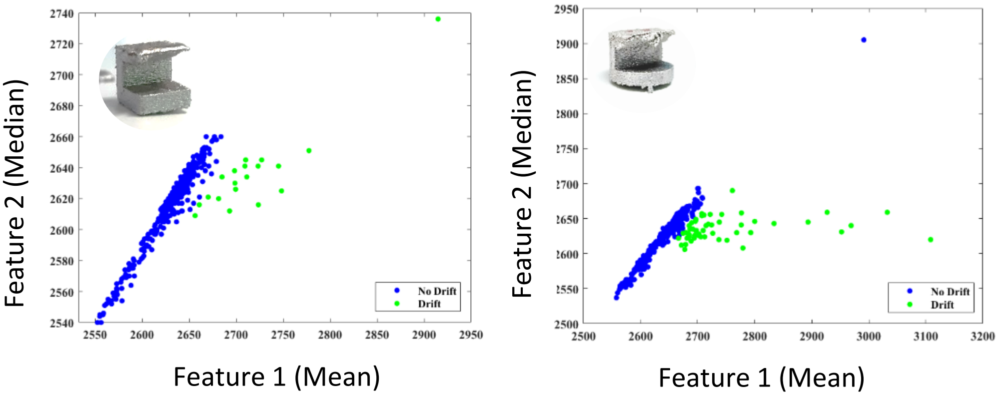

(a)

(b)

Figure 68: SVM model predicted labels for (a) cubic overhang specimen, and (b) cylindrical specimen.

to the overheating of the layers. The specific samples are used for the case study as the location of the overheating drift is known and can visually be verified. The prepared feature dataset is passed to a trained SVM classifier, and labels are predicted, as shown in Figure 69. For the cubic over-hang sample, the layer numbers from 305 to 379 are labeled as “drift,” which can be visually verified (printed part is shown in the top left corner of Figure 69a). The failure of the particular layers is due to poor heat transfer due to the absence of the support structure for the overhang part. Similarly, the labels are predicted for the cylindrical overhang part (Figure 69b) and are in conjunction with the visual inspection of the part.

Lack of Fusion Drift

Lack of fusion is the most common defect in the SLMed parts, which results in internal porosity in the final part. The detection of internal porosity is a challenging task and often requires expensive techniques such as computed tomography. We prepared samples that will lead to internal porosity in the final part, and the location of the porosity is known to check the trained SVM classifier for lack of fusion defect. The feature matric (mean and median) for the lack of fusion part, as shown in Figure 66c, is prepared and passed to the trained SVM classifier. The SVM classifier predicts the labels for each layer, as shown in Figure 70a. The three layers numbered 150, 151, and 152 are predicted as “drift,” which corresponds to the sample's location of porosity. The optical micrograph also verifies the same, as shown in Figure 70b. Therefore, it can be concluded that the trained classifier works well for the presented case studies. However, it shall be noted that the model's effectiveness for other types of drifts shall be studied in the future.

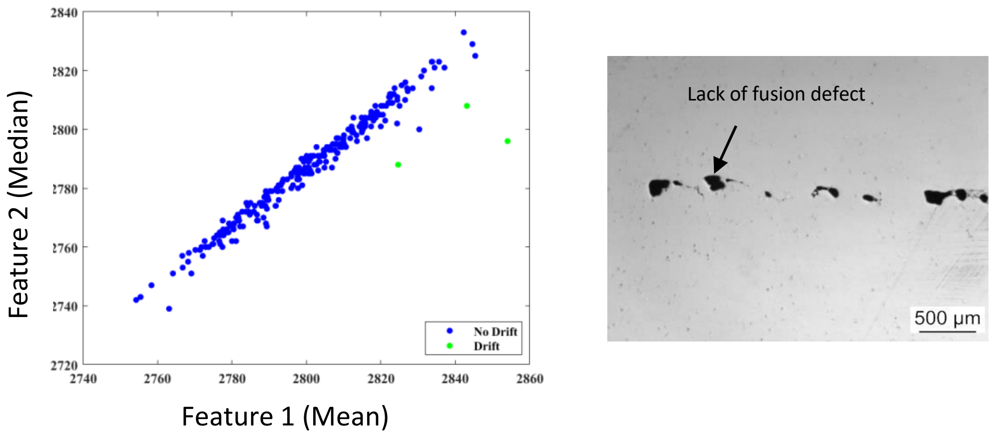

(a) (b)

Figure 69: (a) Predicted labels for the lack of fusion defect, (b) optical micrograph of the defect.

Case Study: Benchmark Part

The two linear SVM classifiers for Photodiode 1 and Photodiode 2, respectively, are trained on the certified training dataset, as discussed in section 4.3.5. The mean and median of each layer are treated as the input features for the trained SVM classifiers. The SVM classifiers predicted the two class labels, i.e., “Drift” and “No-Drift,” for each layer for the respective photodiode, as shown in Figure 71 (a,b). The layers numbered 2436, 2412, 2498, 2541, 2542, 2552, 2560, 2561, 2562, 2563, 2571, 2572, and 2573 are marked as drift layers for photodiode 2, whereas only two layers, i.e., 2541 and 2561, are marked as drift layers for photodiode 1. These predicted last layers lead to failure of the part, as shown in Figure 71c. As presented in the previous section 4.1, the spectral detection range of both photodiodes is different. Therefore, it can be concluded that based on the type of material, one photodiode is more sensitive compared to another for specific materials, i.e., low and high melting materials.

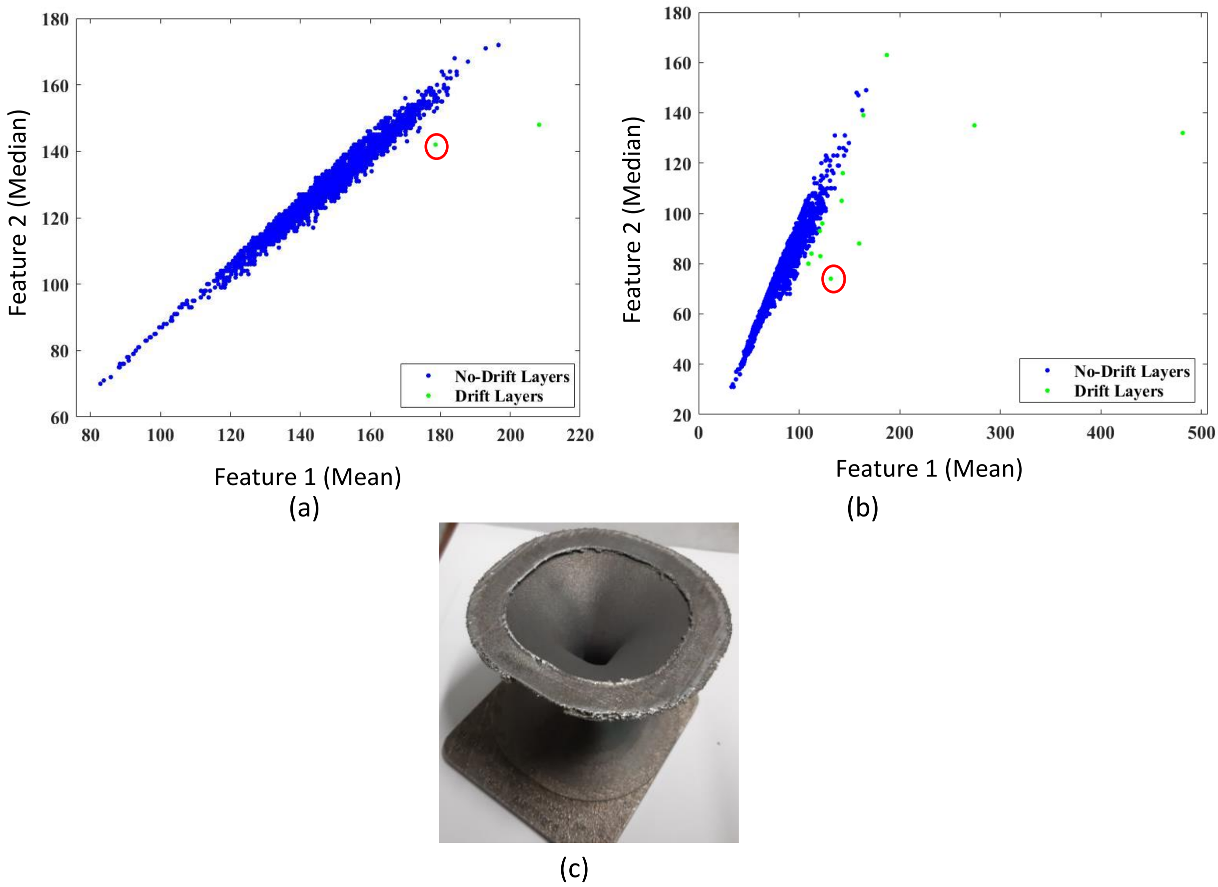

Figure 70: SVM classifier predicted labels for benchmark part for (a) photodiode 1, (b) photodiode 2, and (c) printed benchmark part.

As, we have seen in the above example, the sensitivity and data distribution are different for two ADCs. Also, it effects the overall efficiency of the SVM classifier, leading to detection of lesser drift layers for ADC1 than ADC2. Thus, the need for alternative method to detect drift layers at global scale effectively is must. We have presented a statistical based method in section 4.6 to find the drift layers at global scale, which can be better alternative to SVM classifier limitations.

4.4. Data Analytics: Local Scale

This section discusses the possibility of indicating the exact location of the probable drifts within the layers. As discussed in the last section, with the help of a supervised learning model such as SVM, potential drift layers are identified. Still, identifying the exact location is crucial to monitor the process more efficiently. For this, we have used the LSTM autoencoders (LSTM-AE).

4.4.1. Materials and Parts

Gas-atomized Ti6Al4V spherical powder with a particle size of 20-63 µm and mass density of 4.43 g/cm³ is used on the SLM 280^{HL} machine. The test samples are manufactured as a combination of two cubes where the bottom cube with a size 15*15*10 mm^3 is manufactured with optimized parameters (also highlighted in Table 14). In contrast, the top cube with 15*15*10 mm^3 is manufactured with varied VED based on laser power and scanning speed. As Zhou et al. [183] showed that the different power and scanning velocity combinations can create different zones with varying porosities. Figure 72 shows the 5 different zones based on the laser power and scanning velocity where zone 1 is low laser power—low scanning speed area, zone 2 is low laser power—high scanning speed area, zone 3: high laser power—high scanning speed area, zone 4: high laser power—low scanning speed area, zone V: suitable parameter area. The varying parameters are listed in Table 14.

Table 14: Process parameters used for Ti6Al4V samples (Optimized parameters are marked in bold).

Parameter	**Value**
Laser power (W)	150, 225, 300, **375**
Scanning speed (mm/s)	800, **1000**, 1200, 1400
Layer thickness (mm)	**0.03**
Hatch distance (mm)	**0.12**
Scanning strategy	Stripes with 10 mm and 67° rotation in consecutive layers

The specimen is scanned using a lab-based system at PLACAMAT (UMS 3626, Pessac, France). The facility used is a GE VTomex-s with a xs-180-nf transmission source, a diamond target, and the scan parameters are: 90kV 200µA with no filter. The 1800 projections for a 360° rotation are recorded using a binning factor of 1 and an exposure time of 1 second (total scanning time of two hours). The final voxel size is 9 µm. Tomographic reconstructions are performed using phoenix-datos-x software with default parameters. The visualization, the primary image treatments, and the 3D structural measurements are performed using ImageJ software. In this study, we chose one sample for CT scan based on the visual inspection and the sample which showed the highest visible variability in the quality.

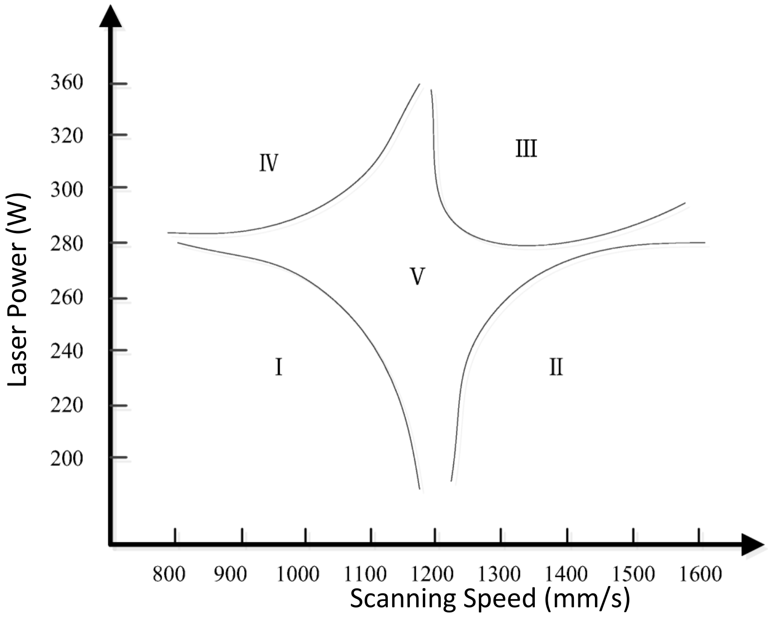

Figure 71: Process window for SLM Ti-6Al-4V powder [183].

4.4.2. Pre-Processing of the Data

This section discusses the methodology used to pre-process and prepare the MPM dataset for training the LSTM-AE. For pre-processing, the characteristics of the principal component analysis are used.

Principal Component Analysis (PCA)

Principal component analysis (PCA), a dimensionality reduction method, is used for pre-processing the raw MPM data. Consider an (m, n) data matrix X where m is the number of melt pool points, and n is the number of parameters (ADC1 and ADC2 in the present case).

Based on the sample mean and covariance, X is scaled to zero mean and unit variance to eliminate the effect of magnitude difference of the 2 parameters, i.e., ADC1 and ADC2.

PCA finds a set of linearly uncorrelated variables, i.e., called “principal components (PCs),” to represent the original information provided. The transformation for the input data matrix X can be expressed as: $T = XP$, where T represents a (m,n) matrix which denotes the scores of the data matrix X, and P is a (n,n) matrix which expresses the loading matrix, also called coefficients which represents the basis vectors of the transformation. So, the PC score t_i, where i represent the number of columns of the T matrix $(1 \leq i \leq m)$, can be regarded as the principal component representation for a given set of original variables. The PCA tries to find the transformation in such a way that the principal component t_i have the highest variance. The variance of PCs is nothing but the eigenvalues λ_i of the covariance matrix of the input data matrix X. Coefficients vector p_i therefore represents the eigenvector [184].

By default, the PCA function in MATLAB uses the singular value decomposition algorithm.

Hotelling's T-Squared Statics

Hotelling's T^2 statics is a statistical measure of the multivariate distance of each observation from the center of the whole dataset. In other words, it is the sum of squares of the standardized scores, i.e., Mahalanobis distances [185]. The hotelling's T^2 statics or Mahalanobis distance can be expressed as:

$$T^2 = (t_i - \mu)\Sigma^{-1}(t_i - \mu)'$$

Equation 14

Where t_i μ and Σ is is the PC score, mean, and covariance of the matrix T, respectively. The obtained hotelling's T^2 statics is then multiplied by the PC coefficient.

To give an example, Figure 73 shows the raw signal and pre-processed signal using PCA and hotelling's T^2 statics for ADC2 as discussed above.

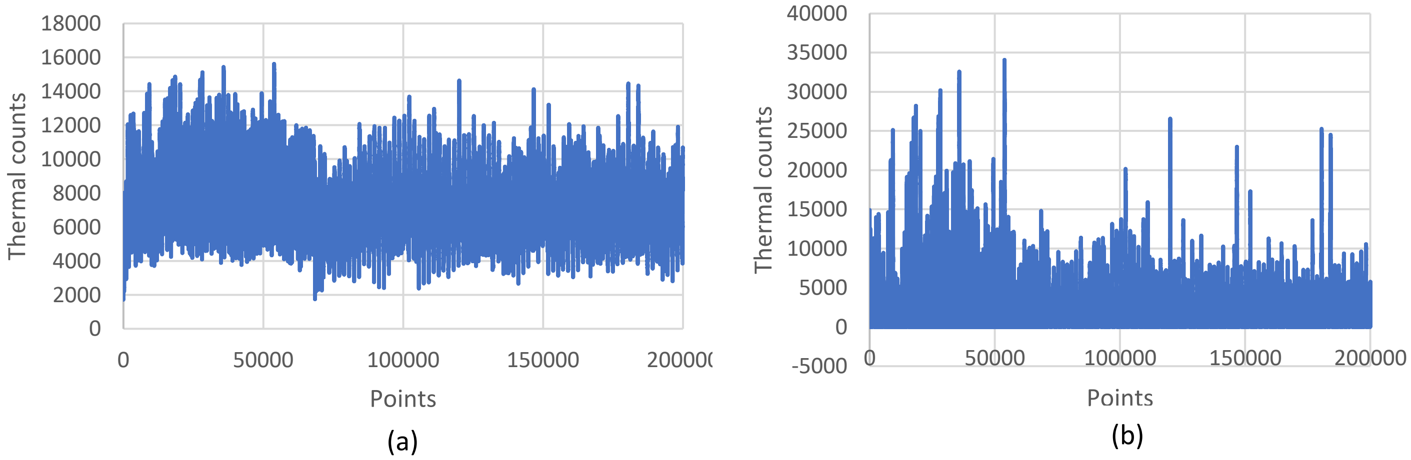

Figure 72: Example of (a) raw, and (b) pre-processed ADC2 signal for layer 31.

4.4.3. Removal of Outliers.

After pre-processing, it is vital to remove the outliers in the signal, if any. Therefore, we used MATLAB built in-function called “Hampel Filter” to identify and remove the outliers. The function computes the median of a moving window that contains the sample and its six neighbors, three on each side. For each sample, standard deviation (σ_i) along the median window is calculated using the median absolute deviation. If the sample differs more than 3σ, it is replaced by the median.

Mathematically it can be expressed as:

- Consider a sequence of samples as $x_1, x_2, x_3 \dots x_n$ and a sliding window of length k
- Then median m_i will be: $median(x_{i-k}, x_{i-k+1}, x_{i-k+2}, x_i, x_{i+k-2}, x_{i+k-1}, x_{i+k})$ and standard deviation be: $\sigma_i = Kmedian(|x_{i-k} - m_i|, \dots |x_{i+k} - m_i|)$ where K= 1.4826. $\frac{\sigma_i}{K}$ is called median absolute deviation (MAD).
- And if the sample x_i is such that $|x_{i+k} - m_i| > 3\sigma_i$ it will be treated as an outlier and will be replaced with m_i.

4.4.4. Data Selection for Model Training

For MPM systems in general, it is easy to collect a considerable amount of data than to accurately know their ground truth labels. Correctly labeling the MPM data is susceptible to process ambiguity as little is known about the extent or size of the drift. Moreover, process drifts are rare events, and having prior knowledge about the drift's size, shape, and extent is a complicated task. Therefore, the attention has been shifted from anomalous behavior to normal behavior of the melt pool, for which a large amount of data is present. The motivation behind the study is that identifying or training the model for normal behavior of the melt pool will help detect the anomalies or drifts that have not been observed before.

Therefore, the results from CT scans and the MPM viewer are considered to confirm this. Only the layers which don't have variability and absence of any possible porosity are considered. The obtained layers are then passed to the LSTM autoencoder (LSTM-AE). In our study, we have used multiple layers based on CT and visual inspection. For example, layer number 31 is used as one of the training layers, with a standard deviation of 1202 and 1447 thermal counts for ADC1 and ADC2, respectively. The CT scan for layer 31 is shown in Figure 74.

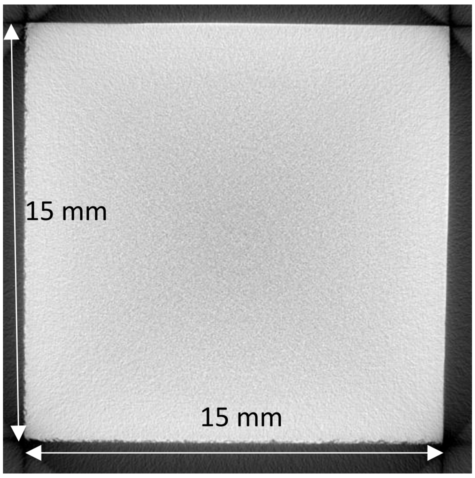

Figure 73: CT scan corresponding to layer 31 (approximately) and its raw data for ADC2 is shown in Figure 73.

4.4.5. Architecture of LSTM

We used LSTM autoencoders (LSTM-AE) architecture to detect the MPM data's drifts. The pre-processed matrix ((M*N), M= no. of data points, N= Photodiodes) is passed as the input to LSTM-AE, which is trained over the melt pool signals via gradient descent to minimize the reconstruction error between the original signal and the reconstructed signal. The autoencoders consist of two parts, i.e., encoder and decoder. The encoder maps an input vector or matrix X to a low-dimensional hidden representation h or compressed input representation. Whereas the decoder correspondingly generates an estimation X' of the input matrix or vector X (reconstruction of the input from the core constituents preserved during compressing). The rationale behind the LSTM-AE architecture is that the model is trained for a typical MPM dataset, and drift is detected based on the resulting reconstruction error.

The encoder and decoder units of the autoencoder are based on the LSTM units. LSTM is one of the types of recurrent neural networks (RNN) that can integrate the temporal data into the model in a hidden vector and use it as a memory for past information. The schematic of LSTM-AE is shown in Figure 75.

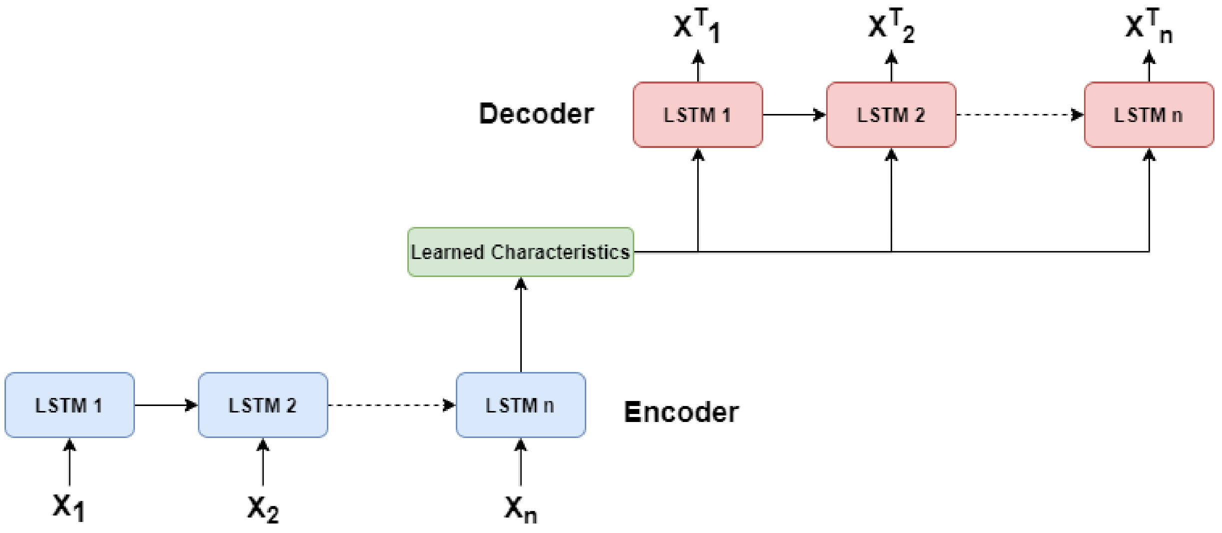

Figure 74: Schematic of LSTM-AE.

Encoder: The input data is given by $X = \left(x^{(1)}, x^{(2)} \dots x^{(N)}\right)$, where $x^{(i)} = \left(x_1^{(i)}, x_2^{(i)} \dots x_T^{(i)}\right)$. This means that for each i $(1 \leq i \leq N)$, there is a d-dimensional time-series sequence with T timesteps each. In our MPM, d equals 2 (photodiode 1 and 2). We use RNN to process the pre-processed MPM data sequence and extract the sequential information as

$$C_t' = Relu(W_c x_t + R_c h_{t-1} + B_c)$$

Equation 15

Where C_t': memory state, x_t: input vector, h_{t-1}: output vector from the last step and W_c, R_c, B_c are input, recurrent, and bias weights. ReLU is used as a non-linear activation function.

The input sequence is passed to the encoder part of the LSTM network that encodes it and updates the hidden state. The final output of the encoder is mathematically given by:

$$h_t = \sigma_\phi^e(x_t, h_{t-1})$$

Equation 16

Where h_t = output of i^{th} LSTM encoder.

Decoder: The characteristics obtained from mapping the MPM signal to lower-dimensional embeddings from the last encoder steps are used by the decoder to reconstruct the original signal. In other words, the output of the previous encoder is the input for the decoder network, which can be expressed as:

$$h'_t = \sigma^d_\varphi(h_t, h'_{t-1});\ x'_t = \sigma(h'_t)$$

Equation 17

Where φ represents a set of decoder parameters and x'_t is the reconstructed input.

Mean absolute error (MAE) is used to calculate the reconstruction error, which is given as:

$$MAE = \frac{1}{n}\sum_{i=1}^{n}|x_i - x|$$

Equation 18

The MAE must update the encoder and decoder parameters and calculate the anomaly score.

During training, the focus of the LSTM-AE is to learn the expected behavior of the MPM data, not the drifts. So, during prediction, a slight deviation from the MPM data's normal behavior will increase reconstruction error, i.e., MAE value. Therefore, monitoring the MAE value increase would help identify the probable drift area within the layers.

Table 15 shows the LSTM-AE architecture used in this work. The first couple of the LSTM network layers are the compressed representation of the input data, i.e., encoder, and the final output layer gives input reconstruction.

Table 15: LSTM-AE architecture used in this study.

Layer (type)	Output Shape	Parameter
input_1 (Input Layer)	(None, 1, 2)	0
lstm_1 (LSTM)	(None, 1, 16)	1216
lstm_2 (LSTM)	(None, 4)	336
Repeat_vector_1	(None, 1, 4)	0
lstm_3 (LSTM)	(None, 1, 4)	144
lstm_4 (LSTM)	(None, 1, 16)	1344
time_distributed_1	(None, 1, 2)	34

We then instantiate the model and compile it using Adam as our neural network optimizer and mean absolute error for calculating our loss function.

4.4.6. Training and Validation

The pre-processed MPM data is normalized to zero mean and unit variance. The selected, trained data is divided into the following sets: Training, validation, and test sets in a ratio of 70:20:10.

The weights of the LSTM-AE are updated via stochastic gradient descent, and an Adam optimizer is used to speed up the training process. The training is performed for 20 epochs. A training and validation loss of 0.0071 and 0.0069 is achieved, respectively.

Loss Distribution

By plotting the distribution of the calculated loss in the training set, we can determine a suitable threshold value for identifying an anomaly. This can ensure that this threshold is set above the "noise level" so that false positive are not triggered.

Based on the above loss distribution as shown in Figure 76 for our case, we set a loss threshold value of 0.065 for flagging an anomaly. Then we calculate the reconstruction loss in the training and test sets to determine when the sensor value drifts from the expected behavior.

After training, the validation set is passed to the trained model to get the reconstruction error (RE). The obtained RE is used to calculate the parameters of a normalized distribution ($\mu \Sigma$) using maximum likelihood estimation (MLE). Finally, the anomaly score for a datapoint $x_t^{(i)}$ can be computed using μ and Σ as follows:

$$a_i = (e_i - \mu_t)^T {\Sigma_t}^{-1} (e_i - \mu_t)$$

Equation 19

Where a_i: anomaly score, e_i: reconstruction error, μ_t: mean, and Σ_t: variance for time series t in data matrix X, respectively.

An anomaly score threshold is also calculated using the validation set. If the new sequence has a greater anomaly score, it will be regarded as drift or anomaly; if less, it will be considered a normal signal.

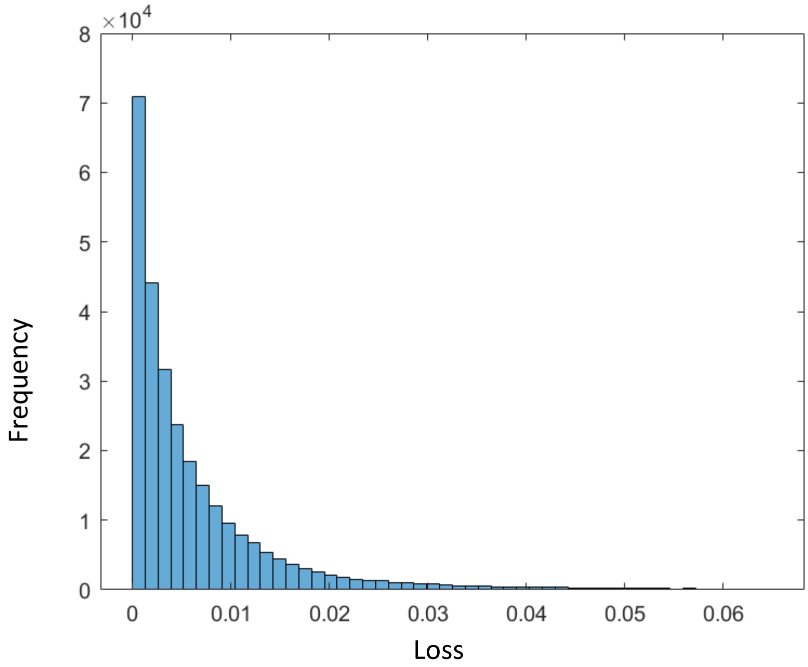

Figure 75: Loss distribution obtained during training.

4.4.7. Case Study

The above-discussed methodology of pre-processing the data using the multivariate statistics method and then training it using the LSTM-AE to predict the drifts points in the respective layers is studied and verified using a tomography sample study. The CT scan cross-section of the observed sample is depicted in Figure 77 along with the printed sample. It can be seen clearly that there are three different regions in the sample: the bottom region with big visible porosities, a stable and less porosity region, and the region with geometrical distortions. So, this variability presents a good case study to show the validity of the proposed methodology. The proposed model successfully identified the so-called “Hotspots” or high probable drift regions. The number of predicted anomaly points per layer is plotted in Figure 78. Similar to CT results and printed part, the obtained results also depicted the three distinct regions where the last layers comprise many hotspot points, which correlates with the geometric distortion region in the printed part.

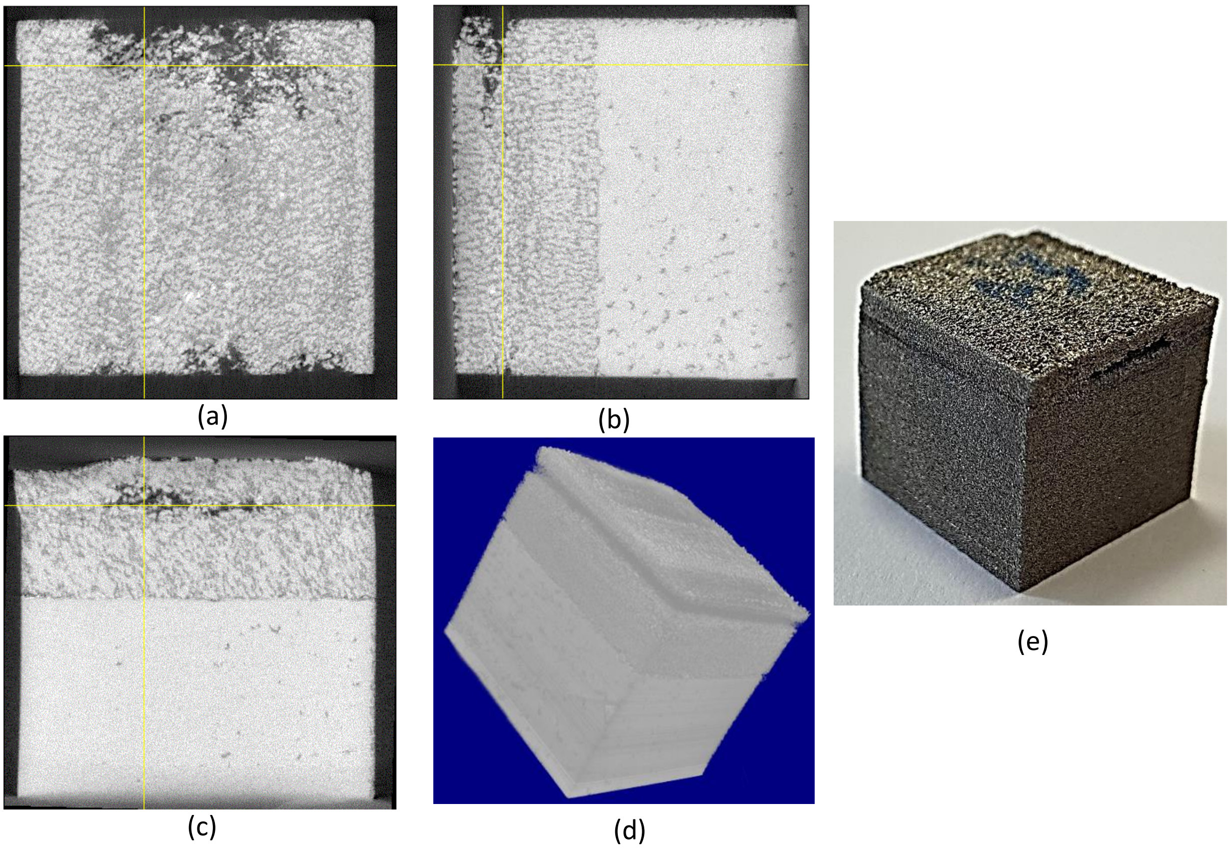
(a) (b) (c) (d) (e)

Figure 76: CT scan projections in (a) X-Y plane, (b) Y-Z plane, (c) X-Z plane, (d) Isometric, and (e) as-printed sample.

Further investigations of the drift layers show that for the geometrically distorted region, i.e., region 3, the MPM viewer images mark the hotspot's presence, which can also be verified with the CT scan that shows the presence of porosity. And the exact location of this hotspot is

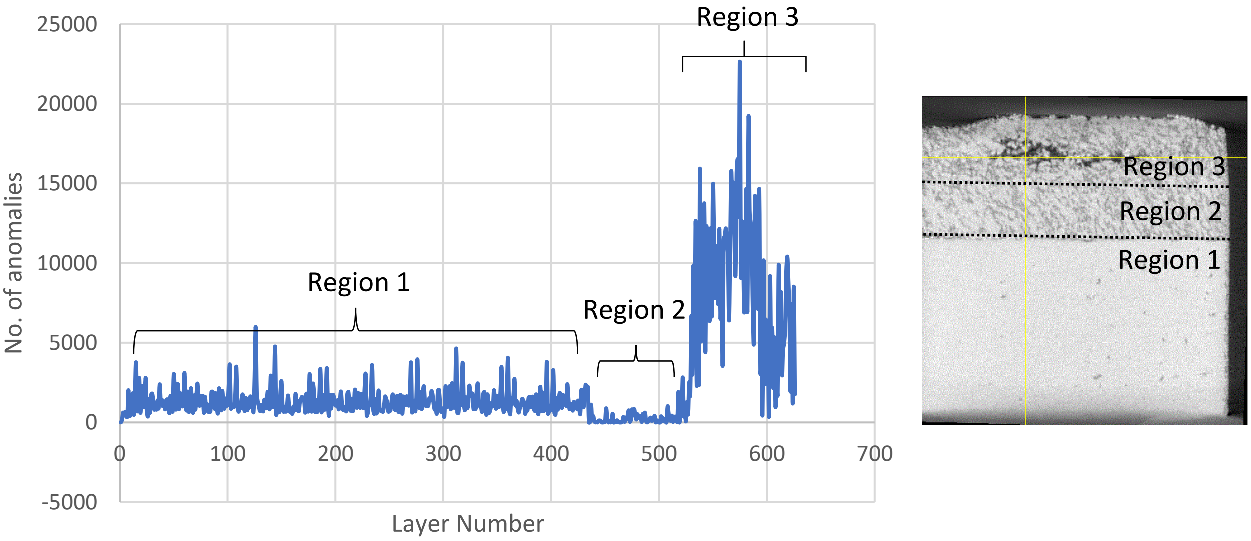

Figure 77: Anomalies predicted by proposed model Vs layer number.

identified by our proposed method. Figure 79 shows the MPM values, CT scan image, and suggested model results for layer 575.

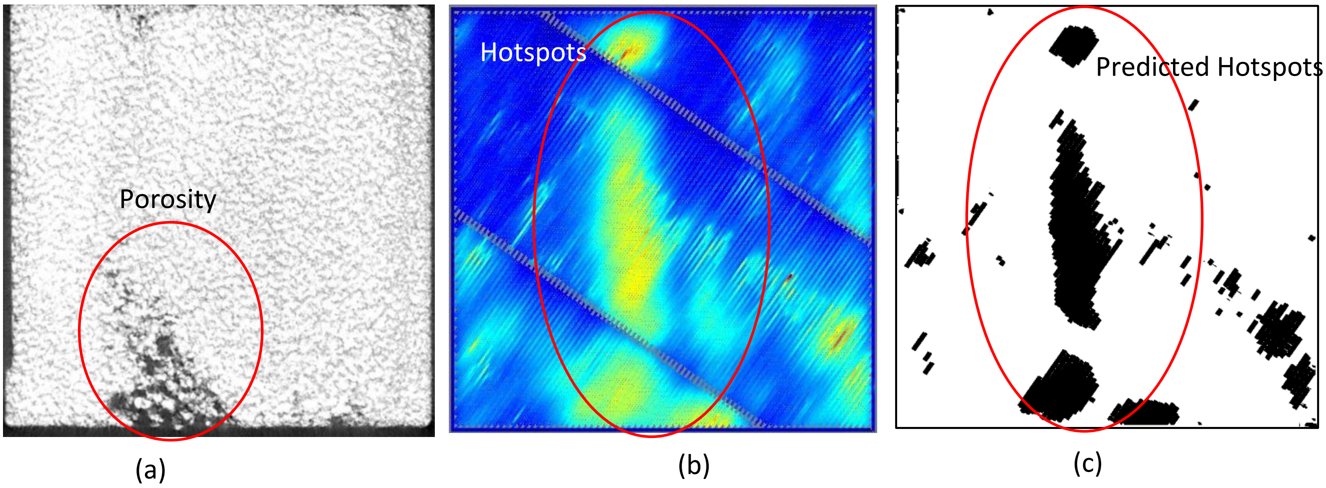

(a) (b) (c)

Figure 78: (a) CT scan, (b) hotspots shown by MPM viewer and (c) hotspot predicted by the proposed model for layer 575.

Interestingly, the geometrical distortion is strongly influenced by the change in powder bed spreadability, which is discussed in section 4.3.

The proposed methodology can help extract the key characteristics from the MPM data and plot the overall part health at a global and local scale. This methodology can help reduce the enormous size of the data without compromising the critical aspects related to the printed part. For example, Figure 80 shows the 3D picture of the anticipated hotspots in each layer. It shall be noted that the 3 distinct regions are identifiable, as shown in Figure 80a.

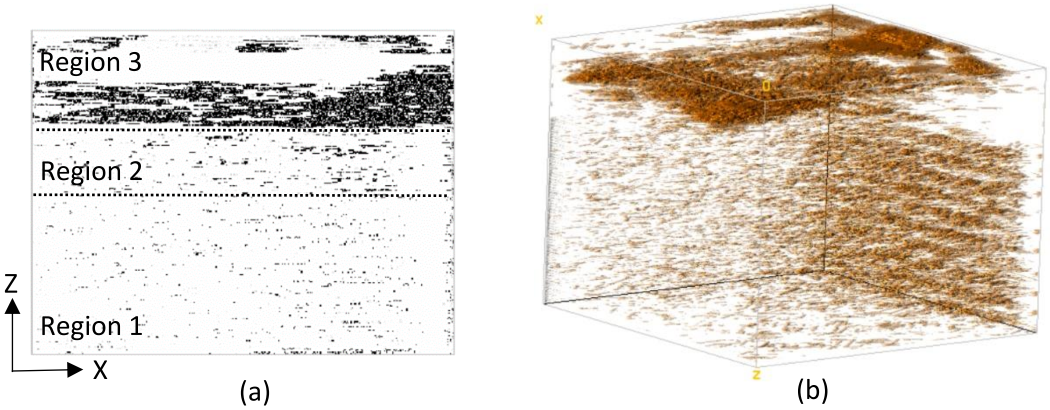

(a) (b)

Figure 79: (a) X-Z projection (Hot spots are depicted by black points) and (b) isometric 3D projection (hotspots are marked by dark yellow) of the hotspots predicted from the proposed methodology (Figures are not subject to scale).

4.5. Conclusions

The robustness of the proposed methodology is that it is trained for the normal behavior of the MPM data, and it is defined for specific process parameters and materials. As we have seen in the sensitivity analysis of the MPM, the MPM module is significantly influenced by the volumetric energy density and material. Therefore, based on the author's experience, it can be concluded that a more robust and fast method is required to be trained for specific process parameters and material. The proposed method provides that option. The steps that need to be followed to train the model for new material or process parameters are shown in Figure 81.

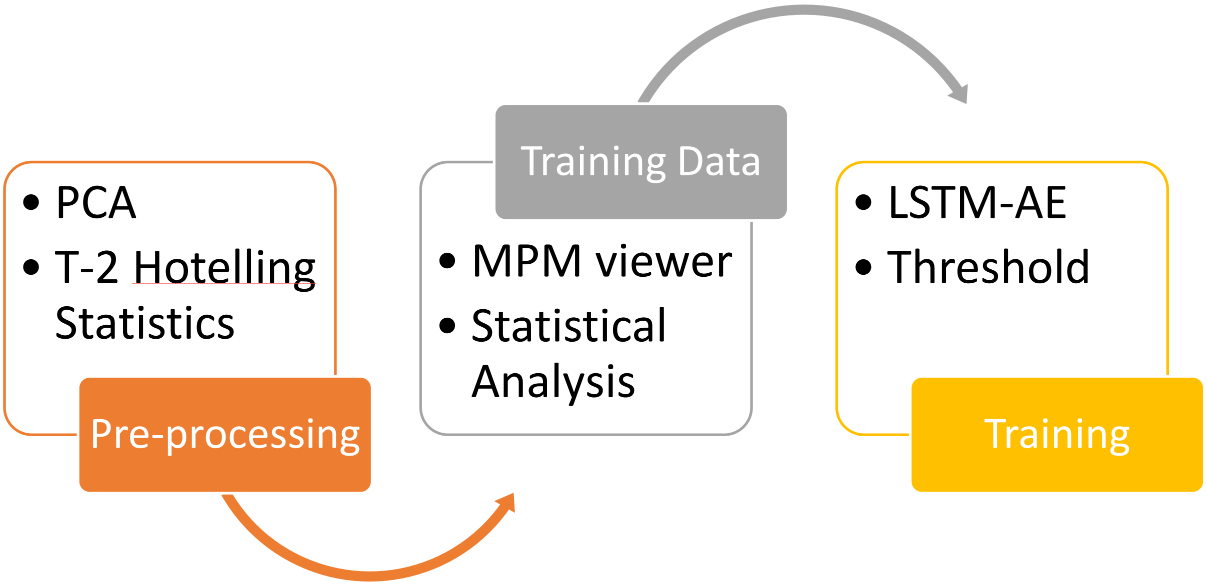

Figure 80: Schematic diagram of the proposed methodology.

Although the significant drawback associated with the proposed method is that obtaining the ground truth dataset for training is complex and prone to human errors, it is advisable to use the MPM viewer and statistical analysis to select the layers free from anomalies or anomalies drifts.

The next step is to find the root cause of the melt pool anomalies, i.e., “Hotspots.” Therefore, it is essential to monitor the L-PBF process at another step, i.e., the Powder bed spread step. Thus we have discussed using computer vision algorithms to monitor and check the quality of powder bed spread using LCS system as presented in Chapter 5. Also, the link between the powder bed spread and melt pool emissions is established.

4.6. Statistical Approach: Global Scale

One of the biggest disadvantages of ML-based approaches is that it requires a labeled dataset for training, and obtaining labels for MPM data can be a time-consuming and challenging task.

Therefore, the statistical approach can be helpful to have a quick overlook of the global health of the part. Here, we discussed one of the statistical approaches called "Average True Range (ATR)." J. Welles Wilder formally develops it to monitor the volatility in the trade and commodities. The measure of volatility can indicate the melt pool stability within the layer. It can be expressed as:

$$TR = \max(high, close_{prev}) - \min(low, close_{prev})$$

Equation 20

Where TR: True range, high, low, and $close_{prev}$ are the highest, lowest, and last closing values in a given interval period. At any time, t, ATR can be calculated as:

$$ATR_t = \frac{ATR_{t-1} \times (n-1) + TR_t}{n}$$

Equation 21

Where n is the number of sample periods (in our case, n=14), ATR values are calculated on the preprocesses data as elucidated in section.

Example 1: Figure 82 shows the variance of the ATR for the benchmark part (See Figure 71c). It can be observed that the volatility of the melt pool is higher for the last layers due to overheating. The two single peaks could be outliers.

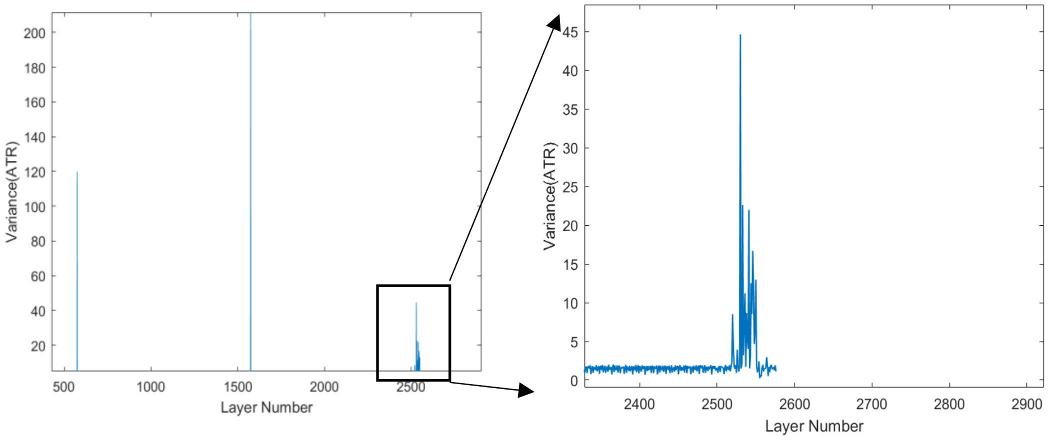

Figure 81: Volatility plot (ATR) for the benchmark part shown in Figure 71c.

Example 2: Similarly, for the overhang sample, it can be seen in Figure 83 that the volatility is higher for the last overheated layer.

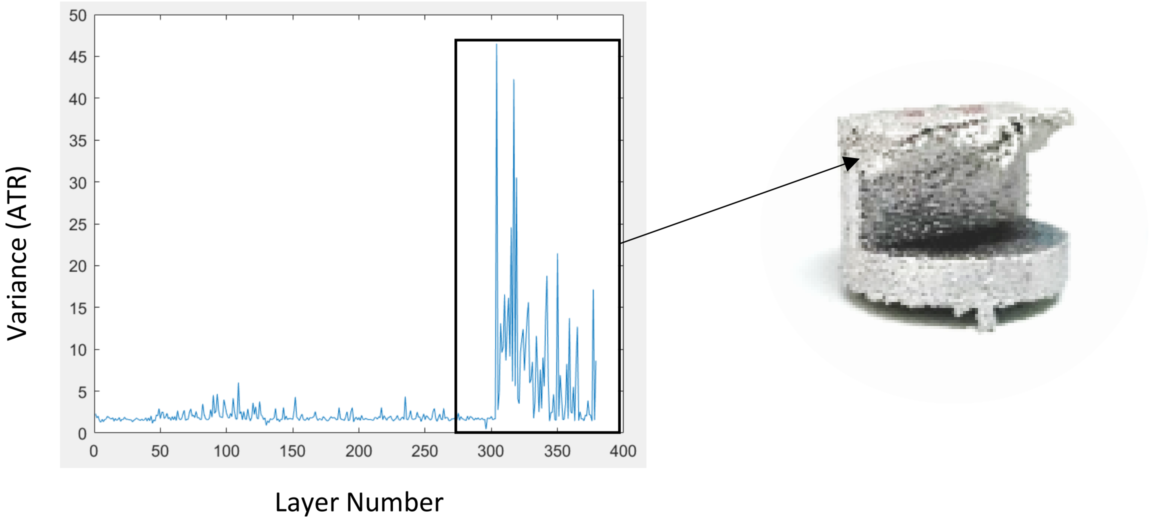

Figure 82: Volatility plot (ATR) for the overhang part.

Although the results are similar to the ML-based method, the statistical analysis is fast, and no labeled dataset is required. This method provides an alternative to ML-based models.

Example 3: Similarly, for the Ti6Al4V part, it can be seen in Figure 84a that the volatility is higher for the last overheated layer (also marked in Figure 84b). The visual inspection of the part also agrees with the calculated volatility graph. It can be concluded that the higher volatility in the last layers is related to the presence of so-called "Hotspots." The exact location of the hotspots will be identified in the following sections. A CT scan of the part is also obtained to obtain a better qualitative comparison. The obtained results are in conjunction with the CT scan and as-built part quality (Figure 77).

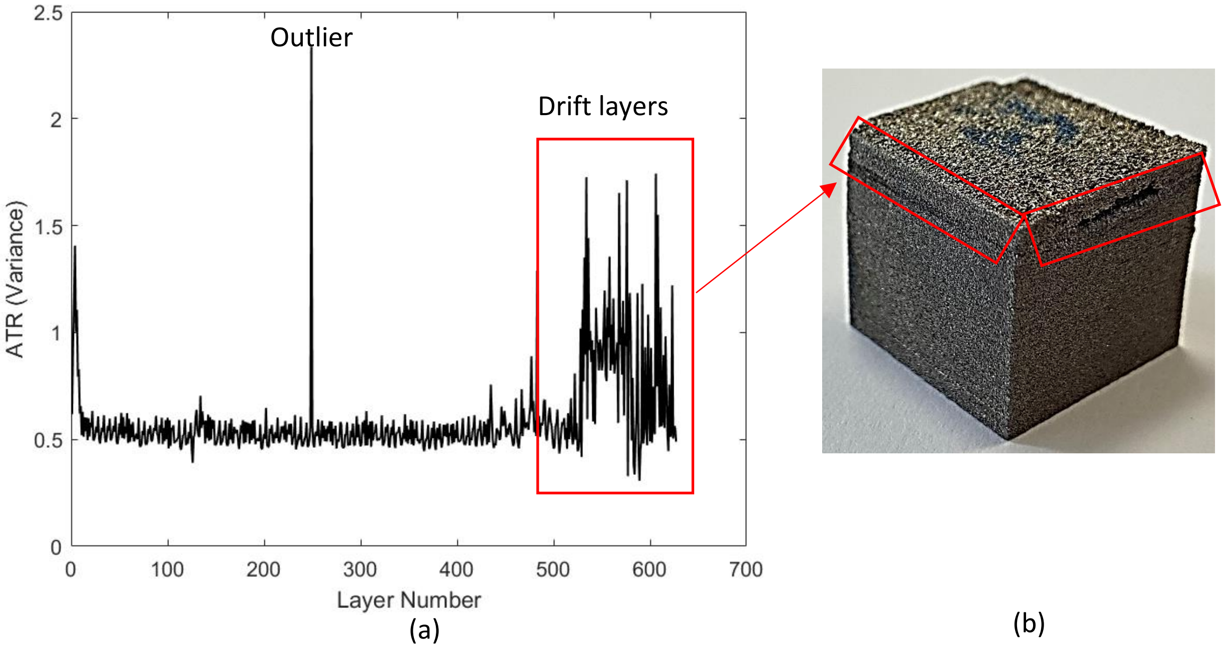

(a)

(b)

Figure 83: (a) Volatility variance, and corresponding (b) as-built Ti6Al4V part.

The statistical analysis is fast, and no labeled dataset is required. This method provides an alternative to ML-based models to rapidly check the printed part's overall quality.

CHAPTER 5

Layer Control System (LCS)

> The SLM machine also allows the powder layers to be controlled before and after the laser exposure. Chapter 5 is focused on this monitoring control system called “Layer Control System (LCS)” and its operation using by CNN and computer vision models
>
> In this chapter, we exploit the Layer control monitoring system (LCS) supplied by SLM solutions. The LCS system is designed to capture the powder spread quality and indicate the uniformity in the powder bed. Although it is not directly related to the laser-material interaction, it captures the powder-bed's significantly essential characteristics, which eventually influences the laser-material interaction phenomena. For example, any local variation associated with the powder bed can influence the material-laser interaction environment, changing the melt pool morphology and affecting the melt pool emissions.
>
> In the end, we tried to interlink MPM and LCS data to better understating the SLM process and its influence on the part quality.

5.1. LCS Setup

The layer control system (LCS) installed on SLM 280^{HL} includes a visible range camera that captures each layer's images for pre and post-exposure. The chamber is illuminated with LEDs from the build chamber's sidewalls to maintain uniformity of light distribution on the overall build plate. The camera is placed outside on top of build chamber at a specific angle of 65o w.r.t normal direction of the build plate, as shown in Figure 60. The machine supplier performs the geometric correction of the captured images for the installed equipment. The camera captures a JPEG image of 1500*1460 px2 size covering an area of 280*280 mm2 of the build plate and neighboring region outside of the build plate that needed to be cropped before processing. The camera has a pixel size of 4.4 μm and a lens focal length of 9 mm.

5.2. Terminology

- *OK:* The "OK" label is used for the block (image patch), free from other considered anomalies such as Recoater Streaking, Uneven Powder Spread, Part Hopping, and Part Overheating.
- *Uneven Powder Spread:* The "Un-even Powder Spread" indicates the areas with non-uniformity in powder spread. Non-uniformity during powder spreading leads to a step-like feature in the powder bed spread, as shown in Figure 91c. Such anomaly can be caused due to recoater silicon lip failure, lack of powder in the recoater hob, and blockage in the powder delivery system.
- *Part Overheating or Local Overheating*: The "Part-Overheating or Local Overheating" is the part area that is distorted due to poor heat conductivity. The poor heat flow phenomenon is linked to the lack of proper support structures, connected to the bulk and powder material [186]. Based on simulations, Yang et al. reported that the overhanging surfaces are prone to overheating [187]. This anomaly is considered only for the post-exposure images.
- *Part-Hopping:* The part area above the powder spread and not fully covered by the powder spread is termed "Part-Hopping." This anomaly is considered only for the pre-exposure images. In the context of this study, the part hopping serves as cross-validation criteria for the anomaly "part-overheating" in the post-exposure images.
- *Recoater Streaking:* Recoater streaking is the horizontal lines observed in the powder bed images due to distortion of the soft silicone lip of the recoater. It is detected in post pre and post-exposure images.

5.3. Types of Machine Learning Models

Image classification using deep learning or machine learning algorithms has various levels of granularity through which algorithms learn to understand the images better. In computer vision (CV), there are limitations associated with each granularity level from fine to coarse. The different level of granularity levels can be defined as:

Image classification: It is a fundamental building block in CV, where algorithms give a discrete label to an image, assuming that there is only a single object in the image. The method presented in section 5.4 (using CNN) is an example. The main limitation of image classification is that it cannot detect multiple objects in the image.

Classification with localization: It is similar to image classification; the only difference is that it tries to localize the object in the image using a bounding box that can be identified or marked with numerical parameters.

Object detection: It is an extension of the image classification with localization. Here, object detection is not constrained to only one object but can classify and localize multiple objects in a single image.

Semantic segmentation: In semantic segmentation, classification and localization of an object on a pixel level. Each pixel of an image is associated with a class, and prediction is done for every pixel. Unlike previous methods, the output is not just the labels or bounding box but a high-resolution image classified by each pixel.

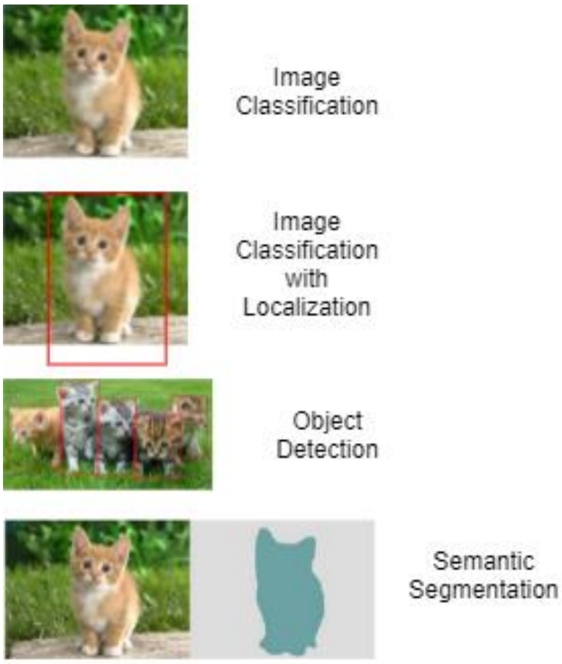

Figure 84: Types of computer vision models for image classification (Medium.com).

The graphical representation of the above-said methods is depicted in Figure 85. We have exploited the possibility of image classification and semantic segmentation for our study.

5.4. Approach 1: Image processing using CNN models

5.4.1. Theory

Convolutional Neural Network (CNN) Architecture

The convolutional neural networks are neural networks that use convolutional mathematical operations instead of general matrix multiplication. The input layer is a 150*150 grayscale image extracted from the pre-processed pre and post-exposure images, respectively. The input layer is then represented by a 2D pixels table when each box contains a number representative of the grayscale. A CNN network usually consists of an input layer, output layer, and multiple hidden layers. A hidden layer results from a convolution operation based on a multiplication operation between the numbers of 2D tables. There are four types of layers for a convolutional neural network: the convolution layer, the pooling layer, the ReLU correction layer, and the fully connected layer. The combination of these different layers and operations of the “batch normalization layer” is called block, as depicted in Figure 86. The detailed descriptions of the hidden layers are discussed in the following sections.

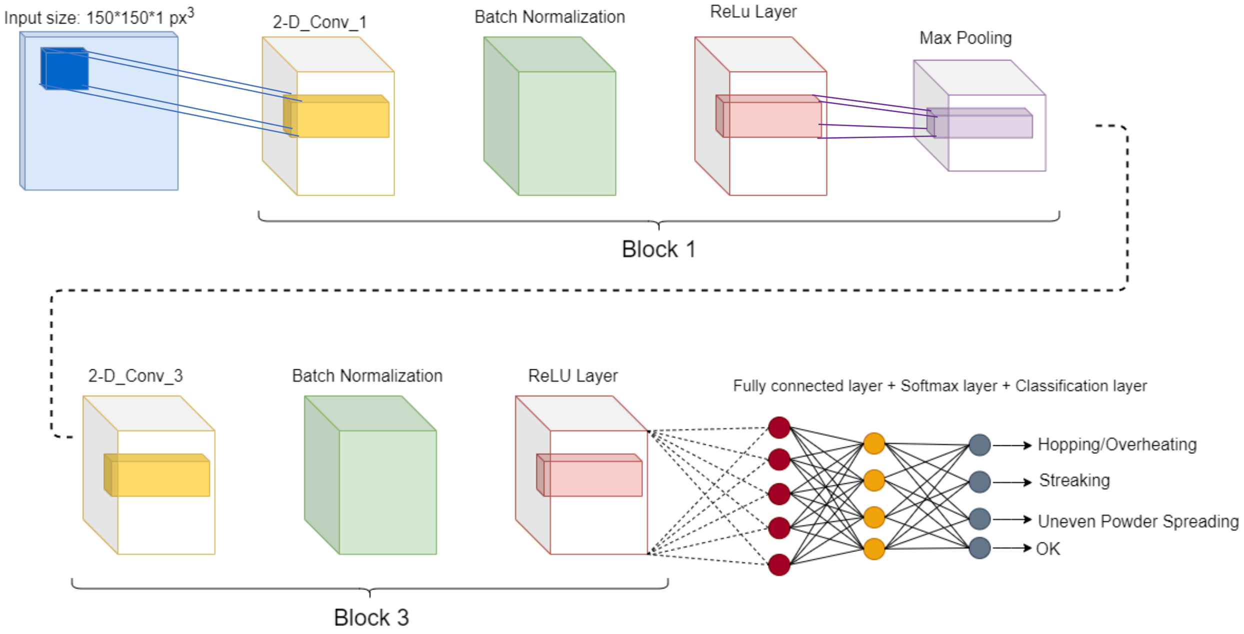

Figure 85: Schematic of the proposed convolutional neural network used in this study.

Convolutional Layer

The purpose of the convolution layer is to identify the presence of a set of features in the input images. To do this, we perform filtering by convolution: the filter matrix slides over the whole input volume, and the dot product between filter matrix and input volume is calculated for every spatial position [188] (Figure 87). The Mathematical expression of convolutional operation is as follows:

$$f_l^k(p,q) = \sum_C \sum_{x,y} i_C(x,y) \cdot e_l^k(u,v)$$

Equation 22

where, $i_C(x,y)$ represents an element of the input image tensor (I_C), which is element-wise multiplied by $e_l^k(u,v)$ index of k^{th} kernel of l^{th} layer. The output feature matrix of the k^{th} convolutional operation is expressed by:

$$F_l^k = [f_l^k(1,1), \dots f_l^k(P,Q), \dots, f_l^k(P,Q)]$$

Equation 23

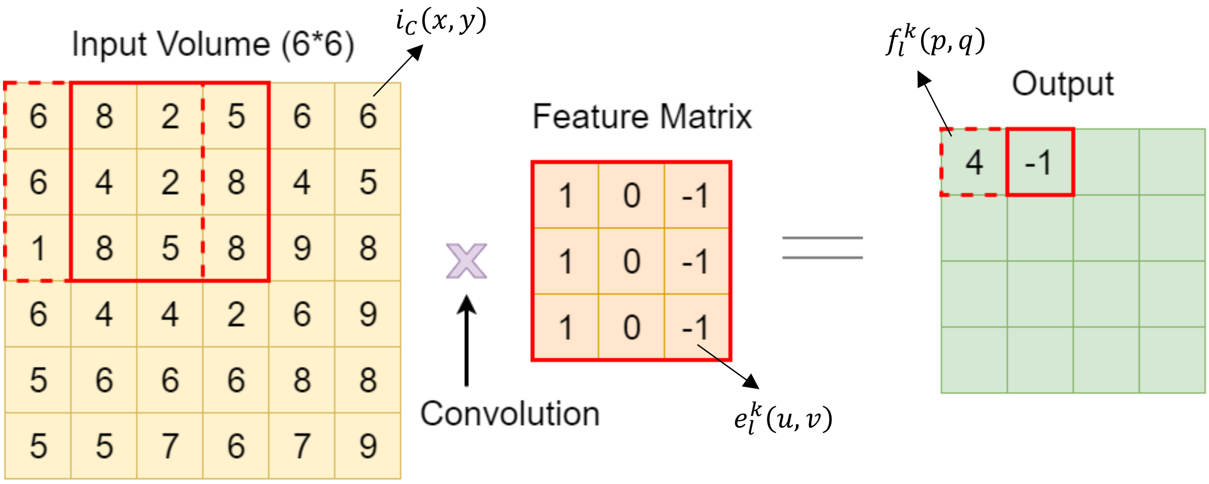

Figure 86: Example of calculation of a convolution layer.

Furthermore, the convolutional operation can be categorized into different types based on padding, the direction of convolutions, size, and type of filters [189].

Batch Normalization

The method of a batch normalization layer is used to refocus the values obtained for the convolution matrix and thus improve the CNN in terms of speed, stability, and reliability. It's based on reducing internal covariate shifts. The batch normalization unifies the distribution of feature map values by setting the distribution feature map values to zero mean and unit variance [190].

$$N_l^k = \frac{F_l^k - \mu_B}{\sqrt{\sigma_B^2 + \epsilon}}$$

Equation 24

N_l^k is normalized feature-map, F_l^k is input feature-map, μ_B is the mean, and σ is the variance of the feature-map for the respective mini-batch. The parameter ϵ is added to avoid division by zero and adds numerical stability to the function.

Pooling Layer

In summary, pooling is a method of reducing the size of an image while preserving the most important information it contains. The feature motifs resulting from the convolutional operation's output can occur at different image locations, but the approximate position of feature motifs is stored. Pooling operation, also called "down-sampling," sums up similar information in the neighborhood of the receptive fields and the outputs the dominant response within the local regions, which can be represented mathematically by [191]:

$$Z_l^k = g_p(F_l^k)$$

Equation 25

Where, Z_l^k represents the pooled feature-map for l^{th} layer and k^{th} input feature-map F_l^k, $g_p(.)$ is the function which defines the pooling operation. Pooling operation helps extract a combination of invariant features to slight distortions and translational shifts. The feature map is reduced and converted into an invariant feature set. Still, it also helps increase the generalization by reducing overfitting and regulating the network's complexity. The various types of pooling formulations such as max, min, average, L_2, overlapping, spatial, .etc can be used in the CNN network based on the application [192], [193].

In our CNN model, we have used the max-pooling layer by applying a max filter to non-overlapping subregions of the initial representation. The decision to use the max-pooling layer is based on training results obtained via the trial and error method. To give an example, let us assume we have a 4*4 matrix representing our initial input, and a 2*2 filter will run over our input. An example is illustrated in Figure 88: for each region defined by the filter, we will take the max of that region and create a new output matrix where each element is the max of a region in the original input.

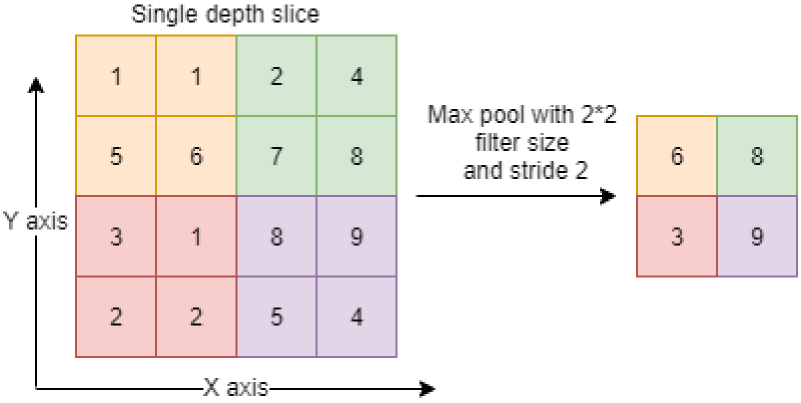

Figure 87: Example of a Max pooling operation.

Activation Function

The activation function is a non-linear transformation function over the input signal, which serves as the decision function and helps learn the patterns. The activation function is vital in

CNN as, without activation function, CNN behaves as the linear model that cannot handle complicated tasks [192]. The activation function can be defined as:

$$T_l^k = g_a\left(F_l^k\right)$$

Equation 26

where, F_l^k is an output from the convolution operation, g_a is a non-linear function that returns T_l^k a transformed out for lth layer. Different activation functions such as ReLU, SWISH, Sigmoid, tanh, maxout can be used based on the specific problem. In our model, we have used the ReLU activation function, which is defined as:

$$f(x) = \begin{cases} x, \text{if } x \geq 0 \\ 0, \text{if } x < 0 \end{cases}$$

Equation 27

The result of a ReLU layer is the same size as the input, with all negative values simply eliminated. ReLU activation is the most used function due to its ability to resolve the optimization problem based on the gradient. Moreover, the ReLU function is computationally inexpensive as it only involves thresholding the activation matrix. Unlike the sigmoid and tanh function, which are computationally expensive [194]–[196].

Fully Connected Layer

We always had 2D tables as input and 2D tables as an output in previous operations. The fully connected layer is always the last layer of a CNN. This type of layer receives a vector of size n as input and produces a new vector of the same size as output: each vector element indicates the probability of the input image belonging to a class. Unlike other layers such as the convolutional layer, the fully connected layer is a 1-Dimensional vector with all the previous layer's activations. As the convolutional layer identifies features with the help of various filters, the fully connected layer combines these features. To do this, it applies weights over the input obtained in the feature analysis to predict accurate labels. The convolutional neural network learns the weight values in the same way as it learns the filters of the convolution layer: during the training phase. It gives a prediction that is close to the desired output. The fully connected layer in our model has inputs from the previous non-linear ReLU function and provides a single result passed to the softmax layer.

The SoftMax function, also known as “softargmax” or “Multi-class logistic regression,” is a function that converts a vector of k real values to a vector of K real values that sums up to 1. The input vector can have any value, but the softmax function converts 0 to 1. The output values can then be interpreted as probabilities [197]. Finally, the CNN architecture of our model is summarized in Figure 89.

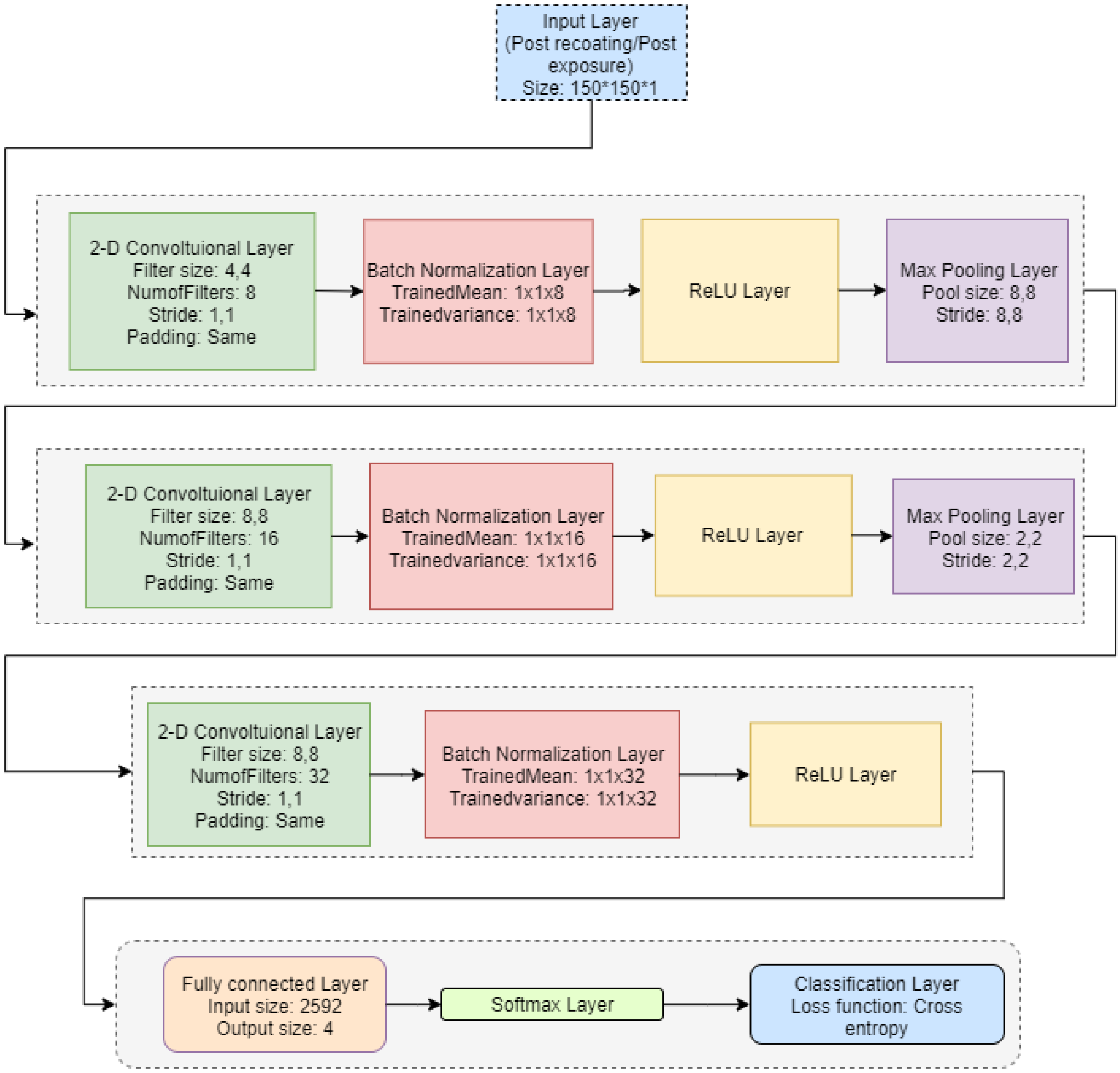

Figure 88: Block diagram proposed CNN architecture used in this study.

5.4.2. Image Processing

The captured raw images (1500*1460 px^2) possess difficulties such as in-homogeneity in light intensity. Therefore, they cannot be used directly for CNN operations. As the camera and environment conditions remain unchanged for all the captured images, the same homogeneity correction factor can be used for all images. For light intensity homogenization, we have used the in-built functions of MATLAB called “imcomplement” and “imreducehaze” [198], [199]. For our studies, we have used the maximum haze value of 1, which removes the maximum haze from the image. Firstly, the captured raw image is converted to a grayscale image to reduce the operation's complexity and our CNN model's requirement. The grayscale image is complemented, which inverts the pixel values. In other words, the black is converted into white and vice-versa. Then the “imreducehaze” function is used on the complemented image:

$$I(x) = J(x)T(x) + L(1 - T(x))$$

Equation 28

$I(x)$: Observed Intensity; $J(x)$: Scene Radiation, $L(x)$: Atmospheric Light, and $T(x)$: Transmission map of the light reaching the camera. Dezhaing operation estimates the Scene radiation $J(x)$ by estimating the $T(x)$, and $L(x)$, which is given by:

$$J(x) = (I(x) - A)/(\max(T(x), T(0) + A)$$

Equation 29

The dehazing function involves steps as follows:

1. Firstly, the atmospheric light ($L(x)$) is estimated using a dark channel.
2. Secondly, the transmission map ($T(x)$) is evaluated.
3. Refinement of the estimated transmission map ($T(x)$).
4. Restoration of the image.
5. Lastly, perform contrast enhancement on the restored image.

Figure 90 shows an example of a raw image and image after preprocessing operation. It can be observed that even after the preprocessing operation, the light intensity is not entirely homogenized at the edges. Therefore, we do not consider the edges for CNN operation and start the algorithm only for an area of 1000*1000 px^2 as marked in the red rectangle box. The dimensions of the region of interest are selected intuitively; most of the time, parts are built at the build plate's center. Intentionally, cropping of the image is avoided to minimize the border effect and prevent operation padding, significantly affecting border patches results. Considering the borders, selecting the blocks with the same center will not be possible as the sizes vary enormously. Secondly, the light intensity at the borders may also affect the accuracy of the overall model.

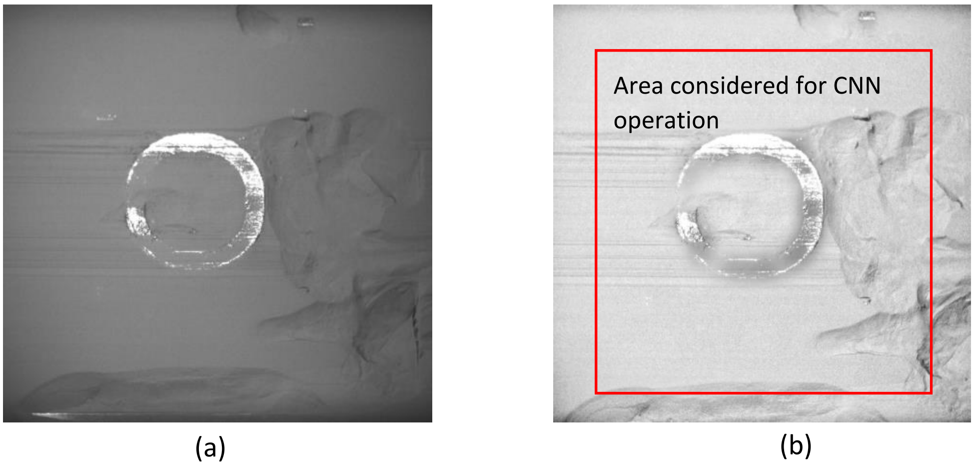

Figure 89: An Example of (a) captured raw image, and (b) pre-processed image.

5.4.3. Anomalies Description

For Pre-Exposure Images

Our study has considered four cases: the CNN network's detection features, which serve as the so-called "labels" shown in Figure 91. Pre-exposure images can have critical information regarding the overall quality of the powder bed spreading. It shall be noted that the labels' selection is based on the visual inspection of the images, and only the most common human visually verified powder bed spread anomalies are considered, as presented in the following. "Recoater-Streaking" is the most common anomaly that occurs due to damage to the silicone lip due to part-hopping (Figure 91b). Another critical anomaly called "incomplete spreading" or "Uneven Powder Spreading" can also be captured by pre-exposure images (Figure 91c). It shall be noted that the pre-exposure image captures not only the powder spreading quality for a particular layer but also captures the information regarding the quality of printing in the preceding step. "Part-hopping" is an anomaly mainly influenced by the printing quality in the previous step (Figure 91a). The fourth category (Figure 91d and 6e), called "OK," represents the areas free from the above-discussed anomalies. Figure 91d is the "OK" image for the case

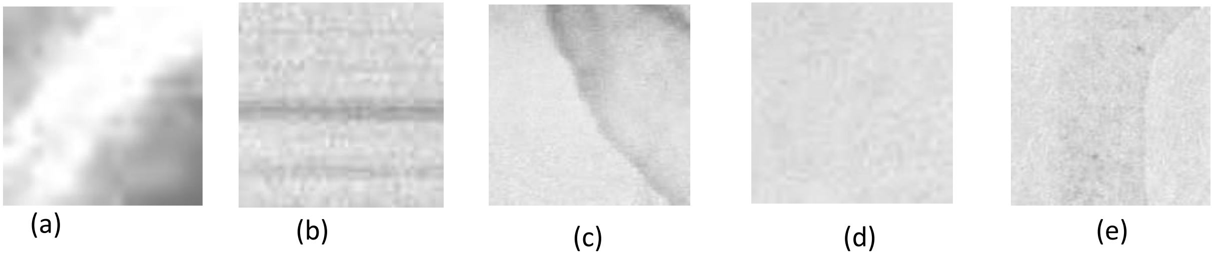

Figure 90: An example of anomalies extracted from pre-exposure images (a)Part-Hopping, (b) Recoater streaking, (c) Uneven powder spreading, (d) OK powder layer, and (e) OK part layer.

where there is no printed area underneath. In contrast, Figure 91e represents the printed part covered with the powder layer.

Post-Exposure Images

Post-exposure images can serve as verification and contain vital information about the part and powder's quality. Our study has considered the same cases as pre-exposure images for our labels. Instead of “Part hopping,” we have labeled it as the areas likely to undergo overheating phenomenon, which leads to hopping in the next recoating step due to internal residual stresses. The labels are summarized in Figure 92. For training the CNN models, a dataset of 500 images for each label is prepared for pre-and post-exposure images. We have considered the most common anomalies, which does not mean these are the only anomalies that occur during the process. Other anomalies such as spatter ejection and burn-out areas are not considered due to the lack of artificial reproducibility of these anomalies for the CNN models' training.

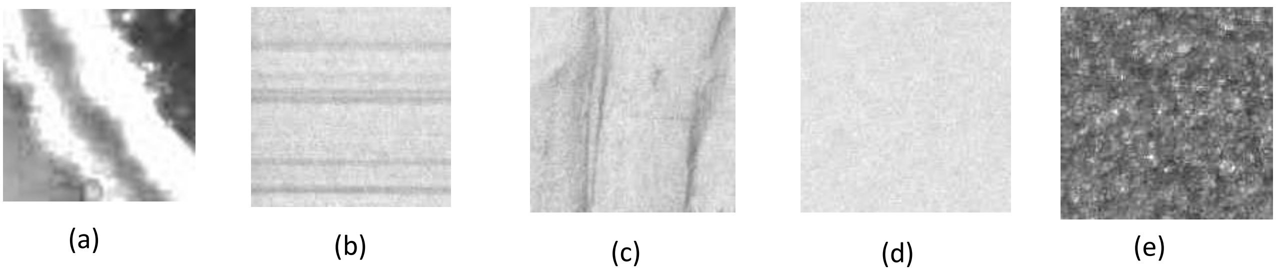

Figure 91: An example of anomalies extracted from post-exposure images (a)Part-overheating, (b) Recoater streaking, (c) Uneven powder spreading, (d) OK powder layer, and (e) OK part layer.

5.4.4. Scale Variant of Anomalies in Pre and Post-Exposure Cases

The scale of the detection area dramatically influences the detection of any particular anomaly. For example, if we consider a scale of 20*20 px^2 (Case 1- red box in Figure 93) for uneven powder spread, it may not be detectable similarly if we consider 150*150 px^2 (Case 2 - green box in Figure 93) for “Part-Hopping” we may end up incorporating other anomalies such as “Recoater-streaking.” Moreover, not all anomalies have the same spatial detection scale. Therefore, it is of great importance to choose the correct spatial scale of the described anomalies such as “Part-Hopping,” overheating, recoater-streaking, and uneven powder spread. Therefore, in our study, we have chosen three different scales for the above-described anomalies based on the trial-error method. Scale 1, i.e., 20* 20 px^2 block, is set for “Part-Hopping” and overheating, as this anomaly should be captured with as small as possible scale. The 20* 20 px^2 scale is a good compromise between the computational time and the proposed CNN model's accuracy. Scale 2, i.e., 75*75 px^2, is chosen for “Recoater-Streaking,” whereas scale 3, i.e., 150*150 px^2, is set for uneven powder spread. It is also noted that all three scale blocks are extracted from the same center, and also the scale 1 blocks are non-overlapping, whereas scale 2 and scale 3 are overlapping blocks that stride with a step of the smallest block size.

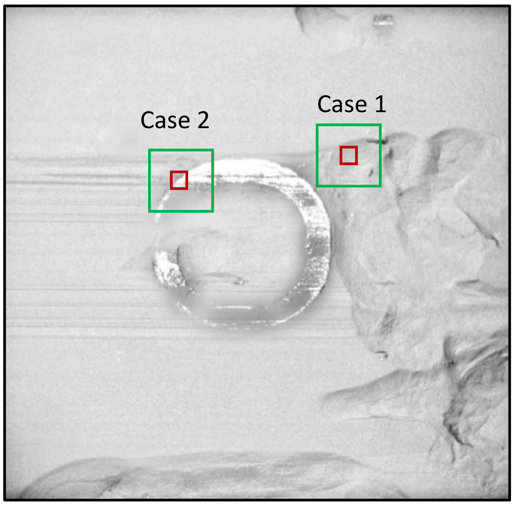

*Figure 92: An example of scale variance of different types of anomalies is shown. Red box represents the scale 1 of size 20*20 px2 whereas the scale 3 represented by green box which has size of 150*150 px2.*

5.4.5. Training and Testing of Models

Training CNN models

The CNN training aims to find the optimal kernels for the given case. In our CNN model, we have used the standard loss function for regression predictions and cross-entropy loss, which is shown as $H(p,q) = -\sum_x q(x) \log p(x)$ where $p(x)$ is the classification function from softmax operation corresponding to the input image used for classification operation whereas $q(x)$ is the ground-truth label of that image. The minimization of loss function during training is the optimal criterion for selecting optimal kernels.

During training, kernel weights are recursively updated by using the training images. The prediction error gradient decides the updating of the weights for each layer backpropagated for that layer. It shows the direction of weight adjustment, which allows a steep decrease in prediction error. We have utilized the sgdm optimizer for our CNN model with an initial learning rate of 10^{-3} for regression, batch size of 20, and max training epoch number of 100. L_2 regularization is applied to all the weights for suppressing over-fitting. The regularization coefficient is set as 10^{-3}. The best-fit settings for both CNN models, i.e., CNN 1 and CNN 2, are the same, showing the highest training accuracy for pre- and post-exposure images. The reported training accuracy of CNN 1 and the CNN 2 models is 93.16 % and 96.20 % for pre and post-exposure images.

Testing of CNN Model

Labeling Test Images

Several conditions shall be imposed on the pre and post labeled data to minimize the probability of mislabeling, and the conditions are different for both pre and post-exposure images. As mentioned earlier, we extract three different scales (20*20 px^2, 75*75 px^2, 150*150 px^2) blocks from the same center, leading to having three various labels for the same center. Therefore, it is necessary to take specific conditions for each block. The conditions for pre-exposure test images are as follows (Figure 94):

- Firstly, scale 1, i.e., 20*20 px^2 block, will be extracted and passed through the trained CNN 1 model. If the scale 1 block overlaps with the part area and is labeled “Part-Hopping,” the program will skip the training operation for scales 2 and 3 for that specific center and proceed to another center.
- If the label is not “Part-Hopping,” the center will not save the predicted label for scale 1 for that center and will decide based on scales 2 and 3, which is decided by the decision matrix shown in Table 16. The reason for this particular condition is that when the “Part-Hopping” occurs, other anomalies cannot happen at the same center. However, when there is no “Part-Hopping,” then there could be “Recoater-Streaking,” “Uneven Powder Spreading,” and “OK” part labels.

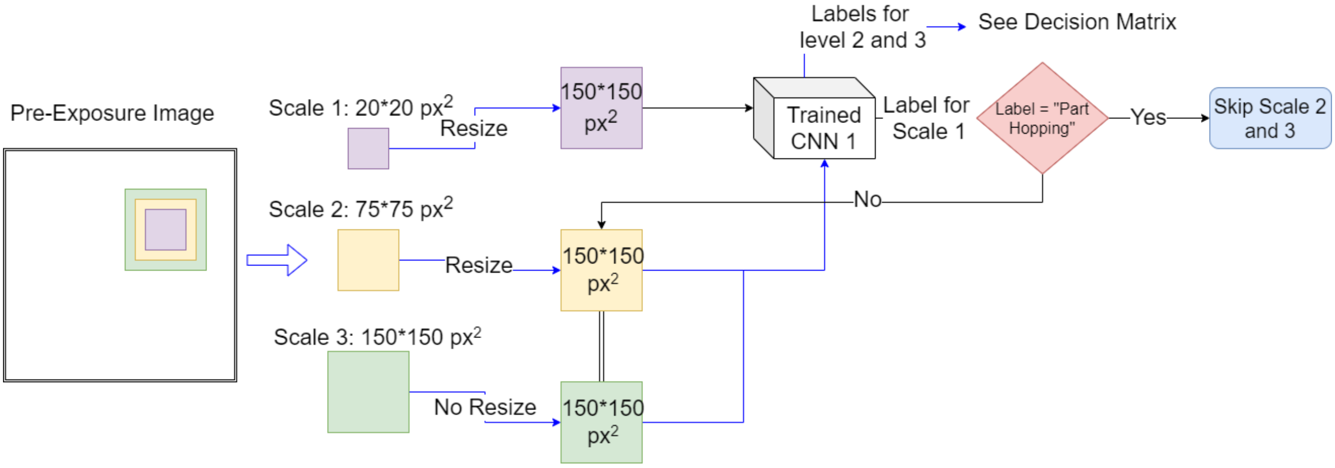

Figure 93: Flow chart for labeling the pre-exposure test images.

The conditions for post-exposure test images are as follows (Figure 95):

- After the exposure step, there is no powder in the part area. Therefore, it is impossible to have defects such as uneven powder spread and “Recoater-Streaking” in that area. Thus, the scale 1 block, i.e., 20*20 px^2, will first pass to a precondition to check whether the block overlaps or intersects with the part are or not. If not, the scale 1 labels will not be predicted for that center as it is not in the part area. If yes, the possible labels can be "Part-Overheating" or "Part OK." If the predicted label is other than "Part-Overheating" and "Part OK," the label will be marked as mislabeling.

- If the scale 1 block does not intersect with the part area, then there can be labels related to powder anomalies, i.e., "Recoater-Streaking," "Uneven Powder Spreading," or "OK." Therefore, for that specific center, the labels will be predicted for scales 2 and 3, i.e., 75*75 px^2 and 150*150 px^2. The final decision will be based on the decision matrix shown in Table 16, like the pre-exposure procedure.

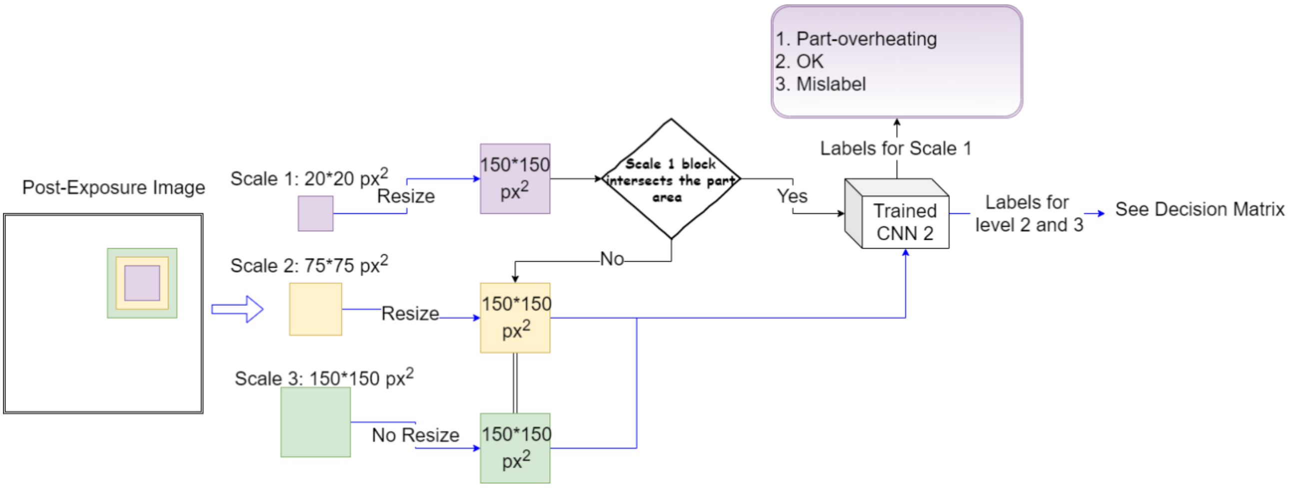

Figure 94: Flow chart for labeling the post-exposure test images.

Scale 2 Labels (75*75 px^2)	Scale 3 Labels (150*150 px^2)	Final Decision
Uneven	Uneven	Uneven
Part Hopping/Overheating	Uneven	Uneven
Uneven	Streaking	Mislabel
Uneven	Part Hopping/Overheating	Uneven
OK	OK	OK
Part Hopping/Overheating	OK	OK
Uneven	OK	OK
Part Hopping/Overheating	Part Hopping/Overheating	Mislabel
Part Hopping/Overheating	Streaking	Streaking
OK	Part Hopping/Overheating	OK
OK	Streaking	Mislabel
OK	Uneven	Uneven
Streaking	Part Hopping/Overheating	Streaking
Streaking	Streaking	Streaking
Streaking	Uneven	Mislabel
Streaking	OK	Streaking

Table 16: The decision matrix for scale 2 and scale 3 labels.

Confusion Matrices

The training dataset is divided into three subcategories, i.e., training set, validation set, and test set with 60:20:20 ratios. The training process aims to fit the ML model into the training dataset. The training process's performance is evaluated by the validation set, which, in return, can be used to find the best-fitted design parameters to obtain the highest validation accuracy. However, it is essential to note that the model may overfit or underfit the validation set and training set. Therefore, the ML model's actual performance is attributed to the testing dataset, and the confusion matrix evaluates the algorithm. The confusion matrix compares the ground truth labels with the predicted labels. In other words, the false positive and false negative attributes of the ML model are indicated by the confusion matrix representation.

The confusion matrices for both cases, i.e., pre and post-exposure images, are shown in Figure 96, where the output class represents the ground-truth label. The target class denotes the predicted label. It is noticeable that the “Uneven powder spread” and “OK” labels are the most complex labels to predict for the trained CNN 1 model and are often confused among each other. Similarly, CNN 2, which predicts labels for post-exposure images, is often confused in predicting “Uneven powder spread” and “OK” labels. This inaccurate prediction of labels is due to the uneven spreading anomaly, which has a signature similar to a good powder bed.

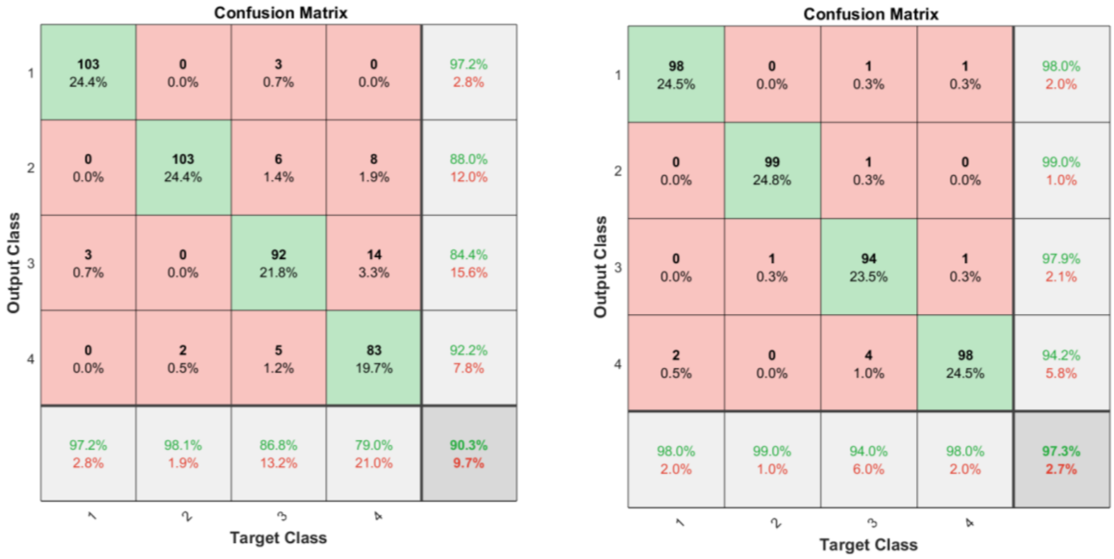

Output Class \ Target Class	1	2	3	4	
1	103 24.4%	0 0.0%	3 0.7%	0 0.0%	97.2% 2.8%
2	0 0.0%	103 24.4%	6 1.4%	8 1.9%	88.0% 12.0%
3	3 0.7%	0 0.0%	92 21.8%	14 3.3%	84.4% 15.6%
4	0 0.0%	2 0.5%	5 1.2%	83 19.7%	92.2% 7.8%
	97.2% 2.8%	98.1% 1.9%	86.8% 13.2%	79.0% 21.0%	90.3% 9.7%

(a)

Output Class \ Target Class	1	2	3	4	
1	98 24.5%	0 0.0%	1 0.3%	1 0.3%	98.0% 2.0%
2	0 0.0%	99 24.8%	1 0.3%	0 0.0%	99.0% 1.0%
3	0 0.0%	1 0.3%	94 23.5%	1 0.3%	97.9% 2.1%
4	2 0.5%	0 0.0%	4 1.0%	98 24.5%	94.2% 5.8%
	98.0% 2.0%	99.0% 1.0%	94.0% 6.0%	98.0% 2.0%	97.3% 2.7%

(b)

Figure 95: Confidence matrices for trained CNN models for (a) pre-exposure images, and (b) post-exposure images.

5.4.6. Case study

Our study performed the analysis on a so-called “Benchmark Part,” used as a benchmark tool in material development in AM. Finding the best fit process parameters is time-consuming and costly, based on trial and error methods. Therefore, specific designs are used as a benchmark tool to find the best process parameters such as critical overhang angle, process settings (Laser Power, Hatch distance, Layer Thickness), border thickness, etc. Knowledge of this angle is essential to position the supports correctly. Indeed, as we know, the critical overhang angle for Al alloys is $30^{0,}$ so we can conclude that the benchmark part is prone to failure at some point due to the absence of supports [200].

Another important reason to choose this model as our case study is that the part's failure could be confirmed via visual inspection without costly computed tomography techniques. It is then used to test the accuracy of our trained CNN model and SVM classifier. Validation of other defects such as porosities requires, on the other hand, expensive techniques such as computed tomography.

A total of 2582 images of the benchmark part are analyzed by our trained two CNN models for pre-exposure and post-exposure images, respectively. The percentage of the predicted anomalies in a specific layer is calculated and plotted along with the building height to monitor the building part's overall quality. Figure 97a shows the anomalies percentage for the pre-exposure images. It can be observed that in the last layers of the build, there is a peak for all the anomalies (“Part-Hopping,” “Recoater-Streaking,” and “Uneven Powder Spreading”). The “Part-Hopping” anomaly percentage gradually increases from layer 2400, whereas the recoating streaking and uneven powder spread anomalies occur after layers 2543 and 2556. The theory can explain that the part hopping destroys the soft silicone lip used for the recoating. When the silicone lip's quality worsens, the recoater lines, also called “Recoater-Streaking,” start to occur on the powder bed. The center of the scale variant blocks (20*20 px^2, 75*75 px2, 150*150 px^2) used as the proposed CNN 1 model input is saved to locate the particular predicted anomalies in the location of the specific layer. For example, the layer's raw image numbered 2579, and the location of predicted anomalies for that layer is depicted in Figure 97b.

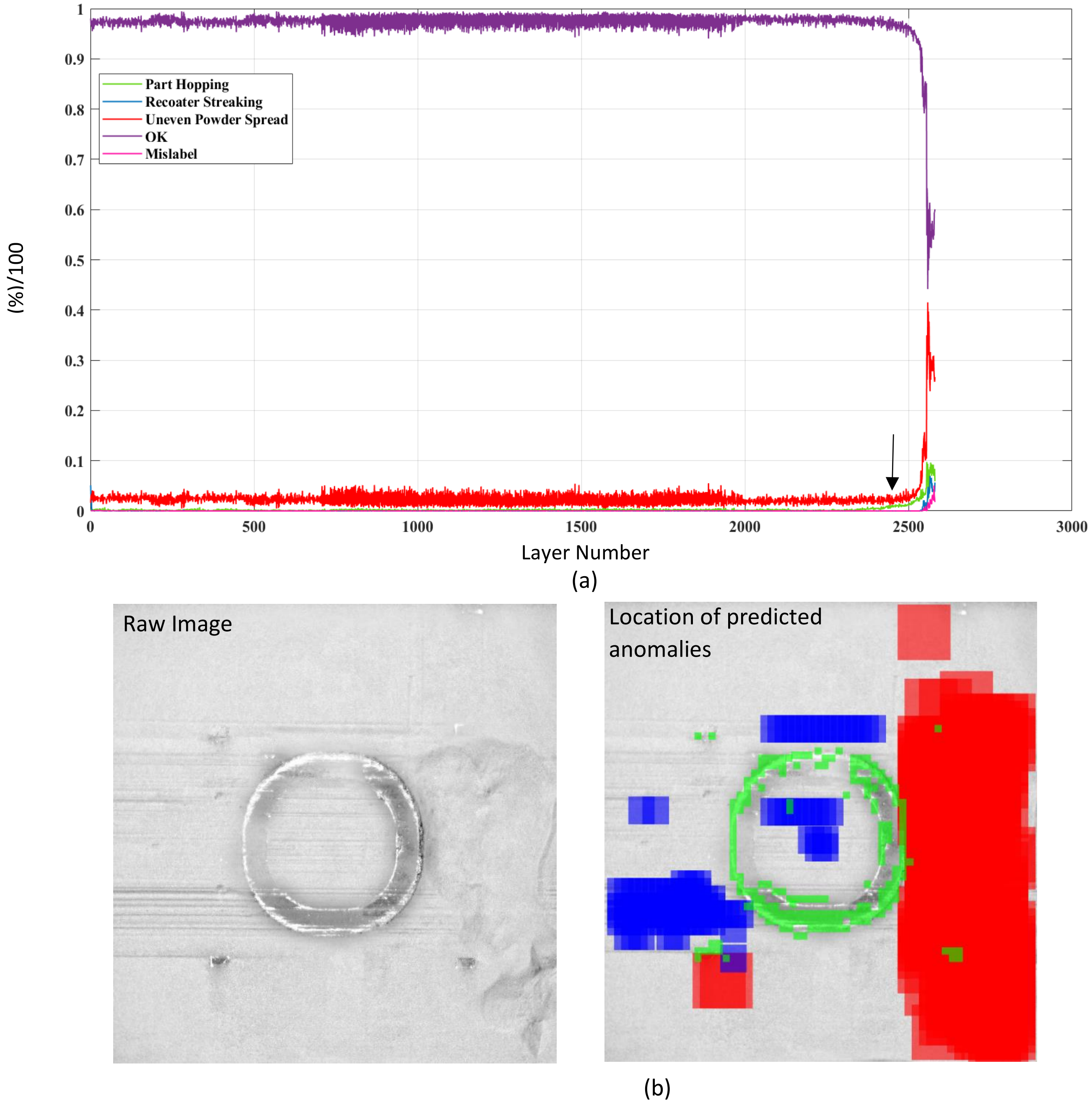

Figure 96: (a) The percentage of pre-exposure anomalies predicted by the CNN model along the build height, (b) An pre-exposure image example showing the exact location of predicted anomalies (Red: "Uneven Powder Spreading", Green: "Part-Hopping", and Blue: "Recoater streaking."

Our study used the post-exposure analysis as the cross-validation for the pre-exposure analysis results and made a confident decision regarding the quality of a particular layer. The anomalies such as recoating streaking, uneven powder spread can be present in both cases, i.e., pre and post-exposure at the same location except for the printed area. "Part-Overheating" anomaly in the post-exposure step due to lack of supports can also lead to "Part-Hopping" anomaly in the pre-exposure step for the subsequent succeeding layers. Both the cases (pre and post-exposure) serve as the two different process steps and are interlinked, and it is crucial to use both images for cross-validation and monitor the build quality. The percentage of the predicted anomalies concerning build height for post-exposure images is plotted in Figure 98a. Like the pre-exposure analysis step, the CNN 2 model predicted the highest percentage of all anomalies in the last layers. Similar to “Part-Hopping,” the “Part-Overheating” anomaly starts to occur gradually from layer numbered 2121. The location of the individual predicted anomalies for

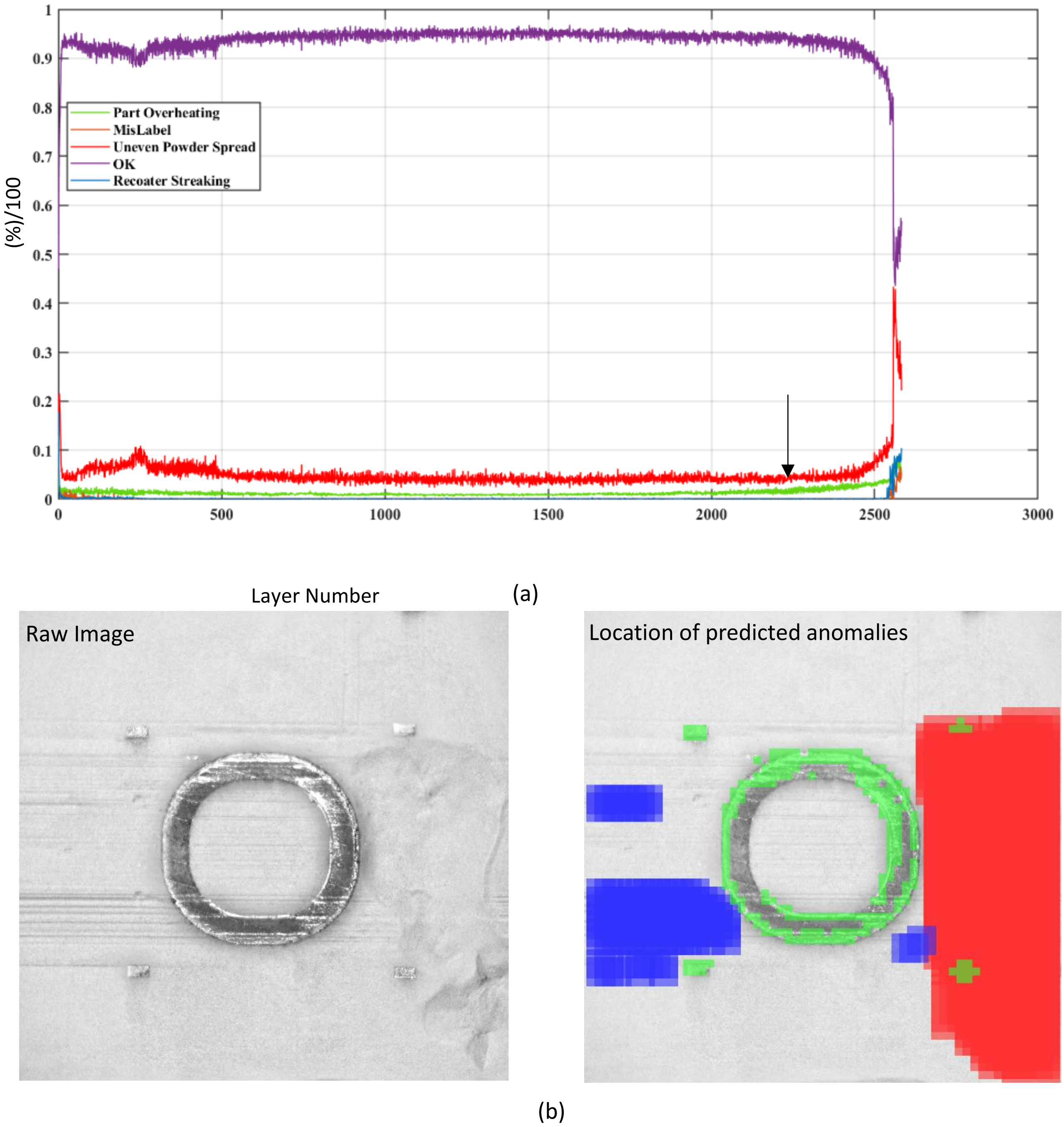

Figure 97: (a) The percentage of anomalies predicted by the CNN model along the build height, (b) A post-exposure image example showing the exact location of predicted anomalies (Red: “Uneven Powder Spreading”, Green: “Part-Overheating”, and Blue: “Recoater-Streaking”) for layer 2580.

layer number 2580 is shown in Figure 98b. The “Part-Hopping” anomaly in pre-exposure images starts to gradually increase from layer numbered 2400 (marked with a black arrow in Figure 97a), whereas the “Part-Overheating” anomaly starts to appear from layer numbered 2121 (marked with a black arrow in Figure 98a) in post-exposure images. Therefore, it can be concluded that the “Part-Overheating” anomaly first reaches a limit before it starts to impact the recoating step. The given layer thickness is not enough to fully cover the overheating anomaly, and it starts to appear in the pre-exposure step as a “Part-Hopping” anomaly.

It is also observed that the mislabel percentage also increases for the last layers in both cases. As shown in the confusion matrix (Figure 96), the proposed CNN models have high confusion probability for “OK” and “Uneven Powder Spread” labels for both cases. As the “Uneven Powder Spread” anomaly occurs only in the last layers, the mislabel percentage increases in the previous layers.

5.4.7. Limitations of CNN models

CNN models are compelling when it comes to the Image classification problem. We have also seen that the CNN models can successfully help predict the powder bed anomalies. But there is a possibility of misclassification associated with it. Also, there are a few limitations associated with the CNN models, which are as follows:

1. The CNN models are developed for the image classification problem, associating the whole image to a particular class. But for powder bed images, it may be the case that the whole image is a combination of other anomalies or features. For example, the Overheating anomaly is only present in the small section of the image. The rest of it is a normal powder bed. Therefore, it is critical to achieving localization; otherwise, the whole image is treated as an anomaly which is not the case in reality.
2. Input image size is another limitation associated with the CNN model. As the CNN models can accept only a particular image size, it hinders the ability to predict scale variant anomalies. If trained for multiple input sizes, training and testing costs are increased, making the prediction slow compared to the single CNN model.

We exploited the semantic segmentation models for pre-exposure powder bed images discussed in the next section to overcome the above-said limitations.

5.5. Approach 2: Image processing using Semantic Segmentation

5.5.1. Semantic Segmentation Using UNet

UNet is first developed by Ronneberger et al. [201] in 2015 for semantic segmentation of biomedical images. Unlike standard CNN, where down-sampling of the convolutional layer ends as dense fully connected layer (D-FC) to predict one outclass label. UNET architecture has two paths. The first part, called “encoder,” consists of a traditional stack of convolutional and max-pooling layers where the image information is contracted and stored. In the second path (also called decoder), the output from the encoder is expanded using transposed convolutions to give a segmentation mask. The skip connections in the encoder and decoder allow recovery of the spatial information lost during max-pooling operation [202].

5.5.2. Residual Networks

Many researchers have argued that deeper neural networks are more potent while extracting the information [203]. The ability to compose the hierarchically shallower feature representation to more profound representation makes the deeper networks more robust. For example, in face recognition, pixels make edges, and edges mark the corners representing facial features such as nose, mouth, eyes, and chin. Finally, these facial features help to define the different faces [204]. However, deep CNNs are challenging due to vanishing gradients problems in the forward and backward feed process. The residual neural network is developed to overcome this problem, shortcut connections parallel to the traditional convolutional layers (Figure 99). Mathematically, the residual block output can be defined as $y = F(x) + x$. The shortcut x acts as highways through which the gradient can easily flow back, resulting in faster and easy training. The ResNet authors proposed a newer model version by adding additional direct

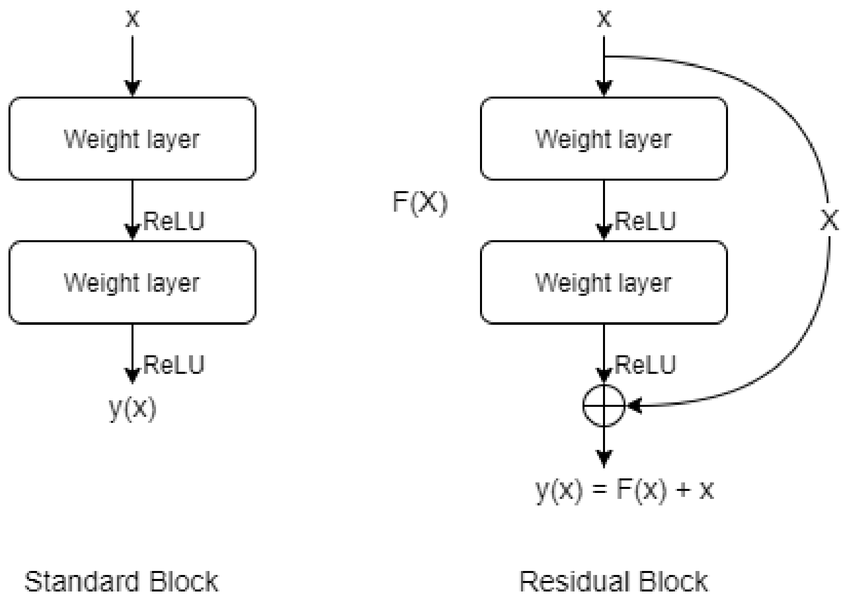

Figure 98:The schematic representation of (a) standard CNN block, and (b) residual block.

identity connections [205]. Apart from ResNet, stochastic depth can tackle gradient vanishing, which randomly drops the whole layer. The dropout enables fast training, but the depth of the model is much smaller than the original. Therefore, for our study, we have used ResNet34 architecture.

5.5.3. Combination of ResNet and UNET

As discussed, ResNet is a robust CNN architecture for feature extraction in object recognition. Therefore, we have used the combination of ResNet34 and UNet for our study. The ResNet34 blocks are used as the encoder or down-sampling path instead of standard CNN architecture (see Figure 100 [206]). Also, the skip connections at the end of every block are used for up-scaling or decoder paths. An input stack of size 128*128 px^2 and corresponding labels for powder recoating images is used. No data augmentation techniques are used in this study.

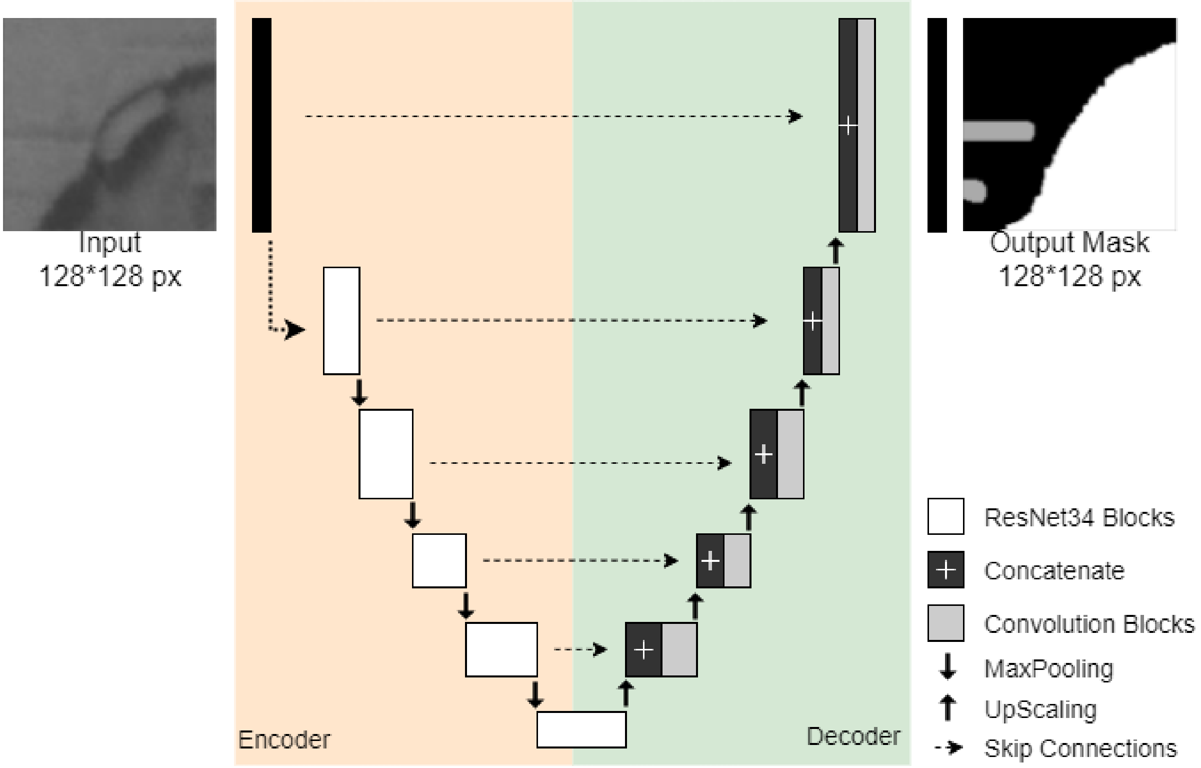

Figure 99: Graphical representation of Res34-UNet used in this study [207].

5.5.4. Training Dataset

For this study, Pre-exposure or post-recoating images captured from LCS are used. The working principle of the LCS is discussed in section 5.1. Anomalies like recoater streaking, uneven powder spreading, and part hopping due to local overheating are labeled (Figure 101a). The pre-exposure images from the benchmark part (see Figure 82 top-right) showing anomalies such as part-hopping, recoater streaking, and uneven powder spreading are used for training the proposed model. The training data is obtained from the benchmark part printed in AlSi7Mg0.6 [208] for a particular case. It is important to note that the powder bed spread anomalies are not affected by the material's choice. A set of 20 layers is used for training. But before training, labeling each pixel and generating a corresponding mask is necessary. The labeling and generation of a mask are done using available online tools such as "apeer" from Zeiss. An example of labeling and mask is shown in Figure 101.

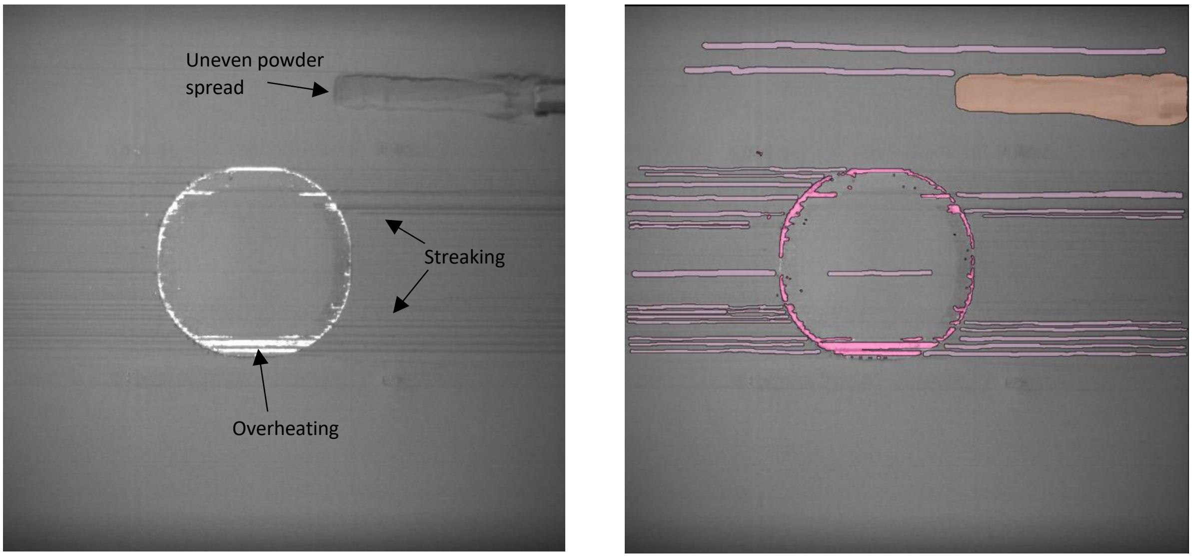

Figure 100: (a) Raw pre-exposure image with types of anomalies (marked by arrows), and (b) corresponding labeled image.

After labeling, the images and masks are cropped in 128*128 px^2 blocks and saved as an image stack for further model training. Unlike CNN models, no additional image processing techniques are used.

The whole dataset is divided into training, testing, and validation data in a ratio of 70:20:10.

5.5.5. Model Training

The proposed model is trained and evaluated using Keras with TensorFlow backend on a python environment. In the model, all the convolutional operations are followed by batch normalization and ReLU function activation function. However, the final convolutional layer is followed by the softmax activation function, i.e., used for multi-class classification. The down-sampling path is initialized from the pre-trained weights of ImageNet [207]. Therefore, the final fully connected layer is removed to employ the pre-trained weights. The intermediate outputs of the down-sampling are connected to the up-sampling path. The up-sampling path is initialized with random weights.

The initial learning rate (LR) is set to 0.0001, and stochastic gradient descent (SGD) is used for the optimization step. A batch size of 8 and softmax activation function is set for training on NVIDIA GTX 1080 GPU with 8 GB onboard memory, Intel(R) Xeon(R) CPU E5-2683 v3 @2.00GHz. Precision (P), recall (R), F1 score, and Intersection over union (IOU) score are calculated to evaluate the quantitative performance of the proposed model for pre-exposure powder bed images. F1 score can be expressed as:

$$F_1 = 2 * \frac{P * R}{P + R}$$

Equation 30

$$P = \frac{TP}{TP + FP} \; and \;\; R = \frac{TP}{TP + FN}$$

Equation 31

Where TP, FP, and FN are true positive, false positive, and false negative, respectively.

P is a measure of the proportion of the matched pixels in the predicted results, and R is the percentage of matched pixels in the ground truth label. IOU measures the similarity between the ground truth and prediction. Mathematically it can be defined as:

$$J\left(G_{r,}P_r\right) = \frac{|P_r \cap G_r|}{|P_r| + |G_r| - |P_r \cap G_r|}$$

Equation 32

Where G_r: true region, and P_r: predicted region

IOU and F1 scores are standard metrics for semantic segmentation tasks. IOU is separately measured for each anomaly class from the ground truth. Then an average is calculated from each anomaly IOU [208], [209].

Loss Functions

The compound loss (L) combining dice loss (L_{dice}) and focal loss (L_{focal}) is used for ResNet-UNet proposed model and can be expressed as:

$$L = L_{dice} + L_{focal}$$

Equation 33

Recently, it has been reported that the combination of different losses improves the semantic segmentation where the class imbalance exists [210]. Dice loss calculates the overlap between the ground truth and prediction and can be expressed as [211]:

$$L_{dice} = 1 - \frac{2\sum_{x\in\Omega} p_l(x) g_l(x)}{\sum_{x\in\Omega} p_l^2(x) + \sum_{x\in\Omega} g_l^2(x)}$$

Equation 34

The focal loss is used to counter the label imbalance that arises due to background and foreground in image classification during training. The focal loss is extracted from the cross-entropy loss, and a focussing parameter γ helps to increase the importance of correcting misclassified examples. Weighting factor $\alpha \in [0, 1]$ gives preference to the foreground or difficult to segment labels compared to background or easy to segment labels. It can be expressed as [212]:

$$L_{focal} = -\sum_{x\in\Omega} \left(\alpha(1 - p_l(x))^{\gamma} g_l(x) log p_l(x) + (1 - \alpha) p_1^{\gamma}(x)(1 - g_l(x)) \log(1 - p_l(x)\right)$$

Equation 35

Where $g_l(x)$: label vector, $p_l(x)$: predicted label vector

For our case, we have used $\alpha = [0.10\ 0.25\ 0.30\ 0.35]$ and $\gamma = 2$ based on the trial and error method and no. of epochs set to 50.

5.5.6. Case Study

Case Study Dataset

To evaluate the performance of the proposed model, we considered the dataset of Ti6Al4V print job as presented in section 4.4. As mentioned earlier, we observed anomalies in the MPM dataset and predicted the probable area of the drifts. Therefore, it will be interesting to use pre-exposure images to further compare and analyze powder bed quality. The most common anomalies such as recoater streaking, uneven powder spread, and part hopping are considered. The raw images are used for the case study, as no modification whatsoever applied to the images. It is assumed that the lighting conditions remain the same for the training benchmark part and case study case. The only difference is related to material, where the benchmark part is printed in AlSi7Mg0.6 and the case study part in Ti6Al4V. It is also assumed the anomalies related to powder bed spreading are independent of the material. A total of 627 images are used, and the anomalies percentage is calculated as follows:

$$\% = \left(\frac{A_{pixel}}{T_{pixel}}\right) \times 100$$

Equation 36

Where, A_{pixel} is the total number of pixels marked as a particular anomaly, T_{pixel}: a total number of pixels for the whole image.

Classification and Evaluation

The ResNet-UNet model achieved 84.61 %, 87.51 % of IOU and F1 score during training, and 73.29 %, 77.28 % of IOU and F1 score for the validation set. A compound loss of 0.399 and 0.572 is reported for training and validation, respectively. The corresponding anomaly % is calculated and plotted as shown in Figure 102. The part hopping anomaly occurs from layer number 473, followed by recoater streaking and uneven powder spread anomaly. The results are per the previous results using the CNN model. However, the localization of the anomalies is more realistic. In our opinion, the overall accuracy of the proposed model can be improved with an extensive training dataset. Due to a lack of training dataset, the model shows discrepancies in identifying uneven powder spread, as shown in Figure 103. Uneven lighting conditions can attribute to such discrepancies.

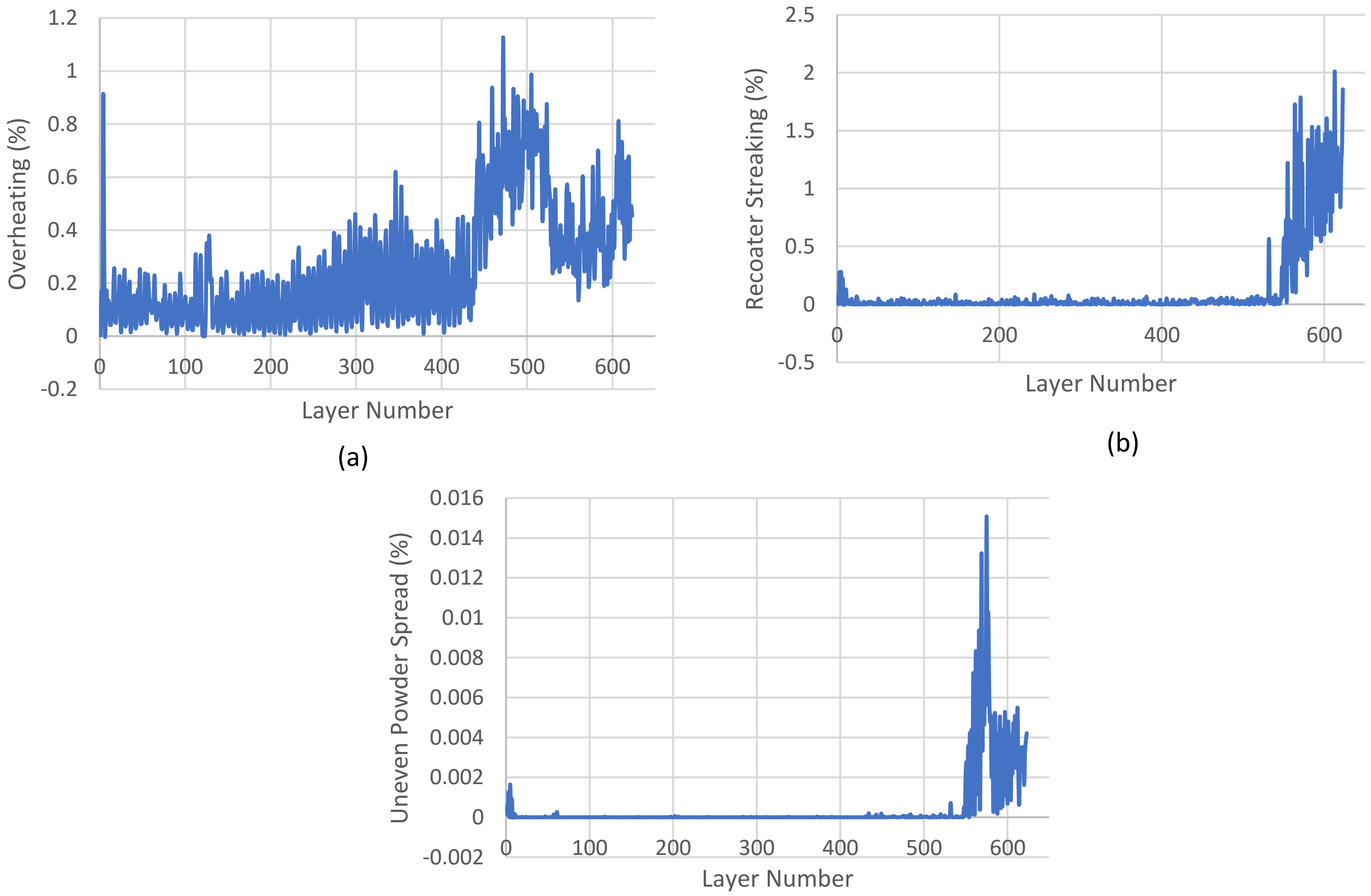

(a)

(b)

(c)

Figure 101: Graphs showing predicted anomaly % for (a) Overheating, (b) Recoater streaking, and (c)Uneven powder spread.

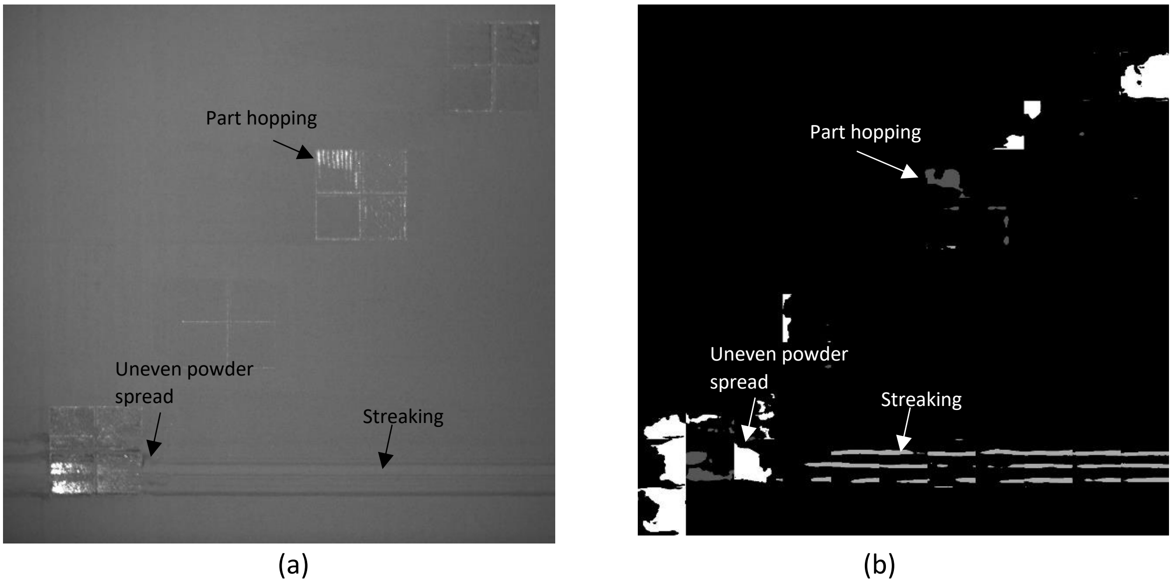

Figure 102: Example of Res-UNet anomalies prediction for layer number 577 (a) raw pre-exposure image, and (b) corresponding predicted labels.

5.6. Relation between MPM and LCS

L-PBF process is a complex manufacturing process in monitoring, as many parameters can influence powder-laser interaction. Starting from powder health (humidity, secondary particle contamination, powder morphology) to powder-bed spread. Therefore, it is vital to monitor the process at different steps and study its influence on the final quality. In this study, we tried to study and elucidate the effect of powder-bed quality on the melt pool signal captured by MPM.

Example 1: Benchmark Part

We have used the MPM viewer installed on the SLM 280^{HL} system to verify the hotspots' presence in the predicted “Drift” layers. The screenshot of the MPM viewer for layer number 2561 (which is predicted “Drift” by both SVM classifiers also circled in red in Figure 71a and 69b in Chapter 4) is shown in Figure 104. It can be observed that there are regions (marked in red) that have higher thermal emissions compared to the rest of the layer for both photodiodes. These hotspots are the highest probable regions of producing defects in final parts. It is also noticeable that the hotspot regions in photodiode 1 (Figure 104a) are not evident as like for photodiode 2 (Figure 104b), which is because the photodiode 2 spectral range is more sensitive to AlSi7Mg0.6 (low melting material).

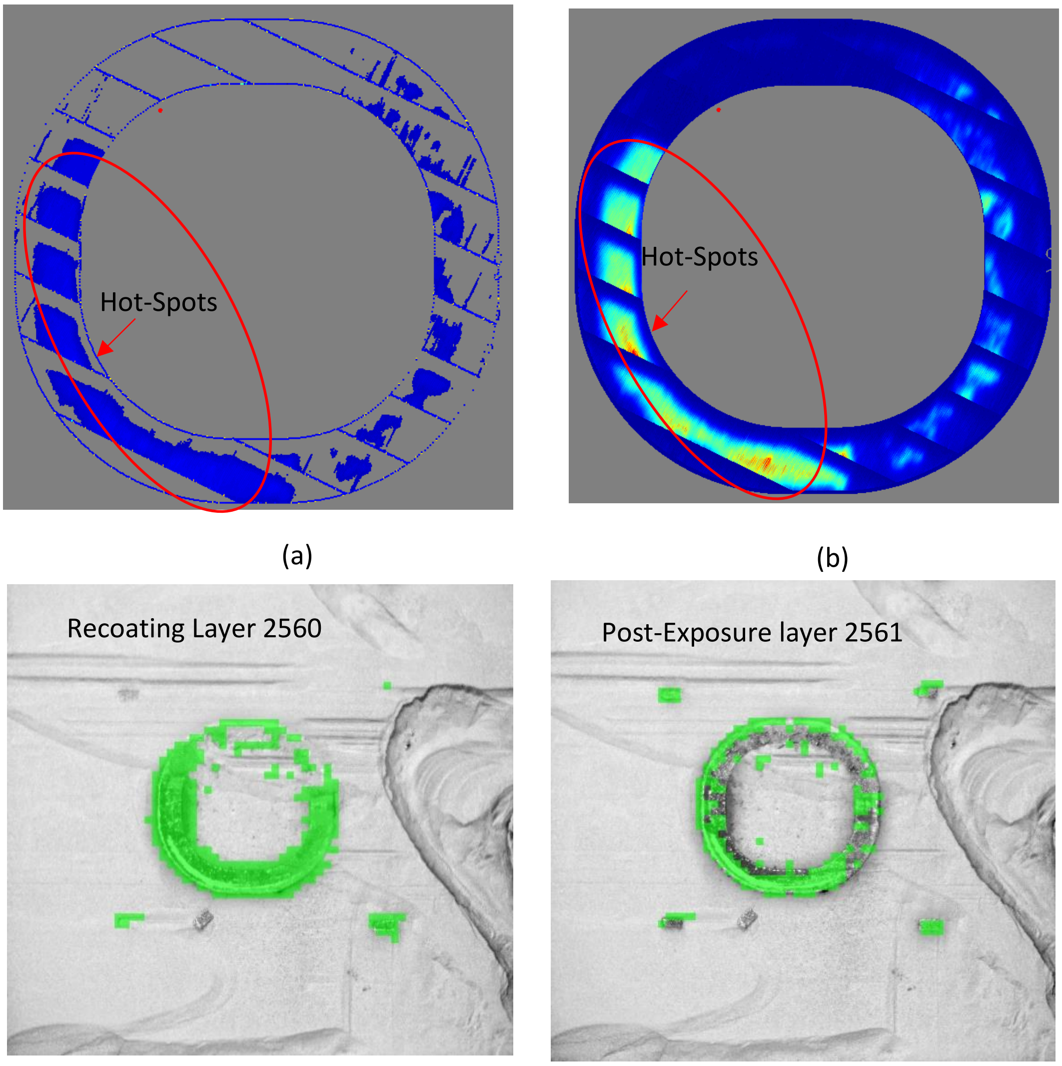

(a) (b)

(c) (d)

Figure 103: Screenshot from MPM viewer showing presence of hotspots in layer 2561 for (a) Photodiode 1 with higher thermal emission values, and (b) Photodiode 2, (c) the pre-exposure powder spread image, and (d) post-exposure image.

The building part layers predicted as drift layers for both photodiodes indicate a link between the powder spread and printed part quality. For example, in this particular layer, the pre-exposure image suggests the region of part-hopping because the powder is not uniformly spread over the whole part (marked by the green block in Figure 104c). As a result, the region not covered by the powder leads to overheating, i.e., predicted by the CNN model as marked by green boxes in Figure 104d. It shall be noted that the additional 4 rectangular bars are also printed along with the benchmark part, which is also visible in Figure 104c, and 100d. These rectangular bars are printed for internal studies and are not included in this study. Therefore, monitoring each process step is vital and linking the different steps to improve quality assurance. The confidence interval based on the various monitoring steps can separate good and bad parts from a batch of parts (in serial production case). It can be decided to use other non-destructive techniques for good parts for quality assessment. It will save time and money by initially marginalizing the bad parts from the good parts.

Example 2: Ti6Al4V Cubes

Similarly, as presented in Chapter 4, the Hotspot % increases from layer 537 for the Ti6Al4V case study (Figure 78). We observed similar behavior in powder bed anomalies, as shown in Figure 102, where the part hopping and streaking anomalies become significantly visible after layer number 500. We have compared the melt pool intensity hotspot to powder bed image anomalies for layer 559, as shown in Figure 105. We can observe the presence of high melt pool intensities for ADC 1 and ADC 2. Similarly, uneven powder spreading is observed for the sample (Figure 105). Therefore, it can be concluded that the non-uniformity in powder bed spread can lead to variation in the melt pool environment confirming higher thermal counts compared to normal conditions. Also, the uneven powder spreading can be linked to the part distortion due to overheating, as identified by the melt pool signals. The part hopping leads to

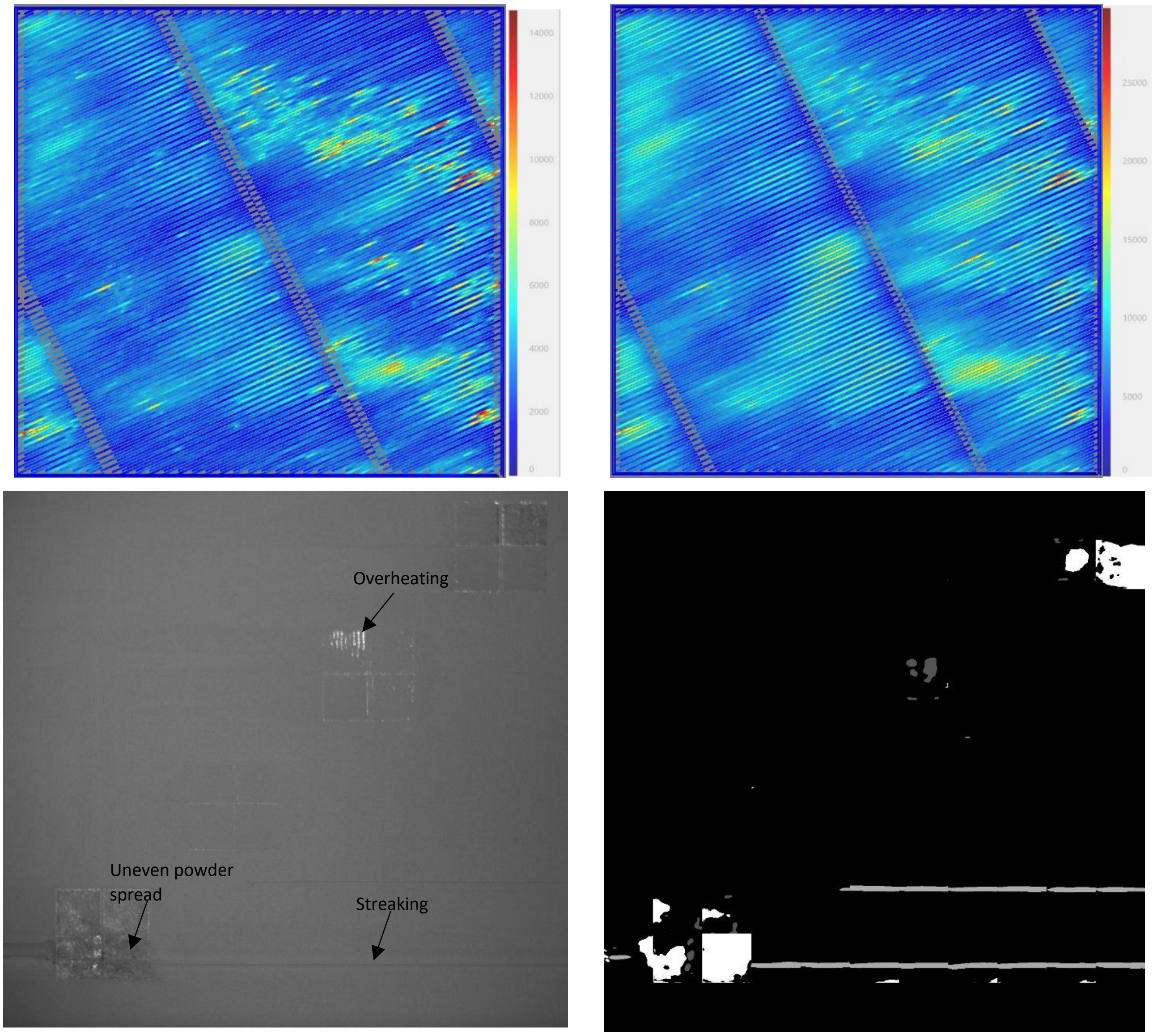

Figure 104: Screenshot from MPM viewer showing presence of hotspots in layer 559 for (a) Photodiode 1 with higher thermal emission values, and (b) Photodiode 2, (c) the pre-exposure powder spread image, and (d) corresponding predicted labels.

recoater silicone lip damage, streaking susbsequently uneven powder bed spreading. Recoater streaking could also be identified along the part (Figure 105).

5.7. Conclusions

The SLM machine also allows the powder layers to be controlled before and after the laser exposure. Chapter 5 is focused on this monitoring control system called "Layer Control System (LCS)" and its operation using by CNN and computer vision models.

Following are the conclusions that can be inferred from the LCS monitoring using image segmentation:

- LCS monitoring comprises two critical steps of the L-PBF process, i.e., pre-exposure and post-exposure. The pre-exposure steps capture the characteristics of the power bed spread over the part and the rest of the layer. Whereas the post-exposure also captures the aspects related to the printed part.
- It is also to be noted that the powder bed spread quality can be influenced by the part design, feedstock properties, and process anomalies. However, the anomalies occurring during the powder bed spread strongly influence the laser-material interaction, i.e., melt pool emissions.
- Various computer vision algorithms such as image classification (CNN method) and semantic segmentation (UNet) can detect and monitor the powder bed spread anomalies. However, for LCS images, semantic segmentation is a powerful tool compared to image classification due to its ability to classify each pixel to specific abnormalities spatially.
- We also observed that the powder bed anomalies follow a hierarchy. The part overheating or part hopping (due to part design) occurs first, followed by recoater streaking and uneven powder spread. However, it shall be noted that this hierarchy is only subjected to SLM machines as their recoater is composed of soft silicone lip. In contrast, other machines may have hard recoater, leading to different types of anomalies (out of scope of this thesis).
- Lastly, to enhance the quality assurance of the L-PBF process, it is essential to correlate the different processing steps to improve the confidence level in the final part. For example, we successfully presented that the anomalies in MPM data are directly linked and influenced by the irregularities occurring in the powder bed spread data, i.e., LCS data. Similarly, it is vital to interlink the other process steps to effectively enhance the reliability and quality assurance of the whole process.

CHAPTER 6

Thermomechanical deformation of SLMed Inconel 718

“

Our study of the phenomena induced by laser/powder interactions had a double objective: (i) to exploit the in-situ measurement systems available on the industrial devices of the different partners of the project; (ii) to characterise the behaviour of the materials during their elaboration by the processes studied within the framework of the ENABLE project with the aim of being able to feed representative behaviour laws of the processes. The last chapter of the thesis is devoted to the study of Inconel 718 produced by SLM

This chapter is dedicated to provide the experimental data for the constitutive-based modeling approach (Work Package 1), the thermomechanical response of the L-PBF processed Inconel 718 alloy is investigated. The influence of deformation conditions, i.e., temperatures and strain rates, are studied using hot torsion tests. It is noticed that the deformation conditions strongly influence the microstructural refinement influenced by dynamic recrystallisation and recovery. Also, the material's initial state, such as production state (in our case, the L-PBF process), plays a critical role. The L-PBF processed Inconel 718 samples showed a deformation activation energy of 353 KJ/mol^{-1}. The samples deformed at 1000℃ showed the highest elongation %, which can be attributed to the dynamic behavior of the material.

6.1. Theory and Background

Nickel-based superalloy “Inconel 718” is the most widely used material for producing critical parts of gas turbine engines, extrusion dies, and aerospace components through the thermomechanical processing route [213], [214]. Inconel 718 exhibits excellent corrosion resistance, high strength, and good weldability. The high strength of the Inconel 718 is predominantly due to the formation of ordered gamma double prime (Ni3Nb) precipitates [215]. However, the control of the microstructure is of paramount interest to obtain superior performance. Therefore, the deformation parameters are controlled and studied at each thermomechanical processing step. The thermomechanical behavior of a material is strongly influenced by the testing parameters such as strain, strain rate, and temperature. In the literature, many studies have been focused on studying the deformation behavior of Inconel 718 using hot compression or gleeble tests. However, the hot compression tests are suitable for studying the material behavior at low strain rates [216]. In comparison, the hot torsion tests can simulate the large deformations of the materials [217].

Thermomechanical processing routes are used to alter the microstructural properties of the metal and alloys. However, the metals and alloys exhibit complex thermomechanical responses, i.e., work hardening (WH), dynamic recovery (DRV), dynamic recrystallization (DRX), depending upon deformation parameters [218], [219]. DRX and DRV are competitive restoration mechanisms in metals and alloys during hot deformation. However, the Inconel 718 is a low stacking fault energy material; therefore, DRX is a predominant mechanism that controls the microstructure evolution during thermomechanical processing. Many published studies discuss the DRX behavior concerning hot working conditions in Inconel 718. Generally, there are two types of DRX mechanisms: Continuous dynamic recrystallization (CDRX) and Discontinuous dynamic recrystallization (DDRX) reported in the literature for Inconel 718 [220], [221]. DDRX mechanism is mainly characterized by the nucleation and growth of the nuclei from the bulging of the grain boundary. In contrast, CDRX is characterized by continuous rotation of the dislocation cell boundaries into sub-grain boundaries, leading to high angle grain boundaries [222]–[224]. Lin et al. [225] reported that DDRX plays a dominant role during the nucleation stage of the DRX mechanism in Inconel 718. However, Wang et al. [226] reported that decreasing the deformation temperature promotes the CDRX mechanism. Similarly, Zhang et al. [227] concluded that the DDRX and CDRX mechanisms co-occur in Inconel 718 superalloys during hot working conditions. Therefore, it can be supposed that there is no clear consensus on the type of DRX mechanism during the hot deformation of Inconel 718.

The good weldability of Inconel 718 due to the low content of Al and Ti makes it a suitable candidate for the L-PBF process [228]. The interest in studying the thermomechanical response of the SLMed Inconel 718 is of great importance due to its design optimization and complexity-free manufacturing. In literature, many studies discuss the flow behavior of cast and wrought Inconel 718 at high-temperature deformation [219], [226], [229]–[231]. However, a crucial understanding of the flow behavior of the SLMed Inconel 718 at high temperatures is required. Therefore, we present a study on the hot deformation of additive manufactured Inconel 718 using hot torsion tests which will be complementary to the more classical hot compression tests. This study meets several objectives: (i) increase the knowledge of the hot behavior of additive manufactured Inconel 718, (ii) make comparisons with the behavior of the same material manufactured with other processes and (iii) obtain data to feed the models of behavior laws developed in the other work packages of the ENABLE project.

The present study investigates the thermomechanical deformation of SLMed Inconel 718 at strain rates of 0.01, 0.1, and 0.1 s^{-1} over a temperature of 800, 1000, and 1100 °C. The understanding between the flow stress behavior and dynamic restoration process is presented.

6.2. Experimental

6.2.1. Material and Methods

The chemical composition of the as-received gas atomized Inconel 718 alloy (supplied by carpenter additive, UK) powder with a particle size distribution of 45-106 µm is listed in Table 17. Cylindrical-shaped specimens of diameter 16 mm and height 55 mm are printed in the vertical direction, where the long axis is parallel to the building direction. The samples are fabricated using commercial machine RenAM 500Q (Renishaw, Germany), i.e., equipped with 4 continuous Yb- fiber lasers achieving a maximum power of 500 W and a laser spot diameter of 85 µm. The processing parameters used for printing are tabulated in Table 18.

Table 17: Chemical composition of Inconel 718 powder.

	Ni	**Cr**	**Fe**	**Nb+Ta**	**Mo**	**Ti**	**Al**
Powder for SLM	50-55	17-21	Bal.	4.75-5.5	2.8-3.3	0.75-1.15	0.30-0.70

Table 18: Process parameters used for this study.

Parameter	**Value**
Laser power (W)	212.5
Scanning speed (mm/s)	850
Hatch distance (mm)	0.09
Layer thickness (mm)	0.06
Scanning strategy	10 mm stripes with rotation of 67° in consecutive layers

The printed samples are heat-treated at 850 °C for 2 h in an Ar gas atmosphere followed by air cooling. The heating cycle is depicted in Figure 106a. The heat-treated samples are machined to torsion test samples with a gauge diameter (2R) of 7.5 mm and gauge length (L) of 18 mm, as shown in Figure 106b.

6.2.2. Torsion Tests

The thermomechanical influence on heat-treated SLMed samples (Figure 106b) is studied experimentally using hot torsion tests (in-house designed by CEIT IK4, Spain). The test conditions are summarized in Table 19. Before testing, the samples are held for 10 min to reach temperature equilibrium. After tests, the samples are water quenched to reach room temperature. The temperature is monitored on one side of the sample using a K-type thermocouple.

Table 19: Hot torsion test conditions.

Parameter	**Value**
Temperature (°C)	800, 1000, 1100
Strain rate (s^{-1})	0.01, 0.1, 1
Heating rate (°C/s)	1

Torque (Γ) and the number of revolutions (N) are measured which later converted to von Mises stress (σ) and strain (ε) using the following equations [232]:

$$\sigma = \frac{3.3\sqrt{3}\Gamma}{2\Pi R^3}$$

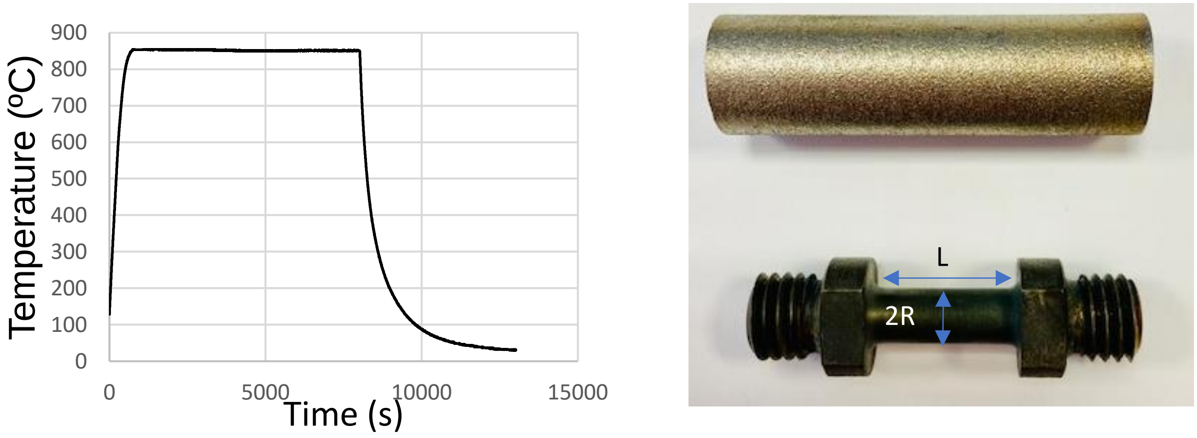

(a) (b)

Figure 105: (a) Heat treatment profile, (b) As built sample and heat-treated machined test sample.

$$\varepsilon = \frac{2\Pi RN}{\sqrt{3}L}$$

Equation 37

Where R and L are the gauge radius and length of the specimen.

6.2.3. Microstructural Observations

The deformed specimens are precision-cut along the cylindrical radial axis from the center of the samples. The sectioned samples are mounted in conductive resin for metallographic preparations. The mounted samples are ground to 2400 grit using SiC papers, and distilled water is used as the coolant. The samples are polished to 1 µm using Diamant solution and finally polished with colloidal silica. The samples are chemically etched using the kalling reagent for 5 min for optical microscopy. For EBSD/SEM observations, the samples are electropolished using a solution of 10 g oxalic acid and 100 ml distilled water for a duration of 12-15 s at 6 V. EBSD analysis is performed on an XY plane at the edge of the samples.

EBSD analysis is done using a Zeiss scanning electron microscope equipped with an EBSD detector provided by Oxford instruments operating at 30 kV. A 200*200 µm area is scanned with a step size of 1 µm and analyzed using OIM software. Before analysis, the obtained EBSD data is cleaned up using a single iteration of grain dilation with a grain tolerance angle of 5° and minimum grain size of 2 pixels. The grain boundaries with a misorientation angle of 2-15 are considered as low angle grain boundaries (LAGBs), whereas high angle grain boundaries (HAGBs) are those with misorientation greater than 15. It also is noted that some of the interpretation of the results contains cropped magnified EBSD images for better visibility. But all the statistical information is reserved.

6.3. Results

6.3.1. Analysis of Stress-Strain Curves

The deformed samples and corresponding flow stress-strain curves of the Inconel 718 torsional samples are shown in Figure 107. The flow stress curves show the material strain resistance level and the intensity of the softening for given conditions. The samples deformed at higher temperatures (i.e., 1000 and 1100 °C) and different stain rates showed typical dynamic recrystallization (DRX) stress-strain curves [233]–[235]. A strong flow stress peak is followed by a constant stress level, i.e., steady-state level.

In samples deformed at 800 °C, no steady-state is observed, but a substantial softening after the peak stress is evident. Also, the samples at 800 °C show a brittle fracture and almost negligible ductility with a maximum strain of only 0.6. Therefore, for further analysis, we have not considered the samples deformed at 800 °C.

The peak stress (σ_p) is extremely sensitive to the deformation temperature and strain rate, i.e., it decreases with an increase in the temperature and increases with an increase in the normal strain rate in Ni-based superalloys [236]–[239]. It is worth mentioning that the peak strain, which corresponds to the peak stress, decreases with a decrease in strain rate.

After attaining the peak stress, softening is followed, attributed to the dynamic recrystallization or recovery phenomena [240]. However, in Ni-based superalloys, dynamic recrystallization is predominant [241]. Large amounts of dislocations are generated during initial hot deformation, i.e., controlled by work hardening and dynamic recovery. With continued deformation, the

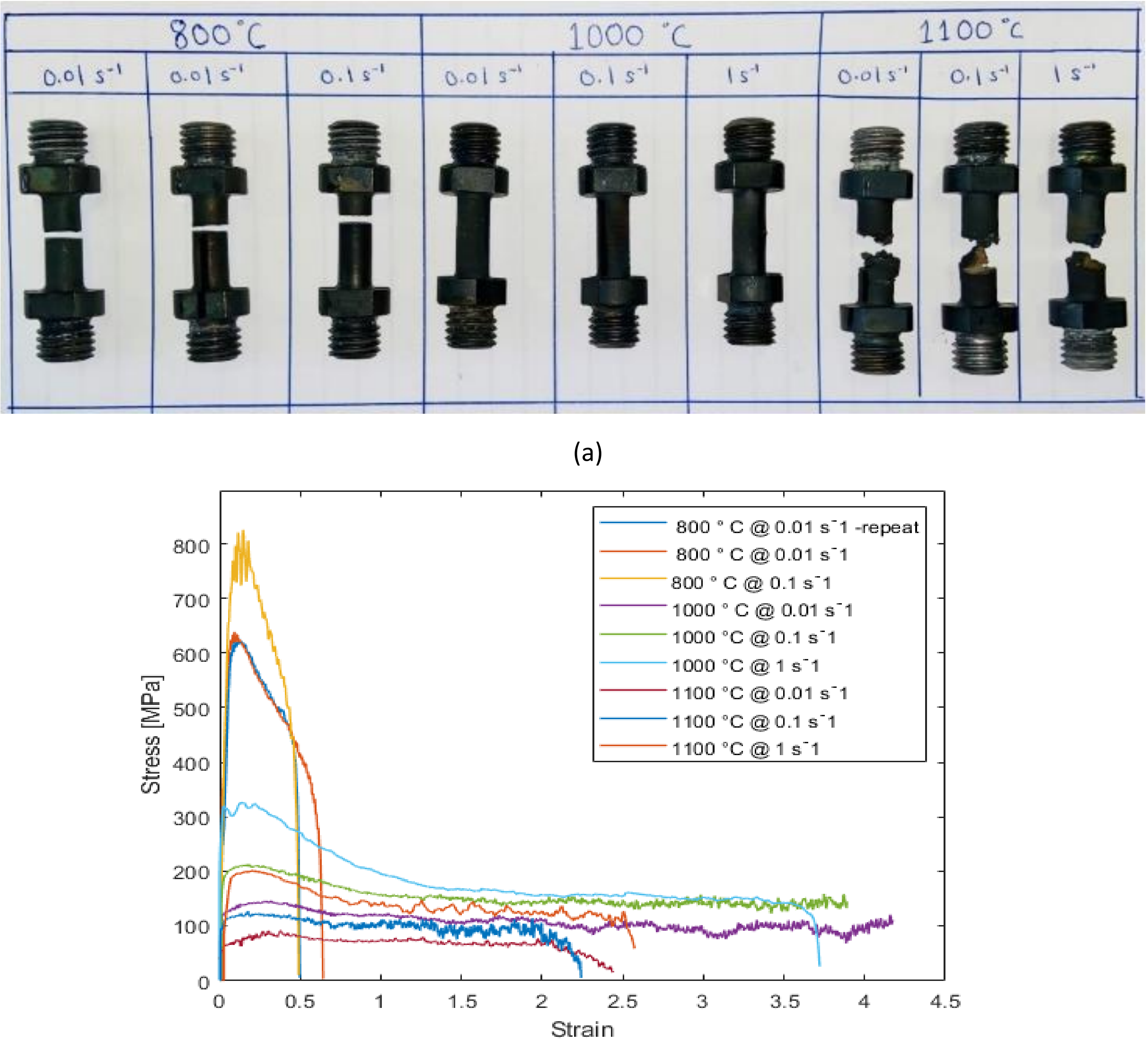

(a)

(b)

Figure 106: (a) Deformed samples, (b) Stress-strain curves for the deformed samples.

accumulated dislocations exceed a critical dislocation density point, after which new grain nucleates and grows, resulting in refined microstructure [242], [243].

Moreover, serrations in the stress-strain curves for all the samples could be observed. Although the magnitude of serrations changes. The serrations in flow stress curves result from the successive multiple cycles of dynamic recrystallization. When the critical dislocation density (ρ_c) is attained, the nucleation of new grains starts. If the ρ_c of the next DRX cycle is attained before completing the last DRX cycle, a single broad peak flow stress-strain curve is obtained. However, if the two DRX cycles do not overlap and the occurrence of DRX cycles follows one another, the serrations are observed in the flow behavior curves. Each serration denotes the individual DRX cycle involving an increase of work hardening rate followed by the generation of new grains [244].

6.3.2. Critical Stress and Strain

Critical parameters usually initiate dynamic recrystallization (DRX) during hot deformation, mainly critical strain (ε_c) and critical stress (σ_c). Therefore, it is essential to determine these critical entities, which are strongly influenced by the thermomechanical deformation conditions such as strain rate and temperature. However, finding of exact values of critical conditions is very difficult.

In literature, several methods to predict the critical strain and stress based on computational or experimental approaches are reported [245]–[250]. For example, Cram et al. [251] found the critical conditions for the nucleation of the DDRX using a physical-based model by coupling polyphase and grain growth models. Although the model results showed good agreement with the experimental values, it is not advised to be used for low alloy metal materials due to its difficulty in predicting material physical parameters. As, Inconel 718 is not as low alloy material , we have used Poliak and Jones [248] method to calculate the critical strain based on stress-strain curves. For example, experimental data -for temperature 1000 °C and strain rate 0.1 is used to show the proposed methodology, as illustrated in Figure 108. Firstly, raw data smoothing is performed using high-order polynomial curve fitting. To calculate the critical strain, which is an onset of the dynamic recrystallization, work hardening rate ($\theta = \frac{\partial \sigma}{\partial \varepsilon}$), i.e., is calculated and plotted as a function of stress until the peak stress. The plastic region of the stress-strain curve consists of three stages, i.e., work hardening, softening, and steady-state. Stage 1 is the work hardening state in which the dislocation density increases linearly and flow stress increases rapidly with increased strain. Stage 2 is softening, when the dislocation density exceeds the critical threshold and DRX onsets. The new recrystallized grains reduced the material's dislocation density, directly related to the decrease in the work hardening (i.e., the work hardening rate decreases much faster) and flow stress. Critical strain is defined at the start of stage 2. The final stage is the steady state in which a balance between work hardening and dynamic softening is reached.

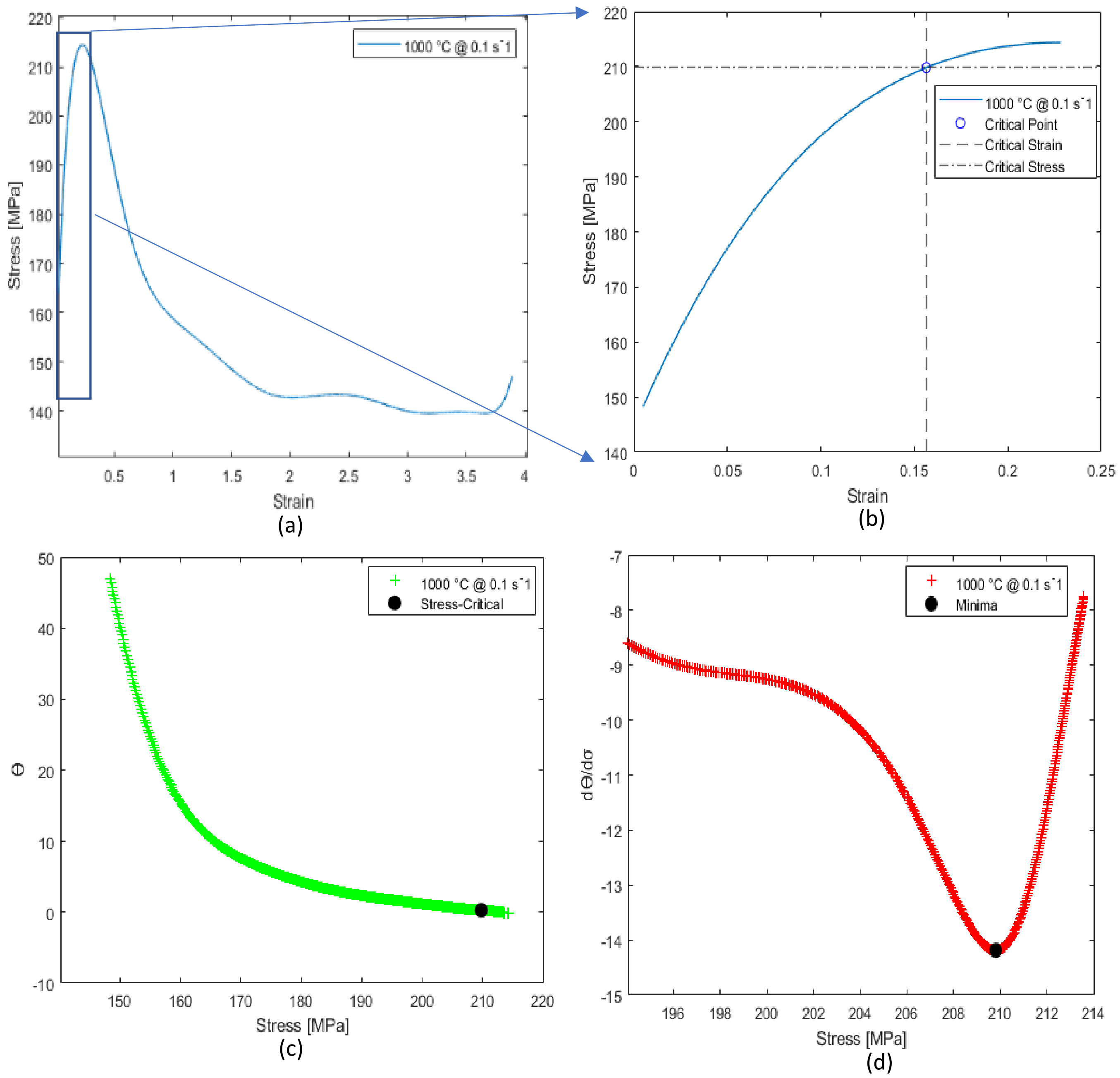

Figure 107: (a) Smoothened stress-strain curve for sample deformed at temperature of 1000 °C and strain rate of 0.1 s-1, (b) indication of critical stress and critical strain on the flow curve, (c) plot of θ *vs* σ*, and (d) plot of* $\frac{\partial\theta}{\partial\sigma}$ *vs* σ.

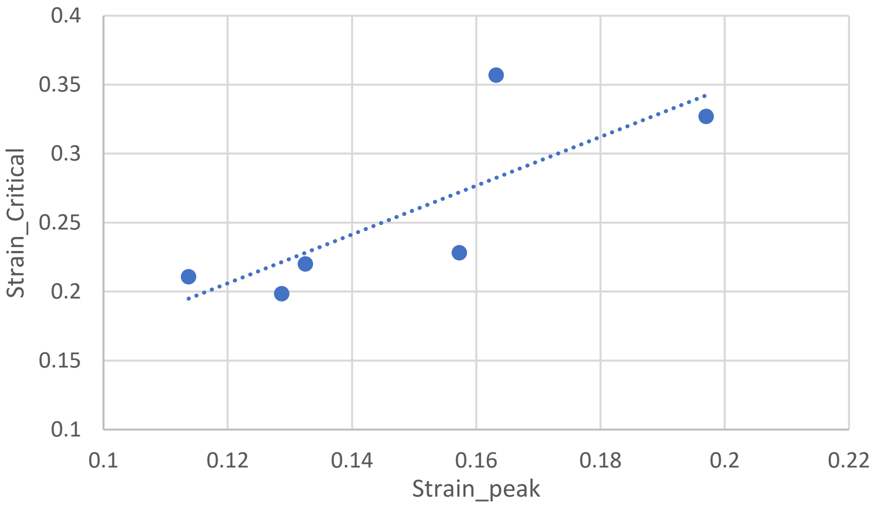

Figure 108: Relationship between peak strain and critical strain.

The minima of derivative work hardening rate and flow stress are obtained in Figure 108 to precisely calculate the critical points. The critical stress is identified as the corresponding strain associated with the minima. The critical strain is marked in the stress-strain curve, as shown in Figure 108. Similarly, the critical strain is calculated for all curves and used further to calculate activation energy and the Zener-Holloman parameter. The critical strain increases with an increase in strain rate and decreases with an increase in temperature. Also, the critical strain is linearly dependent on the peak strain and shows a relationship of Critical strain = 0.6*Peak strain on average (Figure 109).

6.3.3. Zener-Holloman Parameter and Activation Energy

Thermomechanical deformation of metallic alloys is a thermal activation process. Therefore, the metal atoms need to overcome an energy barrier during deformation. In other words, this energy barrier could be considered a difficulty level of the material for hot deformation, which can be calculated from the stress-strain curves obtained by thermomechanical tests.

Sellars and Tegart [252] proposed constitutive equations to show the relationship between the Zener-Holloman parameter (Z), flow stress, strain rate, and deformation temperature. In our study, we used the hyperbolic sine function to calculate the activation energy of deformation (Q).

$$A \sin h\left(\alpha\sigma_p\right)^n = \dot{\varepsilon} \exp\left(\frac{Q}{RT}\right) = Z$$

Equation 38

Where, A, α, n are material constant. R is the universal gas constant (8.31 J mol-1 K-1), T is absolute temperature, and $\dot{\varepsilon}$ is strain rate. α is considered as the adjusted stress multiplier and expressed as

$$\alpha = \frac{\beta}{n'}$$

Equation 39

Parameters β, n', and n can be obtained from the slopes of the plots of ln $\dot{\varepsilon}$ vs σ_p, ln $\dot{\varepsilon}$ vs. lnσ_p,

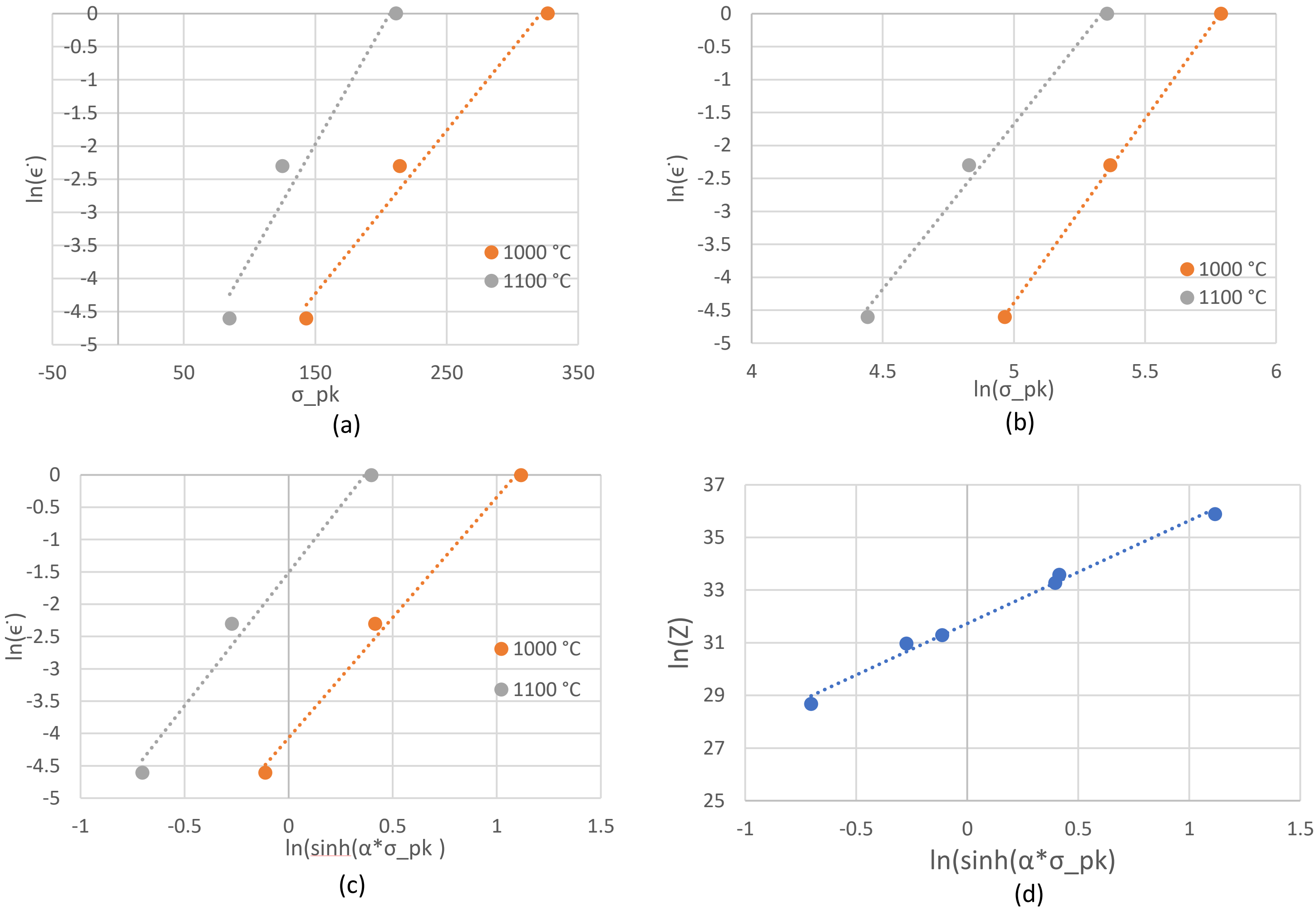

(a)
(b)
(c)
(d)

Figure 109: Plots of (a) ln $\dot{\epsilon}$ vs σ_p, (b) ln $\dot{\varepsilon}$ vs lnσ_p,(c) ln $\dot{\epsilon}$ vs lnsinh ($\alpha\sigma_p$), and (d) ln($\dot{\epsilon}$)- ln(sinh($\alpha*\sigma_p$)).

ln $\dot{\varepsilon}$ vs. lnsinh ($\alpha\sigma_p$), respectively. β = 0.0297 and n' = 5.292 is calculated from the average of the slopes of the plot ln $\dot{\varepsilon}$ vs σ_p, ln$\dot{\varepsilon}$ vs. lnσ_p, respectively, as shown in Figure 110. Based on the equation, α is calculated as 0.0056. n found to be 3.920 by taking the average slope of ln($\dot{\epsilon}$)-ln(sinh($\alpha*\sigma_p$) as shown in the Figure 110. Constant A i.e. A = 6.02787E+13 can be calculated from the intercept of (lnZ- ln(sinh($\alpha*\sigma_p$)) plot as shown in Figure 110.

Q, i.e., 379.62 KJ/mol is calculated based on the hyperbolic sine law curve fitting to the peak stress given by the equation.

$$Q = R\left\{\frac{\partial \ln \dot{\varepsilon}}{\partial \ln \sinh(\alpha\sigma_{pk})}\right\}_T \left\{\frac{\partial \ln \sinh(\alpha\sigma_{pk})}{\partial\left(\frac{1}{T}\right)}\right\}_{\dot{\varepsilon}}$$

Equation 40

The obtained value of Q agrees with the reported values in the literature for Hot compression tests of Inconel 718 alloy [253], [254].

6.3.4. Microstructural Investigations

6.3.4.1. Optical Micrographs

The heat-treated Inconel 718 samples exhibit distinct microstructure with a clear indication of melt pools and scan vectors, as shown in Figure 111. From the micrographs, it can be noticed that columnar grains are grains in the build direction which is the direction of the heat flow. Higher magnification of the optical images perpendicular to the build direction and the build

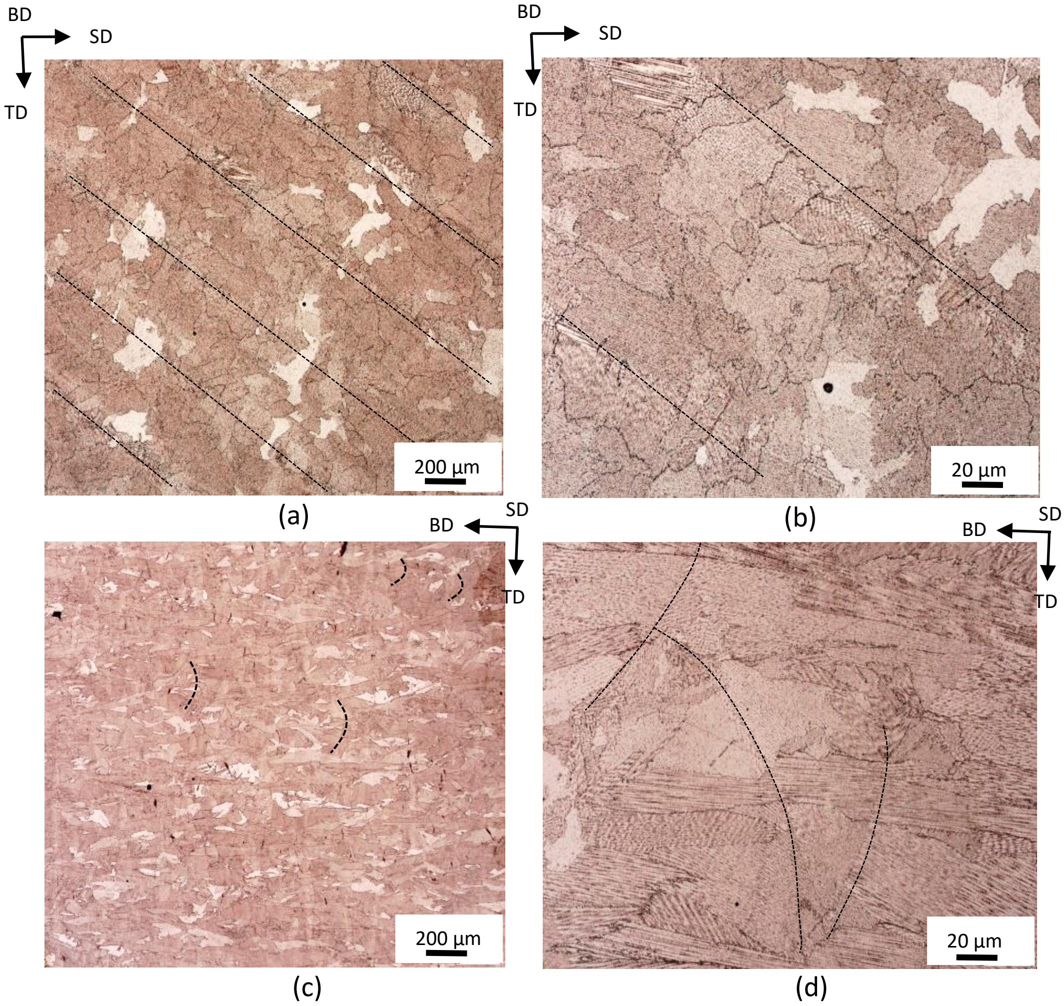

Figure 110: Heat treated samples perpendicular to build direction (a,b), and along build direction (c,d).

direction show dendritic/cellular segregation patterns. As shown in Figure 111, the dendritic growth is spanned across several layers, which implies dendrites' epitaxial growth.

The dendritic/cellular segregation patterns on higher magnification are observed in the Inconel 718 samples as depicted in Figures 111b and 107d, where the image is taken along the build direction and perpendicular to the building direction, respectively. The dendritic growth spans several scan layers, as shown in Figure 111d, indicating the epitaxial growth of grains and dendrites from one layer to the next.

6.3.4.2. Grain Morphology

Figure 112 shows the Inverse pole figures of the samples deformed at different temperatures and strain rates, along with the undeformed sample (Figure 112a). The undeformed sample has an average grain size of 29 µm. Deformation temperature significantly influences the size of the recrystallized grains. At higher temperatures, the recrystallized grains grow more quickly and become coarser, owning the effects of thermally activated phenomena such as dislocation

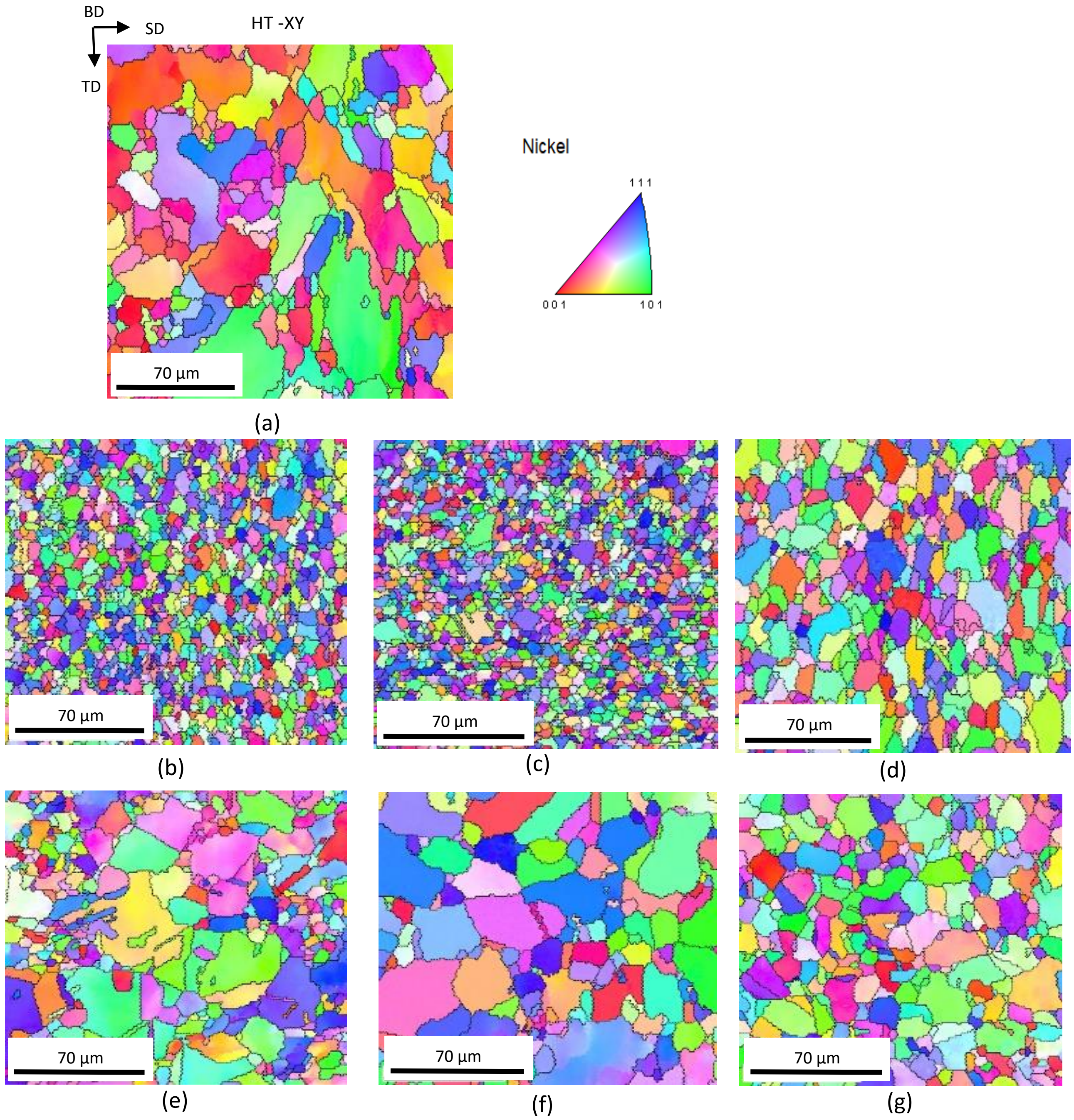

Figure 111: IPF maps for samples (a) Heat treated undeformed, (b) 1000 $^{\circ}$C-0.01s^{-1}, (c) 1000 $^{\circ}$C-0.1s^{-1}, (d) 1000 $^{\circ}$C-1s^{-1}, (e) 1100 $^{\circ}$C-0.01s^{-1}, (f) 1100 $^{\circ}$C-0.1s^{-1}, and (g) 1100 $^{\circ}$C-1s^{-1}.

mobility and diffusion is accelerated as reported in [255]. This may be why samples deformed at 1100 °C shows bigger size than those deformed at 1000 °C (Figure 113).

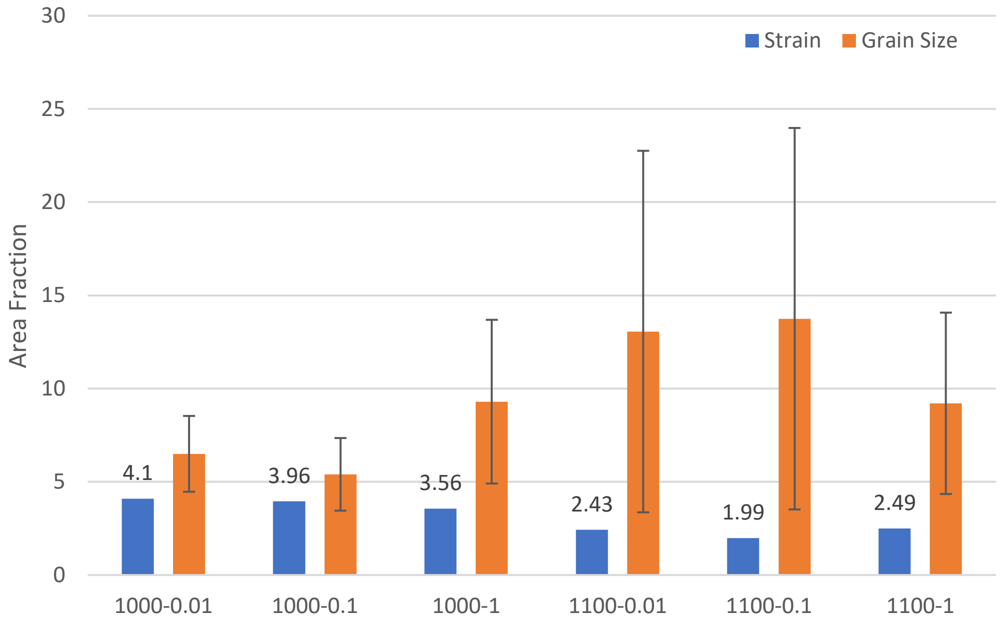

Figure 112: Average grain size of the samples along with the elongation.

Strain rate also plays an essential role in grain size evolution, and it is often reported that the grain size decreases as the strain rate increases. But the evolution is subjected to the strain at which the grains are observed. However, in our case, the samples are studied after the breakage. So, it is not possible to confer a clear relation with strain rates. Although, we observed that the samples with higher strain or elongation show smaller grain sizes, whereas the samples which showed lower elongation have larger grain sizes. It may be because the samples with high elongation undergo recrystallization entirely, whereas samples that show lower elongation have un-recrystallized grains. It can also be conferred from the stress-strain curves where the serrations in the sample deformed at 1000 °C show continuous cycles of work hardening and recrystallization. This can be the reason for the high variation in the grain sizes for samples 1100-0.01, 1100-0.1, and 1100-1 (Figure 113), which shows low elongation, as shown in Figure 107b. Also, the DRX grain size remains constant once during deformation; therefore, this could be the possible reason for low variation in the grain sizes for samples deformed at 1000 °C, which indicated that most of the grains are recrystallized.

6.3.4.3. Misorientation Angle Evolution

The nucleation of recrystallized grains is dominated by the generation and annihilation of the dislocations. Therefore, a change in the substructure's misorientation angle can be observed. To better understand the microstructural evolution, the misorientation angle distribution for LAGBS and HAGBs is plotted in Figure 114. In the case of the undeformed sample (HT), LAGBs (<15°) have an area fraction of 47 %, while the area fraction of the misorientation angle of 60° is only 0.08%. Therefore, it can be concluded that there is a negligible number of twins present before deformation. While the area fraction of LAGBs decreases with an increase in the strain rates as observed for temperatures 1000 and 1100 °C. The increase in the recrystallization degree may induce a decrease in the substructure. In addition, the average misorientation angles at strain rates of 0.01,0.1,1 and temperatures of 1000 and 1100 °C are 24, 27, 28, 22, 24, and 26, respectively. The effect of temperature on the average misorientation angle distribution is not much distinct. Interestingly, in deformed samples, the area fraction of the misorientation angle of 60° is significantly higher due to the generation of twin boundaries during deformation. Twin boundary evolution will be discussed in the following sections.

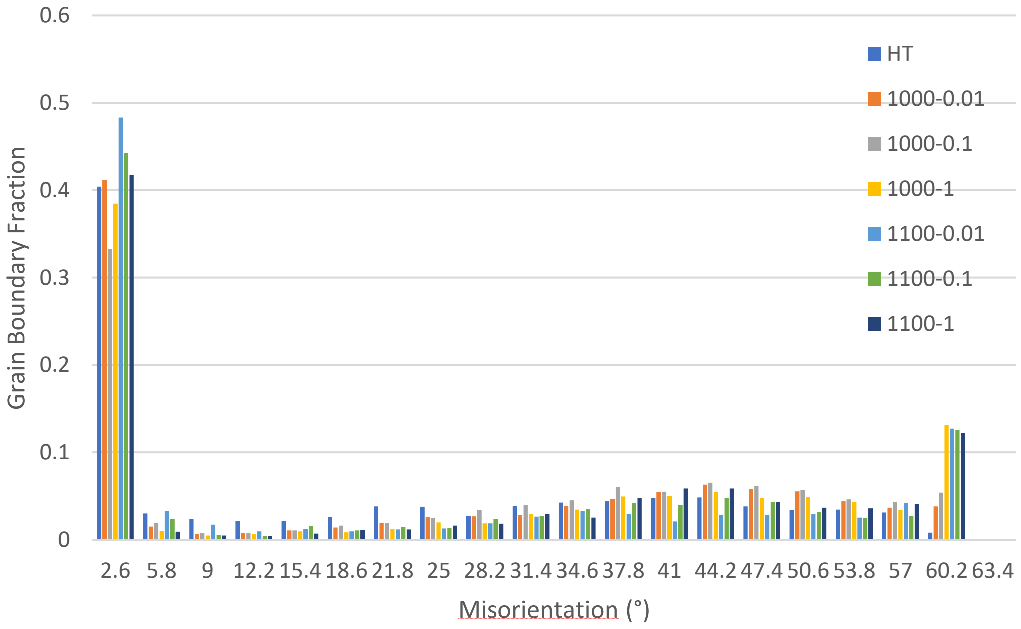

Figure 113: Misorientation angle distribution of the samples.

6.3.4.4. Twining Evolution

The evolution of annealing twins during DRX is commonly observed in low stacking faults materials such as Ni-based superalloys. The annealing twins help reduce the grain boundary energy. Therefore, the DRX mechanism progresses while promoting annealing twinning [225]. During the grain boundary motion, new annealing twins can be formed, which will further enhance the nucleation rate of the DRX process. The dislocation density and misorientations at the interface of the newly formed grain and deformed grains reduce significantly. Thus, the driving force is lowered, which inhibits the further growth of the recrystallized grains. Knowingly, the presence of twins at the interface changes the misorientation and provides additional boundary energy for simulating the grain boundary motion resulting in some degree of grain growth [256][26].

The literature reports that the number of Σ3 boundaries (annealing twins) is proportional to the grain boundary migration velocity and distance moved by the grain boundaries [257]–[260]. In the last section, we observed a clear peak at an angle corresponding to the twin boundary (60°) (see Figure 114). It implies that twining plays a significant role in the deformation behavior in our study as well. Usually, twins can be classified as incoherent and coherent twins. It is believed that the coherent twin is the straight lines, whereas incoherent twins are curves. Also, twins are favorable sites for DRX nucleation due to their high stored energy [261]. In this study, annealing twins are characterized by a misorientation angle of 60° about the axis with a tolerance angle of 8.66° described by Brandon’s criterion [262], regardless of their coherent versus incoherent character.

The area fraction of the twin 60° <111> is shown in Figure 115. Initially, there is a negligible amount of twins in the initial undeformed sample. The number of twins gradually increases as the deformation temperature and strain rate increase.

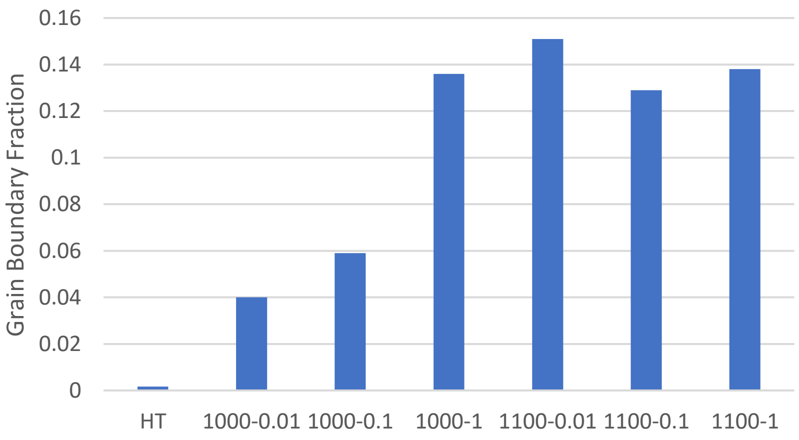

Figure 114: Average area fraction for annealing twins in the deformed samples.

To quantify the annealing twinning, we have calculated the twin boundary per grain and twin density. Twin boundary per grain indicated the twin fraction inside an individual grain and can be expressed as [226].

$$N_G = \frac{N_2 - N_1}{N_1}$$

Equation 41

Where N_2: total grains including the twin boundaries, N_1: number of grains ignoring twin boundaries.

Twin density is considered a number of twin boundaries intercept per unit length and mathematically expressed as [263].

$$N_{\mathrm{L}} = \frac{L_{TB}2}{S\pi}$$

Equation 42

L_{TB} represents twin boundary length, and S is the corresponding area.

The twin boundary per grain increases with an increase in strain rate; also, it is highest for the samples deformed at 1100 °C. It is consistent with the grain size. Smaller the grain size, the smaller the twin boundary per grain. Therefore, it can be implied that the smaller grains are free from twins, which can also be observed in Figure 116. Also, these samples show the highest elongation, and serrations in the flow curves indicate continuous DRX cycles. Therefore, as the DRX progresses, most boundaries lose their twin character [264]. However, the twin density decreases with increased strain rate and temperature. The twin density is inversely proportional to the square of the corresponding grain size, as explained in [265].

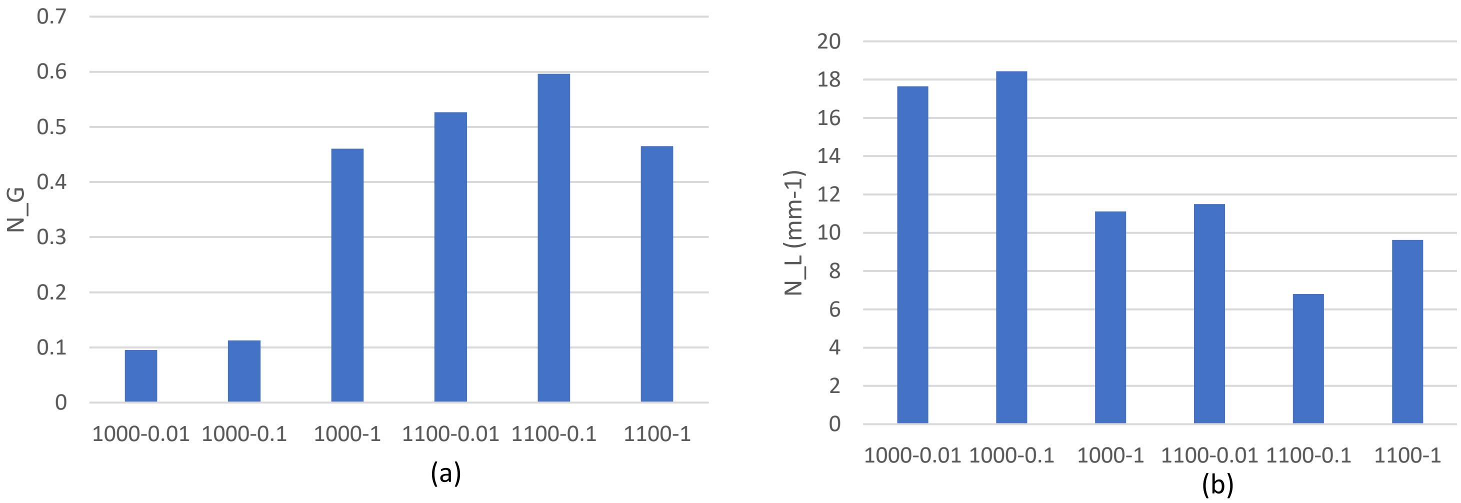

Figure 115: (a) Twin boundary per grain, (b) twin density for the deformed samples.

6.3.4.5. Twin Boundary Interactions

The information regarding the structure of the HAGBs is less known than LAGBs. Some of the HABGs can be regarded as special boundaries. For example, the coherent twin boundaries, also known as low Σ boundaries (annealing twin boundaries, Σ3), have a relatively regular structure and confer special interfacial properties. While the high Σ values, commonly bigger than Σ27, are regarded as general or random boundaries. Therefore, it is interesting to know the interaction behavior of low Σ boundaries.

The interaction between primary twins (Σ3) and high order twins (Σ9, Σ27) characterized by the Brandon rule is studied. The CSL model states that the misorientations must be conserved at the triple points to complete the entire circuit. This conservation can be given by "the sigma combination rule," i.e.

$$\Sigma a \cdot \Sigma b = m \cdot \Sigma c^2$$

Equation 43

, where Σa, Σb, and Σc are the Σ values of the three boundaries that meet at the triple junction. The scalar quantity m can be any common divisor of Σa and Σb.

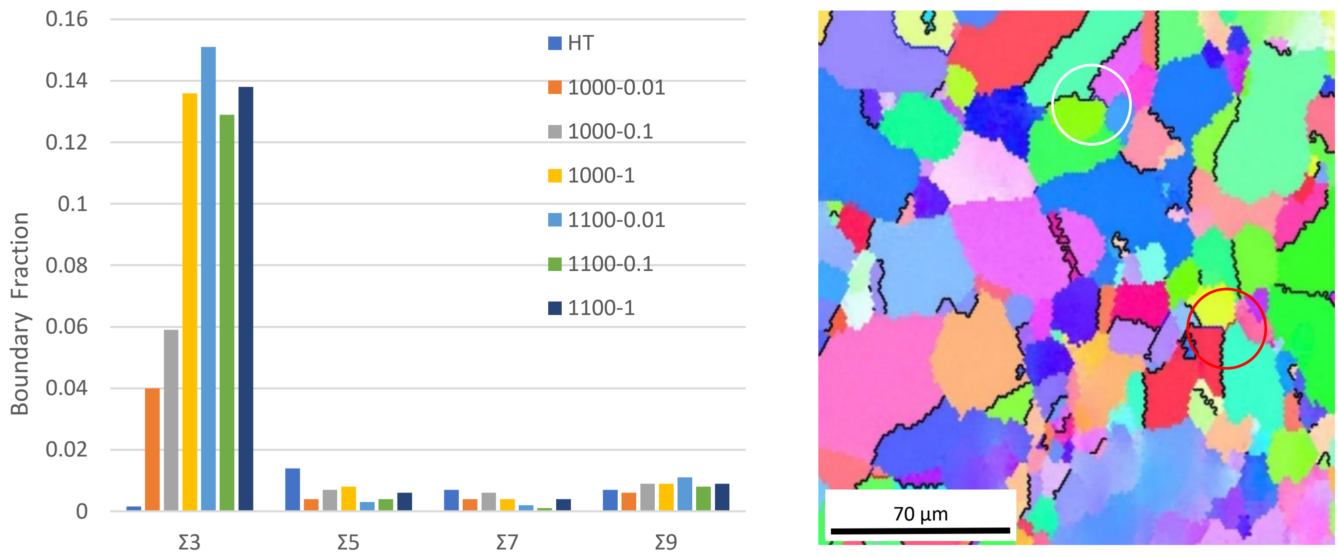

(a)

(b)

Figure 116: (a) Grain boundary character distribution, (b) Interaction between annealing twins in a grain for sample deformed at 1100 C and stain rate 0.1 s-1 (Black lines: Σ3 boundaries, Blue lines: Σ9, Brown line: Σ27).

For example, when the two Σ3 twins meet at a triple junction, it yields to the Σ9 boundary as shown in Figure 117b (marked by white circle). Similarly, when a Σ3 and Σ9 boundary meets at the triple junction, it generates either Σ3 boundary or Σ27 boundary, also shown in Figure 117b (encircled in red). If the number of twins is higher in grain, it can form high order twins by interaction at triple points. The energy and dislocation density at triple points is higher than the neighboring grain boundaries. Therefore, triple pints can also be a nucleating site for DRX [266], [267].

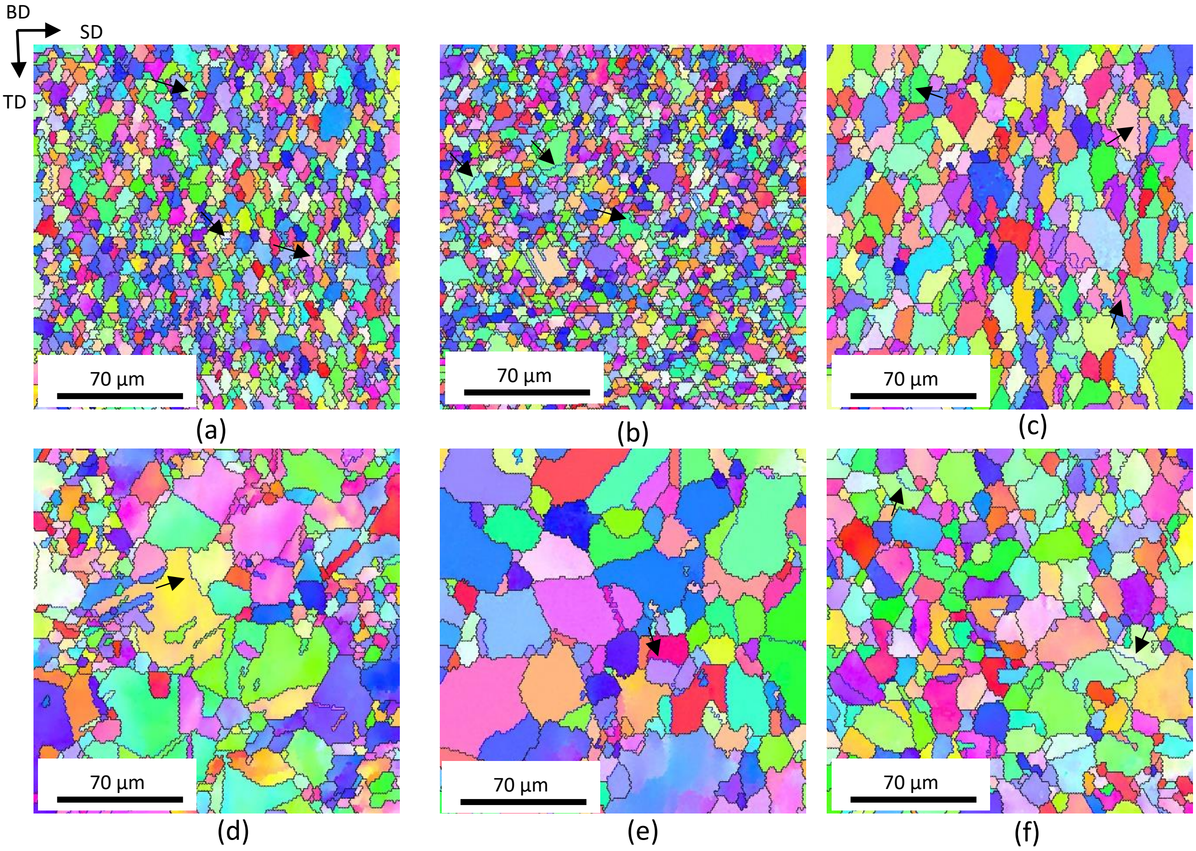

Figure 117: Twin boundaries marked in blue presented for samples. The arrows indicated the evolution of twins behind the moving grain boundary.

Most of the twins are observed in the large grains, and small grains are twin-free. Similar observations have been reported in previous studies as well [268]. It is also noted that the annealing twins typically form inside the recrystallized grains behind the migrating grain boundary. Azarbarmas et al. [268] reported the nucleation of DRX grains through the formation of annealing twins and step-wise explained the process for the sample deformed at 1100 °C and strain rate 0.1 s-1. The serrated grain boundaries are first formed, followed by the bulging phenomenon. Then the twins start to form behind the bulged grains. Similar observations are also reported in our study (Figure 118). It implies that the annealing twinning plays a critical role in the nucleation and growth of new recrystallized grains.

6.3.4.6. Grain Orientation Spread

Different methodologies are reported to distinguish DRX grains and deformed grains. For example, Mandal et al. used grain size to determine the DRX grains from deformed grains

[269]. However, this criterion can only be used when there is a clear difference between DRX grains and deformed grains [40]. Other methods are based on the EBSD image quality (IQ) and calculation of grain orientation spread from the EBSD map. The image quality (IQ) method assumes that the IQ of the recrystallized grain is higher than the deformed grains. But the IQ can be affected by the quality of the polished sample as well. Therefore, it is not advisable to use IQ for portioning the DRX grains from the deformed grains. GOS value represents the average difference of the misorientation angles to the grain mean orientation. GOS can be mathematically expressed as [270]

$$GOS = \frac{1}{N}\sum_{A=1}^{N}\left\{\min\left\{cos^{-1}\left(\frac{trace(g_{ave}[h_i g^A] - 1)}{2}\right)\right\}\right\}$$

Equation 44

Where A: A$^{\text{th}}$ measurement point in a grain consisting N points; g_{ave}: average orientation of the grain; g^A: orientation measured at the A$^{\text{th}}$ position in a grain; h_i: appropriate symmetry element resulting in minimum misorientation angle between the A$^{\text{th}}$ measurement and the average orientation.

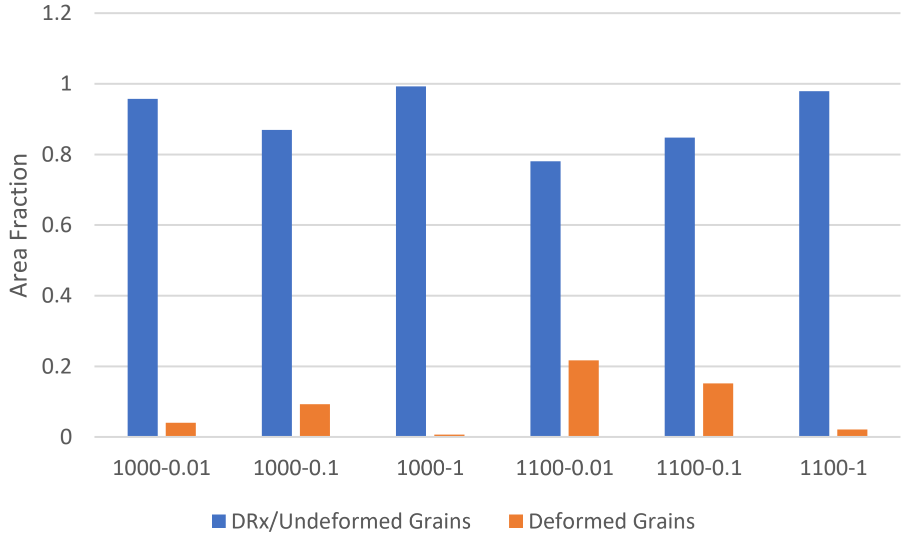

Figure 118: Area fraction of the DRX/undeformed grains and deformed grains based on GOS.

GOS of the DRX or strain-free grains is <2° and for deformed grains >2° [227]. Figure 119 shows the area fraction of the two distinct regions, i.e., DRX grains or Undeformed grains (GOS <2°) and deformed grains (GOS: 5°-10°). The area fraction of the recrystallized grains increases with the strain rate for both temperatures. A slight discrepancy for the 1000-0.1 sample could be arisen due to the variation linked to the sample location of the EBSD measurement. Also, it could be observed that the 1100 °C samples have the highest number of deformed grains compared to 1000 °C. The possible reason for this could be that the samples fracture or break even before the complete recrystallization is achieved due to thermal softening. This can also be proved based on the stress-strain curves that samples at temperature 1100 °C show less strain than samples at 1000 °C.

6.3.5. Recrystallization Mechanism

In metals, especially in low or medium stacking flow energy materials such as Nickel, copper and austenitic iron, the recovery process is slow, leading to dynamic recrystallization if the critical deformation condition is met. In simple terms, new grains nucleate at the old grain boundaries, but as the material continues to deform, the dislocation density of the new grains increases, which inhibits further grain growth. Another factor that could cease the growth of the newly recrystallized grains is the nucleation of other grains at the migrating boundaries. If the clear distinction between stages of nucleation and growth is visible, this is called discontinuous dynamic recrystallization (DDRX) or, generally, DRX [271]–[275]. Another mechanism that leads to the formation of HAGBs during thermomechanical deformation is continuous dynamic recrystallization (CDRX). In DDRX, grain boundary bulging is a prelude to the new grain growth. The development of subgrain boundaries near the pre-existing HAGBs provides the driving force for bulging. New grains nucleate at the boundaries of the growing grains, leading to the thickening of the grains observed. If there is a significant difference between the newly recrystallized grain size and initial grain size, the so-called "necklace" structure could be observed. The mean grain size of the recrystallized grains does not change as the recrystallization proceeds.

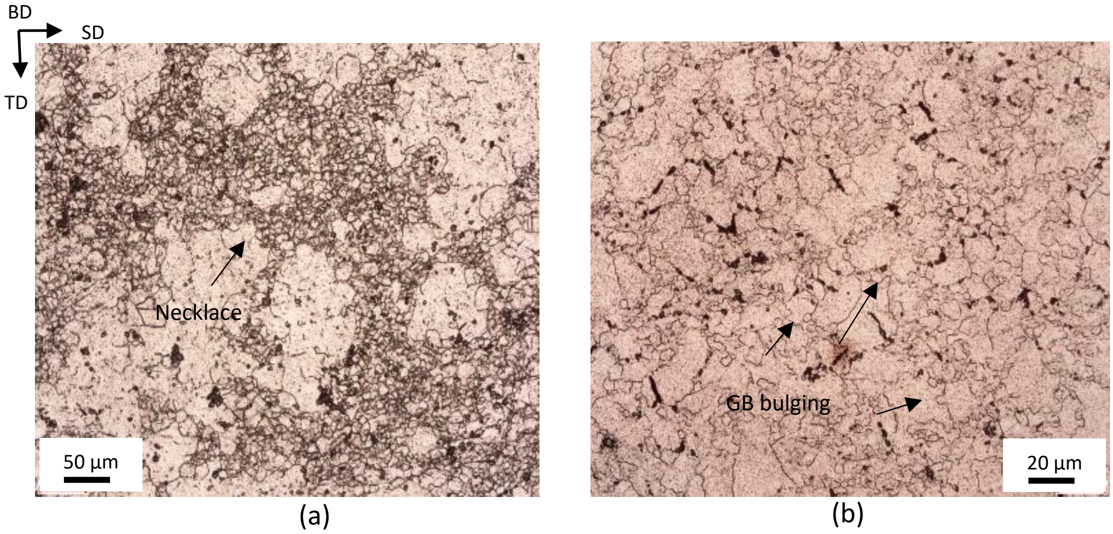

Figure 119: Optical micrographs of etched samples deformed at 1100 °C and strain rate, (a) 0.01 s-1, (b) 0.1 s-1.

Contrary to DDRX, in CDRX, the new grains transform subgrain boundaries into HAGBs. The mechanisms by which the subgrain rotation occurs are not yet evident. Still, it is usually found in the materials in which the dislocation motion is inhibited either by lack of slip systems or solute drags such as High stacking fault materials (Magnesium, Aluminium alloys) [276]. Unlike DDRX, the nucleation and growth stages are not distinguishable.

Grain boundary bulging could be seen in the Optical micrograph shown for sample 1100 °C-0.01 s-1 as shown in Figure 120. Therefore, it can be implied that the DDRX is the primary recrystallization mechanism in Inconel 718, as reported in the literature [268]. The cumulative misorientations along the HAGBs and from grain interior to the grain boundary are examined in Figure 121 and 122. As can be seen, in none of the samples, the misorientation exceeds the 8°. As for CDRX, a misorientation angle between 10-15° is required for the nucleation and growth of new grain [277]. Also, the fraction of LAGBs is not significantly higher in deformed samples. The LAGBs fraction for the samples deformed at temperatures of 1000 and 1100 °C

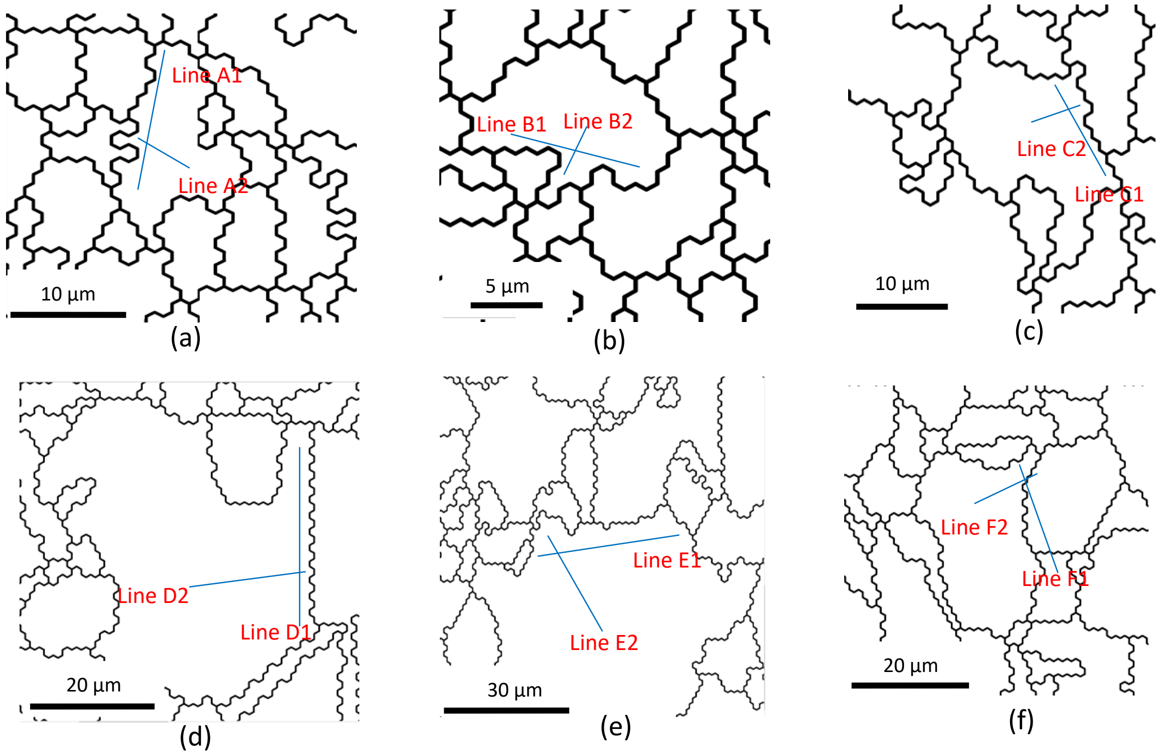

Figure 120: Grains indicating the lines in the grains for cumulative misorientation presented in Figure 122.

and at strain rates of 0.01, 0.1, and 1 s-1 are 0.123, 0.103, 0.096 and 0.158, 0.029, 0.086,

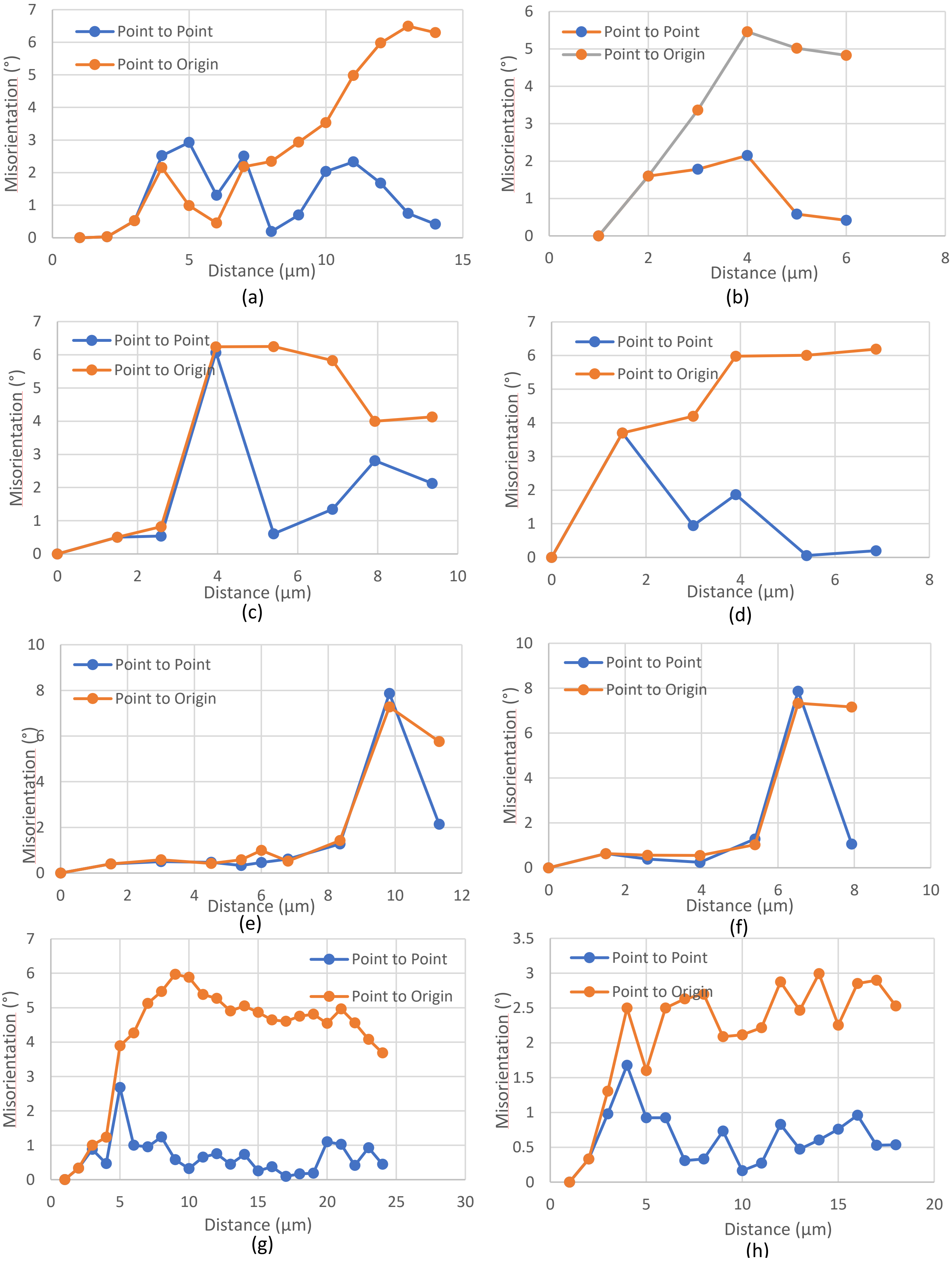

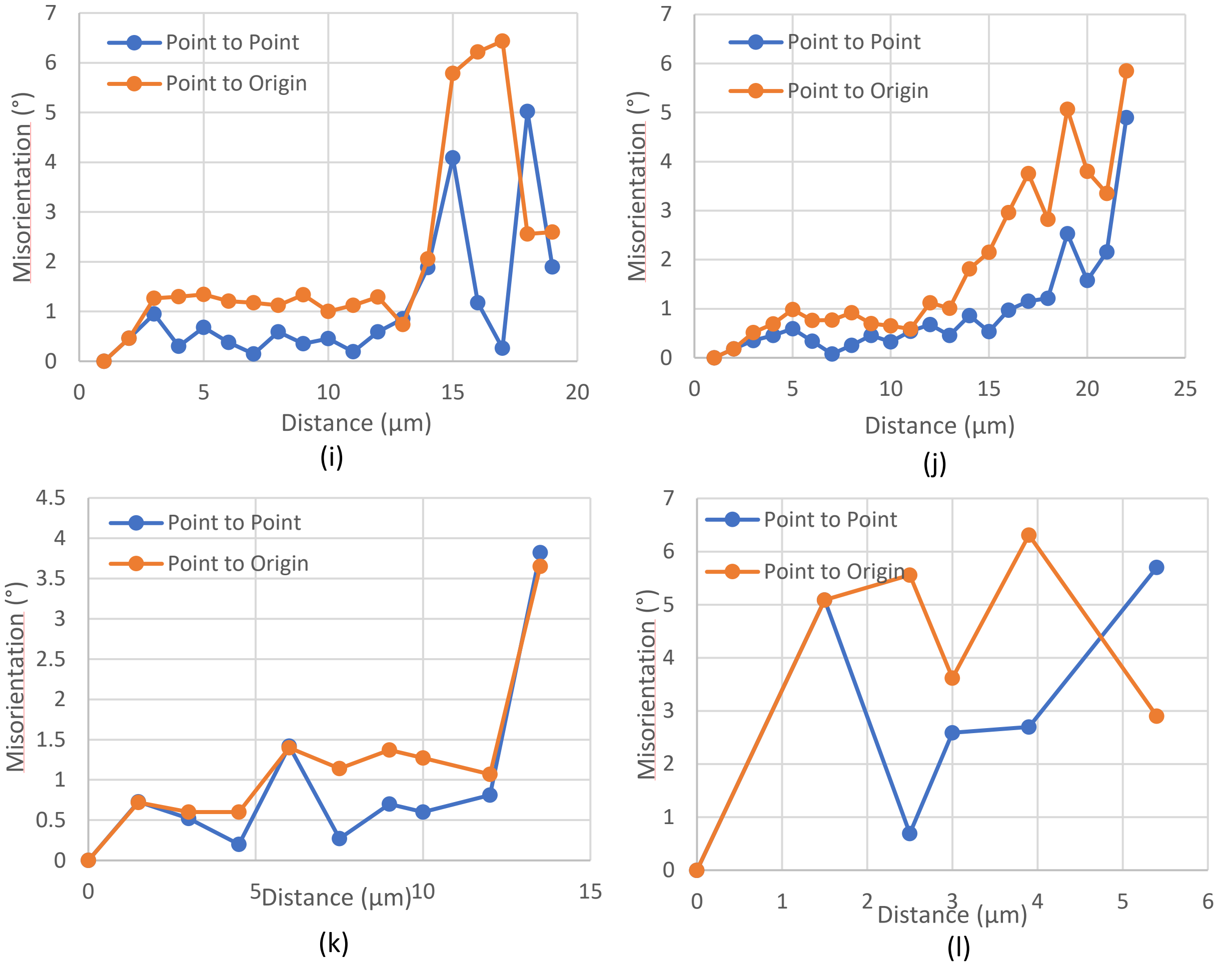

Figure 121: Cumulative misorientation for the lines indicated in Figure 121 (a, b) Line A1 &A2, (c, d) Line B1 & B2, (e, f) Line C1 & C2, (g, h) Line D1 & D2. (i, j) Line E1 &E2, and (k, l) Line F1 & F2, respectively.

respectively.

Although the cumulative misorientations along the grain boundaries and within the grain do not provide concrete evidence of CDRX, we found recrystallized grains inside the grains for the samples deformed at 1100 °C, as shown in Figure 123. No such grain formation is observed for deformation temperature of 1000 °C, and the number of such recrystallized grains is minimal for 1100 °C samples. The reason could be that some of the sub-grain boundaries may have formed in the initial grains at the early stage of deformation in a localized way. As the deformation progresses, the sub-grain boundaries rotate through constant dislocations absorption and finally transform into HAGBs. Therefore, it can be implied that the CDRX could happen at a deformation temperature of 1100 °C in a very localized way. Similar findings are also reported by Wang et al. [226].

This concludes that the DDRX is predominantly the primary DRX mechanism and annealing twinning, but CDRX could also be observed. A further study on the evolution of grains during the CDRX mechanism is highly needed.

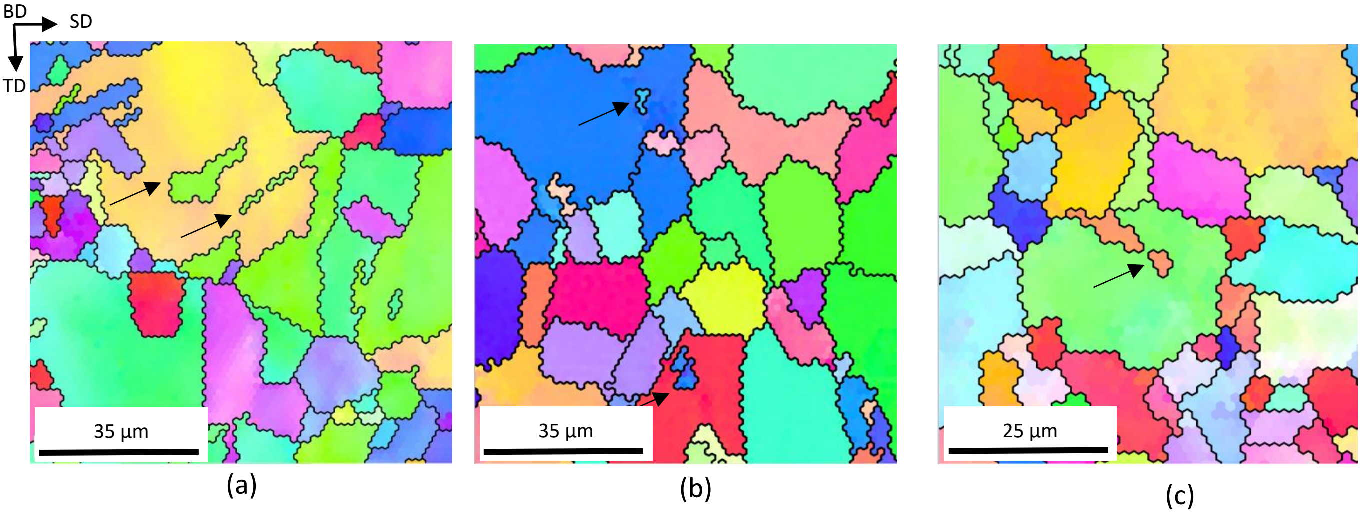

(a) (b) (c)

Figure 122: Evolution of inner grains for samples deformed at 1100 C and strain rates of (a) 0.01 s-1, (b) 0.1 s-1, and (c) 1s-1.

6.4. Conclusions

Our study of the phenomena induced by laser/powder interactions had a double objective: (i) to exploit the in-situ measurement systems available on the industrial devices of the different partners of the project; (ii) to characterise the behaviour of the materials during their elaboration by the processes studied within the framework of the ENABLE project with the aim of being able to feed representative behaviour laws of the processes. The last chapter of the thesis is devoted to the study of Inconel 718 produced by SLM.

The following can be concluded from the above discussed results:

- The flow stress curves obtained for SLMed Inconel 718 samples under hot deformation tests shows that the grain refinement through DRX mechanism is predominant. The presence of serrations confirmed this phenomenon.
- Samples deformed at 1000 °C shows higher elongation compared to the samples deformed at 1100 °C. It can be concluded that the higher softening at elevated temperature of 1100 °C led to the early failure of the samples than 1000 °C samples.
- The calculated Q, i.e., 379.62 KJ/mol for SLMed Inconel 718 samples agrees with the reported values in the literature for Hot compression tests.

- We have also observed that the DRX mechanism progresses with the evolution of the annealing twins. The same is also reported in the literature that commonly, in low stacking fault energy materials the DRX phenomena is followed by the evolution of the annealing twins which helps to reduce the grain boundary energy. The same can also be verified by the misorientation angle which clearly marks that increase in the % of annealing twins during thermo-mechanical deformation.
- Alongside, the interaction among the primary twins (Σ3) and high order twins (Σ9, Σ27) is characterized by the Brandon rule. However, it is noticed the fraction of high order twins (Σ9, Σ27) is limited.
- The characterization of the DRX mechanism into DDRX and CDRX is also investigated. First, the presence of the neckless structure and grain boundary bulging is observed. Therefore, it can be conferred that the DDRX is the predominate mechanism in the SLMed Inconel 718. However, the presence of recrystallized grains inside the primary grains for samples deformed at 1100 °C is also observed which marks the indication of CDRX mechanism. But the frequency of these types of grains is limited and further investigation is needed.

CONCLUSIONS

“

This section concludes the key findings reposted in this thesis. The conclusion is summarized chapter wise. Along with the findings, the industrial benefits of the proposed methodology are also proposed and discussed.

Influence of scanning strategies for AlSi7Mg0.6

- The stripes have higher densification than chessboard strategy due to the present lack of fusion porosity at the junction of the islands. Also, the stripes with rotation exhibit good mechanical properties such as tensile strength and hardness.
- Microstructurally, both equiaxed and columnar grains are observed, which is linked to a higher value of G at the melt boundary. The same microstructure has been reported for AlSi10Mg alloys as well. Three distinct regions within the melt pool are investigated, i.e., fine, coarse, and HAZ zone. A Si-rich phase existed as a fibrous structure in a pseudo eutectic structure.
- Cooling rates are estimated using the cell size within the melt pool, and it can be concluded that the cooling rates vary within the melt pool due to rapid cooling. The center or top of the melt pool has the highest cooling rates, and it decreases gradually at the end edge of the melt pool. However, no significant distinction is observed w.r.t. different scanning parameters.
- Finally, the residual stresses at the surface and 2 mm depth are studied along the scanning direction, i.e., longitudinal and transverse direction. For all the samples, the residual stresses are higher in the longitudinal direction compared to the transverse direction. The higher stresses are observed at the center of the samples compared to the two edges. The higher residual stresses are observed for 2 mm depth. But no significant pattern is observed w.r.t. to scan vector length and rotation.

Melt Pool Monitoring

- The sensitivity analysis of the MPM revealed that the melt pool emissions are proportionally dependent on the input volumetric energy density especially scanning speed and laser power. The effect of the hatch distance is not very significant in the case of MPM sensitivity.

- The detectability of ADC1 and ADC2 also varies as the detection range of both photodiodes is different. It is noticed that ADC2 captures the melt pool anomalies more significantly than ADC1.
- Using of ML techniques such as SVM, showed a possibility to detect the anomalies in the parts. However, the ML techniques require a good set of labelled datasets for training which is often expensive and laborious task. Therefore, need for more two steps data processing is required combining statistical and ML techniques.
- We showed that the statistical approach combining PCA, T2 Hotelling's statistics and average true range is much robust method to detect the most volatile layers with in a part at global scale (layer level).
- We used a ML model called LSTM-AE to detect the exact location of the defects or anomalies mainly hotspots at local scale (melt pool level). However, the global level is robust to check the overall quality of the part very quickly and local scale approach is relatively computationally expensive and should be used in conjunction with the global scale.
- The MPM system provided by SLM solutions is a robust tool to qualitatively monitor the final part's quality. Still, the quantitative comparison of the melt pool signals to CT scan is tricky and complicated. The reason could be that the MPM captures the signal coaxially, which allows it to follow the melt pool in real-time along with the laser. Still, most anomalies, such as porosities, tend to form during the solidification. Therefore, it is hard to make a quantitative comparison for porosity detection.
- Determination of the spatial resolution of the MPM data is also a challenging task as the detection spot of the photodiode is smaller than the laser spot diameter. The exact number cannot be revealed due to the confidentiality clause.

Layer Control System

- The layer control system captures two different process steps, i.e., pre-exposure and post-exposure. It is noticed that LCS can capture the powder-bed spread anomalies such as part over-heating, part hopping, uneven powder spread, recoater streaking, and debris. The quality of the powder-bed spread should be studied in link with the MPM signal.

- The hierarchy of the powder bed anomalies is also clearly observed. Firstly, part overheating and part hopping start to occur, followed by the recoater streaking and uneven powder spread. This hierarchy can help mitigate the anomalies and part failure.
- We proposed two different computer vision algorithms such as CNN and Res-Unet to detect the above discussed anomalies. However, the Res-Unet outperforms the CNN approach in terms of anomalies localization. Also, the problem of scale variancy of defects can also be overcome by the use of semantic segmentation approach.

Optical Tomography

- EOSTATE OT supplied from EOS GmbH is a camera-based co-axial in-situ monitoring system that successfully captures the melt pool emissions, i.e., directly linked to material health. The final image of individual layers compresses the many images obtained along with the laser movement. Therefore, it should be kept in mind that a loss of information occurs during image compression. However, the OT captures the key variabilities and, if used with machine learning approaches, can help improve the quality assurance of the final part.

Thermomechanical Deformation of Inconel 718

- Torsion tests performed at elevated temperatures of 800, 1000, and 1100 °C with strain rates of 0.01, 0.1, and 1 s-1 provides an experimental basis for the development of the constitutive behaviour law for the SLMed Inconel 718 alloys.
- The obtained activation energy results are in conjunction with the reported results for hot compression tests. The presence of the serrations in the obtained curves confirms the onset of the DRX mechanism. Also, the increase in the % of the annealing twins concludes that the annealing twining is also predominate alongside the DRX.
- The so called “Necklace” structure and grain boundary bulging is observed for the SLMed samples which confirms the DDX is dominant by the DDRX mechanism.

Industry Benefits

The completed work in this thesis can be helpful for the industries in several ways, which are as follows:

- The size of the in-situ monitoring data is enormous, making it difficult to process and store for a more extended period. Therefore, the proposed methodology can extract the leading key performance indicators (KPIs) from the in-situ data and prepare a quality chart based on the global and local scale of the part.

- The inter-dependability of the various process steps can also be helpful to mitigate the anomalies and identify the root cause for the melt pool instabilities. No such studies have been reported as per the author’s findings.

FUTURE OUTLOOK

> “
>
> As discussed, L-PBF process monitoring is still in its infancy stage. There is lot scope in terms of enhancing the quality assurance and relatability of the overall process using in-situ monitoring hardware and data analytics techniques. Here we present, some of the possible future perspective related to L-PBF process monitoring using data analytics techniques.

- *Defects specific melt pool signals:* It is pertinent to study and explore the melt pool signals for various defects such as lack of fusion, keyhole, and overheating. The local powder characteristics can significantly lead to multiple defects, and it is essential to classify the melt pool signals based on defects variability.
- *The link between powder bed and melt pool signal:* Our study shows that the melt pool variability is linked to the powder-bed spread characteristics. Therefore, further analysis is required related to the temporal occurrence of powder-bed spread and melt pool signal.
- *Process steps interlinking:* It is vital to develop and interlink the effect of variability of the input parameters on the output results. For example, the humidification of initial feedstock material can strongly influence powder flowability and spreadability, directly affecting melt pool morphology and thermal emissions. Also, the dissociation of oxide layers during the layer can result in the release of hydrogen and oxygen gas in the environment which eventually can affect the final part properties.
- *Closed Feedback Control Loop:* The ultimate aim of using data analytics techniques and in-situ monitoring instrumentation is to develop an intelligent L-PBF process that monitors and controls the process based on the quality of each layer. The proposed methodology can be used for real monitoring and decision making, as shown in Figure 124. It can allow the user to stop manufacturing if the critical characteristics of anomalies are prevalent in respective layers. It can significantly save powder, energy, and other resources. Also, it will be a step forward to a sustainable L-PBF process.

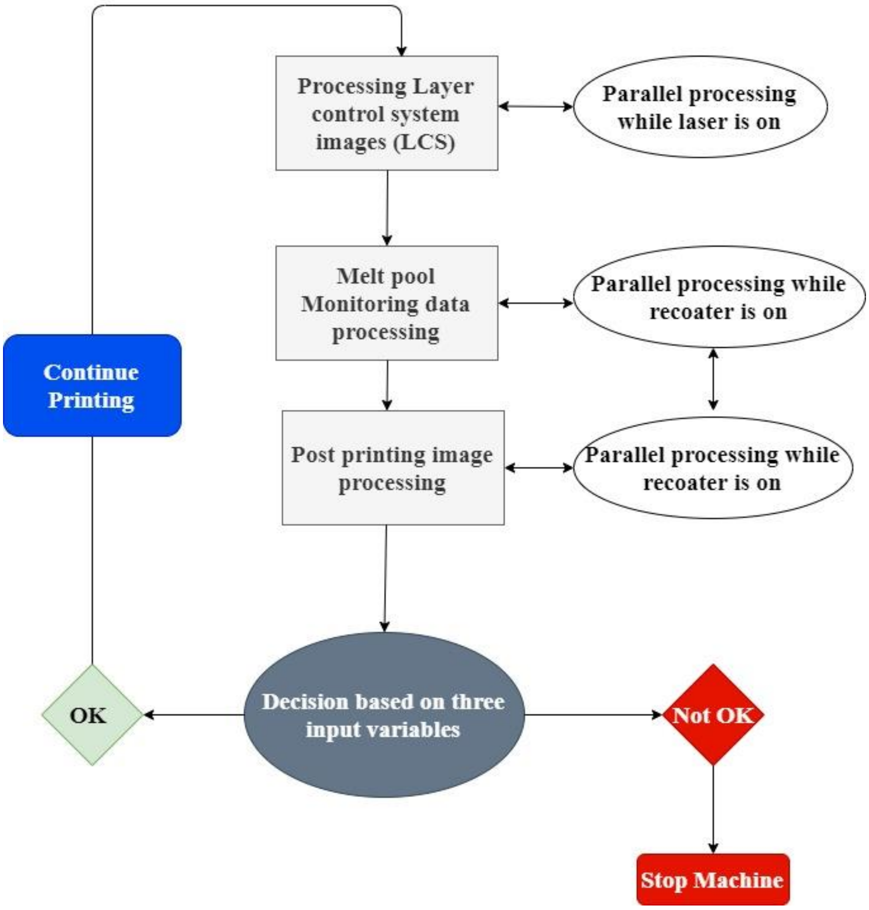

Figure 123: Feedback control loop for L-PBF process.

- *AI-based model:* Developing an AI-based model on overall monitoring of the L-PBF process autonomously will fully realize the data analytics and instrumentation capabilities. The AI-based models are developed based on the input characteristics (powder size distribution, powder morphology, humidity, flowability), process characteristics (inert gas flow, powder spreadability, oxygen monitoring), in-situ process characteristics (melt pool emissions, powder-bed spread, laser power monitoring, strain monitoring, geometrical precision monitoring for individual layers), design characteristics (support structures suitability, design constraints such as overhang) and part characteristics (mechanical properties, geometric accuracy, part density) will provide an ultimate guide for quality assurance of the final part and it will enhance the consumer's confidence-building measures.
- *Development of an open instrumented bench:* The commercial in-situ monitoring systems are very closed and act as "Black-Box" that makes them difficult to study in greater details. Therefore, the understanding of the laser-material interaction behaviour

and its characteristics can be exploited with the development of an open instrumented bench. The know-how and results obtained on these open systems can be homogenized with the commercial systems to improve and check the overall quality of the part in L-PBF process.

- *Constitutive material behavior law:* Other than process monitoring, it is also vital to develop AM part-specific constitutive material behavior law models and should be calibrated with experimental data. Chapter 6 focuses on providing the experimental data for the thermomechanical behavior of the L-PBF processed parts. The same has to be realized for different alloys.
- *Advanced Manufacturing:* Different AM processes discussed in the literature review possess limitations and advantages. Therefore, it is essential to bring different techniques to achieve the full potential of the AM. We presented a feasibility study using the L-PBF process and the LMD process together. Similarly, further investigations on the interface compatibility of the different techniques are required.

REFERENCES

[1] I. ASTM, 'ASTM52921-13 Standard Terminology for Additive Manufacturing-Coordinate Systems and Test Methodologies', *West Conshohocken ASTM Int.*, 2013.

[2] J.-P. Kruth, M.-C. Leu, and T. Nakagawa, 'Progress in additive manufacturing and rapid prototyping', *Cirp Ann.*, vol. 47, no. 2, pp. 525–540, 1998.

[3] C. W. Hull, 'inventor; Uvp, Inc., assignee', *Appar. Prod. Three-Dimens. Objects Ster. U. S. Pat. US*, vol. 4, no. 575, p. 330, 1986.

[4] ISO 17296-2: 2015, 'Additive manufacturing-General principles-Part 2: overview of process categories and feedstock'.

[5] L. A. Dobrzański, A. D. Dobrzańska-Danikiewicz, A. Achtelik-Franczak, L. B. Dobrzański, M. Szindler, and T. G. Gawe\l, 'Porous selective laser melted Ti and Ti6Al4V materials for medical applications', *Powder Metall. Case Stud. InTech Rij. Croat.*, pp. 161–181, 2017.

[6] P. Fischer, V. Romano, H.-P. Weber, N. P. Karapatis, E. Boillat, and R. Glardon, 'Sintering of commercially pure titanium powder with a Nd: YAG laser source', *Acta Mater.*, vol. 51, no. 6, pp. 1651–1662, 2003.

[7] R. J. Hebert, 'Metallurgical aspects of powder bed metal additive manufacturing', *J. Mater. Sci.*, vol. 51, no. 3, pp. 1165–1175, 2016.

[8] J. P. Kruth, M. Bartscher, S. Carmignato, R. Schmitt, L. De Chiffre, and A. Weckenmann, 'Computed tomography for dimensional metrology', *CIRP Ann.*, vol. 60, no. 2, pp. 821–842, 2011.

[9] B. Song, S. Dong, S. Deng, H. Liao, and C. Coddet, 'Microstructure and tensile properties of iron parts fabricated by selective laser melting', *Opt. Laser Technol.*, vol. 56, pp. 451–460, 2014.

[10] P. Karimi, T. Raza, J. Andersson, and L.-E. Svensson, 'Influence of laser exposure time and point distance on 75-μm-thick layer of selective laser melted Alloy 718', *Int. J. Adv. Manuf. Technol.*, vol. 94, no. 5–8, pp. 2199–2207, Feb. 2018, doi: 10.1007/s00170-017-1019-1.

[11] S. Das, 'Physical aspects of process control in selective laser sintering of metals', *Adv. Eng. Mater.*, vol. 5, no. 10, pp. 701–711, 2003.

[12] H. Gong, K. Rafi, H. Gu, T. Starr, and B. Stucker, ‘Analysis of defect generation in Ti–6Al–4V parts made using powder bed fusion additive manufacturing processes’, *Addit. Manuf.*, vol. 1, pp. 87–98, 2014.

[13] C. Weingarten, D. Buchbinder, N. Pirch, W. Meiners, K. Wissenbach, and R. Poprawe, ‘Formation and reduction of hydrogen porosity during selective laser melting of AlSi10Mg’, *J. Mater. Process. Technol.*, vol. 221, pp. 112–120, 2015.

[14] J. Svenungsson, I. Choquet, and A. F. H. Kaplan, ‘Laser Welding Process – A Review of Keyhole Welding Modelling’, *Phys. Procedia*, vol. 78, pp. 182–191, Jan. 2015, doi: 10.1016/j.phpro.2015.11.042.

[15] R. Cunningham *et al.*, ‘Keyhole threshold and morphology in laser melting revealed by ultrahigh-speed x-ray imaging’, *Science*, vol. 363, no. 6429, pp. 849–852, 2019.

[16] Q. C. Liu, J. Elambasseril, S. J. Sun, M. Leary, M. Brandt, and P. K. Sharp, ‘The effect of manufacturing defects on the fatigue behaviour of Ti-6Al-4V specimens fabricated using selective laser melting’, in *Advanced Materials Research*, 2014, vol. 891, pp. 1519–1524.

[17] T. Vilaro, C. Colin, and J.-D. Bartout, ‘As-fabricated and heat-treated microstructures of the Ti-6Al-4V alloy processed by selective laser melting’, *Metall. Mater. Trans. A*, vol. 42, no. 10, pp. 3190–3199, 2011.

[18] S. Clijsters, T. Craeghs, S. Buls, K. Kempen, and J.-P. Kruth, ‘In situ quality control of the selective laser melting process using a high-speed, real-time melt pool monitoring system’, *Int. J. Adv. Manuf. Technol.*, vol. 75, no. 5–8, pp. 1089–1101, Nov. 2014, doi: 10.1007/s00170-014-6214-8.

[19] N. Read, W. Wang, K. Essa, and M. M. Attallah, ‘Selective laser melting of AlSi10Mg alloy: Process optimisation and mechanical properties development’, *Mater. Des. 1980-2015*, vol. 65, pp. 417–424, 2015.

[20] K. Antony and N. Arivazhagan, ‘Studies on energy penetration and Marangoni effect during laser melting process’, *J Eng Sci Technol*, vol. 10, no. 4, pp. 509–525, 2015.

[21] D. Gu and Y. Shen, ‘Balling phenomena in direct laser sintering of stainless steel powder: Metallurgical mechanisms and control methods’, *Mater. Des.*, vol. 30, no. 8, pp. 2903–2910, 2009.

[22] R. Li, J. Liu, Y. Shi, L. Wang, and W. Jiang, ‘Balling behavior of stainless steel and nickel powder during selective laser melting process’, *Int. J. Adv. Manuf. Technol.*, vol. 59, no. 9, pp. 1025–1035, 2012.

[23] N. K. Tolochko *et al.*, ‘Balling processes during selective laser treatment of powders’, *Rapid Prototyp. J.*, 2004.

[24] P. Mercelis and J.-P. Kruth, ‘Residual stresses in selective laser sintering and selective laser melting’, *Rapid Prototyp. J.*, 2006.

[25] N. J. Harrison, I. Todd, and K. Mumtaz, ‘Reduction of micro-cracking in nickel superalloys processed by Selective Laser Melting: A fundamental alloy design approach’, *Acta Mater.*, vol. 94, pp. 59–68, 2015.

[26] P. Mercelis, ‘Control of selective laser sintering and selective laser melting processes’, 2007.

[27] L. N. Carter, C. Martin, P. J. Withers, and M. M. Attallah, ‘The influence of the laser scan strategy on grain structure and cracking behaviour in SLM powder-bed fabricated nickel superalloy’, *J. Alloys Compd.*, vol. 615, pp. 338–347, 2014.

[28] L. Carter, M. Attallah, and R. Reed, ‘Laser Powder Bed Fabrication of Nickel-base Superalloys: Influence of Parameters; Characterisation, Quantification and Mitigation of Cracking’, p. 10.

[29] L. N. Carter *et al.*, ‘Process optimisation of selective laser melting using energy density model for nickel based superalloys’, *Mater. Sci. Technol.*, vol. 32, no. 7, pp. 657–661, May 2016, doi: 10.1179/1743284715Y.0000000108.

[30] J.-P. Kruth, J. Deckers, E. Yasa, and R. Wauthlé, ‘Assessing and comparing influencing factors of residual stresses in selective laser melting using a novel analysis method’, *Proc. Inst. Mech. Eng. Part B J. Eng. Manuf.*, vol. 226, no. 6, pp. 980–991, Jun. 2012, doi: 10.1177/0954405412437085.

[31] L. Mugwagwa, D. Dimitrov, S. Matope, and I. Yadroitsev, ‘Influence of process parameters on residual stress related distortions in selective laser melting’, *Procedia Manuf.*, vol. 21, pp. 92–99, 2018.

[32] T. Mishurova *et al.*, ‘The Influence of the Support Structure on Residual Stress and Distortion in SLM Inconel 718 Parts’, *Metall. Mater. Trans. A*, vol. 49, no. 7, pp. 3038–3046, Jul. 2018, doi: 10.1007/s11661-018-4653-9.

[33] B. Song *et al.*, ‘Differences in microstructure and properties between selective laser melting and traditional manufacturing for fabrication of metal parts: A review’, *Front. Mech. Eng.*, vol. 10, no. 2, pp. 111–125, 2015.

[34] A. Townsend, N. Senin, L. Blunt, R. K. Leach, and J. S. Taylor, ‘Surface texture metrology for metal additive manufacturing: a review’, *Precis. Eng.*, vol. 46, pp. 34–47, 2016.

[35] G. Strano, L. Hao, R. M. Everson, and K. E. Evans, ‘Surface roughness analysis, modelling and prediction in selective laser melting’, *J. Mater. Process. Technol.*, vol. 213, no. 4, pp. 589–597, 2013.

[36] B. M. Sharratt, ‘Non-destructive techniques and technologies for qualification of additive manufactured parts and processes’, *No March*, 2015.

[37] L. Thijs, F. Verhaeghe, T. Craeghs, J. Van Humbeeck, and J.-P. Kruth, ‘A study of the microstructural evolution during selective laser melting of Ti–6Al–4V’, *Acta Mater.*, vol. 58, no. 9, pp. 3303–3312, 2010.

[38] I. Yadroitsev, P. Bertrand, and I. Smurov, ‘Parametric analysis of the selective laser melting process’, *Appl. Surf. Sci.*, vol. 253, no. 19, pp. 8064–8069, 2007.

[39] K. Sun, W. Peng, L. Yang, and L. Fang, ‘Effect of SLM processing parameters on microstructures and mechanical properties of Al0. 5CoCrFeNi high entropy alloys’, *Metals*, vol. 10, no. 2, p. 292, 2020.

[40] N. T. Aboulkhair, N. M. Everitt, I. Ashcroft, and C. Tuck, ‘Reducing porosity in AlSi10Mg parts processed by selective laser melting’, *Addit. Manuf.*, vol. 1, pp. 77–86, 2014.

[41] G. Zenzinger, J. Bamberg, A. Ladewig, T. Hess, B. Henkel, and W. Satzger, ‘Process monitoring of additive manufacturing by using optical tomography’, in *AIP Conference Proceedings*, 2015, vol. 1650, no. 1, pp. 164–170.

[42] T. Kurzynowski, E. Chlebus, B. Kuźnicka, and J. Reiner, ‘Parameters in selective laser melting for processing metallic powders’, in *High Power Laser Materials Processing: Lasers, Beam Delivery, Diagnostics, and Applications*, 2012, vol. 8239, p. 823914.

[43] P. Lott, H. Schleifenbaum, W. Meiners, K. Wissenbach, C. Hinke, and J. Bültmann, ‘Design of an optical system for the in situ process monitoring of selective laser melting (SLM)’, *Phys. Procedia*, vol. 12, pp. 683–690, 2011.

[44] R. J. Smith, M. Hirsch, R. Patel, W. Li, A. T. Clare, and S. D. Sharples, ‘Spatially resolved acoustic spectroscopy for selective laser melting’, *J. Mater. Process. Technol.*, vol. 236, pp. 93–102, 2016.

[45] H. M. Wang, ‘Materials’ fundamental issues of laser additive manufacturing for high-performance large metallic components’, *Acta Aeronaut. Astronaut. Sin.*, vol. 35, no. 10, pp. 2690–2698, 2014.

[46] F. Caiazzo, F. Cardaropoli, V. Alfieri, V. Sergi, and L. Cuccaro, ‘Experimental analysis of selective laser melting process for Ti-6Al-4V turbine blade manufacturing’, in *XIX International Symposium on High-Power Laser Systems and Applications 2012*, 2013, vol. 8677, p. 86771H.

[47] P. Coates and D. Lowe, *The Fundamentals of Radiation Thermometers*. CRC Press, 2016.

[48] G. Held, *Introduction to light emitting diode technology and applications*. Auerbach publications, 2016.

[49] A. Fathi, A. Khajepour, M. Durali, and E. Toyserkani, ‘Geometry control of the deposited layer in a nonplanar laser cladding process using a variable structure controller’, *J. Manuf. Sci. Eng.*, vol. 130, no. 3, 2008.

[50] M. Zeinali and A. Khajepour, ‘Height control in laser cladding using adaptive sliding mode technique: theory and experiment’, *J. Manuf. Sci. Eng.*, vol. 132, no. 4, 2010.

[51] S. Moylan, E. Whitenton, B. Lane, and J. Slotwinski, ‘Infrared thermography for laser-based powder bed fusion additive manufacturing processes’, in *AIP Conference Proceedings*, 2014, vol. 1581, no. 1, pp. 1191–1196.

[52] S. Berumen, F. Bechmann, S. Lindner, J.-P. Kruth, and T. Craeghs, ‘Quality control of laser-and powder bed-based Additive Manufacturing (AM) technologies’, *Phys. Procedia*, vol. 5, pp. 617–622, 2010.

[53] Y. Li and D. Gu, ‘Thermal behavior during selective laser melting of commercially pure titanium powder: Numerical simulation and experimental study’, *Addit. Manuf.*, vol. 1, pp. 99–109, 2014.

[54] T. Wuest, D. Weimer, C. Irgens, and K.-D. Thoben, ‘Machine learning in manufacturing: advantages, challenges, and applications’, *Prod. Manuf. Res.*, vol. 4, no. 1, pp. 23–45, 2016.

[55] E. Alpaydin, *Introduction to machine learning*. MIT press, 2020.

[56] O. Chapelle, B. Scholkopf, and A. Zien, ‘Semi-supervised learning (chapelle, o. et al., eds.; 2006)[book reviews]’, *IEEE Trans. Neural Netw.*, vol. 20, no. 3, pp. 542–542, 2009.

[57] J. Petrich, C. Gobert, S. Phoha, A. R. Nassar, and E. W. Reutzel, ‘Machine learning for defect detection for PBFAM using high resolution layerwise imaging coupled with post-build CT scans’, 2017.

[58] C. Gobert, E. W. Reutzel, J. Petrich, A. R. Nassar, and S. Phoha, ‘Application of supervised machine learning for defect detection during metallic powder bed fusion additive manufacturing using high resolution imaging.’, *Addit. Manuf.*, vol. 21, pp. 517–528, 2018.

[59] F. Imani, A. Gaikwad, M. Montazeri, P. Rao, H. Yang, and E. Reutzel, ‘Layerwise in-process quality monitoring in laser powder bed fusion’, in *International Manufacturing Science and Engineering Conference*, 2018, vol. 51357, p. V001T01A038.

[60] M. Aminzadeh and T. R. Kurfess, ‘Online quality inspection using Bayesian classification in powder-bed additive manufacturing from high-resolution visual camera images’, *J. Intell. Manuf.*, vol. 30, no. 6, pp. 2505–2523, 2019.

[61] Y. Zhang, G. S. Hong, D. Ye, K. Zhu, and J. Y. Fuh, ‘Extraction and evaluation of melt pool, plume and spatter information for powder-bed fusion AM process monitoring’, *Mater. Des.*, vol. 156, pp. 458–469, 2018.

[62] H. Baumgartl, J. Tomas, R. Buettner, and M. Merkel, ‘A deep learning-based model for defect detection in laser-powder bed fusion using in-situ thermographic monitoring’, *Prog. Addit. Manuf.*, pp. 1–9, 2020.

[63] L. Scime and J. Beuth, ‘Using machine learning to identify in-situ melt pool signatures indicative of flaw formation in a laser powder bed fusion additive manufacturing process’, *Addit. Manuf.*, vol. 25, pp. 151–165, 2019.

[64] L. Scime and J. Beuth, ‘Anomaly detection and classification in a laser powder bed additive manufacturing process using a trained computer vision algorithm’, *Addit. Manuf.*, vol. 19, pp. 114–126, 2018.

[65] G. Repossini, V. Laguzza, M. Grasso, and B. M. Colosimo, ‘On the use of spatter signature for in-situ monitoring of Laser Powder Bed Fusion’, *Addit. Manuf.*, vol. 16, pp. 35–48, 2017.

[66] D. Ye, G. S. Hong, Y. Zhang, K. Zhu, and J. Y. H. Fuh, ‘Defect detection in selective laser melting technology by acoustic signals with deep belief networks’, *Int. J. Adv. Manuf. Technol.*, vol. 96, no. 5, pp. 2791–2801, 2018.

[67] S. A. Shevchik, C. Kenel, C. Leinenbach, and K. Wasmer, ‘Acoustic emission for in situ quality monitoring in additive manufacturing using spectral convolutional neural networks’, *Addit. Manuf.*, vol. 21, pp. 598–604, 2018.

[68] M. Grasso, V. Laguzza, Q. Semeraro, and B. M. Colosimo, ‘In-process monitoring of selective laser melting: spatial detection of defects via image data analysis’, *J. Manuf. Sci. Eng.*, vol. 139, no. 5, 2017.

[69] M. Grasso, A. G. Demir, B. Previtali, and B. M. Colosimo, ‘In situ monitoring of selective laser melting of zinc powder via infrared imaging of the process plume’, *Robot. Comput.-Integr. Manuf.*, vol. 49, pp. 229–239, 2018.

[70] I. A. Okaro, S. Jayasinghe, C. Sutcliffe, K. Black, P. Paoletti, and P. L. Green, ‘Automatic fault detection for laser powder-bed fusion using semi-supervised machine learning’, *Addit. Manuf.*, vol. 27, pp. 42–53, 2019.

[71] B. Yuan, B. Giera, G. Guss, and S. McMains, ‘Semi-Supervised Learning for Selective Laser Melting Monitoring via In-Situ Videos’, Lawrence Livermore National Lab.(LLNL), Livermore, CA (United States), 2018.

[72] B. Yao, F. Imani, and H. Yang, ‘Markov decision process for image-guided additive manufacturing’, *IEEE Robot. Autom. Lett.*, vol. 3, no. 4, pp. 2792–2798, 2018.

[73] A. Y. Ng, ‘Feature selection, L 1 vs. L 2 regularization, and rotational invariance’, in *Proceedings of the twenty-first international conference on Machine learning*, 2004, p. 78.

[74] N. Srivastava, G. Hinton, A. Krizhevsky, I. Sutskever, and R. Salakhutdinov, ‘Dropout: a simple way to prevent neural networks from overfitting’, *J. Mach. Learn. Res.*, vol. 15, no. 1, pp. 1929–1958, 2014.

[75] G. E. Totten and D. S. MacKenzie, *Handbook of Aluminum: Vol. 1: Physical Metallurgy and Processes*. CRC Press, 2003.

[76] W. F. Hosford, *Iron and Steel*. Cambridge University Press, 2012.

[77] I. Polmear, D. StJohn, J.-F. Nie, and M. Qian, *Light Alloys: Metallurgy of the Light Metals*. Butterworth-Heinemann, 2017.

[78] N. T. M. Aboulkhair, ‘Strength and ductility of bulk nanostructured aluminum processed by mechanical milling’, *Theses Diss.*, Feb. 2012, [Online]. Available: https://fount.aucegypt.edu/etds/1272

[79] ‘Physical Metallurgy for Engineers - Google Livres’. https://books.google.de/books?hl=fr&lr=&id=y1eTDQRdI2wC&oi=fnd&pg=PA13&dq=Tisza+M.+Physical+metallurgy+for+engineers:+ASM+International+and+Fruend+Publishing+House+Ltd.%3B+2002.&ots=ICkY1g7tOk&sig=_l2Tm40UEkpjXwlgcSmGoBSSqEw#v=onepage&q=Tisza%20M.%20Physical%20metallurgy%20for%20engineers%3A%20ASM%20International%20and%20Fruend%20Publishing%20House%20Ltd.%3B%202002.&f=false (accessed Sep. 18, 2021).

[80] J. Ion, *Laser Processing of Engineering Materials: Principles, Procedure and Industrial Application*. Elsevier, 2005.

[81] E. Scheil, ‘Bemerkungen zur Schichtkristallbildung’, *Int. J. Mater. Res.*, vol. 34, no. 3, pp. 70–72, Mar. 1942, doi: 10.1515/ijmr-1942-340303.

[82] S. Kou, ‘Welding metallurgy’, *N. J. USA*, vol. 431, no. 446, pp. 223–225, 2003.

[83] J. D. Hunt and S.-Z. Lu, ‘Numerical modelling of cellular and dendritic array growth: spacing and structure predictions’, *Mater. Sci. Eng. A*, vol. 173, no. 1, pp. 79–83, Dec. 1993, doi: 10.1016/0921-5093(93)90191-G.

[84] R. Trivedi and W. Kurz, ‘Dendritic growth’, *Int. Mater. Rev.*, vol. 39, no. 2, pp. 49–74, Jan. 1994, doi: 10.1179/imr.1994.39.2.49.

[85] D. Bouchard and J. S. Kirkaldy, ‘Equations and Specification of Predictive Procedures’, *Met. Mater Trans B*, vol. 28, no. 4, pp. 651–663, 1996.

[86] H. J. Hegge and J. T. M. De Hosson, ‘Solidification structures during laser treatment’, *Scr Met.*, vol. 24, pp. 593–599, 1990.

[87] Z. H. Liu, D. Q. Zhang, C. K. Chua, and K. F. Leong, ‘Crystal structure analysis of M2 high speed steel parts produced by selective laser melting’, *Mater. Charact.*, vol. 84, pp. 72–80, 2013.

[88] T. Mahela, D. Cormier, O. Harrysson, and K. Ervin, ‘Advances in electron beam melting of aluminum alloys’, 2007.

[89] D. Buchbinder, W. Meiners, N. Pirch, K. Wissenbach, and J. Schrage, ‘Investigation on reducing distortion by preheating during manufacture of aluminum components using selective laser melting’, *J. Laser Appl.*, vol. 26, no. 1, p. 012004, 2014.

[90] K. Kempen, L. Thijs, J. Van Humbeeck, and J.-P. Kruth, ‘Mechanical properties of AlSi10Mg produced by selective laser melting’, *Phys. Procedia*, vol. 39, pp. 439–446, 2012.

[91] E. Brandl, U. Heckenberger, V. Holzinger, and D. Buchbinder, ‘Additive manufactured AlSi10Mg samples using Selective Laser Melting (SLM): Microstructure, high cycle fatigue, and fracture behavior’, *Mater. Des.*, vol. 34, pp. 159–169, 2012.

[92] D. F. Paulonis and J. J. Schirra, ‘Alloy 718 at Pratt & Whitney: Historical Perspective and Future Challenges’, in *Superalloys 718, 625, 706 and Various Derivatives (2001)*, 2001, pp. 13–23. doi: 10.7449/2001/Superalloys_2001_13_23.

[93] R. C. Reed, *The superalloys: fundamentals and applications*. Cambridge university press, 2008.

[94] T. Baldridge *et al.*, ‘Laser cladding of Inconel 690 on Inconel 600 superalloy for corrosion protection in nuclear applications’, *Opt. Lasers Eng.*, vol. 51, no. 2, pp. 180–184, 2013.

[95] H. X. Hu, Y. G. Zheng, and C. P. Qin, ‘Comparison of Inconel 625 and Inconel 600 in resistance to cavitation erosion and jet impingement erosion’, *Nucl. Eng. Des.*, vol. 240, no. 10, pp. 2721–2730, 2010.

[96] M. J. Donachie and S. J. Donachie, *Superalloys: a technical guide*. ASM international, 2002.

[97] R. Bowman, ‘Superalloys: A primer and history’, 2000.

[98] J. F. Radavich, ‘The physical metallurgy of cast and wrought alloy 718’, *Superalloy*, vol. 718, no. 33, pp. 229–240, 1989.

[99] H. Kitaguchi, *Microstructure-property relationship in advanced Ni-based superalloys*, vol. 2. chapter, 2012.

[100] M. Gao and R. P. Wei, ‘Grain boundary γ ″precipitation and niobium segregation in inconel 718’, *Scr. Metall. Mater.*, vol. 32, no. 7, pp. 987–990, 1995.

[101] M. Gao and R. P. Wei, ‘Grain boundary niobium carbides in Inconel 718’, *Scr. Mater.*, vol. 37, no. 12, 1997.

[102] J. He, S. Fukuyama, and K. Yokogawa, ‘γ ″precipitate in Inconel 718’, *J. Mater. Sci. Technol. N. Y. NY*, vol. 10, no. 4, pp. 293–303, 1994.

[103] M. C. Chaturvedi and Y. Han, ‘Strengthening mechanisms in Inconel 718 superalloy’, *Met. Sci.*, vol. 17, no. 3, pp. 145–149, 1983.

[104] I. Kirman and D. H. Warrington, ‘The precipitation of Ni 3 Nb phases in a Ni- Fe- Cr- Nb alloy’, *Metall. Trans.*, vol. 1, no. 10, pp. 2667–2675, 1970.

[105] M. Dehmas, J. Lacaze, A. Niang, and B. Viguier, ‘TEM study of high-temperature precipitation of delta phase in Inconel 718 alloy’, *Adv. Mater. Sci. Eng.*, vol. 2011, 2011.

[106] S. Azadian, L.-Y. Wei, and R. Warren, ‘Delta phase precipitation in Inconel 718’, *Mater. Charact.*, vol. 53, no. 1, pp. 7–16, 2004.

[107] J. P. Collier, S. H. Wong, J. K. Tien, and J. C. Phillips, ‘The effect of varying Al, Ti, and Nb content on the phase stability of INCONEL 718’, *Metall. Trans. A*, vol. 19, no. 7, pp. 1657–1666, 1988.

[108] Y. Desvallées, M. Bouzidi, F. Bois, and N. Beaude, ‘Delta phase in Inconel 718: mechanical properties and forging process requirements’, *Superalloys*, vol. 718, no. 625, pp. 281–291, 1994.

[109] S. Li, J. Zhuang, J. Yang, and X. S. Xie, ‘The effect of phase on crack propagation under creep and fatigue conditions in alloy 718’, *Superalloys*, vol. 718, pp. 625–706, 1994.

[110] B. Pieraggi and J. F. Uginet, ‘Fatigue and creep properties in relation with alloy 718 microstructure’, *Superalloys*, vol. 718, no. 625, pp. 535–544, 1994.

[111] D. Gopikrishna, S. N. Jha, and L. N. Dash, ‘Influence of microstructure on fatigue properties of Alloy 718’, 1997.

[112] M. J. Cieslak, G. A. Knorovsky, T. J. Headley, and A. D. Romig Jr, ‘The solidification metallurgy of alloy 718 and other Nb-containing superalloys’, Sandia National Lab.(SNL-NM), Albuquerque, NM (United States), 1989.

[113] K.-M. Chang, H.-J. Lai, and J.-Y. Hwang, ‘Exsistence of Laves Phase in Nb-Hardened Superalloys’, 1994.

[114] J. J. Schirra, R. H. Caless, and R. W. Hatala, ‘The Effect of Laves phase on the mechanical properties’, *Miner. Met. Mater. Soc.*, pp. 375–388.

[115] N. L. Richards, X. Huang, and M. C. Chaturvedi, ‘Heat affected zone cracking in cast Inconel 718’, *Mater. Charact.*, vol. 28, no. 4, pp. 179–187, 1992.

[116] Y. Mei *et al.*, ‘Effect of base metal and welding speed on fusion zone microstructure and HAZ hot-cracking of electron-beam welded Inconel 718’, *Mater. Des.*, vol. 89, pp. 964–977, 2016.

[117] M. Sundararaman, P. Mukhopadhyay, and S. Banerjee, ‘Carbide precipitation in nickel base superalloys 718 and 625 and their effect on mechanical properties’, *Superalloys*, vol. 718, pp. 625–706, 1997.

[118] B. Geddes, H. Leon, and X. Huang, *Superalloys: alloying and performance*. Asm International, 2010.

[119] A. Mitchell, A. J. Schmalz, C. Schvezov, and S. L. Cockcroft, ‘The precipitation of primary carbides in alloy 718’, *superalloys*, vol. 718, no. 625,706, pp. 65–78, 1994.

[120] W. J. Boettinger *et al.*, ‘Solidification microstructures: recent developments, future directions’, *Acta Mater.*, vol. 48, no. 1, pp. 43–70, 2000.

[121] S. A. David and J. M. Vitek, ‘Correlation between solidification parameters and weld microstructures’, *Int. Mater. Rev.*, vol. 34, no. 1, pp. 213–245, 1989.

[122] T. Antonsson and H. Fredriksson, ‘The effect of cooling rate on the solidification of INCONEL 718’, *Metall. Mater. Trans. B*, vol. 36, no. 1, pp. 85–96, 2005.

[123] G. A. Knorovsky, M. J. Cieslak, T. J. Headley, A. D. Romig, and W. F. Hammetter, ‘Inconel 718: a solidification diagram’, *Metall. Trans. A*, vol. 20, no. 10, pp. 2149–2158, 1989.

[124] ‘Some preliminary results on the microstructure and mechanical properties of rapidly solidified nickel-based superalloys | Albarrán, J.L.; Campillo, B.; Pérez, R.; Martínez, L.; Juárez-Islas, J.A. | download’. https://fr.booksc.eu/book/24837944/c3b832 (accessed Sep. 18, 2021).

[125] L. Nastac, J. J. Valencia, M. L. Tims, and F. R. Dax, ‘Advances in the Solidification of IN718 and RS5 Alloys’, *Superalloys*, vol. 718, pp. 625–706, 2001.

[126] L. E. Murr, ‘Metallurgy of additive manufacturing: Examples from electron beam melting’, *Addit. Manuf.*, vol. 5, pp. 40–53, 2015.

[127] K. N. Amato *et al.*, ‘Microstructures and mechanical behavior of Inconel 718 fabricated by selective laser melting’, *Acta Mater.*, vol. 60, no. 5, pp. 2229–2239, 2012.

[128] E. Chlebus, K. Gruber, B. Kuźnicka, J. Kurzac, and T. Kurzynowski, ‘Effect of heat treatment on the microstructure and mechanical properties of Inconel 718 processed by selective laser melting’, *Mater. Sci. Eng. A*, vol. 639, pp. 647–655, 2015.

[129] Z. Wang, K. Guan, M. Gao, X. Li, X. Chen, and X. Zeng, ‘The microstructure and mechanical properties of deposited-IN718 by selective laser melting’, *J. Alloys Compd.*, vol. 513, pp. 518–523, 2012.

[130] L. L. Parimi, G. A. Ravi, D. Clark, and M. M. Attallah, ‘Microstructural and texture development in direct laser fabricated IN718’, *Mater. Charact.*, vol. 89, pp. 102–111, 2014.

[131] P. L. Blackwell, ‘The mechanical and microstructural characteristics of laser-deposited IN718’, *J. Mater. Process. Technol.*, vol. 170, no. 1–2, pp. 240–246, 2005.

[132] W. Xiong *et al.*, ‘Effect of selective laser melting parameters on morphology, microstructure, densification and mechanical properties of supersaturated silver alloy’, *Mater. Des.*, vol. 170, p. 107697, 2019.

[133] Y. Lu *et al.*, ‘Study on the microstructure, mechanical property and residual stress of SLM Inconel-718 alloy manufactured by differing island scanning strategy’, *Opt. Laser Technol.*, vol. 75, pp. 197–206, 2015.

[134] F. Trevisan *et al.*, ‘On the selective laser melting (SLM) of the AlSi10Mg alloy: process, microstructure, and mechanical properties’, *Materials*, vol. 10, no. 1, p. 76, 2017.

[135] J. Jhabvala, E. Boillat, T. Antignac, and R. Glardon, ‘On the effect of scanning strategies in the selective laser melting process’, *Virtual Phys. Prototyp.*, vol. 5, no. 2, pp. 99–109, 2010.

[136] P. Köhnen, M. Létang, M. Voshage, J. H. Schleifenbaum, and C. Haase, ‘Understanding the process-microstructure correlations for tailoring the mechanical properties of L-PBF produced austenitic advanced high strength steel’, *Addit. Manuf.*, vol. 30, p. 100914, 2019.

[137] Y. M. Arısoy, L. E. Criales, T. Özel, B. Lane, S. Moylan, and A. Donmez, ‘Influence of scan strategy and process parameters on microstructure and its optimization in additively manufactured nickel

alloy 625 via laser powder bed fusion', *Int. J. Adv. Manuf. Technol.*, vol. 90, no. 5, pp. 1393–1417, 2017.

[138] X. Liu, C. Zhao, X. Zhou, Z. Shen, and W. Liu, 'Microstructure of selective laser melted AlSi10Mg alloy', *Mater. Des.*, vol. 168, p. 107677, 2019.

[139] A. J. Dunbar *et al.*, 'Development of experimental method for in situ distortion and temperature measurements during the laser powder bed fusion additive manufacturing process', *Addit. Manuf.*, vol. 12, pp. 25–30, 2016.

[140] B. Cheng, S. Shrestha, and K. Chou, 'Stress and deformation evaluations of scanning strategy effect in selective laser melting', *Addit. Manuf.*, vol. 12, pp. 240–251, 2016.

[141] A. V. Gusarov, M. Pavlov, and I. Smurov, 'Residual stresses at laser surface remelting and additive manufacturing', *Phys. Procedia*, vol. 12, pp. 248–254, 2011.

[142] L. Parry, I. A. Ashcroft, and R. D. Wildman, 'Understanding the effect of laser scan strategy on residual stress in selective laser melting through thermo-mechanical simulation', *Addit. Manuf.*, vol. 12, pp. 1–15, 2016.

[143] J. C. Pereira, E. Gil, L. Solaberrieta, M. San Sebastián, Y. Bilbao, and P. P. Rodríguez, 'Comparison of AlSi7Mg0. 6 alloy obtained by selective laser melting and investment casting processes: Microstructure and mechanical properties in as-built/as-cast and heat-treated conditions', *Mater. Sci. Eng. A*, vol. 778, p. 139124, 2020.

[144] R. A. O. Heng, S. GIET, Y. Kun, W. U. Xin-hua, and C. DAVIES, 'The influence of processing parameters on aluminium alloy A357 manufactured by selective laser melting [J]', *Mater. Des.*, vol. 109, pp. 334–346, 2016.

[145] K. V. Yang, P. Rometsch, C. H. J. Davies, A. Huang, and X. Wu, 'Effect of heat treatment on the microstructure and anisotropy in mechanical properties of A357 alloy produced by selective laser melting', *Mater. Des.*, vol. 154, pp. 275–290, 2018.

[146] A. B. Spierings, M. u Schneider, and R. Eggenberger, 'Comparison of density measurement techniques for additive manufactured metallic parts', *Rapid Prototyp. J.*, 2011.

[147] I. O. for Standardization, *Metallic Materials: Vickers Hardness Test. Test Method*. International Organization for Standardization, 2000.

[148] A. Standard, 'E8/E8M-13a, standard test method for determining volume fraction by systematic manual point count', *Aug ASTM Int. West Conshohocken PA*, 2013.

[149] D. Rosenthal, 'Mathematical theory of heat distribution during welding and cutting', *Weld. J.*, vol. 20, pp. 220–234, 1941.

[150] M. Tang, P. C. Pistorius, S. Narra, and J. L. Beuth, 'Rapid Solidification: Selective Laser Melting of AlSi10Mg', *JOM*, vol. 68, no. 3, pp. 960–966, Mar. 2016, doi: 10.1007/s11837-015-1763-3.

[151] N. J. Grant, 'Rapid solidification of metallic particulates', *JOM*, vol. 35, no. 1, pp. 20–27, 1983.

[152] H. Ali, H. Ghadbeigi, and K. Mumtaz, 'Effect of scanning strategies on residual stress and mechanical properties of Selective Laser Melted Ti6Al4V', *Mater. Sci. Eng. A*, vol. 712, pp. 175–187, 2018.

[153] 'Alloy Specifications', *Stena Aluminium*. https://www.stenaaluminium.com/Aluminium-alloys-and-services/alloy-specifications/ (accessed Oct. 02, 2021).

[154] J. T. O. de Menezes, E. M. Castrodeza, and R. Casati, 'Effect of build orientation on fracture and tensile behavior of A357 Al alloy processed by Selective Laser Melting', *Mater. Sci. Eng. A*, vol. 766, p. 138392, 2019.

[155] L. Liang, X. Pan, G. Wang, H. Zhang, and H. Zhang, 'Microstructure and mechanical properties of selective laser melted AlSi7Mg', in *Journal of Physics: Conference Series*, 2021, vol. 1939, no. 1, p. 012041.

[156] J. L. Murray and A. J. McAlister, 'The Al-Si (aluminum-silicon) system', *Bull. Alloy Phase Diagr.*, vol. 5, no. 1, p. 74, 1984.

[157] G. P. Dinda, A. K. Dasgupta, and J. Mazumder, 'Evolution of microstructure in laser deposited Al–11.28% Si alloy', *Surf. Coat. Technol.*, vol. 206, no. 8–9, pp. 2152–2160, 2012.

[158] L. Thijs, K. Kempen, J.-P. Kruth, and J. Van Humbeeck, ‘Fine-structured aluminium products with controllable texture by selective laser melting of pre-alloyed AlSi10Mg powder’, *Acta Mater.*, vol. 61, no. 5, pp. 1809–1819, 2013.

[159] J. Liu and A. C. To, ‘Quantitative texture prediction of epitaxial columnar grains in additive manufacturing using selective laser melting’, *Addit. Manuf.*, vol. 16, pp. 58–64, 2017.

[160] M. Gäumann, C. Bezencon, P. Canalis, and W. Kurz, ‘Single-crystal laser deposition of superalloys: processing–microstructure maps’, *Acta Mater.*, vol. 49, no. 6, pp. 1051–1062, 2001.

[161] W. Li *et al.*, ‘Effect of heat treatment on AlSi10Mg alloy fabricated by selective laser melting: Microstructure evolution, mechanical properties and fracture mechanism’, *Mater. Sci. Eng. A*, vol. 663, pp. 116–125, 2016.

[162] S. Nafisi, D. Emadi, M. T. Shehata, and R. Ghomashchi, ‘Effects of electromagnetic stirring and superheat on the microstructural characteristics of Al–Si–Fe alloy’, *Mater. Sci. Eng. A*, vol. 432, no. 1–2, pp. 71–83, 2006.

[163] J. K. Chen, H. Y. Hung, C. F. Wang, and N. K. Tang, ‘Effects of casting and heat treatment processes on the thermal conductivity of an Al-Si-Cu-Fe-Zn alloy’, *Int. J. Heat Mass Transf.*, vol. 105, pp. 189–195, 2017.

[164] M. H. Mulazimoglu, R. A. L. Drew, and J. E. Gruzleski, ‘Solution treatment study of cast Al–Si alloys by electrical conductivity’, *Can. Metall. Q.*, vol. 28, no. 3, pp. 251–258, 1989.

[165] N. Takata, H. Kodaira, K. Sekizawa, A. Suzuki, and M. Kobashi, ‘Change in microstructure of selectively laser melted AlSi10Mg alloy with heat treatments’, *Mater. Sci. Eng. A*, vol. 704, pp. 218–228, 2017.

[166] D. Manfredi *et al.*, ‘Additive manufacturing of Al alloys and aluminium matrix composites (AMCs)’, *Light Met. Alloys Appl.*, vol. 11, pp. 3–34, 2014.

[167] N. T. Aboulkhair, I. Maskery, C. Tuck, I. Ashcroft, and N. M. Everitt, ‘On the formation of AlSi10Mg single tracks and layers in selective laser melting: Microstructure and nano-mechanical properties’, *J. Mater. Process. Technol.*, vol. 230, pp. 88–98, 2016.

[168] U. F. Kocks, C. N. Tomé, and H.-R. Wenk, *Texture and anisotropy: preferred orientations in polycrystals and their effect on materials properties*. Cambridge university press, 1998.

[169] S. Lloyd, ‘Least squares quantization in PCM’, *IEEE Trans. Inf. Theory*, vol. 28, no. 2, pp. 129–137, 1982.

[170] H. Taheri, L. W. Koester, T. A. Bigelow, E. J. Faierson, and L. J. Bond, ‘In situ additive manufacturing process monitoring with an acoustic technique: clustering performance evaluation using K-means algorithm’, *J. Manuf. Sci. Eng.*, vol. 141, no. 4, 2019.

[171] D. Arthur and S. Vassilvitskii, ‘k-means++: The advantages of careful seeding’, Stanford, 2006.

[172] H. A. Abu Alfeilat *et al.*, ‘Effects of distance measure choice on k-nearest neighbor classifier performance: a review’, *Big Data*, vol. 7, no. 4, pp. 221–248, 2019.

[173] H. Dubey and V. Pudi, ‘Class based weighted k-nearest neighbor over imbalance dataset’, in *Pacific-Asia conference on knowledge discovery and data mining*, 2013, pp. 305–316.

[174] W. Liu and S. Chawla, ‘Class confidence weighted knn algorithms for imbalanced data sets’, in *Pacific-Asia conference on knowledge discovery and data mining*, 2011, pp. 345–356.

[175] C. Galy, E. Le Guen, E. Lacoste, and C. Arvieu, ‘Main defects observed in aluminum alloy parts produced by SLM: from causes to consequences’, *Addit. Manuf.*, vol. 22, pp. 165–175, 2018.

[176] D. Alberts, D. Schwarze, and G. Witt, ‘High speed melt pool & laser power monitoring for selective laser melting (SLM®)’, in *9th International Conference on Photonic Technologies LANE*, 2016, vol. 2016.

[177] A. Mahmoudi, S. Takerkart, F. Regragui, D. Boussaoud, and A. Brovelli, ‘Multivoxel pattern analysis for FMRI data: a review’, *Comput. Math. Methods Med.*, vol. 2012, 2012.

[178] D. A. Pisner and D. M. Schnyer, ‘Support vector machine’, in *Machine Learning*, Elsevier, 2020, pp. 101–121.

[179] G. Mohr *et al.*, ‘In-situ defect detection in laser powder bed fusion by using thermography and optical tomography—comparison to computed tomography’, *Metals*, vol. 10, no. 1, p. 103, 2020.

[180] I. Gibson, D. W. Rosen, B. Stucker, and M. Khorasani, *Additive manufacturing technologies*, vol. 17. Springer, 2021.

[181] J. H. Friedman, *The elements of statistical learning: Data mining, inference, and prediction*. springer open, 2017.

[182] M. Pelikan, K. Sastry, and D. E. Goldberg, 'iBOA: The incremental Bayesian optimization algorithm', in *Proceedings of the 10th annual conference on Genetic and evolutionary computation*, 2008, pp. 455–462.

[183] X. Zhou *et al.*, 'X-ray CT analysis of the influence of process on defect in Ti-6Al-4V parts produced with Selective Laser Melting technology', *Int. J. Adv. Manuf. Technol.*, vol. 106, no. 1–2, pp. 3–14, Jan. 2020, doi: 10.1007/s00170-019-04347-0.

[184] C. F. Alcala and S. J. Qin, 'Analysis and generalization of fault diagnosis methods for process monitoring', *J. Process Control*, vol. 21, no. 3, pp. 322–330, 2011.

[185] S. Xiang, F. Nie, and C. Zhang, 'Learning a Mahalanobis distance metric for data clustering and classification', *Pattern Recognit.*, vol. 41, no. 12, pp. 3600–3612, Dec. 2008, doi: 10.1016/j.patcog.2008.05.018.

[186] D. Kastsian and D. Reznik, 'Reduction of local overheating in selective laser melting', *Proc. Simul. Addit. Manuf. SIM-AM Munich Ger.*, pp. 11–13, 2017.

[187] Y. Yang, F. van Keulen, and C. Ayas, 'A computationally efficient thermal model for selective laser melting', *Addit. Manuf.*, vol. 31, p. 100955, 2020.

[188] I. Goodfellow, Y. Bengio, and A. Courville, *Deep learning*. MIT press, 2016.

[189] Y. LeCun, Y. Bengio, and G. Hinton, 'Deep learning', *nature*, vol. 521, no. 7553, pp. 436–444, 2015.

[190] S. Ioffe and C. Szegedy, 'Batch normalization: Accelerating deep network training by reducing internal covariate shift', in *International conference on machine learning*, 2015, pp. 448–456.

[191] C.-Y. Lee, P. W. Gallagher, and Z. Tu, 'Generalizing pooling functions in convolutional neural networks: Mixed, gated, and tree', in *Artificial intelligence and statistics*, 2016, pp. 464–472.

[192] T. Wang, D. J. Wu, A. Coates, and A. Y. Ng, 'End-to-end text recognition with convolutional neural networks', in *Proceedings of the 21st international conference on pattern recognition (ICPR2012)*, 2012, pp. 3304–3308.

[193] M. Ranzato, F. J. Huang, Y.-L. Boureau, and Y. LeCun, 'Unsupervised learning of invariant feature hierarchies with applications to object recognition', in *2007 IEEE conference on computer vision and pattern recognition*, 2007, pp. 1–8.

[194] J. Gu *et al.*, 'Recent advances in convolutional neural networks. eprint', *ArXiv Prepr. ArXiv151207108*, 2015.

[195] S. Hochreiter, 'The vanishing gradient problem during learning recurrent neural nets and problem solutions', *Int. J. Uncertain. Fuzziness Knowl.-Based Syst.*, vol. 6, no. 02, pp. 107–116, 1998.

[196] D. Misra, 'Mish: A self regularized non-monotonic activation function', *ArXiv Prepr. ArXiv190808681*, 2019.

[197] W. Rawat and Z. Wang, 'Deep convolutional neural networks for image classification: A comprehensive review', *Neural Comput.*, vol. 29, no. 9, pp. 2352–2449, 2017.

[198] K. He, J. Sun, and X. Tang, 'Single image haze removal using dark channel prior', *IEEE Trans. Pattern Anal. Mach. Intell.*, vol. 33, no. 12, pp. 2341–2353, 2010.

[199] D. Park, H. Park, D. K. Han, and H. Ko, 'Single image dehazing with image entropy and information fidelity', in *2014 IEEE International Conference on Image Processing (ICIP)*, 2014, pp. 4037–4041.

[200] Q. Han, H. Gu, S. Soe, R. Setchi, F. Lacan, and J. Hill, 'Manufacturability of AlSi10Mg overhang structures fabricated by laser powder bed fusion', *Mater. Des.*, vol. 160, pp. 1080–1095, 2018.

[201] O. Ronneberger *et al.*, 'Medical image computing and computer-assisted intervention–MICCAI 2015. Vol 9351, Lecture Notes in Computer Science', 2015.

[202] M. Drozdzal, E. Vorontsov, G. Chartrand, S. Kadoury, and C. Pal, 'The importance of skip connections in biomedical image segmentation', in *Deep learning and data labeling for medical applications*, Springer, 2016, pp. 179–187.

[203] M. Telgarsky, 'Benefits of depth in neural networks', in *Conference on learning theory*, 2016, pp. 1517–1539.

[204] L. Sun, ‘Resnet on tiny imagenet’, *Submitt. On*, vol. 14, 2016.

[205] K. He, X. Zhang, S. Ren, and J. Sun, ‘Identity mappings in deep residual networks’, in *European conference on computer vision*, 2016, pp. 630–645.

[206] O. Ronneberger, P. Fischer, and T. Brox, ‘U-net: Convolutional networks for biomedical image segmentation’, in *International Conference on Medical image computing and computer-assisted intervention*, 2015, pp. 234–241.

[207] J. Deng, W. Dong, R. Socher, L.-J. Li, K. Li, and L. Fei-Fei, ‘Imagenet: A large-scale hierarchical image database’, in *2009 IEEE conference on computer vision and pattern recognition*, 2009, pp. 248–255.

[208] M. A. Rahman and Y. Wang, ‘Optimizing intersection-over-union in deep neural networks for image segmentation’, in *International symposium on visual computing*, 2016, pp. 234–244.

[209] Y. Sasaki, ‘The truth of the f-measure. 2007’, *URL Httpswww Cs Odu Edu∼ Mukkacs795sum09dmLecturenotesDay3F-Meas.-YS-26Oct07 Pdf Accessed 2021-05-26*, 2007.

[210] W. Zhu *et al.*, ‘AnatomyNet: deep learning for fast and fully automated whole-volume segmentation of head and neck anatomy’, *Med. Phys.*, vol. 46, no. 2, pp. 576–589, 2019.

[211] F. Milletari, N. Navab, and S.-A. Ahmadi, ‘V-net: Fully convolutional neural networks for volumetric medical image segmentation’, in *2016 fourth international conference on 3D vision (3DV)*, 2016, pp. 565–571.

[212] T.-Y. Lin, P. Goyal, R. Girshick, K. He, and P. Dollár, ‘Focal loss for dense object detection’, in *Proceedings of the IEEE international conference on computer vision*, 2017, pp. 2980–2988.

[213] A. Nowotnik, P. Pędrak, J. Sieniawski, and M. Góral, ‘Mechanical properties of hot deformed Inconel 718 and X750’, *J. Achiev. Mater. Manuf. Eng.*, vol. 50, no. 2, pp. 74–80, 2012.

[214] H. Yuan and W. C. Liu, ‘Effect of the δ phase on the hot deformation behavior of Inconel 718’, *Mater. Sci. Eng. A*, vol. 408, no. 1–2, pp. 281–289, 2005.

[215] E. A. Loria, ‘Recent developments in the progress of superalloy 718’, *JOM*, vol. 44, no. 6, pp. 33–36, 1992.

[216] L. X. Li, Y. Lou, L. B. Yang, D. S. Peng, and K. P. Rao, ‘Flow stress behavior and deformation characteristics of Ti-3Al-5V-5Mo compressed at elevated temperatures’, *Mater. Des.*, vol. 23, no. 5, pp. 451–457, 2002.

[217] J. Zrnik, S. V. Dobatkin, and I. Mamuzić, ‘Processing of metals by severe plastic deformation (SPD)–structure and mechanical properties respond’, *Metalurgija*, vol. 47, no. 3, pp. 211–216, 2008.

[218] Q. Guo-Zheng, ‘Characterization for dynamic recrystallization kinetics based on stress-strain curves’, *Recent Dev. Study Recryst.*, pp. 61–64, 2013.

[219] L. X. Zhou and T. N. Baker, ‘Effects on dynamic and metadynamic recrystallization on microstructures of wrought IN-718 due to hot deformation’, *Mater. Sci. Eng. A*, vol. 196, no. 1–2, pp. 89–95, 1995.

[220] K. Chen *et al.*, ‘Transition of deformation behavior and its related microstructure evolution in Nimonic 80A under hot-to-warm working’, *Mater. Charact.*, vol. 106, pp. 175–184, 2015.

[221] S. M. Fatemi-Varzaneh, A. Zarei-Hanzaki, and H. Beladi, ‘Dynamic recrystallization in AZ31 magnesium alloy’, *Mater. Sci. Eng. A*, vol. 456, no. 1–2, pp. 52–57, 2007.

[222] M. R. G. Ferdowsi, M. Mazinani, and G. R. Ebrahimi, ‘Effects of hot rolling and inter-stage annealing on the microstructure and texture evolution in a partially homogenized AZ91 magnesium alloy’, *Mater. Sci. Eng. A*, vol. 606, pp. 214–227, 2014.

[223] A. S. H. Kabir, M. Sanjari, J. Su, I.-H. Jung, and S. Yue, ‘Effect of strain-induced precipitation on dynamic recrystallization in Mg–Al–Sn alloys’, *Mater. Sci. Eng. A*, vol. 616, pp. 252–259, 2014.

[224] Y. Yang *et al.*, ‘Influence of Extrusion on the Microstructure and Mechanical Behavior of Mg-9Li-3Al-x Sr Alloys’, *Metall. Mater. Trans. A*, vol. 44, no. 2, pp. 1101–1113, 2013.

[225] Y. C. Lin *et al.*, ‘EBSD study of a hot deformed nickel-based superalloy’, *J. Alloys Compd.*, vol. 640, pp. 101–113, 2015.

[226] Y. Wang, W. Z. Shao, L. Zhen, and X. M. Zhang, ‘Microstructure evolution during dynamic recrystallization of hot deformed superalloy 718’, *Mater. Sci. Eng. A*, vol. 486, no. 1–2, pp. 321–332, 2008.

[227] H. Zhang, K. Zhang, H. Zhou, Z. Lu, C. Zhao, and X. Yang, ‘Effect of strain rate on microstructure evolution of a nickel-based superalloy during hot deformation’, *Mater. Des.*, vol. 80, pp. 51–62, 2015.

[228] T. Trosch, J. Strößner, R. Völkl, and U. Glatzel, ‘Microstructure and mechanical properties of selective laser melted Inconel 718 compared to forging and casting’, *Mater. Lett.*, vol. 164, pp. 428–431, 2016.

[229] C. I. Garcia, D. E. Camus, E. A. Loria, and A. J. DeArdo, ‘Microstructural refinement of as-cast alloy 718 via thermomechanical processing’, *Superalloys*, vol. 718, no. 625, pp. 925–941, 1991.

[230] A. Thomas, M. El-Wahabi, J. M. Cabrera, and J. M. Prado, ‘High temperature deformation of Inconel 718’, *J. Mater. Process. Technol.*, vol. 177, no. 1–3, pp. 469–472, 2006.

[231] M. J. Weis, M. C. Mataya, S. W. Thompson, and D. K. Matlock, ‘The hot deformation behavior of an as-cast alloy 718 ingot’, Rockwell International Corp., Golden, CO (USA). Rocky Flats Plant, 1989.

[232] ASM International, Ed., *ASM handbook*, 10th editon. Materials Park, Ohio: ASM International, 1990.

[233] E. S. Puchi-Cabrera, M. H. Staia, J.-D. Guérin, J. Lesage, M. Dubar, and D. Chicot, ‘An experimental analysis and modeling of the work-softening transient due to dynamic recrystallization’, *Int. J. Plast.*, vol. 54, pp. 113–131, 2014.

[234] E. I. Galindo-Nava and P. E. J. Rivera-Díaz-del-Castillo, ‘Thermostatistical modelling of hot deformation in FCC metals’, *Int. J. Plast.*, vol. 47, pp. 202–221, 2013.

[235] J. Hajkazemi, A. Zarei-Hanzaki, M. Sabet, and S. Khoddam, ‘Double-hit compression behavior of TWIP steels’, *Mater. Sci. Eng. A*, vol. 530, pp. 233–238, 2011.

[236] S. S. Kumar, T. Raghu, P. P. Bhattacharjee, G. A. Rao, and U. Borah, ‘Constitutive modeling for predicting peak stress characteristics during hot deformation of hot isostatically processed nickel-base superalloy’, *J. Mater. Sci.*, vol. 50, no. 19, pp. 6444–6456, 2015.

[237] X.-M. Chen *et al.*, ‘Microstructural evolution of a nickel-based superalloy during hot deformation’, *Mater. Des.*, vol. 77, pp. 41–49, 2015.

[238] P. Zhang, C. Hu, C. Ding, Q. Zhu, and H. Qin, ‘Plastic deformation behavior and processing maps of a Ni-based superalloy’, *Mater. Des. 1980-2015*, vol. 65, pp. 575–584, 2015.

[239] Y. Kong, P. Chang, Q. Li, L. Xie, and S. Zhu, ‘Hot deformation characteristics and processing map of nickel-based C276 superalloy’, *J. Alloys Compd.*, vol. 622, pp. 738–744, 2015.

[240] F. J. Humphreys and M. Hatherly, *Recrystallization and related annealing phenomena*. Elsevier, 2012.

[241] S. Fulop and H. J. McQueen, ‘Mechanisms of deformation in the hot working of nickel-base superalloys’, in *Superalloys: processing*, 1972.

[242] Y.-X. Liu, Y. C. Lin, and Y. Zhou, ‘2D cellular automaton simulation of hot deformation behavior in a Ni-based superalloy under varying thermal-mechanical conditions’, *Mater. Sci. Eng. A*, vol. 691, pp. 88–99, 2017.

[243] Y. C. Lin, S.-C. Luo, L.-X. Yin, and J. Huang, ‘Microstructural evolution and high temperature flow behaviors of a homogenized Sr-modified Al-Si-Mg alloy’, *J. Alloys Compd.*, vol. 739, pp. 590–599, 2018.

[244] M. J. Luton and C. M. Sellars, ‘Dynamic recrystallization in nickel and nickel-iron alloys during high temperature deformation’, *Acta Metall.*, vol. 17, no. 8, pp. 1033–1043, 1969.

[245] G. Gottstein, M. Frommert, M. Goerdeler, and N. Schäfer, ‘Prediction of the critical conditions for dynamic recrystallization in the austenitic steel 800H’, *Mater. Sci. Eng. A*, vol. 387, pp. 604–608, 2004.

[246] M. Shaban and B. Eghbali, ‘Determination of critical conditions for dynamic recrystallization of a microalloyed steel’, *Mater. Sci. Eng. A*, vol. 527, no. 16–17, pp. 4320–4325, 2010.

[247] Z. Baochun, L. Guiyan, L. Fenglian, H. Xinming, H. Lei, and S. Qingyun, ‘Determination of critical conditions for initiation of dynamic recrystallization by new method’, *Mater. Manuf. Process.*, vol. 30, no. 10, pp. 1235–1239, 2015.

[248] E. I. Poliak and J. J. Jonas, ‘A one-parameter approach to determining the critical conditions for the initiation of dynamic recrystallization’, *Acta Mater.*, vol. 44, no. 1, pp. 127–136, 1996.

[249] H. Mirzadeh and A. Najafizadeh, ‘Prediction of the critical conditions for initiation of dynamic recrystallization’, *Mater. Des.*, vol. 31, no. 3, pp. 1174–1179, 2010.

[250] F. Chen, G. Feng, and Z. Cui, ‘Mathematical modeling of critical condition for dynamic recrystallization’, *Procedia Eng.*, vol. 81, pp. 486–491, 2014.

[251] D. G. Cram, H. S. Zurob, Y. J. M. Brechet, and C. R. Hutchinson, ‘Modelling discontinuous dynamic recrystallization using a physically based model for nucleation’, *Acta Mater.*, vol. 57, no. 17, pp. 5218–5228, 2009.

[252] ‘Sellars: On the mechanism of hot deformation - Google Scholar’. https://scholar.google.com/scholar_lookup?title=On%20the%20mechanism%20of%20hot%20deformation&author=C.%20M.%20Sellars%20&author=W.%20J.%20McTegart&publication_year=1966 (accessed Sep. 19, 2021).

[253] S. C. Medeiros, Y. Prasad, W. G. Frazier, and R. Srinivasan, ‘Microstructural modeling of metadynamic recrystallization in hot working of IN 718 superalloy’, *Mater. Sci. Eng. A*, vol. 293, no. 1–2, pp. 198–207, 2000.

[254] R. Gujrati, C. Gupta, J. S. Jha, S. Mishra, and A. Alankar, ‘Understanding activation energy of dynamic recrystallization in Inconel 718’, *Mater. Sci. Eng. A*, vol. 744, pp. 638–651, 2019.

[255] M. G. Shahri, S. R. Hosseini, and M. Salehi, ‘Formation of nano/ultrafine grains in AISI 321 stainless steel using advanced thermo-mechanical process’, *Acta Metall. Sin. Engl. Lett.*, vol. 28, no. 4, pp. 499–504, 2015.

[256] S. Mandal, A. K. Bhaduri, and V. S. Sarma, ‘Role of twinning on dynamic recrystallization and microstructure during moderate to high strain rate hot deformation of a Ti-modified austenitic stainless steel’, *Metall. Mater. Trans. A*, vol. 43, no. 6, pp. 2056–2068, 2012.

[257] O. N. Senkov, D. B. Miracle, and S. A. Firstov, *Metallic materials with high structural efficiency*, vol. 146. Springer Science & Business Media, 2006.

[258] S. M. Fatemi-Varzaneh, A. Zarei-Hanzaki, J. M. Cabrera, and P. R. Calvillo, ‘EBSD characterization of repetitive grain refinement in AZ31 magnesium alloy’, *Mater. Chem. Phys.*, vol. 149, pp. 339–343, 2015.

[259] Z. Yanushkevich, A. Belyakov, and R. Kaibyshev, ‘Microstructural evolution of a 304-type austenitic stainless steel during rolling at temperatures of 773–1273 K’, *Acta Mater.*, vol. 82, pp. 244–254, 2015.

[260] M. G. Jiang, H. Yan, and R. S. Chen, ‘Twinning, recrystallization and texture development during multi-directional impact forging in an AZ61 Mg alloy’, *J. Alloys Compd.*, vol. 650, pp. 399–409, 2015.

[261] S. H. Park, J. H. Lee, H. Yu, J. Yoon, and B. S. You, ‘Effect of cold pre-forging on the microstructure and mechanical properties of extruded Mg–8Sn–1Al–1Zn alloy’, *Mater. Sci. Eng. A*, vol. 612, pp. 197–201, 2014.

[262] D. G. Brandon, ‘The structure of high-angle grain boundaries’, *Acta Metall.*, vol. 14, no. 11, pp. 1479–1484, 1966.

[263] E. E. Underwood, ‘Quantitative stereology’, 1970.

[264] H. Beladi, P. Cizek, and P. D. Hodgson, ‘Dynamic recrystallization of austenite in Ni-30 Pct Fe model alloy: microstructure and texture evolution’, *Metall. Mater. Trans. A*, vol. 40, no. 5, pp. 1175–1189, 2009.

[265] Y. Jin *et al.*, ‘Evolution of the annealing twin density during δ-supersolvus grain growth in the nickel-based superalloy Inconel^{TM} 718’, *Metals*, vol. 6, no. 1, p. 5, 2016.

[266] S. Shekhar and A. H. King, ‘Strain fields and energies of grain boundary triple junctions’, *Acta Mater.*, vol. 56, no. 19, pp. 5728–5736, 2008.

[267] T. Yu, N. Hansen, and X. Huang, 'Recovery by triple junction motion in aluminium deformed to ultrahigh strains', *Proc. R. Soc. Math. Phys. Eng. Sci.*, vol. 467, no. 2135, pp. 3039–3065, 2011.

[268] M. Azarbarmas, M. Aghaie-Khafri, J. M. Cabrera, and J. Calvo, 'Dynamic recrystallization mechanisms and twining evolution during hot deformation of Inconel 718', *Mater. Sci. Eng. A*, vol. 678, pp. 137–152, 2016.

[269] S. Mandal *et al.*, 'Evolution and characterization of dynamically recrystallized microstructure in a titanium-modified austenitic stainless steel using ultrasonic and EBSD techniques', *Philos. Mag.*, vol. 88, no. 6, pp. 883–897, 2008.

[270] D. P. Field, L. T. Bradford, M. M. Nowell, and T. M. Lillo, 'The role of annealing twins during recrystallization of Cu', *Acta Mater.*, vol. 55, no. 12, pp. 4233–4241, 2007.

[271] N. Bozzolo, N. Souaï, and R. E. Logé, 'Evolution of microstructure and twin density during thermomechanical processing in a γ-γ'nickel-based superalloy', *Acta Mater.*, vol. 60, no. 13–14, pp. 5056–5066, 2012.

[272] C. S. Pande, M. A. Imam, and B. B. Rath, 'Study of annealing twins in FCC metals and alloys', *Metall. Trans. A*, vol. 21, no. 11, pp. 2891–2896, 1990.

[273] W. Wang *et al.*, 'Influence of stored energy on twin formation during primary recrystallization', *Mater. Sci. Eng. A*, vol. 589, pp. 112–118, 2014.

[274] T. S. Prithiv, P. Bhuyan, S. K. Pradhan, V. S. Sarma, and S. Mandal, 'A critical evaluation on efficacy of recrystallization vs. strain induced boundary migration in achieving grain boundary engineered microstructure in a Ni-base superalloy', *Acta Mater.*, vol. 146, pp. 187–201, 2018.

[275] R. Jamaati, M. R. Toroghinejad, S. Amirkhanlou, and H. Edris, 'Microstructural evolution of nanostructured steel-based composite fabricated by accumulative roll bonding', *Mater. Sci. Eng. A*, vol. 639, pp. 298–306, 2015.

[276] S. R. Barrabes, M. E. Kassner, M. T. Pérez-Prado, and E. Evangelista, 'Geometric dynamic recrystallization in α-zirconium at elevated temperatures', in *Materials Science Forum*, 2004, vol. 467, pp. 1145–1150.

[277] D. Feng, X. M. Zhang, S. D. Liu, and Y. L. Deng, 'Constitutive equation and hot deformation behavior of homogenized Al–7.68 Zn–2.12 Mg–1.98 Cu–0.12 Zr alloy during compression at elevated temperature', *Mater. Sci. Eng. A*, vol. 608, pp. 63–72, 2014.

APPENDIX

A.1. Experimental Set-Up

A.1.1. Material

Inconel 718 (chemical composition tabulated in Table 1) powder was used as filler for LMD printing on SLMed Inconel 718 samples which also acts as a substrate. The Inconel 718 powder with a particle size distribution between 45-150 μm is supplied by Flame Spray Technologies (FST, Duiven, the Netherlands). Similarly, for SLMed samples, the gas atomized Inconel 718 powder with particle size distribution 45-106 μm is supplied by the carpenter additive (UK). The chemical composition of the SLMed Inconel 718 powder is also summarized in the Table 1. The powder is kept in an airtight container before printing to avoid humidification.

Table 1: Composition of Inconel 718 alloy powder used for LMD and SLM printing.

	Ni	**Cr**	**Fe**	**Nb+Ta**	**Mo**	**Ti**	**Al**
Powder for LMD	52.8	18.5	18	4.8	3.5	0.75	0.3
Powder for SLM	50-55	17-21	Bal.	4.75-5.5	2.8-3.3	0.75-1.15	0.30-0.70

A.1.2. Machine

Selective Laser Melting (SLM)

SLM samples are fabricated using RenAM 500Q from Renishaw, Germany. The machine is equipped with 4 continuous Yb- fiber lasers achieving a maximum power of 500 W and a laser spot diameter of 85 μm. Also, it has a building platform size of 250*250*300 mm. Before printing, the building plate is preheated to a temperature of 170 C, and an oxygen level of 200 ppm is achieved. Argon is used as an inert gas. The printing parameters are summarized in the Table 2.

Table 2: Process parameters used for SLM printing.

Power (W)	**Scanning Speed (mm/s)**	**Hatch Distance (mm)**	**Layer thickness (mm)**	**Scanning Strategy**	**Rotation**
212.5	850	0.09	0.06	10 mm Stripes	67

Laser Melt Deposition (LMD)

LMD printing is performed in an IBARMIA ZVH45/1600 Add+Process hybrid machine (Figure 1). This multiprocess machine combines the DED technology with 5-axis milling and turning (horizontal and vertical) capability. This machine is equipped with a Precitec YC52 cladding head with a collimating and focusing optics of 125 mm and 250 mm, respectively, a Sulzer Metco TWIN-10-C Powder Feeder, and a Yb-Fiber Rofin FL030 Laser generator of 3 kW with a continuous wavelength of 1.07 µm. For the nozzle, a 4-stream coaxial discrete nozzle from Precitec is used. The SLMed samples are held tight using cylindrical fixtures, as shown in the Figure 1.

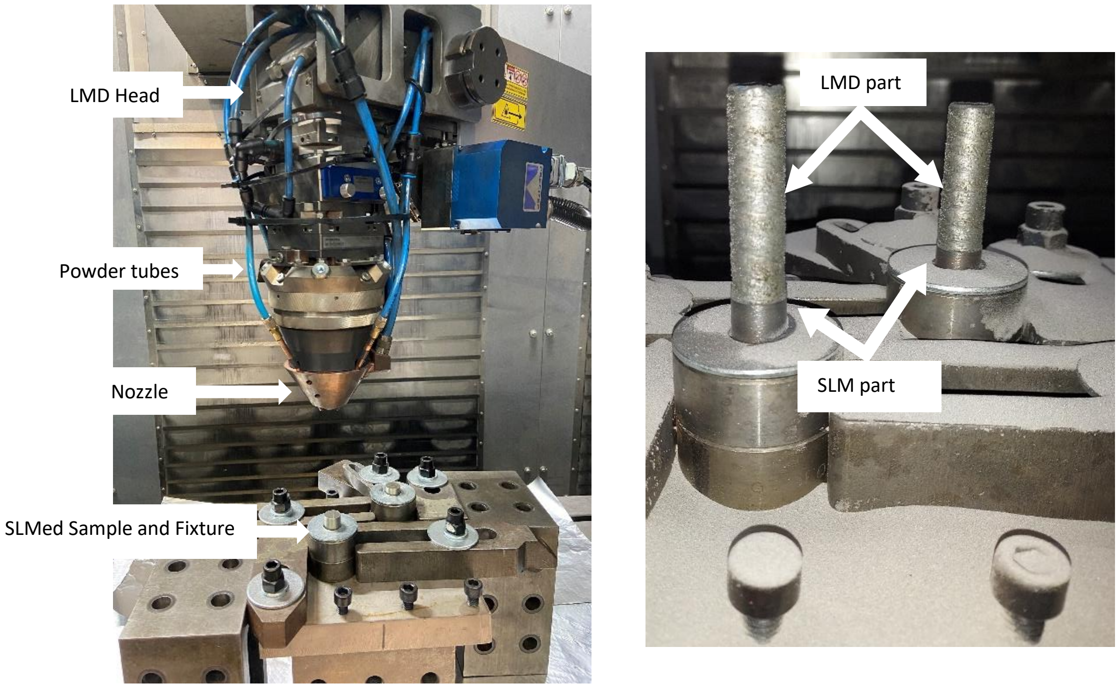

(a) (b)

Figure 1: (a) Experimental setup used for LMD printing, (b) LMD printed parts.

A.1.3. Specimen Geometry

To study the feasibility of advanced manufacturing using LMD and SLM AM processes. Firstly, cylindrical Inconel 718 samples with a diameter of 16 mm and length 55 mm are fabricated using the SLM process. The SLMed samples are then used as a substrate for further LMD printing of Inconel 718 samples. Cylinders with the same geometry as SLM is fabricated using LMD on SLMed samples. The Figure 2 shows the schematic and actual samples combining SLM and LMD printing.

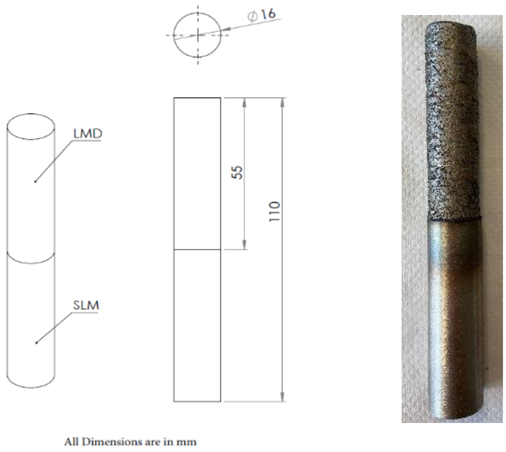

Figure 2. Schematic for the printed samples and actual samples.

A.1.4. Process Parameters

Single clad tracks of 60 mm are printed and analysed to find the best parameters for obtaining defect-free desirable morphology of the tracks for LMD printing. The process parameters used for optimization are tabulated in the Table 3.

Table 3: Process parameters used for SLM printing.

Process Parameter	**Level**
Laser Power (W)	900, 650, 400
Feed rate (mm/min)	700, 500, 300
Powder mass flow (g/min)	8, 6, 4
Type of coaxial nozzle	4-stream Discrete

A.1.5. Analysis

An average of four cross-sections perpendicular to the laser scanning direction is selected for optimization. The clad tracks' first and last 10 mm are avoided due to instabilities subjected to start and stop conditions. The cross-sections are analyzed for porosity, clad morphology, i.e., height (h), width (w), area (A), dilution depth (p), and dilution area (Da), as shown in Figure 3.

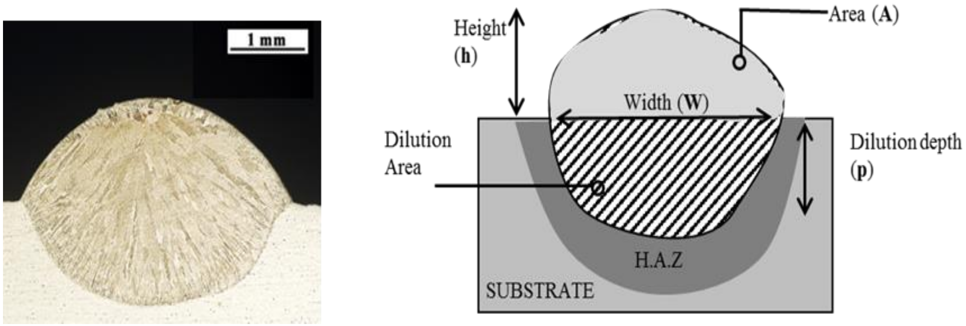

Figure 3. Optical micrograph of clad and schematic of clad characteristics.

The samples are mirror polished and chemically etched using Kallings 2 etchant. The cross-section is measured using the Motic SMZ-143 microscopy (Motic, Hong Kong, China) and Clemex Captiva®software (Clemex, Longueuil, QC, Canada).

A.2. Results

A.2.1. Process parameter optimization

The average four values of the cross-sections of all the clads are used to study the single clad characteristics (w, h, A, p). Each process parameter (i.e., Laser Power, Feed rate, and Mass flow rate) affects the clad characteristics. Therefore, studying the correlation between the process parameter and clad characteristics is crucial. Based on the process optimization results, we used principal component analysis (PCA) to study the correlation, as shown in the figure 4. Here values >0 show the positive correlation, and values <0 represent the negative correlation among the variables. The intensity of the color concerns the scale. For example, it can be noticed that the clad height is positively related to powder mass flow rate and strongly negatively associated with the feed rate. It is important to note that the Area_AR represents the aspect ratio of the clad area, which is Width/Depth, whereas the Dilution_AR represents the dilution area aspect area which is Width/Dilution Depth.

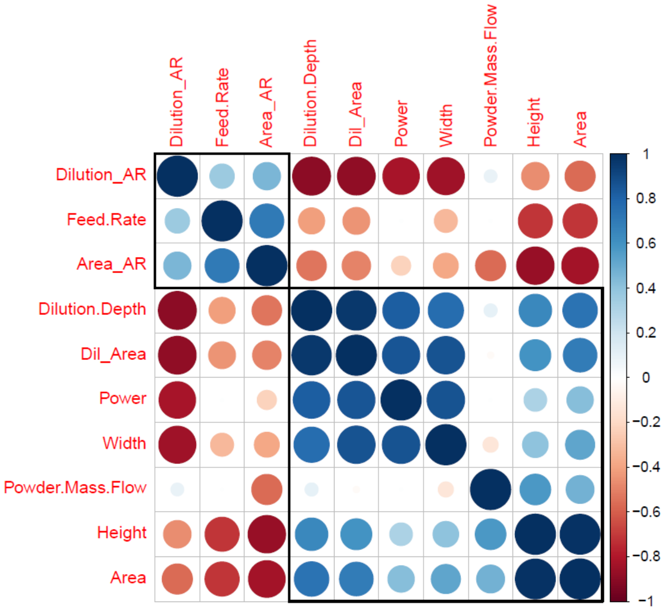

Figure 4. PCA correlation matrix between process parameters and clad characteristics.

The same can be verified from the plots of experimental values, as shown in Figure 5. The figure shows the clad height, width, and aspect ratio (Area_AR) concerning Laser Power, Feed rate, and Mass flow rate. It could be noticed that Laser power had no significant effect on the height, although the width increased at higher laser power. As expected, height and width decreased as the feed rate increased.

The optimal conditions for LMD printing are selected as follows:

1. Firstly, the dilution depth should be higher than the clad height, as it will ensure deeper penetration of the beneath layer to create defect-free and proper adhesion.
2. Secondly, the aspect ratio should be between 3-5, ensuring good overlap between the tracks as reported in the previous study [1,2].
3. Thirdly, a mass flow rate of 6.7 g/min is chosen intuitively as a slower mass flow rate leads to longer printing time, whereas a higher mass flow rate could lead to more thick tracks.

Therefore, in our study, we choose laser power of 650 W, Feed rate of 500 (mm/min), and mass flow rate of 6.7 g/min.

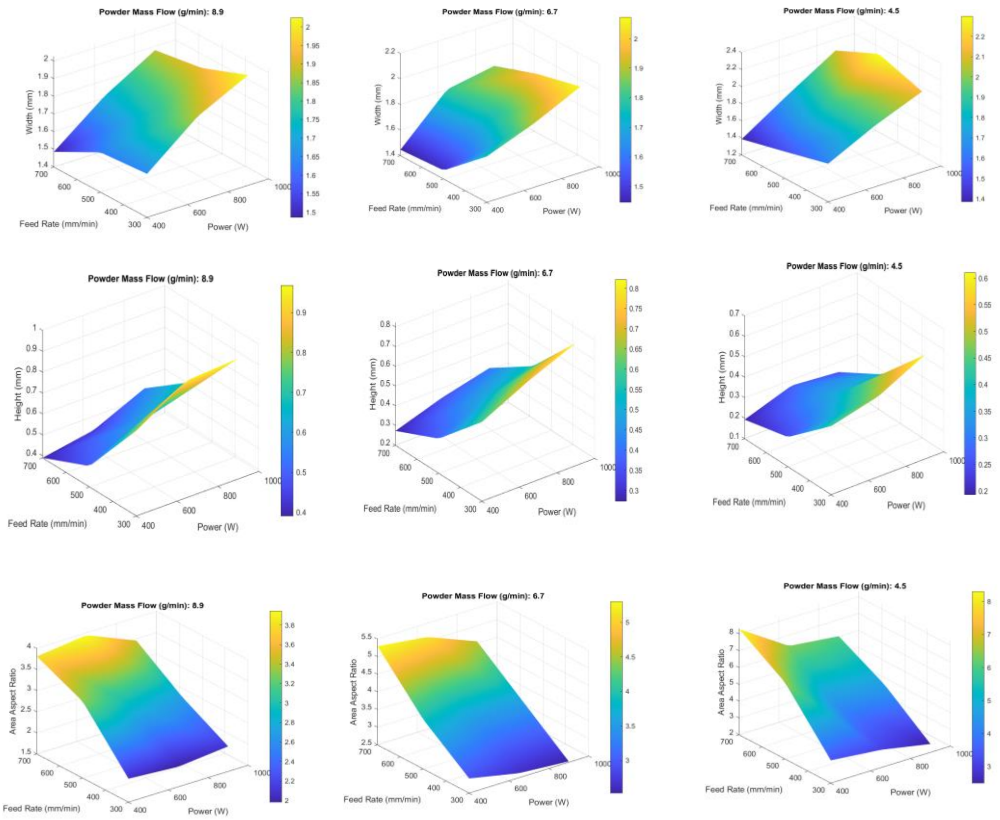

Figure 5. Plots of clad width, height, and area aspect ratio with respect to process parameters: laser power, feed rate and mass flow rate. [Note: Please zoom for better clarity]

A.2.2. Layer height optimization

LMD process is not as stable as other AM processes such as SLM or EBM. Therefore, it is essential to calculate the correct layer height; otherwise, there are high chances of creating porosities between tracks. Therefore, to optimize the layer height theoretically, models already reported in the literature [3]. We have used a simple second-order parabola model that uses the single track's clad characteristics as inputs to find the height and width for future overlap clad tracks. The model showed a high level of accuracy, as reported in [1-3]. The overall methodology and equations are discussed [3].

We calculated the height and width for the first 20 tracks using an overlap of 45 %, as shown in the Figure 5. As can be seen, for the first 4 tracks, the height and width are not stable (related to the LMD process itself). Therefore, the height and width of the 5th track are used while printing.

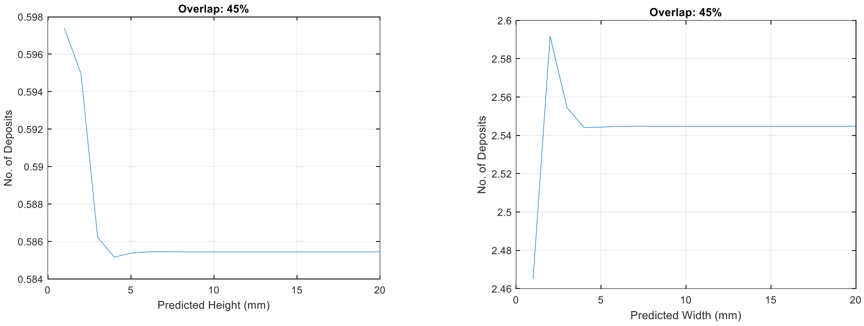

Figure 5. Clad height (left) and width (right) for an overlap of 45 % predicted by second order

A.3. Bibliography

1. RAMIRO, Pedro, ORTIZ, Mikel, ALBERDI, Amaia, et al. Geometrical model and strategy in single and multilayer structures deposited by powder-fed Directed Energy Deposition. Procedia CIRP, 2020, vol. 94, p. 352-356.
2. RAMIRO-CASTRO, Pedro, ORTIZ, Mikel, ALBERDI, Amaia, et al. Effects of Gravity and Non-Perpendicularity during Powder-Fed Directed Energy Deposition of Ni-Based Alloy 718 through Two Types of Coaxial Nozzle. Metals, 2020, vol. 10, no 5, p. 560.
3. RAMIRO, Pedro, ORTIZ, Mikel, ALBERDI, Amaia, et al. Strategy development for the manufacturing of multilayered structures of variable thickness of Ni-based alloy 718 by powder-fed directed energy deposition. Metals, 2020, vol. 10, no 10, p. 1280.

RÉSUMÉ

Ces dernières années, la fabrication additive métallique a connu un énorme changement de paradigme, passant du prototypage à la production en série en raison de sa capacité à pouvoir produire des pièces complexes. De plus, la fabrication additive métallique offre des degrés de liberté supplémentaires en termes de flexibilité et de fonctionnalités de conception. De nos jours, les fournisseurs de machines cherchent à améliorer les performances des machines commerciales en les instrumentant afin de réaliser des mesures in-situ en temps réel. Cette surveillance permettra d'améliorer la qualité, la fiabilité et la répétabilité des pièces. L'enjeu est de pouvoir traiter les données capturées in situ et de les corréler avec les différentes étapes du processus.

Cette thèse présente une méthodologie pour détecter et identifier les anomalies pendant la fabrication d'une pièce par le procédé de fusion laser-lit de poudre (L-PBF) en utilisant les instrumentations commerciales in situ. Dans un premier temps, une étude approfondie basée sur les aspects microstructuraux et mécaniques de l'alliage AlSi7Mg0.6 est réalisée, et la stratégie de balayage la mieux adaptée est identifiée. Cette étude a servi de base pour réaliser des corrélations entre les interactions laser/matériaux et le résultat du processus (signaux du bain de fusion).

Différents types d'instrumentation in situ tels que les caméras infrarouges et les systèmes commerciaux à base de photodiodes sont étudiés pour mieux comprendre l'interaction laser-poudre. La tomographie optique EOSTATE coaxiale basée sur une caméra fournie par EOS GmbH est exploitée, et une étude de cas basée sur des techniques d'analyse de données est proposée pour identifier les couches de dérive potentielles. De même, une méthodologie basée sur l'apprentissage automatique est développée pour extraire les caractéristiques critiques aux échelles globale et locale pour le module in situ de surveillance du bain de fusion de SLM Solutions GmbH basé sur des photodiodes. Comme nous le savons, l'interaction laser-poudre dépend non seulement des paramètres du procédé mais également de l'étalement du lit de poudre. Les caractéristiques critiques du lit de poudre sont ainsi identifiées à l'aide du système de contrôle des couches et d'algorithmes de vision par ordinateur et une méthodologie est proposée pour identifier les anomalies d'étalement du lit de poudre et leur influence sur le signal du bain de fusion. Une étude de cas est présentée pour étudier l'efficacité et la robustesse de la méthodologie proposée.

Mots-clés : L-PBF, apprentissage automatique, surveillance du bain de fusion, assurance qualité, surveillance in situ

Abstract

In recent years, metal additive manufacturing has undergone a huge paradigm shift from prototyping to mass production due to its ability to produce complex parts. In addition, metal additive manufacturing offers additional degrees of freedom in terms of flexibility and design functionality. Today, machine suppliers are looking to improve the performance of commercial machines by instrumenting them to perform real-time in-situ measurements. This monitoring will improve the quality, reliability and repeatability of parts. The challenge is to be able to process the data captured in-situ and correlate it with the different stages of the process.

This thesis presents a methodology to detect and identify anomalies during the manufacturing of a part by the laser-powder bed fusion (L-PBF) process using commercial in situ instrumentation. First, an in-depth study based on the microstructural and mechanical aspects of the AlSi7Mg0.6 alloy is performed, and the most suitable scanning strategy is identified. This study was used as a basis to perform correlations between laser/material interactions and the process outcome (melt pool signals).

Different types of in-situ instrumentation such as infrared cameras and commercial photodiode-based systems are studied to better understand the laser-powder interaction. EOSTATE coaxial optical tomography based on a camera provided by EOS GmbH is exploited, and a case study based on data analysis techniques is proposed to identify potential drift layers. Similarly, a machine learning-based methodology is developed to extract critical features at global and local scales for SLM Solutions GmbH's in situ photodiode-based melt monitoring module. As we know, the laser-powder interaction depends not only on the process parameters but also on the spread of the powder bed. Critical characteristics of the powder bed are thus identified with the help of the layer control system and computer vision algorithms and a methodology is proposed to identify powder bed spreading anomalies and their influence on the melt signal. A case study is presented to investigate the effectiveness and robustness of the proposed methodology.

Keywords: L-PBF, machine learning, melt pool monitoring, quality assurance, in-situ monitoring